

**LOWER-HYBRID HEATING EXPERIMENTS
ON THE VERSATOR II TOKAMAK**

by
Stephen Fuller Knowlton
A.B. Middlebury College
(1975)

Submitted to the Department of Physics
in Partial Fulfillment of the
Requirements of the
Degree of

DOCTOR OF PHILOSOPHY
at the
MASSACHUSETTS INSTITUTE OF TECHNOLOGY
December 1983

© Massachusetts Institute of Technology

Signature of Author  _____
Department of Physics
Oct. 5, 1983

Certified by  _____
Miklos Porkolab
Thesis Supervisor

Accepted by _____
George F. Koster
Chairman, Ph.D. Committee

MASSACHUSETTS INSTITUTE
OF TECHNOLOGY

MAR 14 1984

LIBRARIES

ARCHIVES

LOWER-HYBRID HEATING EXPERIMENTS ON THE VERSATOR II TOKAMAK

by
Stephen Fuller Knowlton

Submitted to the Department of Physics
on October 5, 1983 in partial fulfillment of the
requirements for the Degree of
Doctor of Philosophy in Physics

Abstract

An experimental study of lower-hybrid wave heating has been conducted on the Versator II tokamak. Up to 100 kW of rf power at 800 MHz has been injected into the Versator plasma ($\bar{n}_e = 1-3 \times 10^{13} \text{ cm}^{-3}$, $B_o = 12-15 \text{ kG}$, $T_{e0} = 350-450 \text{ eV}$, $T_{i0} = 100-160 \text{ eV}$) through a four-waveguide grill. Experiments have been performed with a conventional antenna launching waves from the outer major radius of the plasma column, and also with a launcher located at the top of the torus.

A power density of 1.4 kW/cm² transmitted rf power has been achieved in carbon-coated waveguides without breakdown. Rf breakdown has also been successfully suppressed with the use of an auxiliary magnetic field in the grill. Optimal coupling of the rf power to the plasma ($R \leq 15\%$) for the side-launching grill is obtained when the density at the grill mouth is 5-10 times overdense. The coupling results are in reasonable agreement with a modified Brambilla theory.

An energetic ion tail has been observed during rf injection into plasmas with densities $\bar{n}_e \geq 1.3 \times 10^{13} \text{ cm}^{-3}$. The tail has a decay time on the order of 100 μsec , and is oriented perpendicularly to the magnetic field. A maximum bulk ion temperature increase of 50 eV for 50 kW net rf power has been recorded at $\bar{n}_e = 2.6 \times 10^{13} \text{ cm}^{-3}$ but the bulk heating is not consistently observed. Suprathermal electron tails have also been detected during the rf pulse for $\bar{n}_e \leq 2.0 \times 10^{13} \text{ cm}^{-3}$ but significant heating of the bulk electron population did not occur.

Thesis Supervisor: Dr. Miklos Porkolab

Title: Professor of Physics

Acknowledgements

I would like to thank my thesis supervisor, Dr. Miklos Porkolab, for his advice and financial support during the course of this work. I am also grateful to the MIT Physics department for providing me with a fellowship during my first three years of study.

My fellow students (Alan Fisher, Kirk Hackett, Matthew Mayberry, Scott McDermott, Burton Richards, Rajeev Rohatgi, and David Stone) sustained me with their comradeship and help, and performed many of the basic measurements cited in this thesis. I would also like to express my heartfelt thanks to Versator technical staff of Tom Evans, Ed Fitzgerald, Manuel Gonzalez, J.J. McCarthy, and Jack Nickerson. It has become a common practice in recent thesis acknowledgements to thank them for not only constructing and maintaining the equipment but also for showing the novice scientist where to find things in the lab. I concur with the above sentiments, and would also like to thank them for cleaning up after me, and for their patient indulgence in letting me try things my way before I would agree that they were right in the first place.

I would like to acknowledge the guidance and assistance of Drs. Kuo-In Chen and Stanley Luckhardt. Their contributions to this project have been substantial and selfless, and their day-to-day perseverance, questioning, and dedication to research have enlightened me as to what professional science is all about. Kuo-In Chen was also the chief diagnostician of the lower-hybrid ion heating experiment, and I doubt that I could have had more pleasant company during the long runs in search of our elusive quarry.

I am grateful to Dr. William Hooke of PPPL for loaning us the 800 MHz rf system for the heating experiment, and to Nelson Bowen, John Lawson, and Al Martin of that lab for technical assistance. I have also benefitted from discussions with personnel of MIT's Plasma Fusion Center, not to mention loans of equipment from that lab. Among many people there who have contributed to this project, I would like to thank Bob Childs, Dave Griffin, Ken Rice, and Drs. Jack Schuss and Yuichi Takase. Dr. Paul Bonoli of the Research Laboratory of Electronics has been invaluable in performing the detailed toroidal ray tracing and transport calculations presented in this thesis, and in explaining to me many facets of the physics of lower-hybrid heating. ;

I am indebted to Cathy Lydon, who typed most of this manuscript, and Andy Poynor, who is responsible for the professional draftsmanship. My thanks also go to Joel Fajans for teaching me to use the \TeX typesetting system.

My friends have given me unbounded support through this ordeal. Lindy, John, Laura, Frank, and Dick know as well as I do that I could not have made it without them, and I do not pretend to be able to thank them enough. Deborah Fennessey was an enthusiastic supporter and friend to the end of her life, and I hope to keep her memory with this thesis. There is not space to include every stalwart's name, but you and I know who you are. Finally, I would like to express my gratitude to my parents. They have encouraged me through my entire education, and are as happy to see the completion of this study as I am. It is to them that this work is dedicated.

Contents

Abstract	1
Acknowledgements	2
Table of Contents	3
List of Figures	5
Chapter 1 Introduction	7
1.1 Elementary Description of Lower-Hybrid Waves	7
1.2 Other Lower-Hybrid Heating Experiments	8
1.3 The Versator II Tokamak	11
1.4 Outline of This Thesis	11
Chapter 2 Theory of Lower-Hybrid Heating	14
2.1 Lower-Hybrid Wave Propagation	14
2.2 Thermal Effects on Lower-Hybrid Wave Propagation: Mode Conversion	16
2.2.1. Propagation in the Versator Plasma	19
2.3 Thermal Effects on Lower-Hybrid Wave Propagation: Damping	20
2.4 Ion Tail Formation	31
2.5 Energetic Ion Confinement	46
2.6 Toroidicity and Wave Propagation	48
2.6.1. Toroidal Ray-Tracing on Versator: Side-Launching	52
2.6.2. Toroidal Ray-Tracing on Versator: Top-Launching	60
2.7 Other Effects on Lower-Hybrid Heating	68
Chapter 3 Linear Theory of Lower-Hybrid Wave Coupling	70
3.1 General Theory of Antenna-Plasma Wave Coupling	70
3.2 The Brambilla Coupling Code	75
3.3 Calculated $n_{ }$ Power Spectra	78
3.4 Analytic Solutions of the Coupling Problem	79
3.5 Further Modifications of the Plasma Model	83
3.5.1. Exponential Density Gradient	83
3.5.2. Finite Plasma Within the Waveguides	85
3.6 Conclusion	86
Chapter 4 Versator II Lower-Hybrid Heating Experimental Set-Up	87
4.1 The Tokamak	87
4.2 The Diagnostics	88
4.2.1. VUV Spectroscopy	88
4.2.2. Charge-Exchange Analysis	90
4.2.3. Thomson Scattering, Soft X-Ray Spectroscopy	93
4.2.4. Microwave Interferometry	93
4.2.5. Probes	94
4.2.6. Bolometer	95
4.3 Density and Temperature Profiles; Z_{eff}	96

4.4	The Lower-Hybrid Rf System	102
Chapter 5	Experimental Results: Rf Coupling and Conditioning	107
5.1	Edge Density Measurements	107
5.2	Comparison of Calculated and Experimental Rf Coupling Results	114
5.3	High Power Operation of the Grill	125
5.4	Interpretation of the Rf Breakdown Problem	132
5.5	Improvements in Antenna Performance	138
5.6	Discussion of Antenna Improvements	140
Chapter 6	Experimental Results: Rf Heating	148
6.1	Lower-Hybrid Ion Heating with the Side-Launching Antenna	148
6.1.1.	Perpendicular Charge-Exchange Measurements	148
6.1.2.	VUV Doppler Broadening Measurements	158
6.1.3.	Density Variations During Rf Heating	164
6.1.4.	Bolometry	164
6.1.5.	Parametric Decay	171
6.1.6.	Off-Perpendicular Charge-Exchange Measurements	181
6.1.7.	Variability of the Ion Heating Results	181
6.2	Electron Heating Experiments with the Side-Launching Antenna	184
6.3	Ion Heating Experiments with the Top-Launching Antenna	187
6.3.1.	Interpretation of the Top-Launching Experiments	191
6.4	Plasma Power Balance During Rf Injection	199
Chapter 7	Summary and Conclusion	206
7.1	Rf Coupling	206
7.2	Grill Behavior at High Power	206
7.3	Heating Results	207
Appendix A	Derivation of the Warm Plasma Dispersion Relation	210
Appendix B	Calculation of Minimum Ion Loss Energy	213
Appendix C	Rf Probe Tip Construction	215
Appendix D	Measurement of the Diffusion Coefficient in the Edge Plasma	216
References	218

List of Figures

Figure 2.1	Square of Perpendicular Wave Number vs. Minor Radius	21
Figure 2.2	LH Resonant Density and Mode Conversion Densities vs. Minor Radius	26
Figure 2.3	Minimum and Maximum Damping Radius vs. n_{\parallel}	28
Figure 2.4	Contour Plot of Maximum Mode Conversion Radius	29
Figure 2.5	LH Resonant Density and Mode Conversion Densities vs. Minor Radius	30
Figure 2.6	Wave Power vs. Minor Radius	32
Figure 2.7	Contour Plot of Maximum Damping Radius	33
Figure 2.8	Resonant Ion Energy at the Damping Location vs. n_{\parallel}	35
Figure 2.9	Rf Electric Field vs. Minor Radius	39
Figure 2.10	Ion Tail Temperature vs. n_{\parallel}	41
Figure 2.11	Wave Power vs. Minor Radius with Ion Tail in Plasma	44
Figure 2.12	Wave Damping Radius vs. Ion Tail Density	45
Figure 2.13	Minimum Unconfined Ion Energy vs. Minor Radius	49
Figure 2.14	Resonant Ion Energy vs. Minor Radius	50
Figure 2.15	LH Ray Trajectory for $n_{\parallel}=4$; Side-Launch	53
Figure 2.16	LH Ray Trajectory for $n_{\parallel}=6$; Side-Launch	55
Figure 2.17	LH Ray Trajectory for $n_{\parallel}=8$; Side-Launch	56
Figure 2.18	Contour Plot of Damping Radius from Toroidal Ray Tracing: Side-Launch	57
Figure 2.19	Transport Code Heating Results for Rf Injection with Side-Launcher	59
Figure 2.20	LH Ray Trajectory for $n_{\parallel}=4$; Top-Launch	61
Figure 2.21	LH Ray Trajectory for $n_{\parallel}=6$; Top-Launch	62
Figure 2.22	LH Ray Trajectory for $n_{\parallel}=8$; Top-Launch	63
Figure 2.23	LH Ray Trajectory for $n_{\parallel}=-6$; Top-Launch	65
Figure 2.24	Contour Plot of Damping Radius from Toroidal Ray Tracing: Top-Launch	66
Figure 2.25	Transport Code Heating Results for Rf Injection with Top-Launcher	67
Figure 3.1	Coordinate System of Grill Mouth	71
Figure 3.2	Idealized Density Profile near Grill Mouth	74
Figure 3.3	n_{\parallel} Power Spectrum of the Four-Waveguide Side-Launching Grill	80
Figure 3.4	n_{\parallel} Power Spectrum of the Four-Waveguide Top-Launching Grill	81
Figure 4.1	Schematic of the Versator Vacuum Vessel and Diagnostics Lay-Out	89
Figure 4.2	Temporal Evolution of the Plasma Parameters	97
Figure 4.3	Electron Density Profile from Microwave Interferometry	98
Figure 4.4	Electron Temperature and Density Profiles from Thomson Scattering	99
Figure 4.5	Ion Temperature Profile from VUV Doppler Broadening	100
Figure 4.6	Electron Temperature Profile from Soft X-Ray Spectroscopy	101
Figure 4.7	Diagram of the Rf System	103
Figure 5.1	Limiter Configurations During Coupling Experiments	109
Figure 5.2	Edge Density Profiles in Front of the Grill	110
Figure 5.3	Edge Electron Temperature Profiles in Front of the Grill	111
Figure 5.4	Comparison of Densities Obtained Using LaFramboise and Plane Probe Methods	113
Figure 5.5	Edge Density Profiles in Front of an Inner and Outer Waveguide	115
Figure 5.6	Measured Grill Reflectivity for Two Different Limiter Positions	116
Figure 5.7	Comparison of Experimental and Calculated Grill Reflectivities	118
Figure 5.8	Experimental and Calculated Grill Reflectivity: $\Delta\phi=180^{\circ}$	119
Figure 5.9	Experimental Grill Reflectivity: $\Delta\phi=90^{\circ}$	120

Figure 5.10	Calculated Grill Reflectivity: $\Delta\phi=90^\circ$	121
Figure 5.11	Experimental and Calculated Grill Reflectivity: $\Delta\phi=0^\circ$	122
Figure 5.12	Grill Reflectivity vs. $\Delta\phi$	124
Figure 5.13	Maximum Incident Rf Power vs. Hydrogen Fill Pressure	128
Figure 5.14	Maximum Incident Rf Power vs. Magnetic Field at Grill Mouth	129
Figure 5.15	Grill Reflectivity and Reflected Phase Shift vs. Incident Rf Power	130
Figure 5.16	Single Waveguide Rf Breakdown Behavior	131
Figure 5.17	Calculated Electron Impact Energy vs. Magnetic Field	136
Figure 5.18	SEE and ESD Coefficients vs. Electron Impact Energy	137
Figure 5.19	Illustration of Magnetized Grill	141
Figure 5.20	Reflected Phase Shift vs. Incident Power in Magnetized Grill	142
Figure 5.21	Grill Reflectivity vs. Incident Power in Magnetized Grill	143
Figure 5.22	Calculated Magnetic Field in the Grill	144
Figure 5.23	Reflectivity and Reflected Phase Shift in a Single Magnetized Waveguide	145
Figure 6.1	Charge-Exchange Spectrum of Ion Distribution During Rf Injection	149
Figure 6.2	Ion Tail Temperature, and Decay Wave Power vs. Incident Rf Power	151
Figure 6.3	Charge-Exchange Tail Temperature vs. \bar{n}_e	152
Figure 6.4	900 eV Ion Count-Rate vs. $\Delta\phi$	154
Figure 6.5	900 eV Count-Rate vs. Toroidal Field	155
Figure 6.6	Charge-Exchange Spectrum of Ion Distribution During Rf Injection	157
Figure 6.7	Temporal Evolution of Ion Temperature from VUV Doppler Broadening	159
Figure 6.8	Central Ion Temperature Increase During Rf Injection vs. \bar{n}_e	160
Figure 6.9	Central Ion Temperature Increase During Rf Injection vs. $\Delta\phi$	162
Figure 6.10	Intensity of O VII 1623A line with and without Rf Injection	163
Figure 6.11	Density Evolution During Rf Injection into Gettered and Ungettered Discharges	165
Figure 6.12	Temporal Evolution of Bolometric Emission during Rf Injection	167
Figure 6.13	Line-Averaged Bolometric Emission vs. Chord Height	168
Figure 6.14	Profiles of the Enhanced Bolometric Signal During Rf Injection	169
Figure 6.15	Parametric Decay Spectra Showing Ion Cyclotron Harmonics	172
Figure 6.16	Relative Strength of First Lower Parametric Decay Sideband vs. \bar{n}_e	174
Figure 6.17	Parametric Decay Spectra in Cleaner, Higher Current Plasmas	176
Figure 6.18	Sideband and Low Frequency Decay Wave Strength vs. Transmitted Rf Power	177
Figure 6.19	Parametric Decay Spectra at Different Densities	179
Figure 6.20	Parametric Decay Spectra Near the Second Harmonic of the Pump Frequency	180
Figure 6.21	Off-Perpendicular Charge-Exchange Spectrum During Rf Injection	182
Figure 6.22	Soft X-Ray Spectra Before, During, and After Rf Injection	186
Figure 6.23	Charge-Exchange Spectrum During Rf Injection with Top-Launcher	188
Figure 6.24	Apparent Charge-Exchange Ion Temperature During Rf Injection vs. \bar{n}_e	189
Figure 6.25	Charge-Exchange Spectrum During Rf Injection with Top-Launcher	190
Figure 6.26	Evolution of Ion Temperature from Doppler Broadening and Charge-Exchange	192
Figure 6.27	$\Delta T_{i,0}$ from Charge-Exchange vs. $\Delta\phi$	193
Figure 6.28	800 eV Ion Count-Rate vs. $\Delta\phi$	194
Figure 6.29	Line-Averaged Bolometric Emission vs. Chord Height	195
Figure 6.30	Line-Averaged Bolometric Emission vs. $\Delta\phi$	196

1. Introduction

Controlled thermonuclear fusion in a tokamak may be attained by heating the plasma with radio frequency (rf) waves or neutral beams to temperatures above those achieved by ohmic heating. Rf heating of the plasma in the lower-hybrid range of frequencies (0.5–5 GHz for present-day tokamaks) is a possible candidate for a practical and efficient heating scheme.¹ Lower-hybrid waves are predicted to damp on the ion population at a location near the lower-hybrid resonance in the plasma.² Direct heating of the ions is considered desirable because it is the ions that undergo fusion, and in most present tokamaks the ion temperature is lower than the electron temperature by a factor of 1.5 to 3. Furthermore, in present-day devices, the ion energy confinement time is generally longer than that for electrons, suggesting that ion heating should be more efficient in raising the plasma energy than electron heating if the absorption efficiencies on the two populations are comparable. Electron heating via electron Landau damping of lower-hybrid waves is also possible.^{3–5} Since high power sources in this frequency range are commercially available, and as lower-hybrid waves can be efficiently coupled to the plasma via an all-metal antenna consisting of a phased array of waveguides^{6,7} located at the plasma edge, the technology of lower-hybrid heating is believed to present few, if any, major obstacles to applications on present and future devices.

The goal of this thesis work is the experimental investigation of the physics of lower-hybrid ion heating of a tokamak plasma. The emphasis of this study is on determining under what plasma conditions rf heating occurs. An assessment of the efficiency of any such heating is of primary interest. These studies are performed on the Versator II tokamak using an 800 MHz rf system to generate the lower-hybrid waves.

1.1. Elementary Description of Lower-Hybrid Waves

The lower-hybrid wave is so named because of its association with the lower-hybrid resonance of the plasma. In the cold plasma model of wave propagation, two waves of the same frequency but different dispersion characteristics may be excited in the plasma.⁸ In the limit of $\omega_{ce} \gg \omega \gg \omega_{ci}$, the simple electrostatic dispersion relation of the lower hybrid wave is

$$1 + \frac{\omega_{pe}^2}{\omega_{ce}^2} - \frac{\omega_{pi}^2}{\omega^2} - \frac{k_{\parallel}^2}{k_{\perp}^2} \frac{\omega_{pe}^2}{\omega^2} = 0 \quad (1.1)$$

where ω denotes the angular frequency of the wave, $\omega_{c\alpha} = Z_{\alpha}eB/m_{\alpha}c$, and $\omega_{p\alpha} = \sqrt{4\pi n_{\alpha}Z_{\alpha}^2e^2/m_{\alpha}}$ for the particle species α . The quantity e is the electron charge, B the local magnetic field, c the speed of light, Z_{α} the particle charge state, n_{α} the particle number density, and m_{α} the particle mass. The angular frequencies ω_{pe} and ω_{pi} are the electron and ion plasma frequencies, and ω_{ce} and ω_{ci} are the electron and ion cyclotron frequencies, respectively. The wave vectors parallel and perpendicular to the magnetic field are k_{\parallel} and k_{\perp} , respectively. The dispersion relation exhibits a resonance ($k_{\perp}^2 \Rightarrow \infty$) for

$$\omega^2 = \omega_{LH}^2 \equiv \frac{\omega_{pi}^2}{1 + \omega_{pe}^2/\omega_{ce}^2}, \quad (1.2)$$

where we have defined the lower-hybrid frequency ω_{LH} . The resonant frequency is seen to depend on the plasma density, magnetic field, and the ion mass and charge. Collisionless damping of the wave due to finite plasma temperature effects is expected to occur in the vicinity of the resonance, should it exist in the plasma. Close to the resonance the condition $k_{\perp}\rho_{ci} \gg 1$ is valid, where $\rho_{ci} = v_{thi}/\omega_{ci}$ is the ion gyroradius, $v_{thi} = (2T_i/m_i)^{1/2}$ is the ion thermal velocity, and T_i the local ion temperature. If the above inequality is satisfied, wave absorption may take place via ion cyclotron damping if $\omega \approx n\omega_{ci}$, n being an integer,⁸⁻¹⁰ or by perpendicular ion Landau damping when the perpendicular phase velocity of the wave becomes close to the ion thermal velocity: $\omega/k_{\perp}v_{thi} \approx O(1)$.^{9,11}

A resonance for the other cold plasma wave of frequency ω (the fast wave) in this range does not exist. Thus the coupling of the two waves should be detrimental to ion heating, and is to be avoided in a heating experiment. For coupling not to occur, the following accessibility condition must be satisfied:⁸

$$n_{\parallel}^2 > \left(1 - \frac{\omega^2}{\omega_{ce}\omega_{ci}}\right)^{-1} \quad (1.3)$$

or if the resonance is present at the plasma center,¹²

$$n_{\parallel}^2 > 1 + \frac{\omega_{pe}^2}{\omega_{ce}^2} \Big|_{\omega=\omega_{LH}}, \quad (1.4)$$

where n_{\parallel} is the parallel wave number, ck_{\parallel}/ω .

In practice, the frequency ω is determined by the rf generator, and the launched n_{\parallel} spectrum of the lower-hybrid waves is governed by the antenna properties. With these constraints, the minimum required magnetic field in the plasma is determined by the accessibility condition Eq. (1.3). The density is chosen such that the lower hybrid resonance given by Eq. (1.1) lies at or near the center of the plasma. Thermal effects on the propagation of the wave modify this description, and are discussed in detail in the next chapter along with the damping mechanisms.

1.2. Other Lower-Hybrid Heating Experiments

Lower-hybrid heating experiments have also been carried out or are presently being performed on the following tokamaks: ATC¹³⁻¹⁵, Wega¹⁶⁻¹⁹, FT-1,²⁰ Petula²¹⁻²³, Doublet IIA²⁴, Alcator^{25,26}, JFT-2²⁷⁻³¹, JIPP T-II^{32,33}, Alcator C³⁴⁻³⁷, and PLT^{38,39}. Ion and/or electron heating were reported to occur in all of the above experiments.

Historically, the Versator experiment is a direct continuation of the ATC lower-hybrid studies in that the same rf source is employed in the present experiment as was used in the latter, and the plasma parameters of the two tokamaks are somewhat similar. In the ATC experiment, ion

temperature increases of approximately 100 eV were measured during rf injection by perpendicular charge-exchange analysis and Doppler broadening of the O VII impurity line at 1623Å. However, it was reportedly unclear from those experiments if the apparent temperature increases were truly thermal effects.¹³ Above an injected power level of 120 kW, the apparent temperature increase diminished with increasing rf power.¹⁴ In general, a perpendicularly-oriented fast ion population with a confinement time of $\leq 100 \mu\text{sec}$ was also created during the rf pulse for plasma densities above $\bar{n}_e \approx 1.0 \times 10^{13} \text{ cm.}^{-3}$. Here, \bar{n}_e refers to the measured line-averaged electron density of the plasma. Little or no increase in the ion temperature was observed by parallel charge-exchange measurements.¹³ Parametric decay of the lower-hybrid wave was also observed in these experiments. The threshold for the onset of the decay was found to depend on the target plasma density, and was suggested to be responsible for the creation of the fast ion tail and possibly the bulk heating.¹⁵

The short-lived perpendicular ion tail generated during the rf pulse is a common feature of all lower-hybrid ion heating experiments to date. Generally, the central plasma density must be above a threshold level on the order of one-half of the lower-hybrid resonant density for tail formation to occur. The tail is usually detected in conjunction with observation of parametric decay.

In many of the experiments, heating of the bulk ion distribution was purportedly observed. Heating efficiencies are often reported with the figure of merit $\bar{n}_e \Delta T_i / P_{rf}$ ($\text{eV/kW} \cdot 10^{-13} \text{ cm.}^3$), where ΔT_i is the measured increase of the central ion temperature and P_{rf} is the transmitted (incident minus reflected) rf power. The central heating is usually inferred from charge-exchange measurements, but corroborating evidence of plasma heating is often provided by a rise in the impurity ion temperatures as measured by Doppler-broadening of the VUV spectroscopic lines of O VII and C V.^{13,14,16,17,27-33} In the case of deuterium plasmas, an increase in the neutron flux is also used to indicate ion temperature changes during rf injection.^{13,25,26,34,38,39}

On the JFT-2 experiment, heating rates of up to $3 \text{ eV/kW} \cdot 10^{-13} \text{ cm.}^3$ were obtained for injection of 200 kW at 750 MHz.^{30,31} In addition to an ion tail in the perpendicular direction, a tail was observed in the parallel ion energy spectrum, indicating that isotropization and thermalization of the fast ion population occurred. The lifetime of the parallel tail was 1-2 ms., corresponding to the calculated slowing down time of fast ions in the central plasma. The heating efficiency was reported to vary significantly with the electron temperature at the plasma edge, with better heating achieved with higher edge temperatures.^{30,31,40,41} The reason cited for the variation is that the threshold for parametric decay is generally higher for higher plasma temperatures, which is to be expected on theoretical grounds.^{42,43} The amplitude of the parametric decay waves is believed to be high at the plasma edge in that experiment, and the decay process represents a loss mechanism for the inward propagating lower-hybrid wave.

A similar heating efficiency is reported from the most recent experiments on the Petula tokamak in which a central ion temperature rise of 280 eV is recorded for an injected power of

450 kW at 1.25 GHz for a line-averaged density of $4.9 \times 10^{13} \text{ cm}^{-3}$. A parallel ion tail was also observed in these studies.²³

Qualitatively similar results with lower efficiencies were obtained on the JIPP T-II^{32,33} and Wega¹⁹ tokamaks. In both cases, a heating efficiency of approximately $1.2 \text{ eV/kW} \cdot 10^{-13} \text{ cm}^3$ resulted from injection of 150 kW rf power at 800 MHz. Again, the temperatures in both cases were inferred from parallel charge-exchange measurements. Earlier experiments at 500 MHz with loop couplers on the Wega tokamak¹⁶⁻¹⁸ achieved a lower heating efficiency ($0.8 \text{ eV/kW} \cdot 10^{-13} \text{ cm}^3$), and no parallel ion tail was observed. The measured central density increased by a factor of two during the rf pulse in that experiment. A heating efficiency of $1.3 \text{ eV/kW} \cdot 10^{-13} \text{ cm}^3$ as measured by perpendicular charge-exchange was reported from the early Petula experiments for a net rf power of 540 kW at 1.25 GHz.^{21,22}

No bulk ion heating was measured in the Alcator A 2.45 GHz, 90 kW lower-hybrid heating experiment, although a perpendicular ion tail was observed.^{25,26} Similarly, ion heating by wave damping on the ion population has not been seen to date in the Alcator C 4.6 GHz lower-hybrid studies.³⁴ In recent experiments at 800 MHz on PLT, tails on the parallel and perpendicular ion distributions were measured during the rf pulse, but the bulk heating was reportedly inefficient,^{38,39} of the order of $1 \text{ eV/kW} \cdot 10^{-13} \text{ cm}^3$. The observed parallel tail was not localized to the center of the plasma.

Changes in the line-averaged density were often reported to occur during the rf pulse, but with the exception of the early Wega experiments,¹⁶⁻¹⁸ the changes were limited to 10-20%. On JFT-2, it was found that the sign of the density change depended on the cleanliness of the vacuum vessel wall: with little or no titanium gettering of the chamber prior to the discharge, the density increased during the rf pulse, while with strong gettering, the density was observed to decrease.⁴⁴ The explanation suggested for this phenomenon is that the flux of ions to the wall is increased during the rf pulse due to the presence of the poorly confined perpendicular ion tail. The varying density behavior during the pulse resulted from the suspected different recycling coefficient of the wall under the comparatively dirty and clean chamber conditions.

Electron heating has also been observed in most of the experiments mentioned above. The heating was usually obtained when the density was below that at which ion tail formation and ion heating were noted. Electron heating is predicted to result from parallel Landau damping of the lower-hybrid wave on suprathermal electrons which collisionally heat the bulk population. On Wega,¹⁹ the measured electron heating efficiency was $4 \text{ eV/kW} \cdot 10^{-13} \text{ cm}^3$; on JFT-2,^{30,31} the similar number was $1 \text{ eV/kW} \cdot 10^{-13} \text{ cm}^3$. An electron heating efficiency of $10-20 \text{ eV/kW} \cdot 10^{-13} \text{ cm}^3$ has been reported from the Alcator-C experiments.³⁵⁻³⁷ In addition, suprathermal tails on the electron distribution have been measured by soft X-ray spectroscopy and synchrotron emission. At very low plasma densities, e.g., $\bar{n}_e \leq 8 \times 10^{12} \text{ cm}^{-3}$ for PLT or $\bar{n}_e \leq 5 \times 10^{13} \text{ cm}^{-3}$ for

Alcator C, current-drive on the fast electron population is observed in many tokamak experiments, including Versator.^{23,31,33,34—39,45—52}

To summarize the ion heating results of other experiments, we reiterate that superthermal ion tails oriented in the perpendicular direction are always generated during the rf pulse when the plasma density is in a specific range: ion tails are generally observed when the central plasma density is greater than one-half the density of the lower-hybrid resonance. The short confinement time of the perpendicular tail is commonly believed to indicate that the tail is present in the outer layers of the plasma, and may result from damping of parametric decay waves created near the edge of the plasma. However, in the JFT-2^{27,28} and Alcator A^{25,26} experiments in which radial scans of the charge-exchange neutral emission were performed, the observed ion tails were not localized to the plasma periphery. The physical processes responsible for producing the ion tails are still in question. Furthermore, bulk heating of the ion distribution has not been observed in all of these experiments, and the heating results are reportedly variable on the same device for similar gross plasma parameters.^{30,31,40,41} At present, the reasons for the discrepancies between the results of the different experiments are not fully understood, nor is the mechanism of lower hybrid heating in these studies particularly clear. The experimental work of this thesis has been motivated in part by the somewhat puzzling nature of these results, with the hope that an additional investigation would help to clarify the physics behind the observed phenomena.

1.3. The Versator II Tokamak

The device on which our experiment is performed is the Versator II research tokamak, associated with the Plasma Fusion Center and Research Laboratory of Electronics of M.I.T. The tokamak itself has been described elsewhere,^{53—57} and aspects of the tokamak and diagnostics relevant to this work are presented in Chapter 4.

Lower-hybrid waves are coupled into the Versator plasma with a phased-array waveguide antenna, or grill. Two grills have been used at different times in the course of this work: a four-waveguide array which launches waves into the torus from the midplane at the outer major radius, and another four-waveguide grill launching waves from the top of the plasma column. The antennas and the rest of the rf system are also described further in Chapter 4. The basic plasma and rf system parameters for the lower-hybrid ion heating experiment are listed in Table 1.

1.4. Outline of This Work

The thesis is organized as follows: in Chapter 2, the theory of lower-hybrid wave propagation and damping is discussed with the purpose of qualitatively assessing the general effectiveness of rf heating in Versator and determining the optimal conditions for its occurrence. The theory of the coupling of the lower-hybrid wave to the plasma is described in detail in Chapter 3. The experimental set-up is described in Chapter 4, with emphasis placed on the diagnostics used in this study and the rf system itself. In Chapter 5, the application of the rf coupling theory to our

work is compared with the experimental measurements of antenna reflectivity. Also treated in this chapter is the preparation and conditioning of the lower-hybrid antenna for high-power operation. The experimental heating results are presented and discussed in Chapter 6. In Chapter 7, the experimental work is summarized, and the applicability of our findings to future lower-hybrid heating projects is discussed.

Table 1

Versator II Tokamak and Lower-Hybrid Rf System Parameters for Ion Heating Experiments.

Tokamak

Major radius R_o	40.5 cm.
Limiter radius a	13 cm.
Toroidal magnetic field B_o	≤ 15 kG
Plasma Current I_p	40–55 kA
Loop voltage V_l	1.6–2.5 V
Line-averaged electron density \bar{n}_e	$1-3.2 \times 10^{13} \text{ cm}^{-3}$ parabolic profile
Central electron temperature T_{eo}	350–450 eV
T_e profile width (Gaussian) λ_{te}	7.5 cm.
Central ion temperature T_{io}	120–150 eV
T_i profile width (Gaussian) λ_{ti}	10.5 cm.
Effective ion charge Z_{eff}	2 (gettered discharges)
Safety factor q	6 at limiter

Rf System

Frequency $\omega/2\pi$	800 MHz
Maximum power P_{rf}	140–160 kW from klystron; 100–110 kW into plasma
Antenna (2)	4-waveguide phased arrays; one with waveguide width 2.45 cm, $n_{ }(\text{typ.}) \simeq 5.5$ for $\Delta\phi = 180^\circ$; the other with waveguide width 1.0 cm, $n_{ }(\text{typ.}) \simeq 15$ for $\Delta\phi = 180^\circ$

2. Theory of Lower-Hybrid Ion Heating

In this chapter, the theory related to the experimental rf heating work is presented. The purpose is to provide a framework in which the results of the experiment may be analyzed. The basic physics of the propagation of lower-hybrid waves in a cold plasma is outlined first, followed by a discussion of thermal effects on lower-hybrid wave propagation with particular emphasis placed on those aspects, which are relevant to the ion heating experiment; namely mode conversion and absorption. Calculations of the propagation characteristics in the Versator plasma are made in the approximation of cylindrical slab geometry with the spatial variation of the toroidal field included. Next, the wave damping mechanism as it is presently understood is presented, and the expected wave absorption regions of the Versator plasma are computed. The problems of energetic particle confinement pertinent to this experiment are also discussed, and their effects on the plasma heating efficiency are qualitatively considered. Lastly, the full effect of the toroidal geometry of the tokamak on the wave propagation is described with the use of numerical computations performed for Versator parameters by Dr. Paul Bonoli. Applications and discussions related specifically to the experimental heating results are left to Chapter 6.

2.1. Lower-Hybrid Wave Propagation

Wave propagation in a cold plasma is described by the following wave equation⁸ for the rf electric field \mathbf{E} :

$$\nabla \times \nabla \times \mathbf{E} - \frac{\omega^2}{c^2} \mathbf{K} \cdot \mathbf{E} = 0 \quad (2.1)$$

where \mathbf{K} is the dielectric tensor:

$$\mathbf{K} = \begin{pmatrix} K_{xx} & iK_{xy} & 0 \\ -iK_{yx} & K_{yy} & 0 \\ 0 & 0 & K_{zz} \end{pmatrix}.$$

The magnetic field of the tokamak, B_0 , is assumed to lie in the z -direction. For the lower-hybrid range of frequencies, the inequality $\omega_{ci} \ll \omega \ll \omega_{ce}$ is valid. The components of the dielectric tensor may be approximated as

$$\begin{aligned} K_{xx} = K_{yy} &= 1 + \frac{\omega_{pe}^2}{\omega_{ce}^2} - \frac{\omega_{pi}^2}{\omega^2} \\ K_{zz} &= 1 - \frac{\omega_{pe}^2}{\omega^2} \\ K_{xy} = K_{yx} &= \frac{\omega_{pe}^2}{\omega \omega_{ce}}. \end{aligned} \quad (2.2)$$

For a homogeneous plasma, the wave equation (2.1) may be written as

$$\mathbf{n}(\mathbf{n} \cdot \mathbf{E}) - n^2 \mathbf{E} + \mathbf{K} \cdot \mathbf{E} = 0 \quad (2.3)$$

where n is the refractive index, ck/ω . The condition that a solution to Eq. (2.3) exists gives the dispersion relation for $n(\omega)$. As the plasma parameters are nearly constant along the z -axis, the equation is written in a standard form in which n_{\parallel} is an independent variable, fixed by the launching structure, and n_{\perp} is the dependent variable:

$$An_{\perp}^4 + Bn_{\perp}^2 + C = 0 \quad (2.4)$$

where

$$\begin{aligned} n_{\perp}^2 &= n_x^2 + n_y^2 \\ A &= K_{xx} \\ B &= (n_{\parallel}^2 - K_{xx})(K_{xx} + K_{zz}) + K_{xy}^2 \\ C &= K_{zz} \left[(n_{\parallel}^2 - K_{xx})^2 - K_{xy}^2 \right]. \end{aligned}$$

The dispersion relation has two solutions corresponding to the slow and fast waves:

$$n_{\perp}^2 = \frac{-B \pm \sqrt{B^2 - 4AC}}{2A} \quad (2.5)$$

which are de-coupled from one another if

$$B^2 \gg 4AC. \quad (2.6)$$

In the approximation $\omega_{ce}, \omega_{pe} \gg \omega$, the above inequality reduces to

$$n_{\parallel}^2 \gg |K_{xx}/K_{zz}|^{\frac{1}{2}} K_{xy} \approx \frac{\omega_{pe}}{\omega_{ce}} \approx O(1) \quad (2.7)$$

if $n_{\parallel}^2 > K_{xx} - K_{xy}^2/K_{zz}$. In this limit, the approximate roots of the cold dispersion relation Eq. (2.5) are $n_{\perp s}^2 \simeq -B/A$ and $n_{\perp f}^2 \simeq -C/B$, or¹²

$$n_{\perp s}^2 \simeq -\frac{K_{zz}}{K_{xx}} \left[n_{\parallel}^2 - K_{xx} - K_{xy}^2 \right] \quad (2.8a)$$

$$n_{\perp f}^2 \simeq \frac{K_{xy}^2 - (n_{\parallel}^2 - K_{xx})^2}{n_{\parallel}^2 - K_{xx} + K_{xy}^2/K_{zz}} \quad (2.8b)$$

where the "f" and "s" subscripts refer to the fast and slow branches. From Eq. (2.2), K_{xx} can vanish if $\omega^2 < \omega_{ce}\omega_{ci}$ and the density is sufficiently high; hence a resonance ($n_{\perp}^2 \Rightarrow \infty$) for the slow wave of Eq. (2.8a) exists at the location where

$$\frac{\omega_{pe}^2}{\omega_{ce}^2} = \left(\frac{\omega_{ce}\omega_{ci}}{\omega^2} - 1 \right)^{-1}. \quad (2.9)$$

As will be discussed in Sections 2.2 and 2.3, the large $n_{\perp s}^2$ values of the slow wave near the resonance are expected to give rise to ion heating.

The solutions corresponding to the fast and slow waves converge if $B^2 - 4AC = 0$ in Eq. (2.5). Using this condition, we find that if⁸

$$n_{\parallel}^2 > \left(1 - \frac{\omega^2}{\omega_{ce}\omega_{ci}}\right)^{-1} = n_{\parallel crit}^2 \quad (2.10)$$

the juncture of the two roots is avoided, and the resonance is accessible to lower-hybrid waves incident from lower densities. This is the so-called accessibility condition. If the relation (2.10) is not satisfied, the inward propagating slow wave is converted to an outward propagating fast wave at a density below the resonant density. If the lower-hybrid resonance indeed exists in the plasma, the above inequality reduces to ¹²

$$n_{\parallel}^2 > 1 + \frac{\omega_{pe}^2}{\omega_{ce}^2} \Bigg|_{\omega=\omega_{LH}} \quad (2.11)$$

For the Versator heating experiment with $B_o = 14$ kG, only waves with $n_{\parallel} > 2.1$ are accessible to the center.

2.2. Thermal Effects on Lower-Hybrid Wave Propagation: Mode Conversion

Though the lower-hybrid wave is well described by the cold plasma dispersion relation Eq. (2.4) in the limit $k_{\perp}\rho_{ci}, k_{\perp}\rho_{ci} \ll 1$, the perpendicular wave vector k_{\perp} can become large in the vicinity of the lower-hybrid resonance, allowing $k_{\perp}\rho_{ci}$ to become larger than 1. Thermal effects on the propagation of lower-hybrid waves near the resonance must be considered for an accurate treatment of the problem. With the inclusion of thermal effects, mode conversion of the slow wave to a shorter wavelength ion plasma wave is predicted to occur at a density below the resonant density². More importantly, heating of the plasma by collisionless damping of the lower-hybrid waves is also expected. In this section, we discuss the thermal corrections to the cold plasma dispersion relation and the phenomenon of mode conversion. The damping of the lower-hybrid wave is described in the next section.

The effect of finite plasma temperature on the propagation of lower-hybrid waves is obtained from the dispersion relation for electrostatic waves in a hot plasma:⁸

$$D = 1 + \chi_e + \chi_i = 0 \quad (2.12)$$

where $\chi_{e,i}$ are the electron and ion susceptibilities, given by

$$\chi_{\alpha} = \frac{1}{k^2\lambda_{D\alpha}^2} \left[1 + \sum_{n=-\infty}^{\infty} I_n(b_{\alpha}) \exp(-b_{\alpha}) \xi_{o\alpha} Z(\xi_{n\alpha}) \right] \quad (2.13)$$

for a general species α . Here, I_n is the modified Bessel function of the first kind of order n , Z is the plasma dispersion function⁵⁸, $\lambda_{D\alpha} = v_{th\alpha}/\sqrt{2}\omega_{p\alpha}$ is the Debye length, $b_{\alpha} = k_{\perp}^2\rho_{c\alpha}^2/2$, $\xi_{n\alpha} = (\omega - n\omega_{c\alpha})/k_{\parallel}v_{th\alpha}$, $v_{th\alpha}^2 = 2T_{\alpha}/m_{\alpha}$, and $\rho_{c\alpha} = v_{th\alpha}/\omega_{c\alpha}$.

We expand the susceptibilities Eqs. (2.13) to lowest order in v_{the} and v_{thi} to obtain the real part of the warm plasma dispersion relation. It is assumed that $k_{\perp}^2\rho_{ce}^2, k_{\perp}^2\rho_{ci}^2 \ll 1$ and $|\xi_{ne}|, |\xi_{ni}| \gg 1$. The expansion is performed in Appendix A. The results are:

$$\begin{aligned}
\text{Re } \chi_e \simeq & \frac{k_{\perp}^2}{k^2} \frac{\omega_{pe}^2}{\omega_{ce}^2} \left(1 - \frac{3}{8} \frac{k_{\perp}^2 v_{the}^2}{\omega_{ce}^2} \right) \\
& - \frac{k_{\parallel}^2}{k^2} \frac{\omega_{pe}^2}{\omega^2} \left(1 + \frac{3}{2} \frac{k_{\parallel}^2 v_{the}^2}{\omega^2} - \frac{1}{2} \frac{k_{\perp}^2 v_{the}^2}{\omega_{ce}^2} \right)
\end{aligned} \tag{2.14a}$$

$$\text{Re } \chi_i \simeq -\frac{\omega_{pi}^2}{\omega^2} \left(1 + \frac{3}{2} \frac{k_{\perp}^2 v_{thi}^2}{\omega^2} \right) \tag{2.14b}$$

In the opposite limit for the ions, $k_{\perp}^2 \rho_{ci}^2 \gg 1$, the ion susceptibility Eq. (2.13) may be rewritten with the use of a Hadamard expansion^{10,59} in powers of $(k_{\perp} \rho_{ci})^{-1}$:

$$\chi_i = \frac{1}{k^2 \lambda_{Di}^2} \left(1 + \zeta_i \text{Re } Z(\zeta_i) - \zeta_i \text{Im } Z(\zeta_i) \left[\cot \left(\pi \frac{\omega}{\omega_{ci}} \right) + \frac{1}{2\pi} \sum_{n=-\infty}^{\infty} \frac{\omega_{ci}}{\omega - n\omega_{ci}} \frac{dZ(\xi_{ni})}{d\xi_{ni}} \right] \right) \tag{2.15}$$

where $\zeta_i = \omega/k_{\perp} v_{thi}$ is the ratio of the perpendicular phase velocity of the wave to the ion thermal velocity. Equation (2.15) may easily be expanded in the limit $\zeta_i \gg 1$ (also performed in Appendix A) to obtain the same result for the real part of the ion susceptibility as Eq. (2.14b). Therefore the warm plasma corrections to the dispersion relation are valid for all values of $k_{\perp} \rho_{ci}$, subject to the condition $\zeta_i \gg 1$. Regarding the real part of the dispersion relation then, we find that unless the perpendicular phase velocity of the wave becomes comparable to the ion thermal velocity, the ions are effectively unmagnetized. The result may be generalized to include electromagnetic effects such that the warm plasma dispersion relation is identical in form to Eq. (2.4) with the most significant correction made to \mathcal{A} , which, in the cold plasma approximation, goes to zero at the lower-hybrid resonance. The new element \mathcal{A} is²

$$\mathcal{A} = K_{xx} - K_{xx1} n_{\perp}^2 \tag{2.16}$$

where

$$K_{xx1} = \frac{3}{2} n_{\perp}^2 \frac{\omega_{pi}^2}{\omega^2} \frac{v_{thi}^2}{c^2} \left(1 + \frac{1}{4} \frac{\omega^4}{\omega_{ce}^2 \omega_{ci}^2} \frac{T_e}{T_i} \right). \tag{2.17}$$

The warm plasma dispersion relation is third order in n_{\perp}^2 and has three roots. The new solution corresponds to an ion plasma wave. As with the fast and slow waves discussed in Section 2.1, the slow wave and hot wave branches are distinct except near the mode conversion point where the modes couple to one another. Approximate dispersion relations can be written for the slow and hot wave solutions in the electrostatic (high n_{\perp}^2) limit. If the electromagnetic terms in the dispersion relation Eq. (2.4) are neglected and the thermal term of Eq. (2.16) is included ($\mathcal{B} \Rightarrow -n_{\parallel}^2 K_{zz}$, $\mathcal{C} \Rightarrow 0$), the following dispersion relation is obtained:

$$n_{\perp}^4 K_{xx1} - n_{\perp}^2 K_{xx} - n_{\parallel}^2 K_{zz} = 0. \tag{2.18}$$

As before, the approximate dispersion relations for the two waves are obtained in the limit of the inequality (2.6):

$$n_{\perp h}^2 \simeq \frac{K_{xx}}{K_{xx1}} - n_{\parallel}^2 \frac{K_{zz}}{K_{xx}} \quad (2.19a)$$

$$n_{\perp s}^2 \simeq -\frac{K_{zz}}{K_{xx}} n_{\parallel}^2 \left(1 + n_{\parallel}^2 \frac{|K_{zz}|K_{xx1}}{K_{xx}^2} \right) \quad (2.19b)$$

where the “h” subscript refers to the hot ion plasma wave branch. The slow wave branch Eq. (2.19b) is identical to that of Eq. (2.8a), given the approximations made in the derivation of the former and neglect of the electromagnetic and thermal terms in the latter. The mode conversion of the lower-hybrid wave to the hot plasma wave occurs when the two roots of Eq. (2.18) converge, which takes place for

$$\frac{\omega_{pe}^2}{\omega_{ce}^2} = \left[\left(\frac{\omega_{ce}\omega_{ci}}{\omega^2} - 1 \right) + \left(12n_{\parallel}^2 \frac{\omega_{ce}^3\omega_{ci}}{\omega^4} \frac{T_i}{m_i c^2} \left[1 + \frac{1}{4} \frac{\omega^4}{\omega_{ce}^2\omega_{ci}^2} \frac{T_e}{T_i} \right] \right)^{\frac{1}{2}} \right]^{-1} \quad (2.20)$$

For a toroidal field of 14 kG, central electron and ion temperatures of 400 and 150 eV, respectively, and an n_{\parallel} of 6, the mode conversion density is $2.2 \times 10^{13} \text{ cm}^{-3}$.

At mode conversion, the ratio of wave phase velocity to ion thermal velocity is found by solving the dispersion relation Eq. (2.18) using Eq. (2.20):

$$\frac{\omega}{k_{\perp} v_{t hi}} = \left(\frac{\omega}{k_{\parallel} v_{t hi}} \right)^{\frac{1}{2}} \left[\frac{3 m_e}{2 m_i} \left(1 + \frac{\omega^4}{4\omega_{ce}^2\omega_{ci}^2} \frac{T_e}{T_i} \right) \right]^{\frac{1}{4}} \quad (2.21)$$

The term containing the electron temperature is comparable to or smaller than one. The ratio of phase to thermal velocity at mode conversion is thus dependent only on the ion temperature and the local parallel wavenumber. For $n_{\parallel} = 5$ and $T_i = 150\text{eV}$ we find $(\omega/k_{\perp} v_{t hi}) \simeq 3.8$, or $(k_{\perp} \rho_{ci}) = 10$. This result is useful as it allows us to predict in a very simple manner the energy of an ion resonant with the wave at mode conversion where wave damping is likely to occur.

If mode conversion takes place, the ion plasma wave propagates outward toward lower densities and n_{\perp} continues to increase. The inequality $\zeta_i \gg 1$ is no longer valid in this situation, and the full expression for the ion susceptibility Eq. (2.15) must be used. For propagation in a homogeneous magnetic field, a further conversion to an inward-propagating ion Bernstein wave is predicted.² This second mode conversion may not occur in a plasma in an inhomogeneous magnetic field.⁶⁰ It is possible, however, that the wave will damp before the second mode conversion is reached. Because the perpendicular phase velocity of the lower-hybrid wave is so close to the ion thermal velocity at the first mode conversion layer, wave damping is often considered to take place at or near this mode conversion, as will be discussed in the next section.

Though the presentation of the wave theory thus far has been done under the assumption of a single ion species plasma, the results may be generalized to a plasma with impurities. As

the lower-hybrid resonance represents a balance between electron and ion motions in the wave fields, the wave propagation is profoundly affected by the presence of impurity ions. The effects of impurities are two-fold: the average ion charge and mass are increased, but the ion density is decreased relative to the electron density so as to preserve charge neutrality. The effects counteract one another with the latter being the larger of the two. The effective ion plasma frequency, assuming for simplicity a single impurity species of density n_I , charge Z_I , and atomic weight A_I , is

$$\omega_{pi}^2 = \omega_{pe}^2 \left(\frac{m_e}{m_p} \right) \left[1 - \frac{n_I Z_I}{n_e} (1 - Z_I/A_I) \right] \quad (2.22)$$

where m_p is the proton mass. With the effect of impurities included, the accessibility condition becomes⁶¹

$$n_{\parallel}^2 > \left[1 - \frac{\omega^2}{\omega_{ce}\omega_{ci}(1 - C_I)} \right]^{-1} \quad (2.23)$$

where $C_I = Z_I(1 - Z_I/A_I)(n_I/n_e)$. For an assumed impurity species of five-times ionized oxygen, the fractional impurity density $n_I/n_e = .05$ for a plausible Z_{eff} of 2. Here, Z_{eff} is the effective ionic charge of the plasma, and is defined as

$$Z_{eff} = \sum_{\text{all ion species}} \frac{(n_i Z_i^2)}{(n_i Z_i)}. \quad (2.24)$$

Then $C_I = .14$ and $n_{\parallel crit} = 2.9$ for $B_o = 14$ kG.

Similarly, the calculated mode conversion density is shifted upward by the inclusion of impurities. The new turning point criterion is

$$\frac{\omega_{pe}^2}{\omega_{ce}^2} = \left[\left(\frac{\omega_{ce}\omega_{ci}}{\omega^2} \right) (1 - C_I) - 1 + \left(12n_{\parallel}^2 \frac{\omega_{ce}^3 \omega_{ci}}{\omega^4} \frac{T_i}{m_i c^2} \left[1 - \frac{n_I Z_I}{n_e} + \frac{1}{4} \frac{\omega^4}{\omega_{ce}^2 \omega_{ci}^2} \frac{T_e}{T_i} \right] \right)^{\frac{1}{2}} \right]^{-1} \quad (2.25)$$

For the same impurity density and plasma parameters used previously, the mode conversion density is $3.2 \times 10^{13} \text{cm}^{-3}$, a 45% increase from the case of the pure hydrogen plasma. Equation (2.21) may be treated in the same manner, in which case $\omega/k_{\perp} v_{thi}$ is reduced to 3.6 for the parameters chosen. The impurity level clearly influences the necessary parameters for ion heating.

2.2.1. Propagation in the Versator Plasma

In concluding this section, we consider some of the effects of tokamak geometry on wave propagation, and plot the three solutions of Eqs. (2.4) including the thermal correction Eq. (2.16) for the Versator plasma parameters. Implicit in the presentation thus far is the assumption of slab, or cylindrical, geometry. The magnetic field is constant and the density and temperature gradients are perpendicular to the magnetic field; thus the plasma parameters do not vary along the field lines. In this case, the parallel wave number is a conserved quantity, and the mode

conversion locations are determined knowing the density and temperature profiles, the magnetic field, and the launched n_{\parallel} . However, the tokamak magnetic field is not constant. The toroidal field varies inversely with the plasma major radius, while the poloidal field varies both with major and minor radii. These departures from one-dimensional geometry result in the dispersion relation, as expressed in the toroidal coordinates (r, θ, ϕ) , being somewhat more complicated and n_{\parallel} no longer being a conserved quantity throughout the wave propagation. The first modification—that of the incorporation of an inhomogeneous magnetic field into the dispersion relation—is relatively simple to analyze. The discussion of the more accurate treatment of lower-hybrid wave propagation in a tokamak which takes into account the variation of n_{\parallel} is somewhat more involved and is continued in Section 2.6.

In determining the roots of the dispersion relation Eq. (2.4) in toroidal coordinates, the following assumptions are made: the toroidal field B_{ϕ} is much larger than the poloidal field B_{θ} ; hence the latter is neglected. The impurity concentration is considered to be constant, with five-times ionized oxygen the only impurity. The impurity concentration is set by specifying Z_{eff} , which is a measured, global quantity. The flux surfaces are assumed to be concentric. The density profile is parabolic, while the electron and ion temperature profiles are Gaussian with respective widths of 7.5 and 10.5 cm, corresponding to reasonable fits to the measured data.

The three solutions of the dispersion relation are plotted in Fig. 2.1. Instead of the approximations of the last section, the three roots of the full electromagnetic dispersion relation Eq. (2.4) with thermal corrections are found simultaneously using a numerical routine. The values of the real part of n_{\perp}^2 for local values of $n_{\parallel} = 2$ and 5 are plotted versus minor radius in the midplane in Fig. 2.1a for a line-averaged electron density of $2.6 \times 10^{13} \text{ cm}^{-3}$ central electron and ion temperatures of 400 and 150 eV, respectively, toroidal field on axis of 14 kG, and Z_{eff} of 2. As predicted in Section 2.1, waves with $n_{\parallel} = 2$ are inaccessible to the plasma center because of conversion to the fast wave. However, for $n_{\parallel} = 5$, the slow wave undergoes conversion to the hot plasma wave near the center of the plasma and approximately 7 cm. off axis on the high field side. Though not shown on this graph, mode conversion also occurs off the midplane at radii intermediate between these two values. The variation in the mode conversion radius with poloidal angle is due to the inhomogeneous toroidal field. At the mode conversion layer in the center, $n_{\perp} \simeq 530$ and $\omega/k_{\perp} v_{t hi} \simeq 3.3$, in reasonable agreement with the prediction of Eq. (2.21). Figure 2.1b is a plot of n_{\perp}^2 for the same parameters except that $Z_{eff} = 1$. The effect of the change in impurity level on the wave propagation is evident from the outward shift of the location of the slow/hot mode conversion. Furthermore, the slow wave with $n_{\parallel} = 2$, which is unable to reach the mode conversion point on the low field side because of inaccessibility, is seen to undergo conversion to the hot wave on the high field side before the fast/slow coalescence.

2.3. Thermal Effects on Lower-Hybrid Wave Propagation: Damping

The theoretical damping rates of the lower-hybrid wave may be obtained from the imaginary

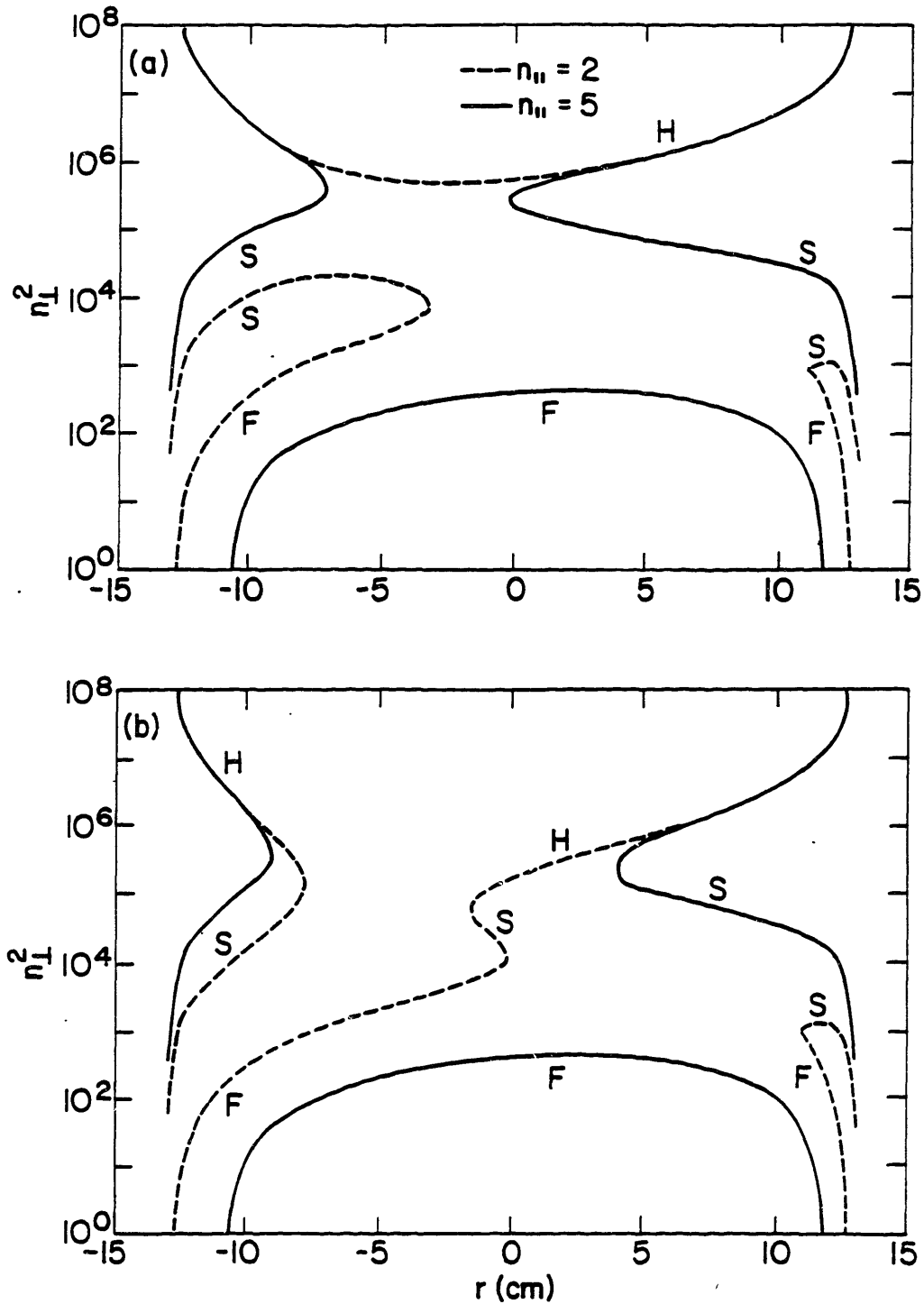


Figure 21. The real part of n_{\perp}^2 versus minor radius in the midplane for the three solutions of Eq. (2.4) with the thermal correction term of Eq. (2.16) included. The dashed lines indicate the case of $n_{\parallel} = 2$; the solid lines the case of $n_{\parallel} = 5$. The label "F" denotes the fast wave branch. "S" denotes the slow wave branch, and "H" denotes the hot plasma wave branch. The gradient of the magnetic field is to the left in this illustration. In (a), the plasma parameters are: $\bar{n}_e = 2.6 \times 10^{23} \text{ cm}^{-3}$, $B_0 = 14 \text{ kG}$, $T_{e0} = 400 \text{ eV}$, $T_{i0} = 150 \text{ eV}$, and $Z_{eff} = 2$, and in (b); the same as for (a) except that $Z_{eff} = 1$.

part of the hot plasma dispersion relation Eq. (2.12):

$$\begin{aligned} \text{Im } k_{\perp} &\simeq -\frac{\text{Im } D}{\partial D / \partial k_{\perp}} \\ &\simeq -\text{Re } k_{\perp} \frac{\text{Im } D}{2\partial D / \partial k_{\perp}^2}, \end{aligned} \quad (2.26)$$

where the imaginary part of D is given by the sum of the imaginary parts of the electron and ion susceptibilities. The damping leads to a decrease of the net wave power P in the plasma:

$$P(r) = P(a) \exp\left(-2 \int_0^r \text{Im } k_{\perp} dr'\right) \quad (2.27)$$

where we assume the perpendicular propagation to be entirely in the radial direction. In general, the imaginary part of the plasma dispersion function is

$$\text{Im } Z(\xi_n) = \sqrt{\pi} \exp(-\xi_n^2). \quad (2.28)$$

Using Eq. (2.13) for the electron susceptibility and Eq. (2.15) for the ion susceptibility, we may write

$$\text{Im } \chi_e = 2\sqrt{\pi} \frac{k_{\parallel}^2 \omega_{pe}^2}{k^2 \omega^2} \xi_{0e}^3 \exp(-\xi_{0e}^2) \quad (2.29a)$$

$$\text{Im } \chi_i = 2\sqrt{\pi} \frac{\omega_{pi}^2}{\omega^2} \zeta_i^3 \exp(-\zeta_i^2) \left[\frac{1}{\sqrt{\pi}} \sum_{n=-\infty}^{\infty} (\omega_{ci}/\omega) \xi_{0i} \exp(-\xi_{ni}^2) \right]. \quad (2.29b)$$

Because $k_{\perp}^2 \rho_{ce}^2 \ll 1$, only Landau damping ($n = 0$) is considered for the electrons. In general, however, several values of n must be considered in the ion damping term. The mechanism of damping on ions is cyclotron damping at the high harmonics ($n \approx 35$).

To determine the region of wave absorption, the integral in Eq. (2.27) may be evaluated with the appropriate density and temperature profiles. For the electron damping term Eq. (2.29a), the procedure is straight-forward, and damping is generally found to be complete when $\omega/k_{\parallel} v_{the} \approx 3$, or⁵ $n_{\parallel} = \delta/\sqrt{T_e(k_e V)}$, where $\delta = 5-7$. For Versator parameters, electron Landau damping is predicted to occur in the plasma center if $n_{\parallel} = 8-11$.

Evaluation of the ion damping term Eq. (2.29b) is more difficult because of the summation over cyclotron resonances. Furthermore, in the damping region, the inequality $\zeta_i \gg 1$ is no longer valid; hence the real part of the ion susceptibility must be obtained from Eq. (2.15) and not from the approximation Eq. (2.14b). The exact propagation and damping behavior for $\zeta_i \approx O(1)$ must be computed numerically.^{9,10,60} For plasmas with density and magnetic field gradients, the resulting lower-hybrid wave propagation can be quite complicated. A simplification which is often invoked is that of "unmagnetized" ion damping.^{9,11,62} In the limit $\zeta_i \gg 1$, the ion dynamics described by the real part of the ion susceptibility are unaffected by the magnetic field (see Eq. 2.14b). Furthermore, the $\exp(-\zeta_i^2)$ term in Eq. (2.29b) suggests that the ion damping may be equivalent to

straight-line orbit damping,^{9,62} i.e. Landau absorption, in the perpendicular direction as the spatial average of the term in brackets in Eq. (2.29b) is 1. However, numerical studies^{9,60} have shown that the assumption of unmagnetized ion orbits leads to significantly different damping behavior than does use of the exact cyclotron damping treatment. Some simple differences are evident from the above discussion. In particular, cyclotron damping requires the existence of a finite k_{\parallel} , whereas unmagnetized damping does not. In addition, no heating by straight-line perpendicular ion Landau damping can take place unless some phase decorrelation of the wave and particle occurs on a time scale less than the ion cyclotron period and over a spatial scale smaller than the perpendicular wavelength.⁶³ The modelling of cyclotron damping by unmagnetized ion damping does not appear to be valid in this simple linear treatment of lower-hybrid wave propagation.

Several mechanisms have been proposed to account for a phase decorrelation so as to justify the use of unmagnetized ion damping. With strong enough rf electric fields, ion motion in the wave may become stochastic. Karney has shown that if the electric field of the wave exceeds a threshold value, the ion motion in a single perpendicularly-propagating wave becomes stochastic.⁶⁴ The threshold electric field required for the onset of stochastic ion motion is calculated to be⁶⁴

$$E_{thr}/B_0 = \frac{1}{4n_{\perp}} \left(\frac{\omega_{ci}}{\omega} \right)^{\frac{1}{2}} \quad (2.30)$$

Other effects may lower this threshold. The broad n_{\perp} spectrum of the launched rf power may satisfy the requirements of quasi-linear diffusion.⁶⁵ The gradient of the magnetic field may also reduce the threshold for stochasticity because the ion orbits will not be exact helices.^{9,66} In short, invoking unmagnetized ion damping of the lower-hybrid wave when the wave speed becomes several times the ion thermal speed may be justified on a number of grounds, though the specific conditions required for the applicability of this treatment are still subject to debate. Further implications of unmagnetized ion damping will be discussed in the next section. For the calculations in this thesis, we assume the wave damping mechanism on ions to be straight-line orbit damping in the perpendicular direction. The overall damping rate is then

$$Im k_{\perp} = Re k_{\perp} \frac{\sqrt{\pi}}{\partial D / \partial k_{\perp}^2} \frac{\omega_{pi}^2}{\omega^2} \left[\frac{m_i}{m_e} \frac{k_{\parallel}^2}{k_{\perp}^2} \xi_{0e}^3 e^{-\xi_{0e}^2} + \xi_i^3 e^{-\xi_i^2} \right] \quad (2.31)$$

where the first term in the brackets is the electron Landau damping term and the second is responsible for unmagnetized ion damping. In this approximation for the ion damping, power absorption by the ions should also be complete when $\xi_i = \omega/k_{\perp} v_{thi} \approx 3$. This value of ξ_i is comparable to that required for mode conversion (see Eq. 2.21), indicating that wave absorption on ions is expected to occur near the mode conversion layer, should it exist in the plasma.

The effect of collisional damping of the wave on electrons may be estimated with the use of the cold electrostatic dispersion relation in which m_e is replaced with $m_e(1 + i\nu_e/\omega)$, where ν_e is

the electron collision frequency.⁴ The perpendicular wave vector from the cold dispersion relation Eq. (1.1) is

$$k_{\perp} = k_{\parallel} \sqrt{\frac{m_i}{m_e} \left(\frac{\omega^2}{\omega_{LH}^2} - 1 \right)^{-\frac{1}{2}}}. \quad (2.32)$$

The imaginary part of k_{\perp} due to collisions is

$$Im k_{\perp} \simeq -\frac{\nu_e k_{\parallel}}{2\omega} \sqrt{\frac{m_i}{m_e} \left[\frac{\omega^2}{\omega_{LH}^2} - 1 \right]^{-\frac{1}{2}}} \left[1 + \frac{\omega^2}{\omega_{ce}\omega_{ci}} \left(\frac{\omega^2}{\omega_{LH}^2} - 1 \right)^{-1} \right], \quad (2.33)$$

and if we consider only the outer part of the plasma ($\omega^2 \gg \omega_{pi}^2, \omega_{LH}^2$), we obtain the lowest order result

$$\begin{aligned} Im k_{\perp} &\simeq n_{\parallel} \sqrt{\frac{m_i}{m_e}} \frac{\omega_{LH} \nu_e}{2\omega c} \\ &\simeq 0.18 n_{\parallel} \left(\frac{n(10^{13} \text{cm}^{-3})}{T_e(\text{eV})} \right)^{3/2} \text{cm}^{-1} \end{aligned} \quad (2.34)$$

For the analytic profile shapes described earlier (Gaussian electron temperature profile of width λ_{te} and parabolic density profile), the predicted collisional damping rate above is found to have a maximum at $r = \sqrt{a^2 - \lambda_{the}^2}$ or at $r = 11$ cm, giving a maximum $Im k_{\perp}$ of $3.4 \times 10^{-3} \text{cm}^{-1}$ for $n_{\parallel} = 5$. The corresponding perpendicular damping length is 290 cm, which is much larger than the plasma radius. Waves with purely radial perpendicular wave number in Versator should thus experience less than 10% power loss to collisions in propagating to the core. However, this may not be the case for a lower-hybrid wave with a significant n_{θ} component. Collisional damping of such a wave is discussed in further detail in Section 2.6.

To summarize, we see that the perpendicular wave number increases with plasma density up to the linear mode conversion point; ion damping is predicted to occur if the perpendicular wave speed slows to the order of the ion thermal velocity, which will take place near the mode conversion layer. Electron Landau damping is expected to occur if the parallel phase velocity of the wave is comparable to the local electron thermal velocity. The wave damping rate on ions and electrons is given by Eq. (2.31), though we note that an accurate treatment would require the inclusion of quasi-linear effects.^{64,65}

The most efficient heating of the plasma should occur if the waves damp at or near the axis of the plasma column. In the remainder of this section, we estimate the maximum penetration of the lower-hybrid wave into the plasma as determined by: (1) the location of the mode conversion layer Eq. (2.25), and; (2) the wave absorption calculated from Eq. (2.27). In Fig. 2.2, the cold lower-hybrid resonant density, the warm mode conversion densities and fast/slow mode conversion densities for several values of n_{\parallel} are plotted versus minor radius in the midplane with the variation

of the toroidal field included. The plasma parameters are the same as for the previous figure, with Z_{eff} taken to be 2. Also plotted is the density profile for $n_e = 2.6 \times 10^{13} \text{ cm}^{-3}$ although the calculated mode conversion densities are correct for any density profile for the given temperature and magnetic field variation. The dashed line segments indicate the region where electron Landau damping is expected to occur for the given electron temperature profile. In this estimate, we assume the electron Landau damping to take place for $(\omega/k_{\parallel}v_{the}) \leq 3.2$.

The effect of the inhomogeneous magnetic field mode conversion and resonant densities is clearly demonstrated in the figure, with the mode conversion densities shifting to higher values at lower fields. The lowering of the mode conversion density with increasing temperature is evident only for $n_{\parallel} \geq 8$. Except at low densities ($n_e < 2 \times 10^{13} \text{ cm}^{-3}$), waves of $n_{\parallel} \leq 2$ are inaccessible to the plasma core from either side.

From the point of view of the ion heating experiment, several aspects of this figure are instructive. If ion heating is to occur at the core of a plasma with a central density of $4 \times 10^{13} \text{ cm}^{-3}$ then the local value of the parallel wave number must be $n_{\parallel} \simeq 4-8$, assuming that wave damping takes place at or near the mode conversion layer. For the same n_{\parallel} values, however, damping should also occur between minor radii of 5 and 8 cm. on the high magnetic field side. Because of the rotational transform of the field due to the plasma current, waves propagating to the plasma core circulate in the poloidal direction. The inward radial distance traveled as the wave propagates from the outer to inner side of the tokamak can be estimated using the cold plasma dispersion relation Eq. (1.1) and assuming n_{\perp} to be a purely radial wave number:

$$\Delta r \simeq \pi R_o q \frac{\omega}{\omega_{pe}} \sqrt{K_{xx}} \quad (2.35)$$

where $q = (rB_{\phi}/R_o B_{\theta})$ is the safety factor. For Versator parameters, $\Delta r \lesssim 2$ cm, or a fraction of the minor radius. Thus in the cylindrical slab model, the lower-hybrid waves may be significantly damped before the innermost mode conversion location is reached. In Fig. 2.3 the minimum and maximum minor radii of damping are plotted versus n_{\parallel} for two values of the central density. Damping at the higher minor radii occurs on the inner side of the plasma, while damping at the lower radii takes place on the outer side. Though heating at a more central location is predicted for a lower plasma density, the required n_{\parallel} is higher, and if n_{\parallel} is increased above 8, electron damping becomes predominant. The calculations of the absorption regions for different n_{\parallel} and plasma densities are summarized in Fig. 2.4. The predicted damping loci are plotted for specified n_{\parallel} and central plasma densities. The contour lines of equal values of r/a represent the maximum minor radii at which damping is calculated to occur. Because of the simple criterion assumed for electron heating, the electron damping location is independent of density. As discussed above, the wave damping region for ions is relatively broad even for a single value of n_{\parallel} , and there is no combination of density and n_{\parallel} for which the maximum damping radius can be unambiguously set to the plasma axis at $r/a = 0$. However, a cautionary remark should be made regarding the validity

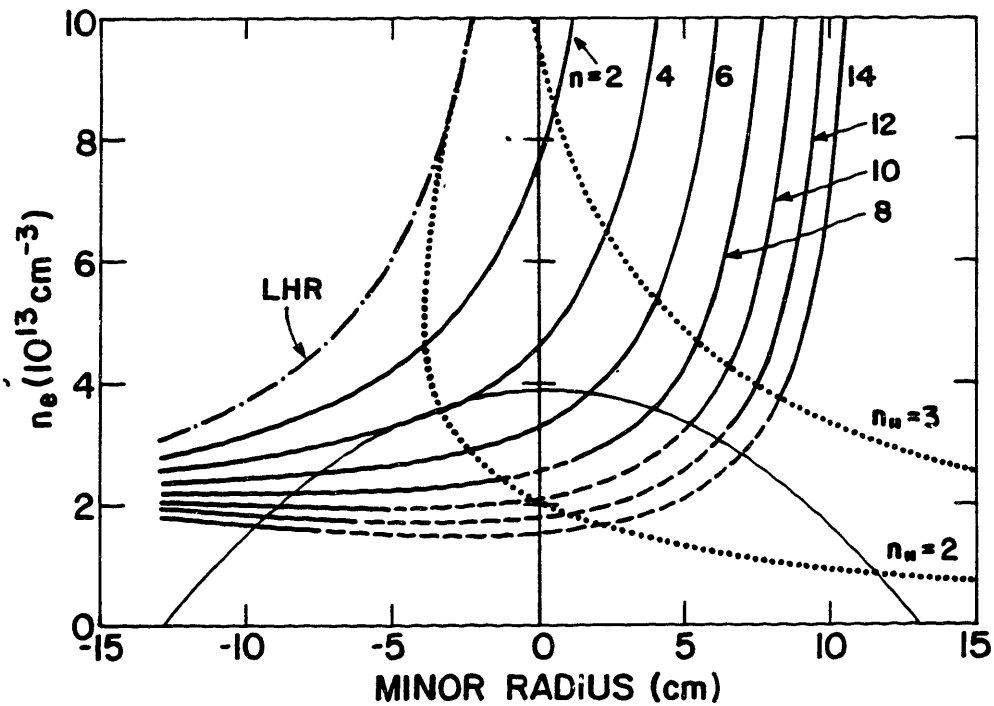


Figure 2.2. The cold lower-hybrid resonance density (dot-dash line), the hot/slow mode conversion densities (solid lines), and the slow/fast mode conversion densities (dotted lines) versus minor radius in the midplane. The plasma parameters are: B_o (on axis)=14 kG, $T_{e0}=400$ eV, $T_{i0}=150$ eV, and $Z_{eff}=2$. The temperature profiles are taken to be the same used in Fig. 2.1. Also shown is a representative density profile for $\bar{n}_e = 2.6 \times 10^{13} \text{ cm}^{-3}$. The gradient of the magnetic field is to the left in the figure. The other plasma parameters are the same as for Fig. 2.1a. The dashed portions of the lines indicate the region of electron damping for the given $n_{||}$.

of this relatively simple model. We note that wave propagation described by the more accurate toroidal ray tracing model discussed in Section 2.6 is considerably different from the picture provided by this cylindrical slab model. Nonetheless, the major point of the previous discussion, that the predicted damping radius of the lower-hybrid wave in a tokamak is not well-localized, is still generally true, although for somewhat different reasons in the toroidal propagation model. We will return to this point in Section 2.6.

The penetration problem is not improved if the tokamak is operated at a higher toroidal field or lower impurity content, as indicated in Fig. 2.5. In Fig. 25a, the lower-hybrid resonant densities and mode conversion densities are plotted in the same manner as in Fig. 2.2, except that the toroidal field on axis is taken to be 15 kG. The resonant density and slow/hot mode conversion densities are lower than in the previous case, and the fast/slow mode conversion densities are higher. A similar effect is illustrated in Fig. 25b, in which the same quantities are plotted for $Z_{eff} = 1$, and B_0 on axis is again set to 14 kG. In these cases, the predicted minor radius of mode conversion for a given $n_{||}$ still spans a significant fraction of the plasma radius. The low aspect ratio of Versator is responsible for the strong increase in the mode conversion density with major radius. Because of broad density profile, the derivative of the mode conversion density with respect to the minor radius is larger than that of the electron density, as is evident from Figs. 2.2 and 2.5. Hence mode conversion for a given $n_{||}$ can span a region ranging from the plasma center to a point well away from the axis, which may result in inefficient ion heating. This problem is not necessarily endemic to low aspect ratio tokamaks, however. For instance, the PLT tokamak has an aspect ratio similar to that of Versator, yet the higher temperature of the plasma in the former leads to a significant lowering of the calculated mode conversion density at the plasma center, thus allowing most of the power of a particular $n_{||}$ component to be damped near the axis. For Versator, similar thermal effects are significant only for higher $n_{||}$ (≥ 10), which are predicted to damp at the edge in high density plasmas or on electrons in low density plasmas. We note from Fig. 2.2, however, that the damping locations obtained from these calculations are strongly dependent on the shape of the density profile. If the true profile is narrower than the parabolic one used in these estimates, the absorption region for a given $n_{||}$ would be more localized and the heating efficiency might be quite different. Generally, though, we find that the application of this cylindrical slab model to lower-hybrid wave propagation in the Versator plasma predicts the ion damping region to be rather broad. Regarding accessibility, waves with $n_{||} \geq 2.5$ will not convert to the fast wave. Nonetheless, mode conversion to the hot plasma wave and wave damping on ions cannot be unambiguously localized to the plasma center. The broad deposition profile of the rf power may have an adverse effect on the heating efficiency since the confinement of high energy ions which are generated off-axis is expected to be poor. This point will be discussed in more detail in Section 2.5.

In the present understanding of lower-hybrid wave propagation, the mode conversion point is the location of maximum penetration into the plasma. The damping on ions is very strong

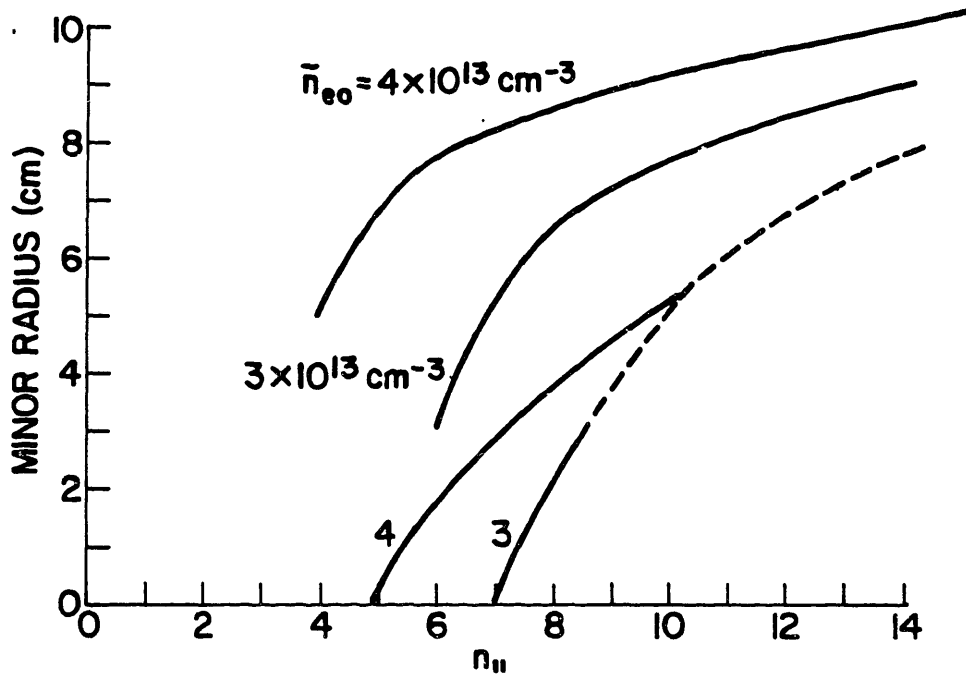


Figure 23. Minimum and maximum minor radii of damping versus $n_{||}$ for central densities $n_{e0} = 3$ and $4 \times 10^{13} \text{ cm}^{-3}$ and the same plasma parameters as in Fig. 2.2. The dashed line portions indicate where electron Landau damping is predominant.

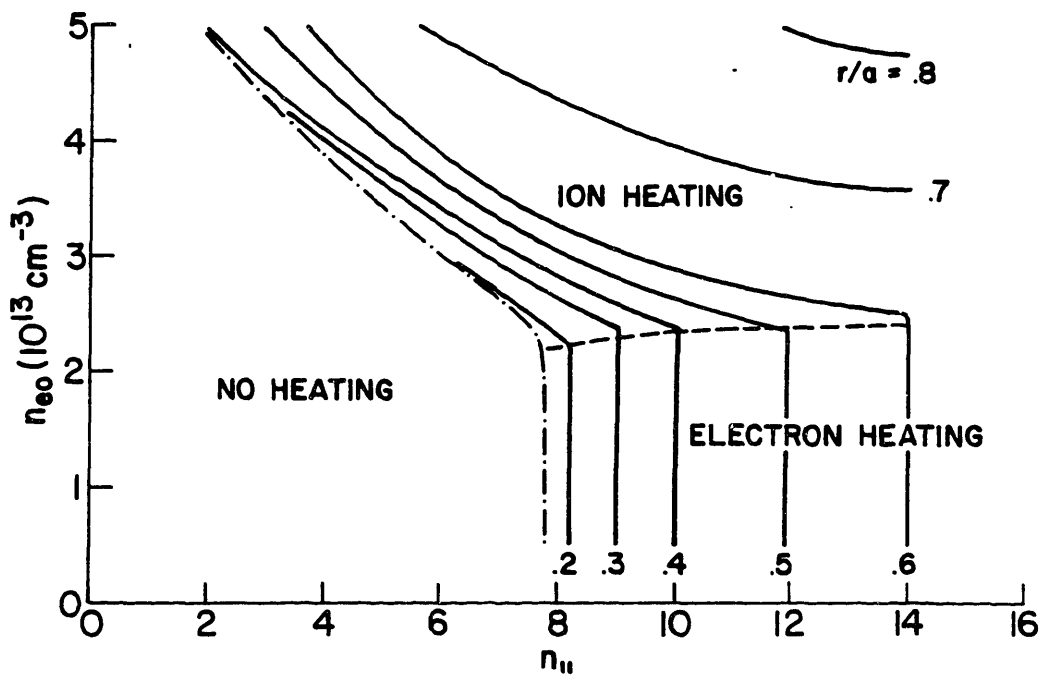


Figure 2.4. Contour plot of the maximum damping radius (r/a) for different values of $n_{||}$ and central density n_{e0} with the same plasma parameters as Fig. 2.2. The dashed line separates the regions of electron and ion heating. Heating is not predicted to occur for $n_{||}$ values in the region to the left of the dot-dash line.

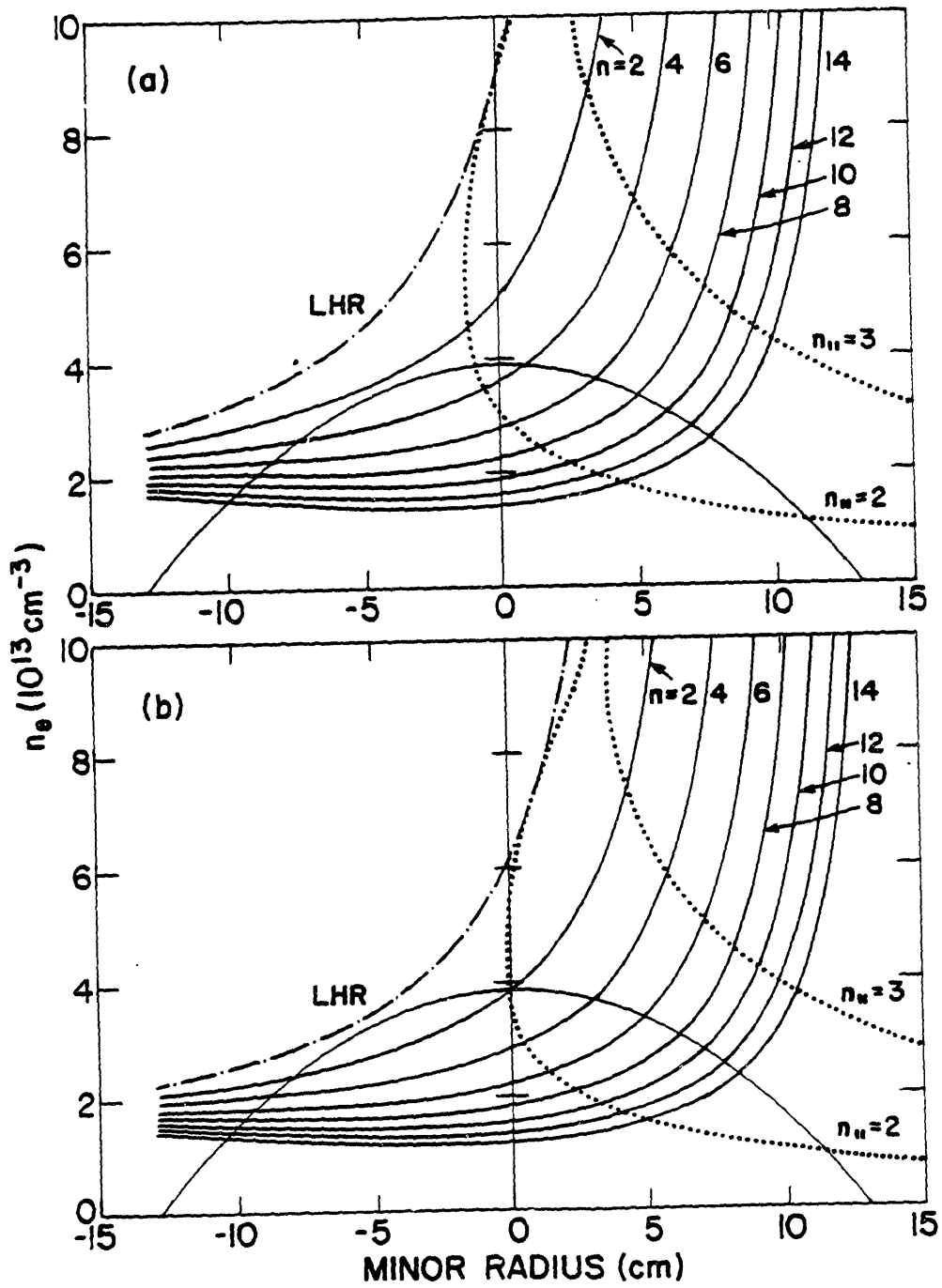


Figure 2.5. Same quantities as Fig. 2.2, except: (a) $B_0 = 15 \text{ kG}$; and (b) $Z_{eff} = 1$ and $B_0 = 14 \text{ kG}$.

near the mode conversion because the denominator of Eq. (2.31) becomes very small (zero in the electrostatic limit) at the point of conversion. However, under some conditions ion damping is complete before the mode conversion point is reached as is shown by evaluation of Eq. (2.27) for plasma conditions similar to those used above. In Fig. 2.6 we show a plot of $P(r)$ (normalized to 1 at the edge), ξ_{0e} , and ζ_i versus minor radius for the plasma conditions of Fig. 2.1a and $n_{\parallel} = 8$. As in the last section, we consider propagation from both the inner and outer major radii to obtain the minimum and maximum minor radii of damping with the understanding that the propagation path of the wave, even in this cylindrical model of the tokamak plasma, is a spiral in the poloidal plane. As with the mode conversion layer, the maximum damping radius is located on the high field side, and is 8.8 cm. in this example, corresponding to $\zeta_i = 3.2$. The damping length is seen to be very short (≤ 1 cm.) due to the rapid increase of n_{\perp} with decreasing radius near the mode conversion layer.

The mode conversion layer is shown just to the inside of the damping region. Over a span of plasma parameters and n_{\parallel} , ion Landau damping is always calculated to occur in the range $3.0 < \zeta_i < 3.2$. For $n_{\parallel} < 8$ mode conversion is reached before the wave is fully damped, and vice versa for $n_{\parallel} > 8$. In Fig. 2.7, we show a contour plot of the maximum minor radius at which damping occurs, similar to that of Fig. 2.4. The major difference between the evaluation of the damping from Eq. (2.27) and the assumption of heating to be at the mode conversion location is the reduction of the parameter space for which electron heating is likely. The reason for this is that at the higher n_{\parallel} 's, at which electron heating is normally thought to occur, the ion damping region is displaced outward from the conversion point. The density must be lowered for the electron heating to be recovered.

For electron Landau damping to occur within the core of the plasma ($r/a \leq 0.5$) with the use of the four-waveguide side-launching grill (n_{\parallel} (peak) ≈ 5.5), we require $n_{e0} < 2 \times 10^{13} \text{cm}^{-3}$ and $n_{\parallel} > 8$. The latter requirement is not fulfilled by this launcher. Unless quasi-linear damping of the lower-hybrid wave on the electron population is considered,^{67,68} we expect electron heating to be inefficient based on these slab geometry calculations.

2.4. Ion Tail Formation

It has thus far been assumed that ion heating occurs at or near the mode conversion density, at which point the perpendicular wave phase velocity is only several times the ion thermal speed. Unmagnetized ion damping is responsible for wave energy loss when the wave reaches these low phase speeds; consequently, wave damping is expected to be insensitive to the location of an ion cyclotron harmonic. As discussed in the last section, the damping condition for ions in a Maxwellian plasma is similar to that for electrons:

$$\frac{\omega}{k_{\perp} v_{thi}} \approx 3. \quad (2.36)$$

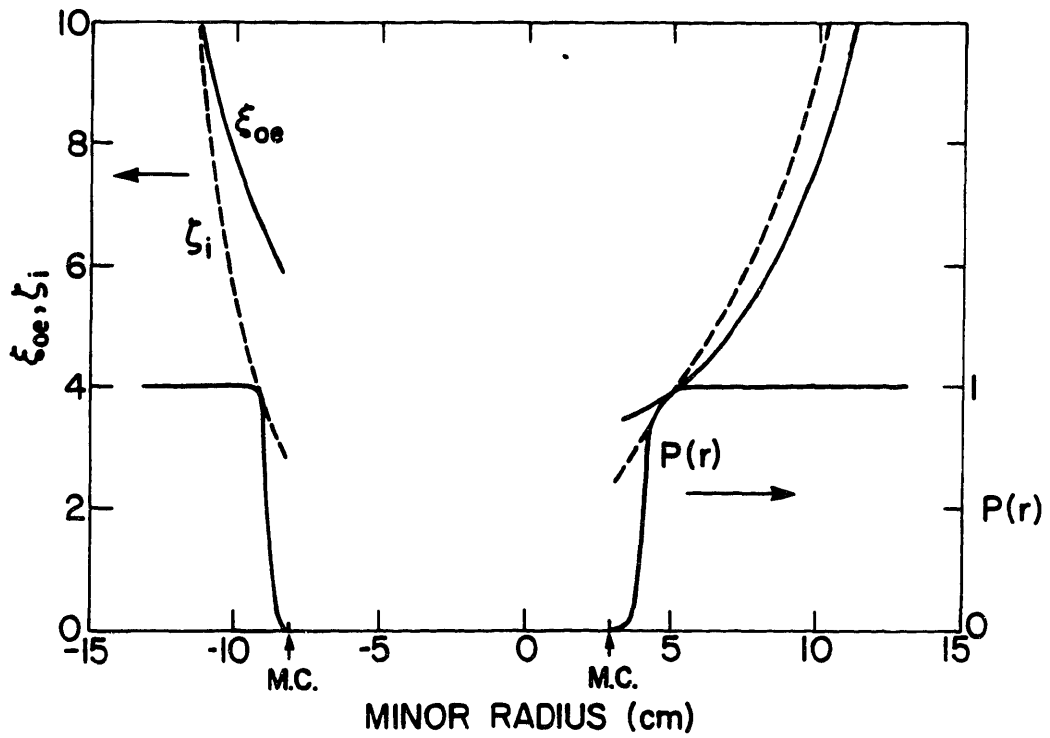


Figure 2.6. The local wave power $P(r)$ from Eq. (2.27) versus minor radius in the midplane for plasma conditions of Fig. 2.1a and $n_{||} = 8$. Also plotted are the local values of ξ_i and ξ_{oe} . The mode conversion locations for this $n_{||}$ are indicated.

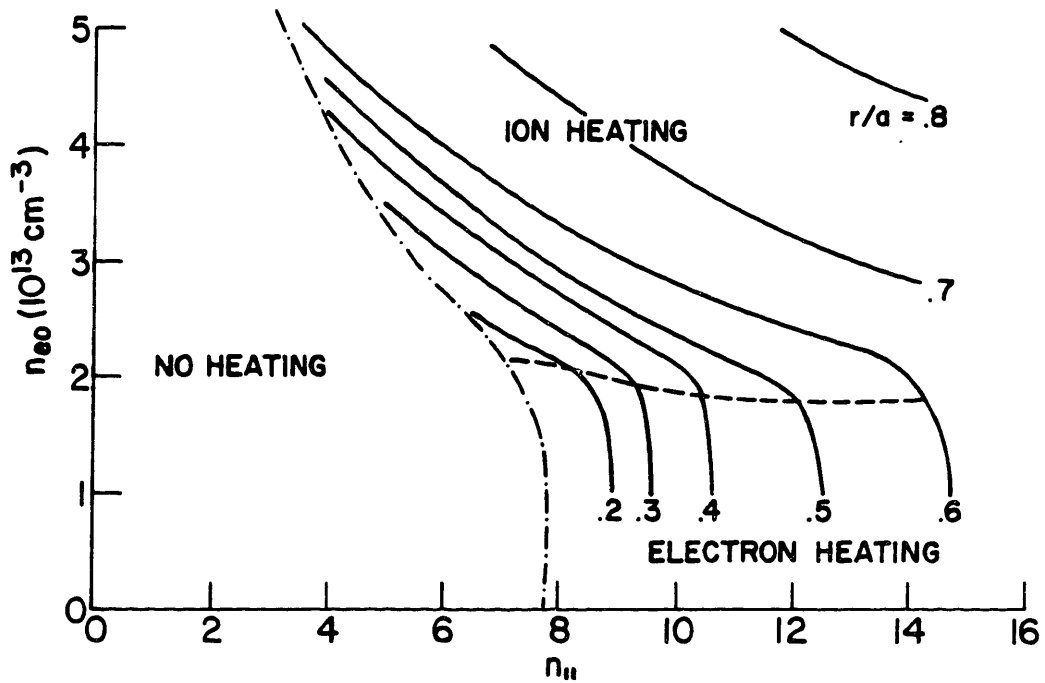


Figure 2.7. Contour plot similar to Fig. 2.4 of the maximum damping radius (r/a) based on an evaluation of Eq. (2.27).

In general, though, quasi-linear effects may play a role in the wave absorption. Implications of unmagnetized quasi-linear damping are often considered in the interpretation of the experimental data.¹⁸ In particular, stochastic ion heating theory predicts the creation of a fast, perpendicularly-oriented ion tail, a feature which is observed in most lower-hybrid ion heating experiments. Suprathermal ions gain energy from the lower-hybrid wave and allow increased absorption of energy from faster waves. Thus for a spectrum of waves, the absorption efficiency increases with coupled rf power. According to recent treatments, quasi-linear ion heating is expected to distort the ion distribution such that a perpendicular ion tail is created. The tail exhibits a mean energy or effective temperature roughly proportional to the rf power in the plasma.⁶⁴ Flattening of the tail distribution is prevented by: (1) collisions of the fast ions with slower ones, resulting in heating of the bulk distribution, or by: (2) direct orbit losses of the energetic ions. In quasi-linear wave damping calculations for typical tokamak parameters, wave absorption is generally complete before the wave reaches the linear turning point of the warm lower-hybrid wave.⁶⁵ This supports the earlier use of the linear turning point as a limit of maximum wave penetration into the plasma.

The energy of the ion resonant with the wave at the point of damping (see Eq. 2.21) may easily be calculated once the local values of ζ_i and T_i are known. This energy is determined solely by the local ion temperature,

$$\mathcal{E}_{res} \simeq 9T_i(r), \quad (2.37)$$

and represents the energy of the slowest ion that can absorb power from the wave. In principle, the damping location can thus be determined indirectly if the ion temperature profile is known. The calculated resonant ion energy at the damping location as a function of $n_{||}$ are plotted in Fig. 2.8 for several values of the central densities. For $n_{||} = 5.5$, the resonant energies are 1.3 to 1.8 keV. At higher $n_{||}$, the resonant energy is lower because the damping occurs in regions of lower ion temperature away from the plasma center. Experimentally, the minimum resonant ion energy is inferred from the “knee” in the measured ion distribution which represents the apparent juncture of the bulk and tail distributions. The energy corresponding to the knee location is thus believed to be a measure of the slowest wave speed (highest $n_{||}$) represented in the spectrum.¹⁸ We will return to this point with the presentation of the charge-exchange measurements in Chapter 6.

Results of a many-particle simulation in which the lower-hybrid wave fields are calculated self-consistently⁶⁹ generally support Karney’s model of lower-hybrid wave damping. In the simulation, stochastic ion heating occurs when the perpendicular wave phase speed has decreased to $\omega/k_{\perp} \simeq 4v_{thi}$, and a bi-Maxwellian distribution is created. Linear mode conversion does not occur, even for electric field thresholds of 1/10 the magnitude of Karney’s criterion Eq. (2.30).

As ion Landau damping requires a minimum perpendicular ion speed relative to the perpendicular component of the wave phase velocity before significant interaction can occur, lower-hybrid waves propagating in an initially isotropic distribution preferentially damp on ions with purely perpendicular speeds. Furthermore, the energy dissipated by the wave increases the

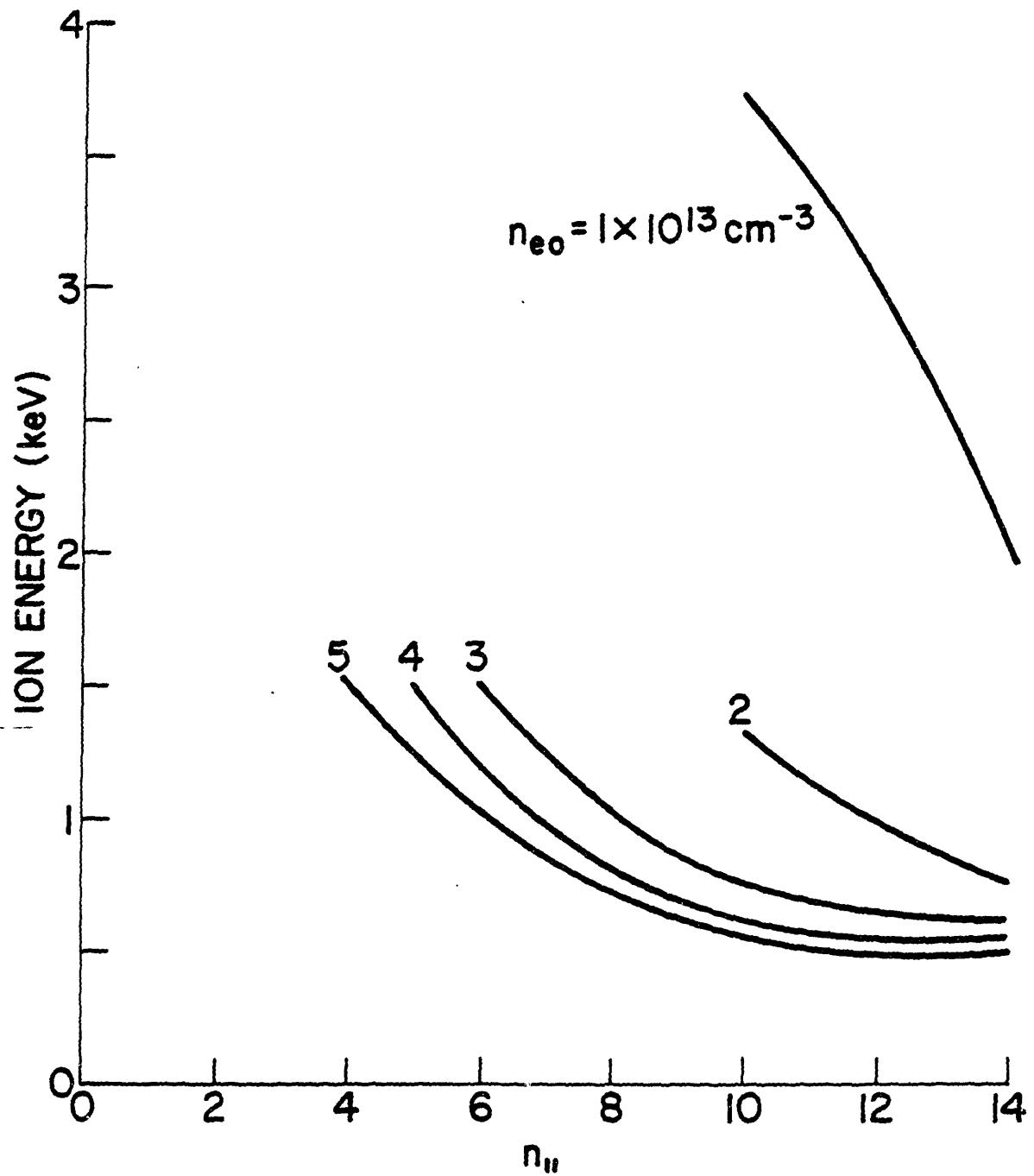


Figure 2.8. Resonant ion energy at the damping location versus $n_{||}$ for several values of the central density.

perpendicular energy of the ion leading to the creation of the perpendicular tail containing ions with energy $\mathcal{E} \geq \mathcal{E}_{res}$. The lower-hybrid wave does not gain a high enough value of n_{\perp} to interact with the bulk ion distribution. The suprathermal ions should collisionally heat the bulk ions if the former are confined sufficiently long. Consequently, we remark that though quasi-linear wave absorption efficiency is predicted to be higher than the linear absorption efficiency,⁶⁵ the ion bulk heating may be less efficient for the former than the latter since a substantial fraction of the fast ions may be lost before they are collisionally slowed.

The ion tail distribution obtained by Karney from the diffusion equation for unmagnetized ions has a simple analytic form if a number of simplifying assumptions are incorporated. We begin by writing the diffusion equation for ions in the presence of rf electric fields with a Fokker-Planck collision term:⁶⁴

$$\frac{\partial f}{\partial t} = \frac{1}{v_{\perp}} \frac{\partial}{\partial v_{\perp}} v_{\perp} D_{rf} \frac{\partial f}{\partial v_{\perp}} + \left(\frac{\partial f}{\partial t} \right)_{coll} \quad (2.38)$$

where $f = f(v_{\parallel}, v_{\perp})$ is the distribution function of the parallel and perpendicular components of the velocity components, and D_{rf} is the rf diffusion coefficient for stochastic ion heating. The diffusion coefficient is non-zero only for $v_{\perp} > \omega/k_{\perp} - 2v_{tr}$, where v_{tr} is the trapping velocity $(eE_{\perp}/m_i k_{\perp})^{1/2}$ and E_{\perp} is the rf electric field in the perpendicular direction. This lower limit is plausible from a simple picture of quasi-linear diffusion in which the wave-particle interaction region in the frame of reference of the wave is determined by the trapping width of the wave. For $v_{\perp} > \omega/k_{\perp}$, the diffusion coefficient is⁶⁴

$$D_{rf} = \frac{1}{8\pi} \frac{e^2 Z_i^2 E_{\perp}^2}{m_i^2} \left(\frac{\omega}{k_{\perp} v_{\perp}} \right)^2 \frac{1}{(k_{\perp}^2 v_{\perp}^2 - \omega^2)^{1/2}}. \quad (2.39)$$

As the waves interact only with tail ions, the distribution function is only altered significantly in the velocity range $v_{\perp} \gg v_{thi}$. The distribution function in the parallel direction is assumed to be Maxwellian. This simplification allows the diffusion equation to be written in terms of $F(v_{\perp})$, the perpendicular distribution function:

$$\frac{\partial F}{\partial t} = \frac{1}{v_{\perp}} \frac{\partial}{\partial v_{\perp}} v_{\perp} \left[D_{rf} \frac{\partial F}{\partial v_{\perp}} + C \left(\frac{\partial F}{\partial v_{\perp}} + \frac{2v_{\perp}}{v_{thi}^2} F \right) \right] \quad (2.40)$$

where C is the Fokker-Planck collision operator for fast protons on the bulk protons, impurity ions, and electrons. Following Karney's notation, we write the collision operator as⁷⁰

$$C = \frac{3}{4} v_{thi}^2 \nu_{ii} \left[\frac{v_{thi}^3}{v_{\perp}^3} \left(1 + \frac{n_I Z_I^2}{n_e A_I} \right) + \frac{v_{thi}^3}{v_o^3} \right] \quad (2.41)$$

where $v_o \simeq 4.4v_{thi}$, and ν_{ii} is the ion-ion (proton-proton) collision frequency

$$\nu_{ii} = \frac{4\pi n_i e^4}{m_i^2 v_{thi}^3} \ln \Lambda. \quad (2.42)$$

The quantity $\ln \Lambda$ is the Coulomb logarithm. Collisions of fast protons on electrons are represented in the term containing v_o . This term is only important when $v_{\perp} \geq v_o$, or

$$\frac{\omega}{k_{\perp} v_{thi}} \geq 4.4. \quad (2.43)$$

However, we recognize that this term theoretically determines the high energy limit of the tail.

The steady state solution to Eq. (2.40) is⁶⁴

$$F(v_{\perp}) = F_o \exp \int_0^{v_{\perp}} \frac{2v_{\perp}/v_{thi}^2}{1 + D_{rf}/C} dv_{\perp} \quad (2.44)$$

which is obtained by setting the quantity in brackets in Eq. (2.40) equal to zero and integrating over v_{\perp} . For $\omega/k_{\perp} < v_{\perp} < v_o$, both D_{rf} and C are roughly proportional to v_{\perp}^{-3} , and the denominator in the above equation is independent of v_{\perp} . Over the velocity region specified, we can write the distribution function as

$$F \approx \exp - (m_i v_{\perp}^2 / 2T_t) \quad (2.45)$$

where

$$\begin{aligned} T_t &\simeq (1 + D_{rf}/C)T_i \\ &= \left(1 + \frac{1}{8\pi} \frac{\gamma E_{\perp}^2}{(3/2)n_i T_i \nu_{ii} (v_{thi} n_{\perp}/c)^3} \frac{\omega}{\nu_{ii} (v_{thi} n_{\perp}/c)^3} \right) T_i \end{aligned} \quad (2.46)$$

is the effective tail temperature of the fast ion distribution. The quantity γ is a geometric factor which accounts for the spatial variation of the lower-hybrid wave strength, and represents the fraction of time an ion spends in the lower-hybrid field. From Eqs. (2.37) and (2.43), we estimate the tail to extend from 1.5 keV to 3 keV in the Versator plasma with a typical central ion temperature of 150 eV. In practice, the upper energy limit of the fast ion tail may be determined by the finite width of the n_{\perp} spectrum rather than the onset of collisional losses on electrons, but we will not address that question.

With the distribution function known, in principle the rf absorption efficiency of the plasma and the collisional transfer of power from the tail to the bulk could be estimated. To do so, the theoretical tail temperature must be calculated from Eq. (2.46) if the electric field in the plasma is known. The perpendicular electric field in the plasma may be calculated from the inward power flux in the radial direction where we take the polarizations for the transverse electric and magnetic fields to be the appropriate ones for the slow wave:⁸

$$-S_r = \frac{c}{8\pi} (E_{\phi} B_{\theta}^*) - \frac{\omega}{8\pi} |E_r|^2 \frac{\partial K_{xx}}{\partial k_r}, \quad (2.47)$$

where we neglect absorption. The first term on the right-hand side is the electromagnetic power flow and the second term on the right is due to the coherent motion of the particles. The rf magnetic field is

$$B_\theta = n_{\parallel} E_r - n_{\perp} E_\phi. \quad (2.48)$$

The relationship of E_ϕ to E_r for the slow wave is obtained from the x -component of Eq. (2.3):

$$E_\phi = \frac{n_{\parallel}^2 - \mathcal{A}}{n_{\parallel} n_{\perp}} E_r \quad (2.48)$$

Since

$$\frac{\partial K_{zz}}{\partial k_r} = -2 \frac{c}{\omega} K_{zz1} n_{\perp}, \quad (2.49)$$

the power flux is

$$S = \frac{c |E_r|^2}{8\pi} \left[\mathcal{A} \frac{n_{\parallel}^2 - \mathcal{A}}{n_{\parallel}^2 n_{\perp}} - K_{zz1} n_{\perp} \right]. \quad (2.50)$$

Letting $n_{\parallel}^2 - \mathcal{A} \rightarrow n_{\parallel}^2$ (which is valid if $n_{\parallel}^2 \gg 1$) and substituting for \mathcal{A} from Eq. (2.16), we can write the inward power flux as⁷¹

$$S = \frac{c E_{\perp}^2}{8\pi} \frac{(K_{zz} - 2K_{zz1} n_{\perp}^2)}{n_{\perp}} \quad (2.51)$$

where we have replaced E_r with E_{\perp} . However, to estimate the power flux in a tokamak plasma is somewhat difficult. Lower-hybrid waves in the cold electrostatic approximation are predicted to propagate in resonance cones; however, laser scattering measurements of the lower-hybrid wave in the Alcator A tokamak have shown that the waves are not restricted to resonance cones.⁷² Accordingly, we estimate the power flux in two ways which may give two bounds on the electric field. In the first method, we obtain the field by assuming that the waves propagate in resonance cones such that the effective cross-sectional area for power flow is $hL_{oz}(r/a)$, where L_{oz} is the width of the grill in the z -direction and (r/a) is a cylindrical focusing factor. In the other extreme, we assume the wavefront to extend over the entire flux surface of area $4\pi^2 R_o r$. The calculated electric field for the two conditions are plotted in Fig. 2.9 along with Karney's threshold field for stochastic ion heating. We assume the same plasma conditions as in Fig. 2.1a and pick $n_{\parallel} = 2$ and 5, and $P_{rf} = 50$ kW. The average electric field at the launcher for this power level is $E = 0.5$ kV/cm. In the plasma interior, the calculated electric field can exceed 5 kV/cm for both propagation scenarios, while Karney's threshold field is about 1 kV/cm. Thus we expect the stochastic heating mechanism to be important in wave absorption.

The calculated ion tail temperatures Eq. (2.46) are plotted versus n_{\parallel} in Fig. 2.10 for several different densities. The geometrical factor γ cancels the difference between the electric fields of the two assumed propagation methods. What is not accounted for is the finite radial extent of the lower-hybrid wave packet. If this width $(\Delta x \simeq (\omega^2/\omega_{LH}^2 - 1)(m_e/m_i)^{1/2} L_z)$ is comparable to an ion Larmor radius, then the ion will spend a fraction of its orbit outside the wave fields and

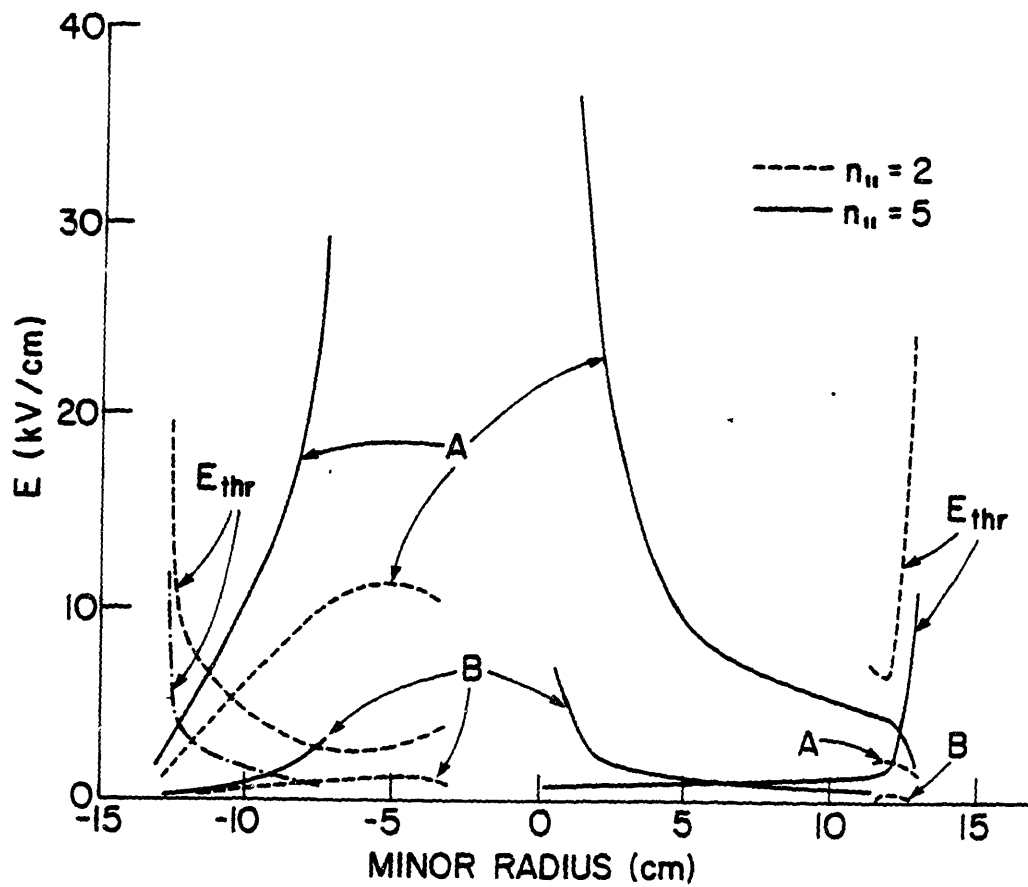


Figure 2.9. Calculated electric field in the plasma versus minor radius in the midplane. The field is calculated from Eq. (2.51) for the two cases considered in the text with an injected power of 50 kW and the same plasma conditions as Fig. 2.1a. Also shown are the threshold fields for the onset of stochasticity. The dashed lines denote the fields for $n_{||} = 2$, the solid lines for $n_{||} = 5$. The curves labelled "A" denote the electric fields calculated using the resonance cone model, and those labelled "B" are calculated in the diffuse, cylindrically symmetric propagation scenario described in the text.

the stochastic heating theory is not valid. In Versator, $L_{oz} \simeq 10$ cm. and $\Delta x \lesssim 0.2$ cm, and the Larmor radius of a 1 keV ion exceeds the typical width of the resonance cone. However, multiple radial passes of the lower-hybrid wave because of weak damping, radial reflections, or drift wave scattering may eliminate radial localization of the rf fields. Therefore, calculation of the electric field strength under realistic experimental conditions is a difficult problem.

The predicted ion tail temperatures are on the order of 100 keV. The high values of the tail temperature are due to the large electric field near the mode conversion layer and the weak collisional slowing of the fast ions. As noted earlier, such a tail in the Versator plasma should only extend to an energy of about 3 keV. Thus the theoretical fast ion distribution should be characterized by a rather flat plateau for $1.5 \lesssim \mathcal{E}_i \lesssim 3$ keV. In contrast, we will see in Chapter 6 that the experimental fast ion distribution for $\mathcal{E}_i \geq 1.2$ keV has an effective temperature $T_i \lesssim 1$ keV, or roughly two orders of magnitude less than the typical calculated value. The discrepancy between the theoretical and experimental tail temperatures has been noted in previous numerical treatments of quasi-linear damping.⁶⁵ Though quasi-linear theory is invoked to explain the ion tail temperature measurements in the Wega experiment,¹⁸ the assumed electric field at the damping location is only 0.7 times that at the launcher, which is much smaller than that predicted by Eq. (2.51). A number of arguments may be invoked to explain why the predicted ion tail temperature may be an overestimate. Drift wave scattering,^{73,74} collisional^{14,34} and parametric absorption^{30,31,41} at the plasma edge, and toroidal effects on propagation^{62,74,75} may prevent a significant fraction of rf power from reaching the damping region; hence the electric field in the plasma may be much lower than that given in Eq. (2.51). Equally importantly, the ions may be removed from the tail at a greater rate than predicted by the Coulomb collision operator of Eq. (2.41). Because of neoclassical effects, particles with primarily perpendicular velocity are not well confined, as discussed in the next section.

Nonetheless, the rate of rf power absorption by the ion tail can be estimated from the experimental measurements of the ion distribution function. To do so, we will employ the same model of the perpendicular distribution function described above except that the tail temperature is taken as a measured quantity rather than a calculated one. It is assumed that a Maxwellian tail of effective temperature T_i intersects the thermal bulk distribution at the velocity value $v_{\perp} = v_1$, which represents the minimum perpendicular speed of the lower-hybrid wave at the damping location. From linear theory, it has been shown (see Eq. 2.31) that $v_1 \approx 3v_{thi}$. This value may be lowered by quasi-linear effects in the same manner as for electron Landau damping, in which case a numerical solution may be employed to determine the velocity coordinate of the intersection of the ion tail with the bulk. For typical tokamak parameters, Karney finds⁶⁴ $v_1 \simeq 2.2 v_{thi}$. Generally, the value of v_1 depends on the applied power.⁶⁵ Again, it is possible that v_1 can be experimentally determined. The velocity v_o characterizes the theoretical upper limit of the tail, but we take the tail temperature to be sufficiently low such that we may set $v_o = \infty$ in the velocity space integrals.

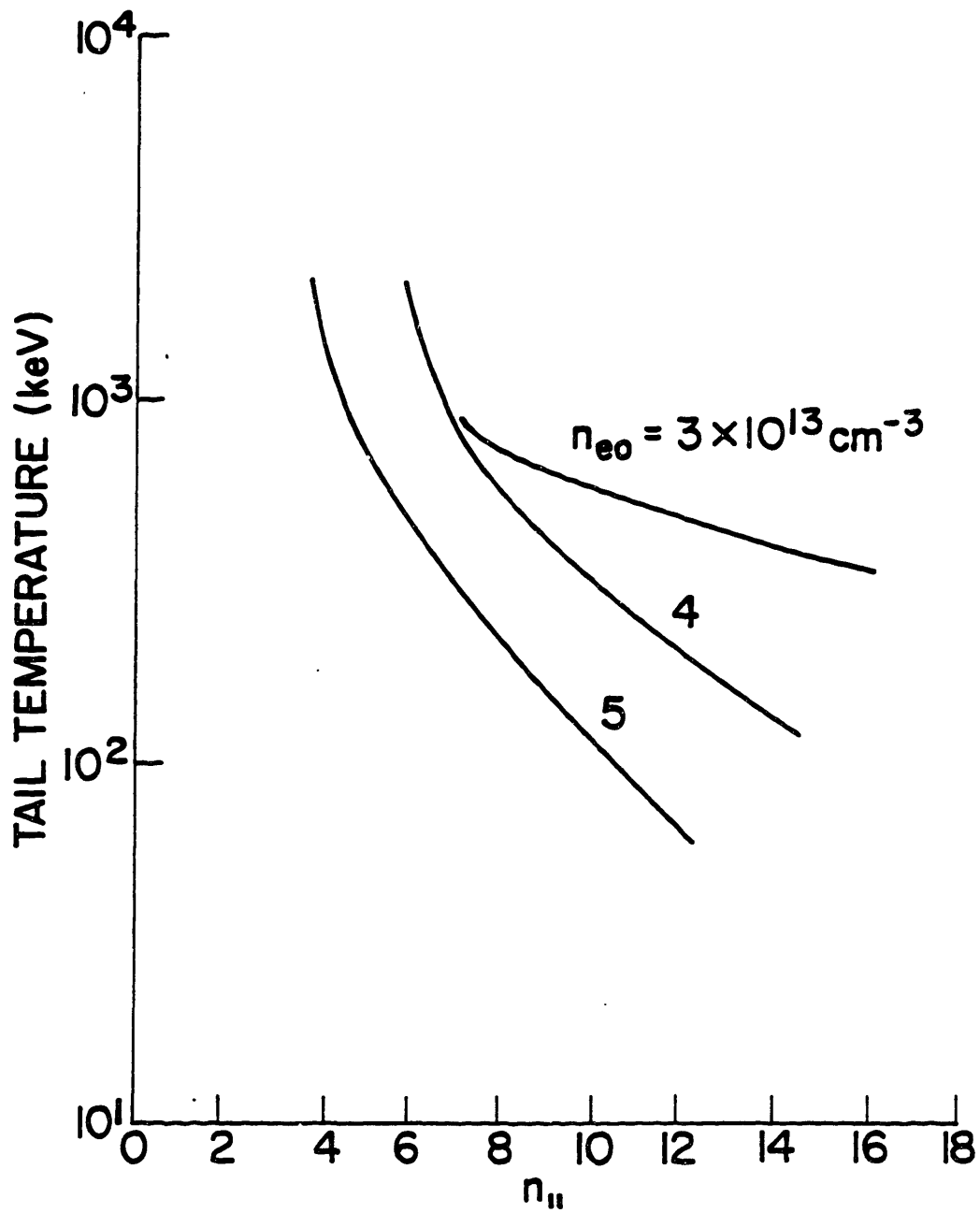


Figure 2.10. Calculated tail temperature at the damping location versus $n_{||}$ for several values of the plasma density and an injected power of 50 kW.

With these simplifications, the distribution function Eq. (2.44) may be written as:

$$F(v_{\perp}) \simeq \frac{1}{\pi v_{thi}^2} \begin{cases} \exp -(v_{\perp}^2/v_{thi}^2), & v_{\perp} \leq v_1; \\ \exp -[(v_1^2/v_{thi}^2)(1 - T_i/T_t)] \exp -[(v_{\perp}^2/v_{thi}^2)T_i/T_t], & v_{\perp} > v_1. \end{cases} \quad (2.52)$$

Because $v_1^2 \gg v_{thi}^2$, the normalization term in front of the bracket is taken to be the same as for the thermal Maxwellian distribution of temperature T_i .

The tail density is

$$\begin{aligned} n_t &= n_i \int_{v_1}^{v_0} F(v_{\perp}) 2\pi v_{\perp} dv_{\perp} \\ &= n_i (T_t/T_i) \exp -(v_1^2/v_{thi}^2) \end{aligned} \quad (2.53)$$

For the parameters $T_i = 150$ eV, $T_t = 1000$ eV, and $v_1 = 2.8v_{thi}$, the fractional ion density of the tail is 0.26%. We note that the number of ions in the tail is strongly dependent on the value of v_1 ; hence it is of primary importance to know this quantity in the experiment in order to evaluate the absorption efficiency.

The energy density in the tail is

$$\begin{aligned} \mathcal{E}_t &= \frac{n_i m_i}{2} \int_{v_1}^{\infty} v_{\perp}^2 F(v_{\perp}) 2\pi v_{\perp} dv_{\perp} \\ &= n_t T_t \left(1 + \frac{v_1^2 T_i}{v_{thi}^2 T_t} \right) \end{aligned} \quad (2.54)$$

If the confinement time of the tail, τ_t , is known, the rf power required to maintain the tail is

$$P_t = \frac{\mathcal{E}_t}{\tau_t}. \quad (2.55)$$

The collisional power delivered by the tail to the bulk ion distribution is⁶⁴

$$P_c = n_i m_i \int_{v_1}^{\infty} v_{\perp} C \left(\frac{\partial F}{\partial v_{\perp}} + \frac{2v_{\perp}}{v_{thi}^2} F \right) 2\pi v_{\perp} dv_{\perp} \quad (2.56)$$

where the collision operator is obtained from Eq. (2.41). Inserting the value of C and performing the integral gives

$$\begin{aligned} P_c &= \frac{6\sqrt{2}e^4 \ln \Lambda}{\sqrt{m_i}} n_i^2 \frac{\sqrt{T_t}}{T_i} \left(1 - \frac{T_i}{T_t} \right) \\ &\quad \times \exp -[(v_1^2/v_{thi}^2)(1 - T_i/T_t)] \int_{x(v_1)}^{\infty} \exp -x^2 dx \end{aligned} \quad (2.57)$$

where $x(v_{\perp}) = \sqrt{(v_{\perp}^2/v_{thi}^2)T_i/T_t}$. From Eqs. (2.54) and (2.56) the collisional heating time is

$$\tau_c = \frac{\mathcal{E}_t}{P_c}. \quad (2.58)$$

In this manner, the rf absorption and collisional heating efficiencies can be estimated directly from the experimental measurements of the ion distribution. Such estimates are presented in Chapter 6 with the use of ion energy spectra obtained from charge-exchange analysis.

In concluding this section, we reiterate that the ion Landau damping mechanism, as it is presently understood, explicitly leads to the formation of a suprathermal ion tail. Wave energy is transferred to particles with perpendicular speeds equal to that of the wave, irrespective of the location in the plasma. However, significant wave damping occurs only if the phase speed is approximately three times the ion thermal speed since the number density of ions in the tail is strongly dependent on the ratio of the wave phase velocity to the thermal velocity (see Eq. 2.53). In a self-consistent treatment of the quasi-linear absorption problem, the presence of the tail has been shown to increase the overall absorption efficiency of the plasma.⁶⁵

This point may be illustrated for the Versator plasma parameters in the following ad hoc manner. We assume the plasma ions to be represented by the superposition of a hot Maxwellian distribution of constant temperature T_t and density n_t on a background plasma with the previously-described temperature and density profiles. With $T_t \leq 10 T_{i0}$ and $n_t \leq 0.02 n_{i0}$, the addition of the hot Maxwellian component changes the thermal correction term K_{xx1} of Eq. (2.16) by less than 20%. Thus the real part of the dispersion relation is largely unaffected by the presence of a relatively small number of hot ions. However, the correction to the damping rate Eq. (2.31) is significant because of its strong dependence on $\omega/k_{\perp} v_{tht}$, where $v_{tht} = \sqrt{2T_t/m_i}$. Accordingly, we add the term $(n_t/n_i)\zeta_t^3 e^{-\zeta_t^2}$ to the quantity in brackets in Eq. (2.31) to account for the wave absorption on the tail, and solve Eq. (2.27) in the same manner as before.

We consider the case of a hot Maxwellian distribution of temperature 1 keV and density $0.002 n_{i0}$ present in the plasma. The hot ion distribution is assumed to exist only inside a minor radius of 10 cm. The background plasma has a central density of $n_{e0} = 3 \times 10^{13} \text{ cm}^{-3}$ otherwise the plasma parameters are the same as in Fig. 2.1a. The n_{\parallel} of the lower-hybrid wave is taken to be 6. In Fig. 2.11, the local wave power of Eq. (2.27) is plotted as a function of minor radius in the midplane. For comparison, the damping for the case with no tail present is also shown. Though the damping length on the fast ion distribution is larger than that on the bulk, absorption of the wave is essentially complete before the linear damping region is reached. Absorption by the ion tail takes place on the low field side where damping on a thermal plasma is not predicted to occur at all. Also plotted in Fig. 2.11 is the energy of an ion which is locally resonant with the wave. While damping takes place on 1.5–1.8 keV ions in the case with no tail, absorption on the tail occurs in the 3–5 keV range. As we will see in the next section, the latter ions should be more poorly confined than the former because of their higher energy and the fact that damping on the tail occurs at larger radii.

Plotted in Fig. 2.12 is the maximum (high field side) damping radius of the lower-hybrid wave versus tail density for two tail temperatures and the conditions assumed in the previous

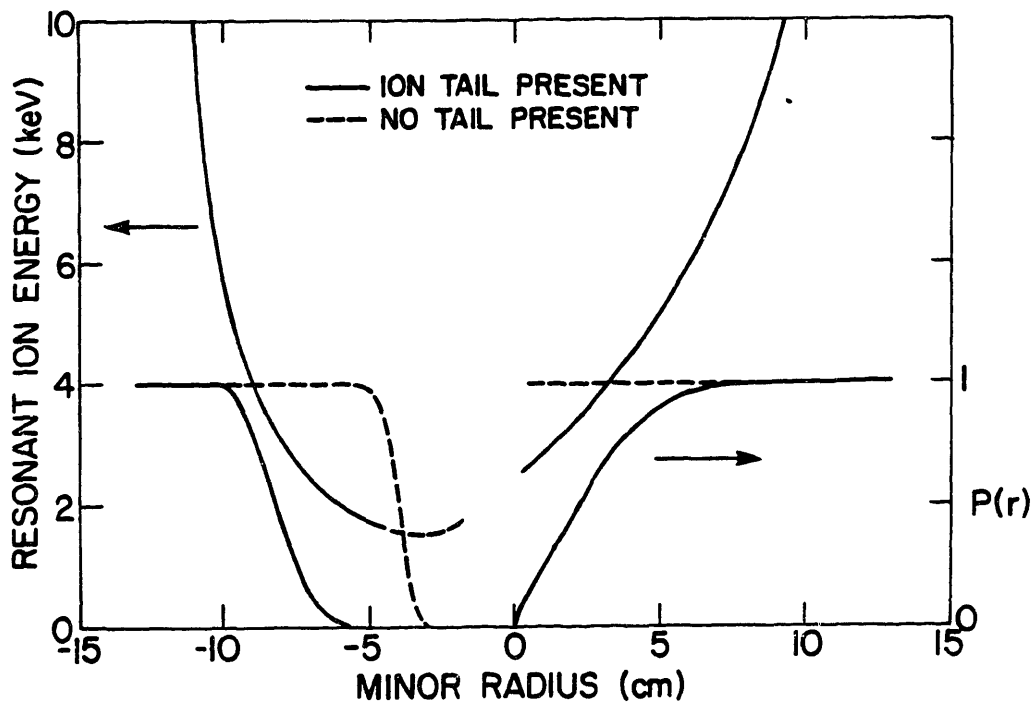


Figure 2.11. $P(r)$ versus minor radius in the midplane for $n_{\parallel} = 6$. A Maxwellian distribution of fractional density $.002 n_{10}$ and temperature 1 keV is assumed to be present within a plasma radius of 10 cm. The central density is $3 \times 10^{13} \text{ cm}^{-3}$ and the other plasma parameters are the same as in Fig. 2.1a. The solid lines indicate the local power with the tail present and the dashed lines are for the situation with no tail present. For the case of the wave incident on the plasma core from the low field side, no damping is calculated to take place before the wave reaches the axis. Also shown is the ion energy resonant with the wave.

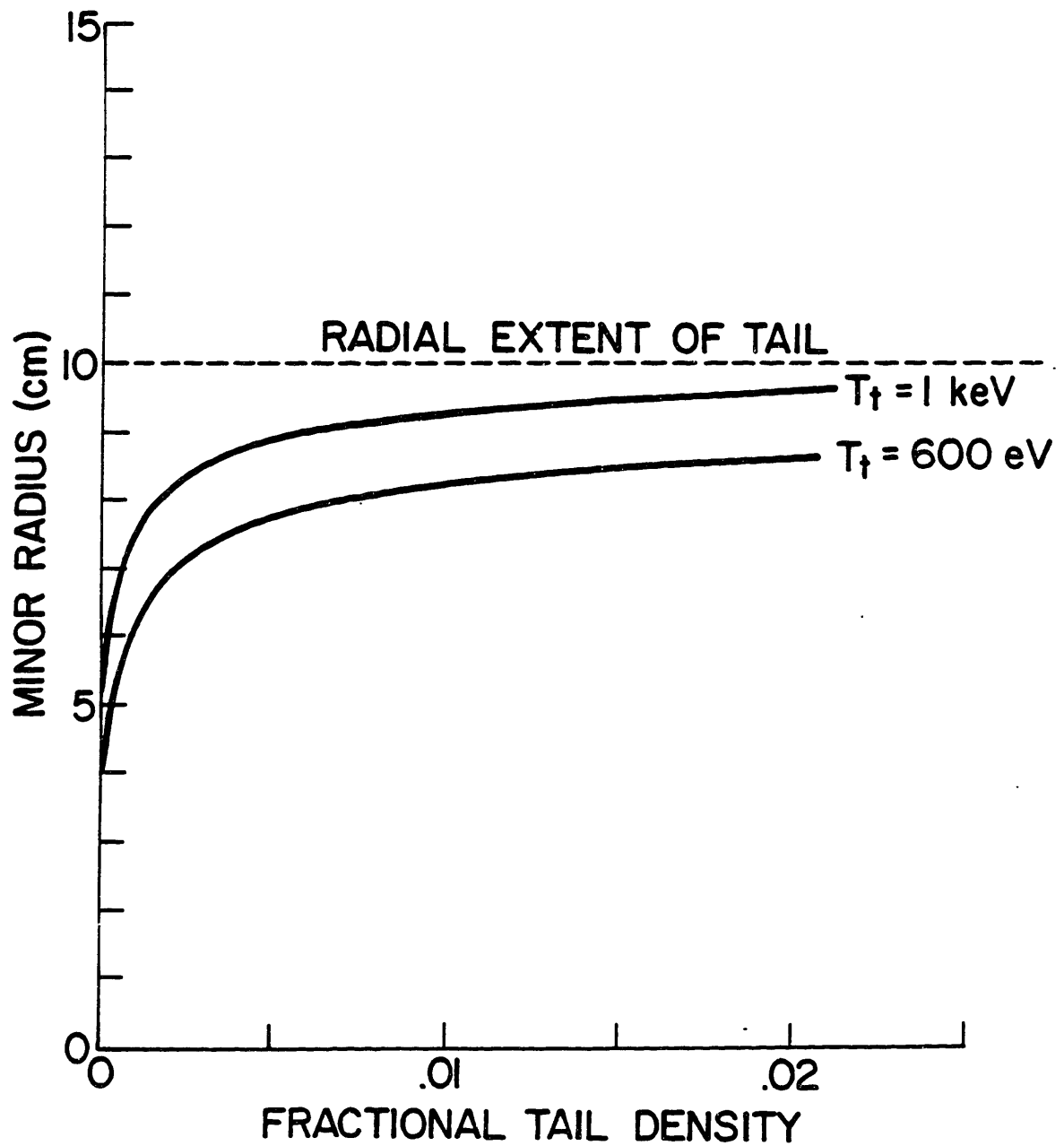


Figure 2.12. Maximum damping radius versus fractional tail density for the same plasma parameters as in Fig. 2.11 and $T_t = 600 \text{ eV}$ and 1000 eV .

figure. Only a small tail density relative to the bulk is needed to permit a significant outward shift of the damping region, and as mentioned earlier, this effect should be more prominent at lower values of n_{\parallel} . Of course, the spatial extent and profiles of the tail distribution have been chosen somewhat arbitrarily; hence these results should not be interpreted as a quantitative prediction of the damping location. Nonetheless, it is clear from the above discussion that the presence of a tail with a number density consistent with the theoretical prediction of Eq. (2.53) substantially modifies the damping behavior of the lower-hybrid wave. Such an effect may be of importance with respect to the confinement of fast ions, as treated in the next section, and possibly with regard to toroidal effects on wave propagation, which is discussed in Section 2.6.

2.5. Energetic Ion Confinement

Regarding the ion tail energy, the only power loss explicitly considered thus far has been collisional coupling to the bulk plasma. However, ions with primarily perpendicular components of velocity such that

$$|v_{\parallel}/v| \leq \sqrt{2r/R_o} \quad (2.59)$$

are banana-trapped, and are subject to orbit losses. Due to the ∇B and centrifugal drifts, the trapped ion suffers a displacement from its flux surface of roughly⁷⁶

$$\Delta r \simeq \left(\frac{m_i c}{e B_{\theta}} \right) v_{\parallel} \quad (2.60)$$

where B_{θ} is the poloidal magnetic field. The excursion from the flux surface corresponds to the size of the ion Larmor radius evaluated for the poloidal magnetic field. As the suprathermal ions are accelerated in the perpendicular direction by the lower-hybrid wave, these particles are certainly trapped, and are poorly confined relative to the circulating thermal ions. For sufficiently fast ions, the poloidal gyroradius may become comparable to the plasma minor radius, and ions are lost directly to the limiter or wall.

Though these neoclassical effects on the heating rate of ions are not quantitatively evaluated in this thesis, we can show that trapped particle losses in Versator are likely to drastically limit the ion heating efficiency; energetic ions created by lower-hybrid wave damping are expected to be lost to the edge before thermalization can occur. The minimum energy required for loss to the limiter may be estimated analytically⁷⁶ by assuming that the most poorly confined trapped ion at a given minor radius on the midplane has a banana trajectory which intersects the limiter. The tips of the widest banana for a specific ion energy are located almost on the midplane on the inner side of the torus. The flux surface on which the tips lie is approximately halfway between the minimum and maximum minor radii of the orbit. The pitch angle ψ_m (defined by $\sin \psi_m = v_{\perp}(\min)/v$) of the ion at its minimum minor radius r_b may be estimated using the conservation of magnetic moment of the ion Larmor orbit. The minimum ion energy for loss to the limiter can then be

obtained by invoking conservation of canonical angular momentum in the toroidal direction. This value of ψ denotes the so-called vertex of the loss region for trapped particles. The derivation for the loss energy is taken from Ref. 75, and is outlined in Appendix B.

In Fig. 2.13, the minimum ion energy for loss and the corresponding pitch angle of the vertex are plotted versus minor radius for several values of the total plasma current. Most ion heating experiments in this work were performed at $I_p \simeq 50$ kA. It is evident from the figure that only ions of energy less than several kiloelectron volts are well confined in Versator. Ions undergoing mirror reflection near the midplane on the high field side of the axis are the most poorly confined of all banana-trapped particles. In Fig. 2.14, the energy of an ion resonant with the lower-hybrid wave is plotted versus the minor radius for several different values of n_{\parallel} . The curves of resonant energy are terminated at the ion damping location for that particular value of n_{\parallel} . The energetic ions are assumed to be created at or near these locations. Also plotted are the neoclassical confinement regions for plasma currents of $I_p = 50$ kA (inner shaded region) and $I_p = 100$ kA (sum of inner and outer shaded regions). For the given current, ions with energies within these regions are confined. The results show that much of the predicted region for ion damping lies outside the neoclassical confinement zone for the typical Versator plasma current of $I_p = 50$ kA. After pitch-angle scattering into the loss region, fast ions will be lost to the edge plasma and limiter. Though higher n_{\parallel} components damp on lower energy ions, the damping region for these values occur at larger radii where confinement is poorer. We note, however, that the confinement problem would be significantly reduced if the plasma current could be doubled to 100 kA.

The maximum effective loss rate of banana trapped ions which are lost to the wall is the bounce frequency of the ion in the magnetic well,

$$\begin{aligned} \omega_B &\simeq \frac{v_i}{qR_o} \left(\frac{a}{R_o} \right)^{\frac{1}{2}} \\ &\simeq 3 \times 10^3 \sqrt{\mathcal{E}_i(\text{eV})} \text{ sec}^{-1} \end{aligned} \quad (2.61)$$

For comparison, the ratio of this rate to collision frequency for thermalization of fast ions given earlier is about $2 \times 10^{-4} \mathcal{E}_i^2(\text{eV})/n_i(10^{13} \text{ cm}^{-3})$. For 1.5 keV ions, the orbit loss rate may be up to 2 orders of magnitude higher than the collisional heating rate. High energy ions which merely traverse the edge region but do not intersect the limiter are also subject to charge-exchange losses which are comparable to the above thermalization rate if the edge neutral density is as high as 10^{10} cm^{-3} . Furthermore, ripple losses of particles trapped in the local magnetic field well between toroidal field coils are calculated to be significant for suprathreshold ions in Versator. Ripple-trapped ions of energy⁷⁸

$$\begin{aligned} \mathcal{E}_i &\geq \left[\frac{\pi n_i e^4 \ln \Lambda m_i^{1/2} a R \omega_{ci}}{2^{1/2} \delta} \right]^{2/5} \\ &\geq 2.3 \text{ keV} [n_i (10^{13} \text{ cm}^{-3})]^{2/5} \end{aligned} \quad (2.62)$$

are expected to escape the plasma before isotropizing. Here, δ is the toroidal field ripple, $|\Delta B/B|$, which is calculated to be approximately 0.002 on axis for Versator. This mechanism is believed to be possibly responsible⁷¹ for the inefficient Alcator A ion heating results and could also be detrimental to fast ion confinement in Versator.

The quantitative effects of orbit losses on the tail temperature and bulk ion heating rate is not assessed here because of the difficulty of the required calculations. However, we note that for numerical computations in which stochastic ion heating theory is combined with neoclassical confinement for the JFT-2 tokamak and lower-hybrid system parameters,⁷⁹ the results expected from the previous discussion are obtained. The plasma ions are predicted to be accelerated stochastically and form a high energy tail within 100–200 μsec after rf is turned on, as in the uniform plasma model of Karney. More importantly, the fraction of ions lost from the tail is significant, and is indeed strongly dependent on the plasma current and the radial location of the damping region.

According to Eqs. (2.46) and (2.57), the tail temperature and bulk ion heating rate are dependent on the ion collision frequency. Because of the high neoclassical loss rate of fast ions and the fact that orbit losses of the tail ions are worse for higher energy ions in contrast to collisional losses, the tail temperature should be much lower than that given by Eq. (2.46). Hence we may expect the true bulk ion heating rate to be lower than that predicted by quasi-linear theory. Clearly, the confinement of near-perpendicular high energy ions in Versator is poor, and off-axis wave damping should give rise to inefficient bulk heating. The results of the previous section show that off-axis heating is indeed likely. Though the toroidal effects discussed in the next section are expected to have a profound effect on the wave propagation and damping, the inclusion of these modifications in fact does not generally lead to improved transmission of wave energy to the plasma core.

2.6. Toroidicity and Wave Propagation

As mentioned earlier, the inhomogeneous magnetic field of the tokamak and the presence of the poloidal field significantly change the propagation of the lower-hybrid wave. The parallel wave number is not a constant of the motion, and the poloidal wave number n_θ , initially assumed to be zero and heretofore also a constant of motion, can become large and even become comparable to the radial component of n_\perp . The inclusion of finite n_θ must reduce the value of n_r for a given n_\parallel because $n_\perp = (n_r^2 + n_\theta^2)^{1/2}$ is fixed by the dispersion relation. In the extreme case of $n_\theta = n_\perp$ and $n_r = 0$, the lower-hybrid wave propagates perpendicularly to the density gradient and cannot penetrate to the core.

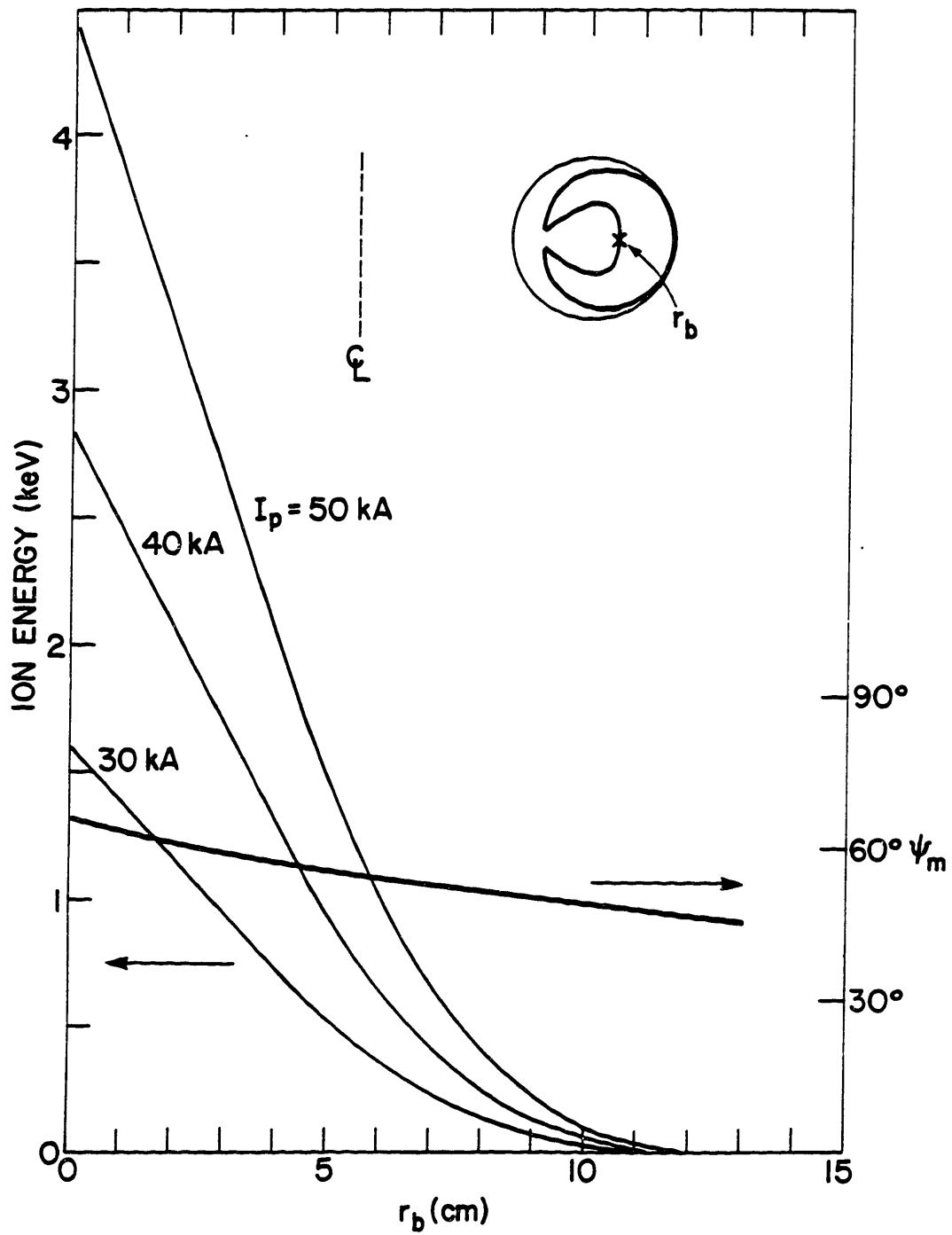


Figure 2.13. Minimum ion energy for loss to the limiter versus minimum minor radius of ion orbit, r_b , for several values of the plasma current. The pitch angle ψ_m of the ion trajectory at r_b is also plotted.

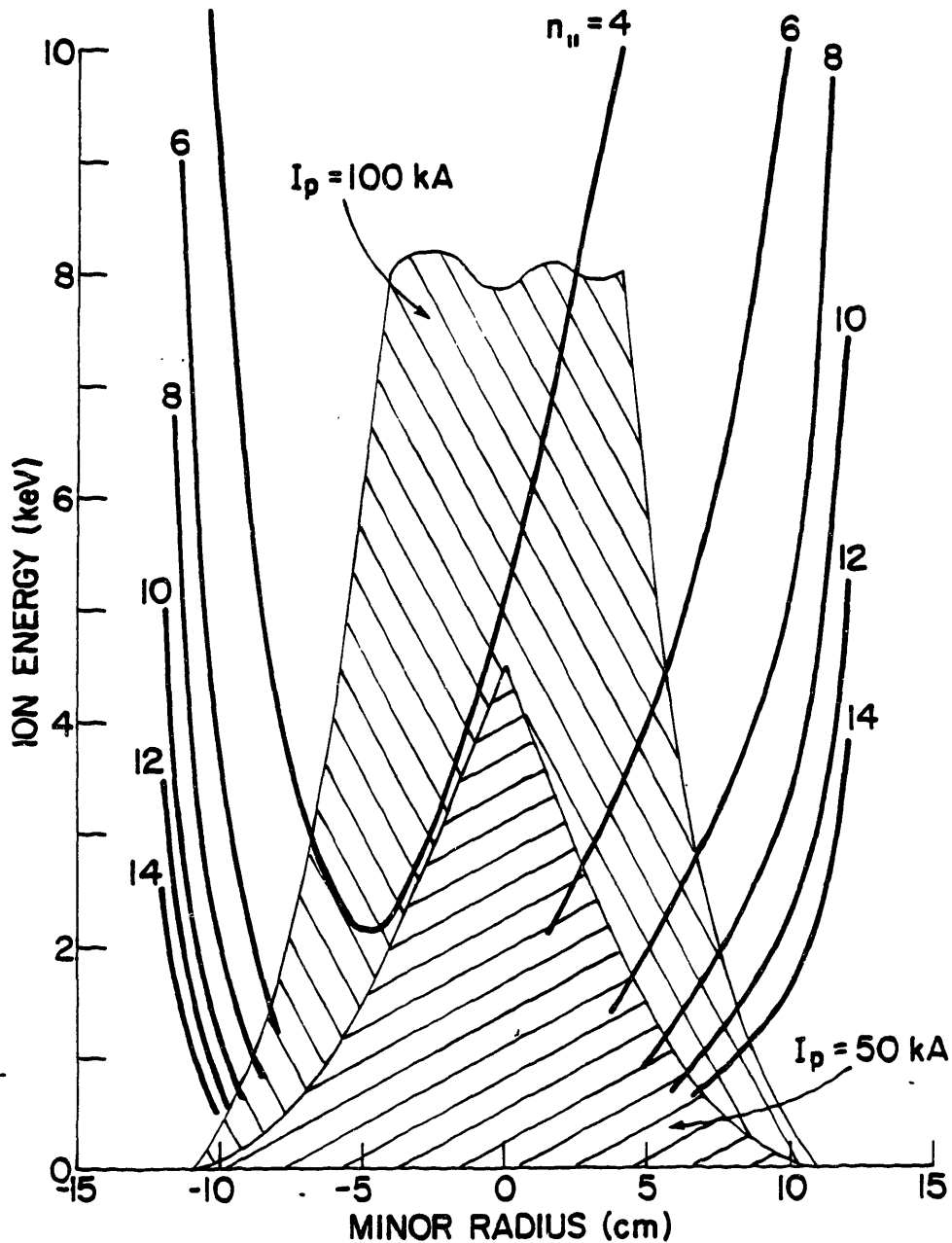


Figure 2.14. Energy of an ion resonant with the lower-hybrid wave versus minor radius in the midplane for several values of $n_{||}$. The curves are terminated at the ion damping locations predicted in Section 2.3. The inner shaded area represents the neoclassical ion confinement region for $I_p \approx 50 \text{ kA}$; the sum of the inner and outer shaded areas represents the confinement region for $I_p = 100 \text{ kA}$.

The evolution of the wave parameters may be calculated using ray tracing theory in which the lower-hybrid wave fields are Fourier-decomposed into a number of plane waves of specified initial n_{\parallel} . Though the use of this model with regard to lower-hybrid waves in tokamaks is still in some question,⁸⁰ the method is widely used to estimate the wave behavior in tokamak geometry.^{62,74,75,81} The major tenet of the theory is that wave propagation is describable by WKB theory^{8,82} and hence the path of the wave in wave vector and configuration space evolves as

$$\frac{dk}{dt} = \frac{\partial D / \partial \mathbf{r}}{\partial D / \partial \omega} \quad (2.63a)$$

$$\frac{d\mathbf{r}}{dt} = -\frac{\partial D / \partial \mathbf{k}}{\partial D / \partial \omega}, \quad (2.63b)$$

which are known as the ray equations. In general, the parallel wave number in tokamak geometry can be written as

$$n_{\parallel} = [n_{\theta} B_{\theta} + n_{\phi} B_{\phi}] / |\mathbf{B}| \quad (2.64)$$

where $n_{\theta} = Mc/\omega r$ and $n_{\phi} = Nc/\omega(R + r \cos \theta)$; M and N being the poloidal and toroidal mode numbers of the wave. The trajectory of the wave in k space, given by Eq. (2.63a) is

$$\frac{dk_r}{dt} = \frac{\partial D / \partial r}{\partial D / \partial \omega}; \quad (2.65a)$$

$$\frac{dM}{dt} = \frac{\partial D / \partial \theta}{\partial D / \partial \omega}; \quad (2.65b)$$

$$\frac{dN}{dt} = \frac{\partial D / \partial \phi}{\partial D / \partial \omega} = 0. \quad (2.65c)$$

The first equation describes the evolution of n_{\perp} similarly to that presented in the last sections, while the second equation indicates that M is variable because of the finite value of $\partial D / \partial \theta$. The third equation reflects the axial symmetry of the toroidal plasma. With the ordering $B_{\theta} \ll B_{\phi}$, the parallel wave number can be approximated from Eq. (2.64):

$$n_{\parallel} \approx \frac{N}{(R_o + r \cos \theta)} \left(1 + \frac{M}{Nq} \right) \quad (2.66)$$

The inhomogeneity of the toroidal field imposes a small variation of n_{\parallel} with major radius, but the major effect on n_{\parallel} is due to the non-constancy of M . Using the cold electrostatic dispersion relation, we find^{62,74,75} from Eq. (2.65b) that dM/dt is proportional to $-r \sin \theta$. Since the sign of n_{\parallel} is the same as that of $d\theta/dt$, $|n_{\parallel}|$ decreases as the wave moves from larger to smaller major radii. Thus any wave launched from the outer major radius (the conventional antenna position) will suffer a drop in n_{\parallel} and an increase in $|n_{\theta}|$. If the launched n_{\parallel} is too low, the wave may become inaccessible and convert to the fast wave. In a less severe case, the down-shifted n_{\parallel} may be still be accessible but the n_{\perp} from the dispersion relation is too low for ion damping to occur (and the n_{\parallel} is too low for electron damping to occur). In addition, if $|M|$ becomes large enough, $|n_{\theta}|$ can increase to the value of $|n_{\perp}|$, whereupon n_r goes to zero and reverses sign, causing the

slow wave to propagate outward. The opposite effects occur for waves propagating from smaller to larger major radii. Though it is impractical to launch waves from the inner side of the torus, waves launched from the top or bottom of the plasma column such that their trajectory carries them to larger major radii will in general experience an upshift in n_{\parallel} leading to better penetration and absorption. However, the lower-hybrid wave damping may take place well off-axis in this case because of the overall tendency for n_{\parallel} , and hence n_{\perp} , to increase significantly.

2.6.1. Toroidal Ray Tracing in Versator: Side Launching

Though the above discussion of the initial evolution of the ray trajectory is useful in visualizing the physics of wave propagation in this geometry, detailed calculations are required for an accurate prediction of the path of the lower-hybrid waves. Such computations have been done for Versator plasma parameters by Dr. Paul Bonoli. In his simulations, a wave with a single n_{\parallel} value and localized to a specified initial poloidal angle is incident on the plasma at the limiter radius. The wave propagation is governed by the ray equations (2.63) in which the full electromagnetic dispersion relation with the warm plasma correction is used. Electron Landau damping and ion damping rates calculated from the imaginary parts of the dispersion relation; for the ions, unmagnetized damping is invoked. The presence of an ion tail is not included in the model, and the wave power absorbed by the ions is used to calculate the increase in the bulk ion temperature. Collisional damping of the wave along the trajectory is also tallied in a manner similar to that described by Eq. (2.33). Results of the simulation are shown in Figs. 2.15–2.17 for initial n_{\parallel} values of 4, 6, and 8. As will be shown in the next chapter, these values are representative of the n_{\parallel} power spectrum of the side-launching grill for a relative phase angle between adjacent waveguides of $\Delta\phi = 180^{\circ}$ (see Fig. 3.3). The plasma parameters are similar to those for Fig. 2.1a. The launch point is taken to be the outer major radius on the midplane. The central density is $4 \times 10^{13} \text{ cm}^{-3}$. In this set of figures, (a) is a projection of the ray trajectory in the poloidal plane; (b) shows the evolution of n_{\parallel} , ζ_i , and ξ_{0e} for the same case. We first consider the case of $n_{\parallel} = 4$, illustrated in Fig. 2.15: from the path of the ray, it is evident that n_r reverses sign on the high magnetic field side. Though n_{\parallel} drops to a minimum of 2 on the inner side, the wave does not penetrate to a high enough density to convert to the fast wave, but is reflected as the slow wave. Also note that the reduction of n_{\parallel} prevents the wave from damping at the lower mode conversion densities on the inner side.

The outward propagating slow wave is assumed to reflect from the slow wave cut-off layer near $\omega = \omega_{pe}$ (or perhaps from the chamber wall, since the cut-off layer is close to the wall), whereupon it travels inward again. The cycle usually repeats until the wave bounces off the bottom of the plasma column. As outlined earlier, n_{\parallel} then increases as the wave travels to lower magnetic fields, and resonant damping can occur. In this case, however, collisional damping on electrons accounts for 88% of the total power loss because of the long path length, and the ray tracing is terminated before collisionless absorption becomes effective.

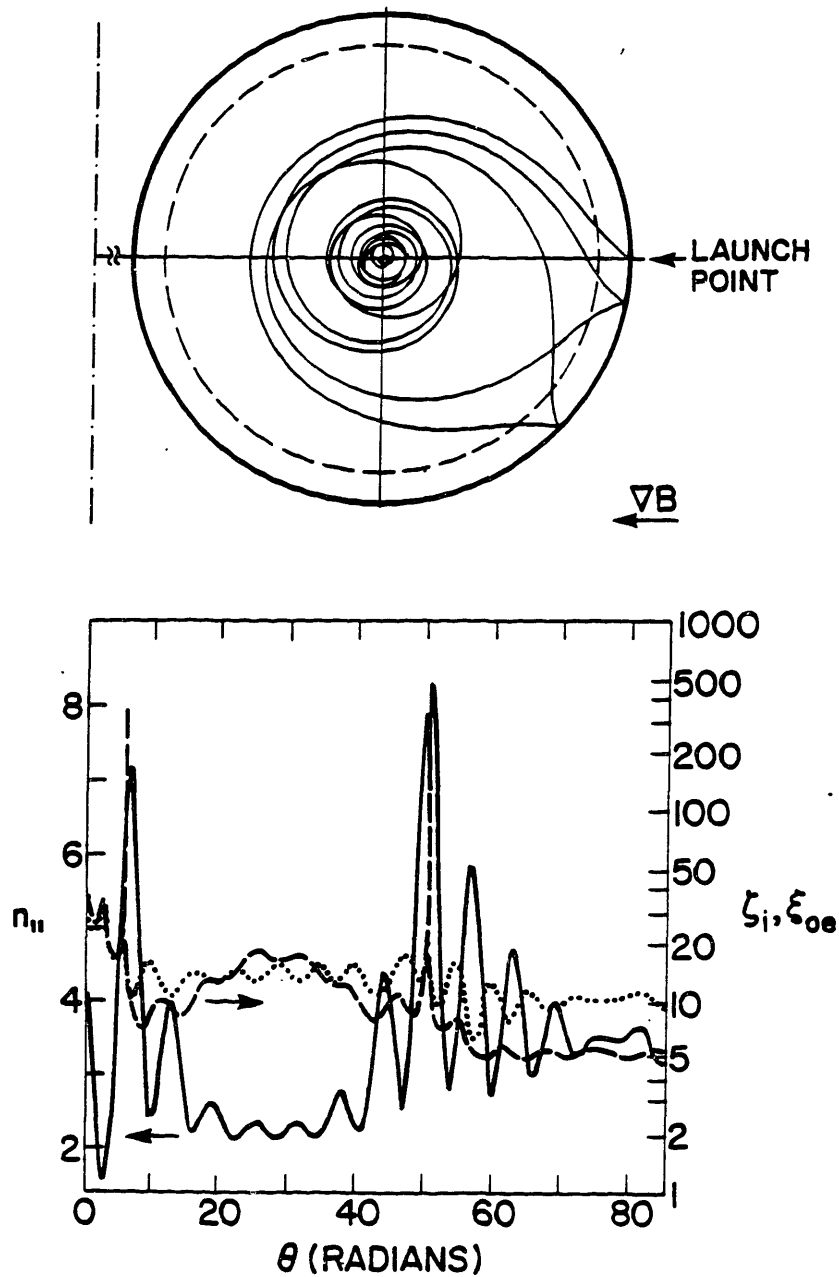


Figure 2.15. (a) Projection in the poloidal plane of the predicted path of the lower-hybrid wave. The plasma parameters are the same as in Fig. 2.1a and the initial $n_{||}$ is 4. The wave is launched from the outer major radius ($\theta = 0^\circ$). The inner circle (dashed line) represents the limiter radius, while the outer circle is the plasma boundary defined by the chamber size. The centerline of the tokamak lies to the left in this diagram. (b) Evolution of $n_{||}$ (solid line), ζ_i (dashed line), and ξ_{oe} (dotted line) along the poloidal trajectory of the ray.

The same quantities illustrated in Fig. 2.15 are plotted in Fig. 2.16 for an initial n_{\parallel} of 6, and in Fig. 2.17 for an initial n_{\parallel} of 8 for the same plasma conditions as before. The final n_{\parallel} values at the damping locations are about 24. Poor radial penetration is predicted for these cases as well. For $n_{\parallel} = 6$, the collisional damping accounts for 80% of the power loss, and resonant absorption on electrons for 19%. The value of ξ_{0e} at the damping location is about 3, while ζ_i is approximately 4. For $n_{\parallel} = 8$, 88% of the rf power is lost to collisions and 9% to ion heating, and the final values of ζ_i and ξ_{0e} are both approximately 3.

Most other ray trajectories in the density range $2 \times 10^{13} < n_{e0} < 5 \times 10^{13} \text{ cm}^{-3}$ appear similar to these. None penetrate the plasma without suffering bounces at the plasma edge. In a plot similar to Fig. 2.7, the calculated damping locations are plotted in Fig. 2.18. The dotted line separates the region of ion heating from collisionless electron heating. The line is drawn where the resonant absorption on each species is approximately equivalent. The shaded region indicates the parameters for which over 90% of the rf power is lost to collisions. Though several contour lines of equal damping radius have been drawn to fit the computed results, there is no simple relationship between the plasma parameters and the specific fate of the wave. As indicated in Fig. 2.18, collisional damping in the outer plasma is the predominant power loss mechanism for densities $n_{e0} \geq 3 \times 10^{13} \text{ cm}^{-3}$ and $n_{\parallel} \geq 8$. In fact, collisional losses account for over 50% of the absorbed power in all cases except for $n_{\parallel} \leq 2$ or $n_{e0} \leq 2 \times 10^{13} \text{ cm}^{-3}$. An examination of the ray trajectories shown in Figs. 2.15–2.17 indicates why collisional damping should be important for the case of side-launching: because of the toroidal effects discussed above, the ray path traverses the edge region many times. The collisional damping can be calculated in a manner similar to that indicated by Eq. (2.27) with $Im k_{\perp}$ given by the expression appropriate for collisional absorption (e.g, Eq. 2.33). For these calculations, the electron temperature at the limiter radius was taken to be 20 eV. As the typical value of $Im k_{\perp}$ due to collisions in the edge region is not insignificant, the collisional damping integrated over the entire path length of the ray can be large.

Electron Landau damping, generally occurring farther than halfway out, is responsible for power absorption at lower n_{\parallel} 's while ion heating only occurs for $n_{e0} \geq 3 \times 10^{13} \text{ cm}^{-3}$ and $n_{\parallel} \leq 4$ and a few other points. The effect of toroidicity on the damping behavior of the wave is evident from a comparison of Fig. 2.18 to Fig. 2.7. The plasma conditions for ion heating are seen to be even more restrictive when toroidal effects are considered. The scatter of damping points for the toroidal propagation case shown in Fig. 2.18 is indicative that the trajectory of the wave on its final pass is determined primarily by the poloidal location of its last bounce rather than the initial conditions. Also, waves launched with slightly different n_{\parallel} 's do not necessarily damp close to one another or even on the same species. Moreover, we note that the interaction of the outgoing wave with the edge plasma may not be a simple specular reflection as assumed by the calculation. Collisions of the wave with the limiter are likely to scatter the wave unpredictably and, in the case of Versator, the non-circular vacuum vessel may well complicate the reflection patterns. Furthermore, WKB theory may not be valid in representing lower-hybrid wave propagation. Taken

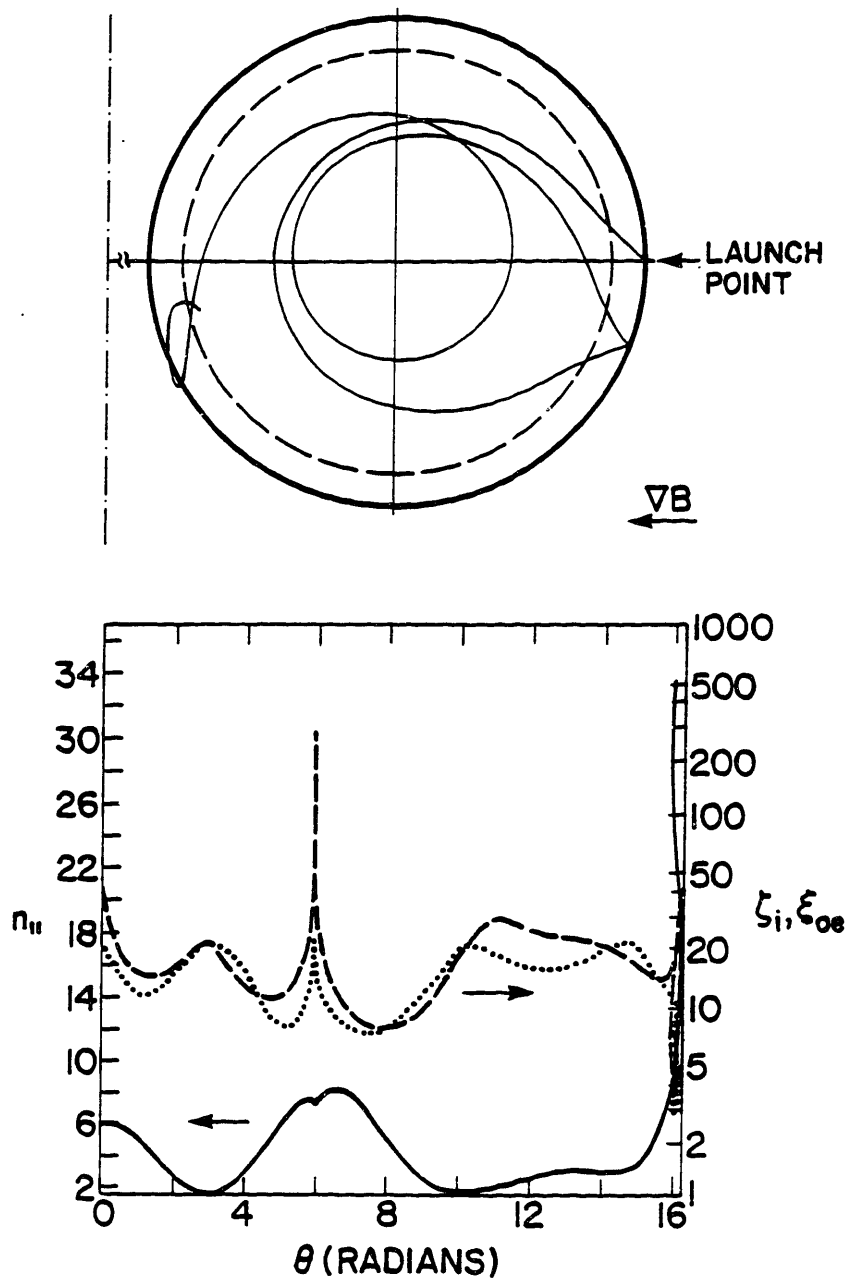


Figure 2.16. (a) Projection in the poloidal plane of the predicted path of the lower-hybrid wave. The plasma parameters and antenna location are the same as in Fig. 2.15, and the initial $n_{||}$ is 6. (b) Evolution of $n_{||}$ (solid line), ζ_i (dashed line), and ξ_{oe} (dotted line) along the poloidal trajectory of the ray.

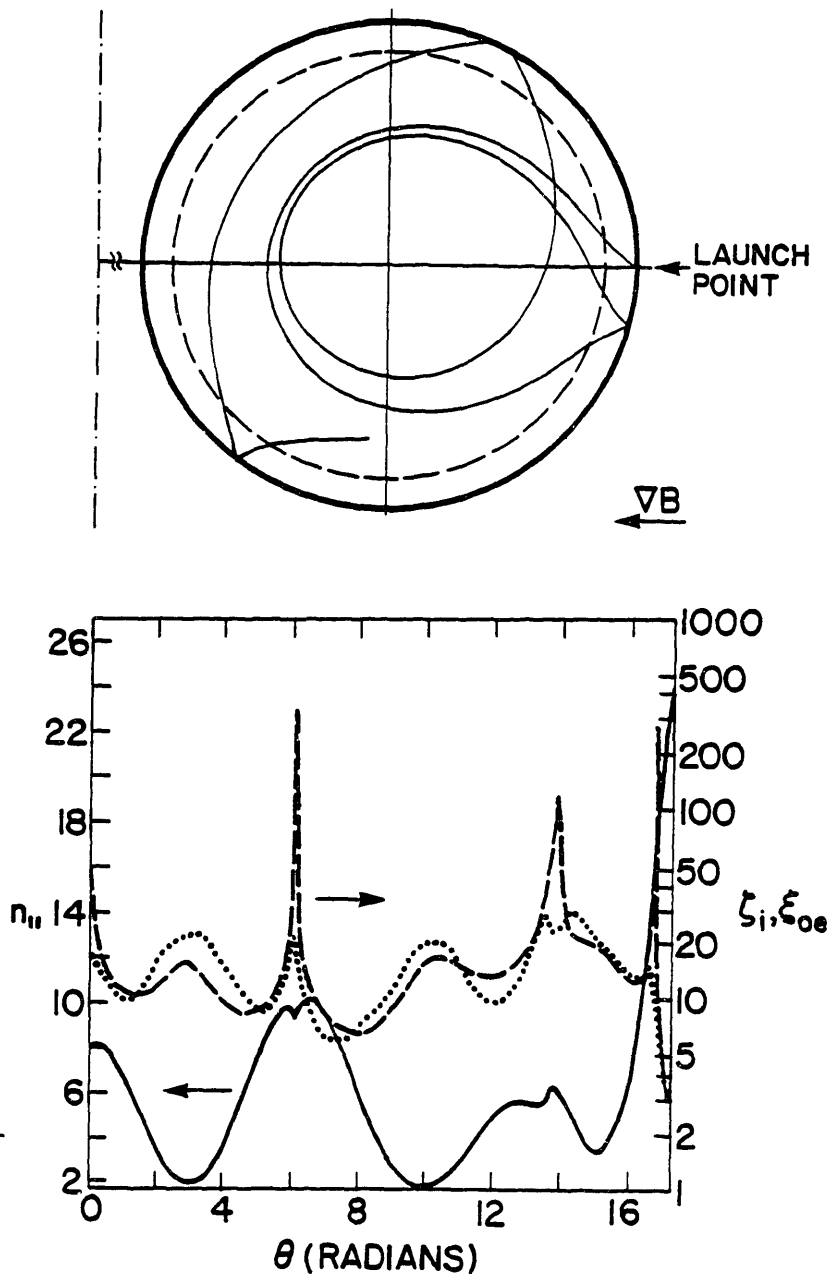


Figure 2.17. (a) Projection in the poloidal plane of the predicted path of the lower-hybrid wave. The plasma parameters and antenna location are the same as in Fig. 2.15, and the initial $n_{||}$ is 8. (b) Evolution of $n_{||}$ (solid line), ζ (dashed line), and ξ_{oe} (dotted line) along the poloidal trajectory of the ray.

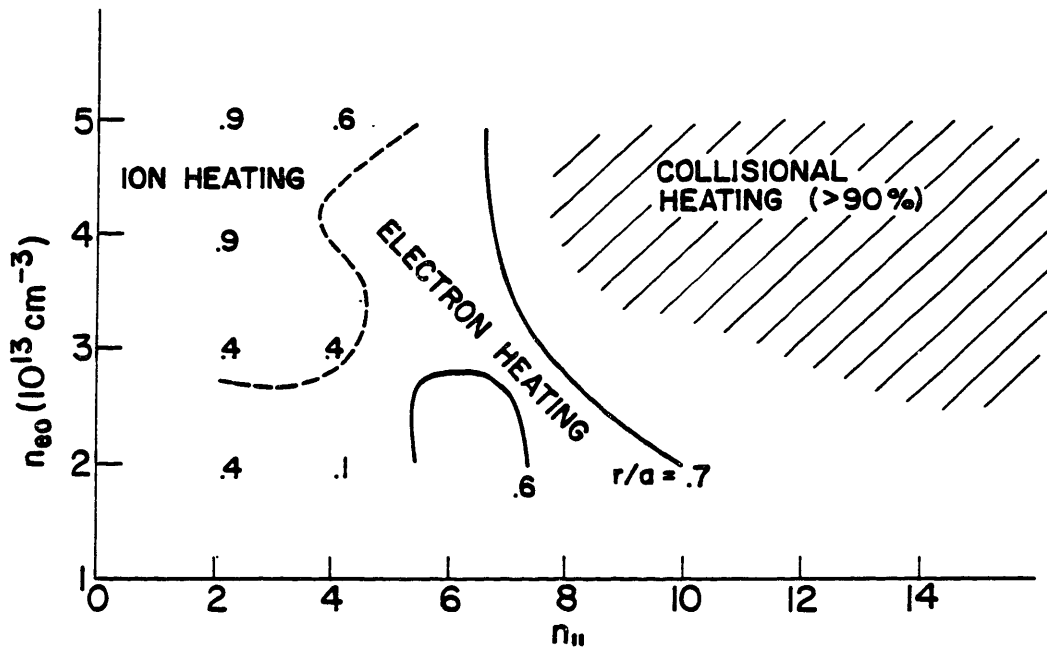


Figure 2.18. Contour plot of the damping radius (r/a) from toroidal ray-tracing analysis for lower-hybrid waves launched from the outer major radius. The assumed plasma parameters are the same as in Fig. 2.7.

at face value, the results of the toroidal theory suggest that the heating efficiency may be extremely sensitive to the plasma parameters and profiles, and could exhibit large variations.⁷⁴

Though the predictions of ray tracing theory may not be entirely valid because of the complex ray paths, it is clear that the initial evolution of the lower-hybrid waves as described by the theory leads to poor rf penetration to the plasma center in Versator. Linear collisionless damping of the lower-hybrid wave is generally weak because of the downshift in n_{\parallel} ; consequently, other damping mechanisms having relatively long damping lengths can be significant. We have illustrated the importance of collisional damping in this model; for the same reasons, we note that damping on an ion tail in the outer region of the plasma (which is not explicitly considered in this numerical treatment of ray propagation and wave damping) may also be more significant in this toroidal model than in the case of slab geometry described in Section 2.4. Non-linear effects, e.g. parametric decay, may similarly play an important role in wave absorption at the edge. Given this picture, neither ion nor electron heating on Versator can be expected to be particularly efficient with lower-hybrid waves launched from the conventional side location.

Transport code simulations combined with the type of ray-tracing calculations presented above have been performed for the parameters of the Versator ion heating experiment by Drs. Paul Bonoli and Ronald Engle.^{34,83} The code models a one-dimensional plasma with the ion energy transport given by the neoclassical value of Hazeltine and Hinton,⁸⁴ scaled by an appropriate value (3–7, typically) to make the initial parameters in the ohmic plasma self-consistent. The electron transport is modelled by Coppi-Mazzucatto diffusion.^{84,85} The launched n_{\parallel} power spectrum used in these simulations is provided by the Brambilla coupling code⁷ described in the next chapter. Damping is assumed to take place on a thermal plasma distribution in the same manner as described above for the ray-tracing calculations.

The predicted heating efficiency for rf injection with the side-launching antenna is found to vary significantly with the edge electron temperature (T_e at $r = a$), with larger temperature increases noted for higher edge temperatures. The initial and final calculated ion and electron temperature profiles are shown in Fig. 2.19 for the conditions $\bar{n}_e = 2.6 \times 10^{13} \text{ cm}^{-3}$, $B_o = 13.5 \text{ kG}$, $I_p = 55 \text{ kA}$, and $P_{rf} = 50 \text{ kW}$ with the relative phase between adjacent waveguides $\Delta\phi = 180^\circ$. In this simulation the ion thermal conductivity is taken to be 3 times the neoclassical value of Hazeltine and Hinton. The curves labeled T_{e1} and T_{i1} are the initial profiles, while T_{e2} and T_{i2} are the profiles at the end of the 5 msec rf pulse. In Fig. 2.19a, the assumed edge electron temperature is 30 eV, and in Fig. 2.19b, the edge temperature is 10 eV. The predicted central ion temperature increase of 100 eV in the former case is about four times larger than that of the latter. The difference in the calculated heating efficiency is due to the stronger collisional damping in the colder edge plasma of the second case. These simulations clearly show the ion heating efficiency to be very sensitive to subtle changes in the electron temperature profile.

The computed ion temperature profile is also broader in the rf-heated plasma than in the

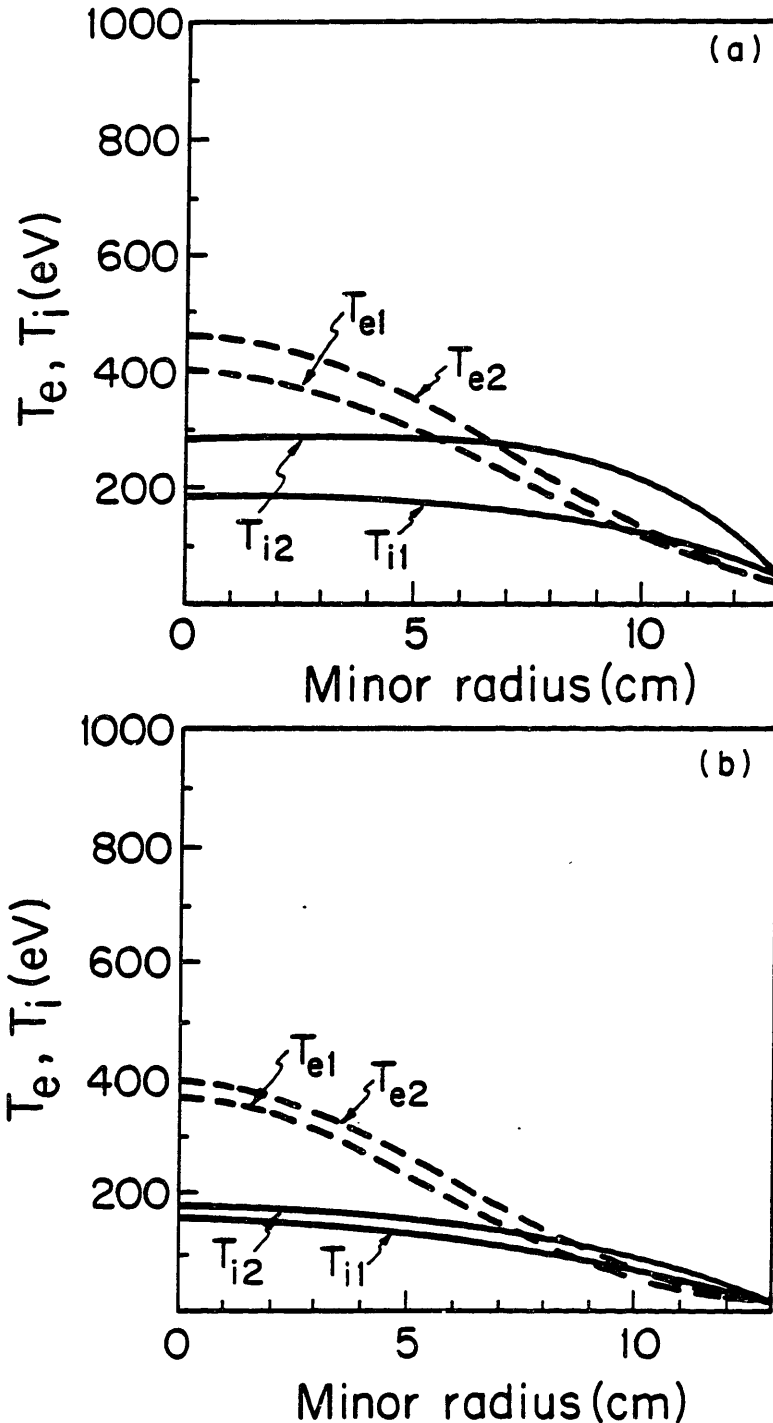


Figure 2.19. Transport code predictions of the electron and ion temperature profiles in Versator during rf heating with the side-launching antenna. T_{e1} and T_{i1} represent the initial electron and ion temperature profiles before the rf is turned on; T_{e2} and T_{i2} are the calculated profiles at the end of the 5 msec rf pulse. The rf power is 50 kW; the plasma parameters are given in the text. In (a), the assumed electron temperature at the limiter radius is 30 eV; in (b), the edge temperature is 10 eV.

initial ohmically-heated discharge. This is generally consistent with the predictions of off-axis wave damping illustrated in Figs. 2.15–2.17.

2.6.2. Toroidal Ray Tracing on Versator: Top-Launching

For the same reason that lower-hybrid waves launched from the side of the torus suffer a downshift in n_{\parallel} , waves launched towards larger major radii are predicted to experience an upshift in n_{\parallel} . Because of the better radial penetration of the latter waves, a top-launching rf antenna has been designed and built for operation on Versator. The primary experimental application of this grill is the improvement of electron heating efficiency, but ion heating may also be facilitated with the use of this grill in the appropriate density range. However, the n_{\parallel} spectrum of this antenna is optimized at high values for electron damping. Furthermore, the narrow ports on the top of the vacuum vessel can only accommodate a grill with narrow waveguides, also necessitating a spectrum characterized by high n_{\parallel} ; for a relative phase angle between waveguides of $\Delta\phi = 180^\circ$, the representative n_{\parallel} is about 15 (see Table 1 and the calculated spectrum in Fig. 3.4 of the next chapter). In light of the discussion of the previous sections, especially with the recognition that the n_{\parallel} should initially upshift, the launched n_{\parallel} spectrum for $\Delta\phi = 180^\circ$ is too high for ion heating to occur on axis. In practice, the grill can of course be phased at a lower angle, but the high antenna reflectivity for $\Delta\phi < 90^\circ$ limits the efficient coupling of rf power.

Graphs of the poloidal ray trajectories and evolution of n_{\parallel} , ζ_i , and ξ_{0e} for the case of top-launching are shown in Figs. 2.20–2.22. The plasma parameters are the same as before. The case of the initial $n_{\parallel} = 4$ is illustrated in Fig. 2.20. The local parallel wave number varies from 3 to 7 along the trajectory, and upon damping, n_{\parallel} is only 4.8. A total of 78% of the rf power is predicted to be lost to ions, with the remainder going to collisional heating. The damping radius is predicted to be $r/a \simeq 0.3$.

The similar plots for $n_{\parallel} = 6$ and 8 are shown in Figs. 2.21 and 2.22. As expected, these waves are predicted to damp at larger minor radii ($r/a \simeq 0.5$ and 0.6 , respectively) than that for the previous case. For the initial n_{\parallel} of 6, 62% of the power is predicted to be lost to ions, while for the initial n_{\parallel} of 8, only 40% of the power is absorbed by ions. In the latter case, resonant damping on electrons accounts for 23% of the power loss, with collisional absorption being responsible for the remainder. For the initial n_{\parallel} value of 6, the n_{\parallel} value at the damping location is about 12, but is only 3 for the wave launched with an n_{\parallel} of 8. Even though the radial penetration rate is much greater for the top-launched rays, the parallel wave number is still seen to vary significantly along the ray trajectory.

We remark that rays launched with negative n_{\parallel} (toward smaller major radii in this example) have trajectories similar to those launched from the side. In Fig. 2.23, the ray trajectory and evolution of n_{\parallel} , ζ_i , and ξ_{0e} are plotted for the top-launched ray with initial n_{\parallel} of -6 ; i.e. for a ray launched toward the high field side. For this ray, only 8% of the power is predicted to damp on ions, while 23% goes to resonant electron absorption and the remainder to collisional damping.

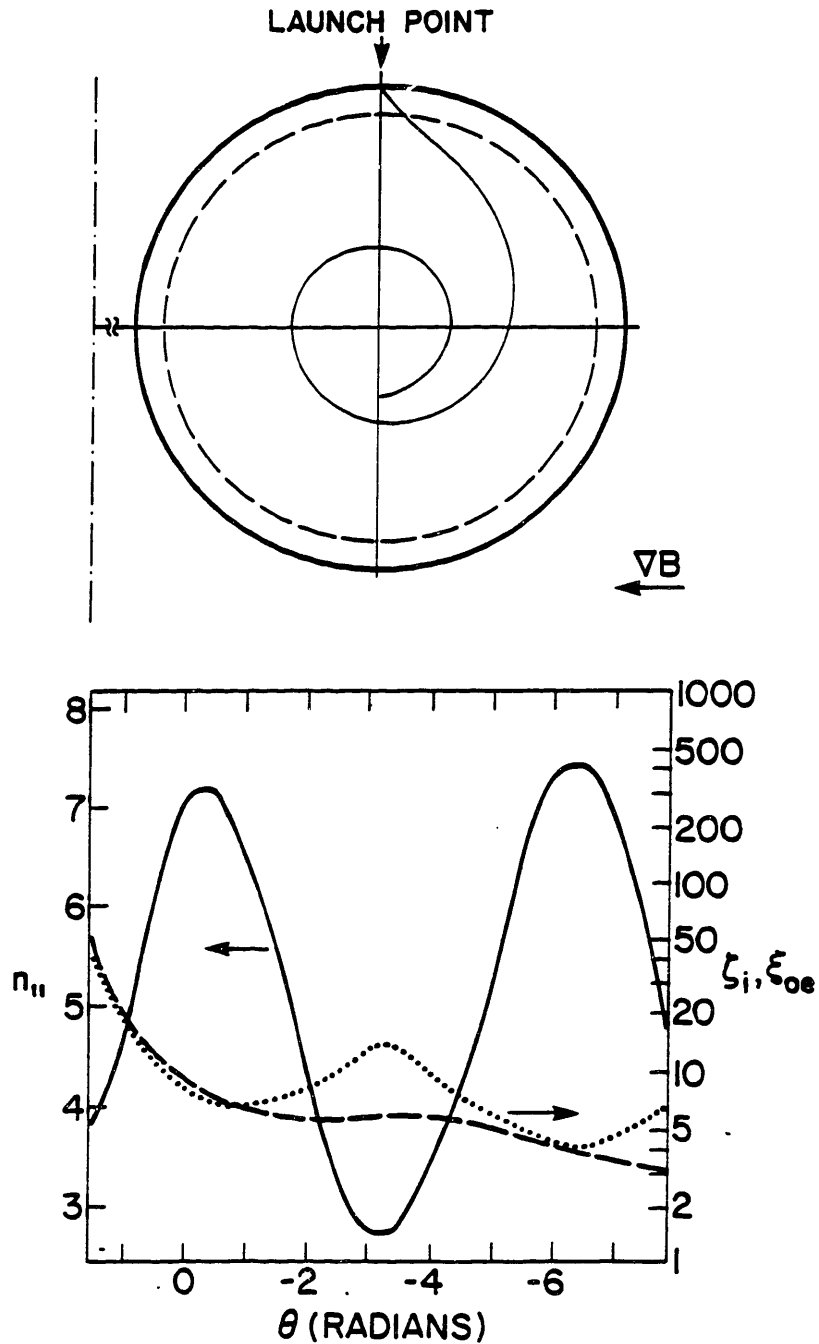


Figure 2.20. (a) Projection in the poloidal plane of the predicted path of the lower-hybrid wave. The plasma parameters are the same as in Fig. 2.1a and the initial $n_{||}$ is 4. The wave is launched from the top of the plasma column ($\theta = 90^\circ$) toward the low field side. (b) Evolution of $n_{||}$ (solid line), ζ_i (dashed line), and ξ_{oe} (dotted line) along the poloidal trajectory of the ray.

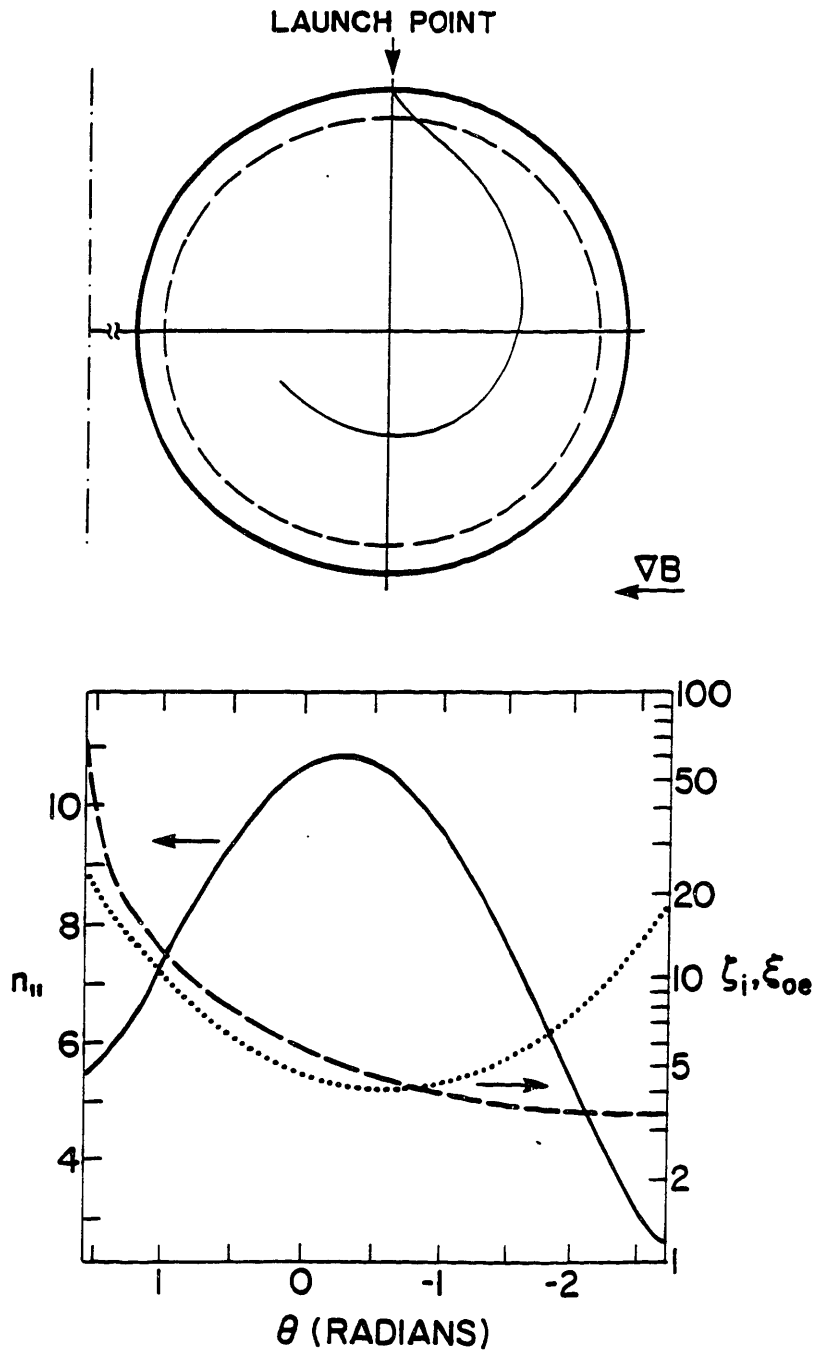


Figure 2.21. (a) Projection in the poloidal plane of the predicted path of the lower-hybrid wave. The plasma parameters and antenna location are the same as in Fig. 2.20, and the initial $n_{||}$ is 6. (b) Evolution of $n_{||}$ (solid line), ζ_i (dashed line), and ξ_{oe} (dotted line) along the poloidal trajectory of the ray.

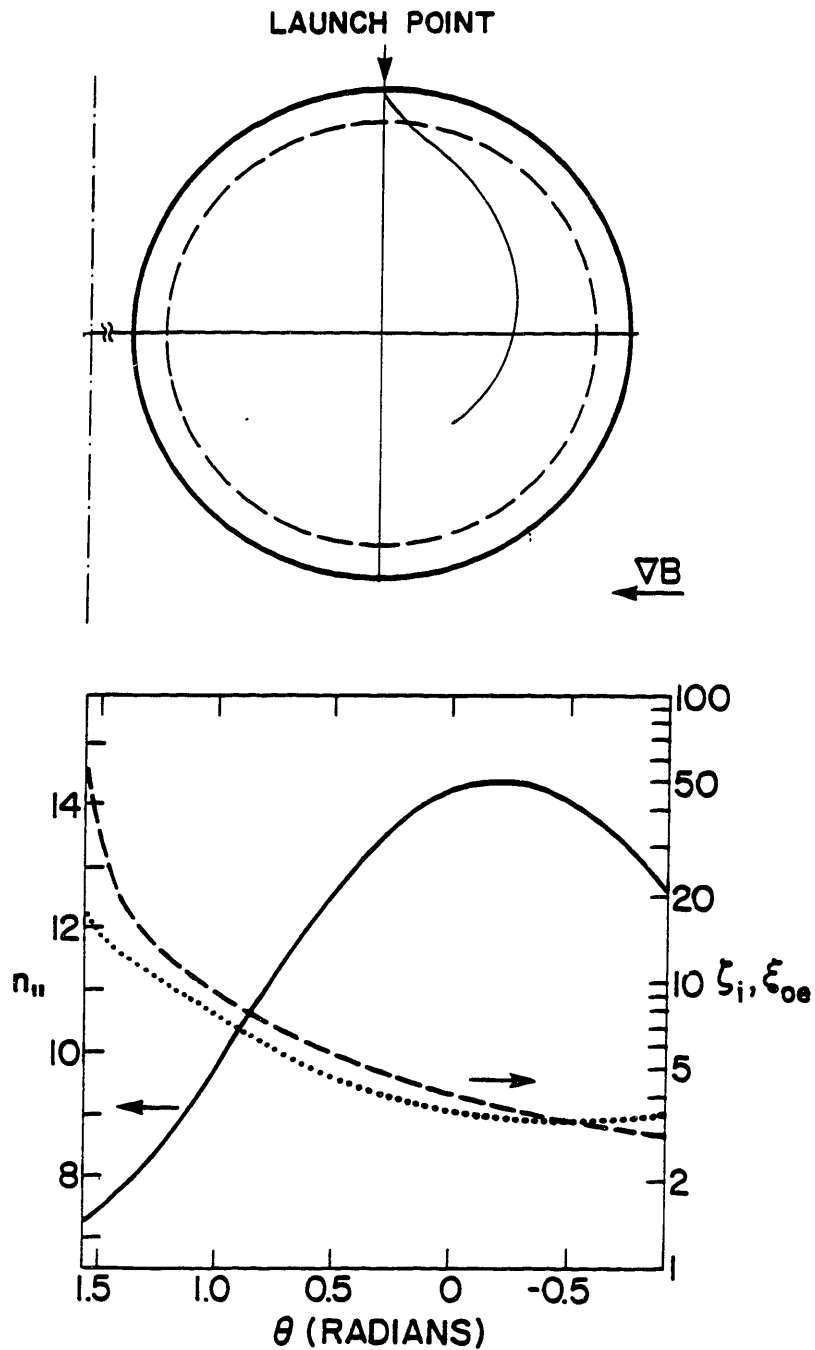


Figure 2.22. (a) Projection in the poloidal plane of the predicted path of the lower-hybrid wave. The plasma parameters and antenna location are the same as in Fig. 2.20, and the initial $n_{||}$ is 8. (b) Evolution of $n_{||}$ (solid line), ζ_i (dashed line), and ξ_{oe} (dotted line) along the poloidal trajectory of the ray.

For a relative phase between waveguides of $\Delta\phi = 90^\circ$, roughly 30% of the launched power is represented by waves with negative n_{\parallel} (see Fig. 3.4 in the next chapter). Because of the predicted difference in the heating behavior between positive and negative waveguide phasings, experiments with the top launcher should provide a test of the toroidal ray tracing theory if the actual damping mechanisms are similar to those used in these calculations.

A contour plot of the damping locations for top launching of positive n_{\parallel} rays is shown in Fig. 2.24. The penetration of rf power to the center is better in this case than for side launching. Because the waves usually damp on the first traverse of the plasma interior, the ray lengths are shorter, and collisional damping is less than for the case of side-launching. Only for the highest central density of $5 \times 10^{13} \text{ cm}^{-3}$ does the total collisional damping of a ray exceed 50%. Nonetheless, the parameter space for ion heating near the plasma center is still relatively small because of the calculated upshift in n_{\parallel} . For central ion heating to occur, the central density must be approximately $3 \times 10^{13} \text{ cm}^{-3}$ and the launched n_{\parallel} spectrum should peak near 4. The latter qualification is difficult to satisfy with the available grill. At higher densities, ion heating is possible over a wider range of n_{\parallel} , but only at larger minor radii.

Preliminary transport code simulations of the top-launching ion heating experiments have been performed with nearly the same plasma parameters used in the previously-described simulation with the following differences: the ion thermal conductivity is taken to be 7 times the theoretical neoclassical value, and the electron transport is given by modified Coppi-Mazzucatto diffusion which simulates increased electron energy transport in rf-heated plasmas.⁸⁷ Consequently, the rf heating efficiencies are lower in this simulation than in the previous one. The specific plasma parameters in this case are taken to be $n_{e0} = 3.9 \times 10^{13} \text{ cm}^{-3}$, $B_0 = 14 \text{ kG}$, $I_p = 55 \text{ kA}$, $T_{e0} = 400 \text{ eV}$, $T_{i0} = 160 \text{ eV}$, and $T_e(r = a) = 30 \text{ eV}$. The transmitted rf power is 100 kW.

The resulting ion and electron temperature profiles are shown in Fig. 2.25. In Fig. 2.25a, the relative phase between adjacent waveguides is $\Delta\phi = +90^\circ$ (most of the power launched toward the high field side; $n_{\parallel}(\text{typ.}) = 7$), and in Fig. 2.25b, $\Delta\phi = -90^\circ$ (most of the power launched toward the low field side; $n_{\parallel}(\text{typ.}) = -7$). The heating is best for the case of $\Delta\phi = -90^\circ$. For $\Delta\phi = +90^\circ$, the upshift in n_{\parallel} caused by toroidal effects allows most of the rf power to be resonantly absorbed on electrons between a minor radius of $r = 6$ and 11 cm. Only about 8% of the power damps on ions, and the predicted central ion temperature rise is only 35 eV. For $\Delta\phi = -90^\circ$, the ion temperature increase is about three times as great, and the ion temperature profile is significantly broadened relative to the ohmic profile. In this case, the ions are predicted to absorb 35–40% of the power, since the downshift in n_{\parallel} of most of the launched spectrum does not favor electron Landau damping. The simulation for $\Delta\phi = 180^\circ$ (Fig. 2.25c) shows a heating efficiency intermediate between the above two examples for the reason that half of the launched power spectrum experiences an upshift in n_{\parallel} while the other half is downshifted.

In summary, the heating efficiency of the top-launching grill is expected to show a strong

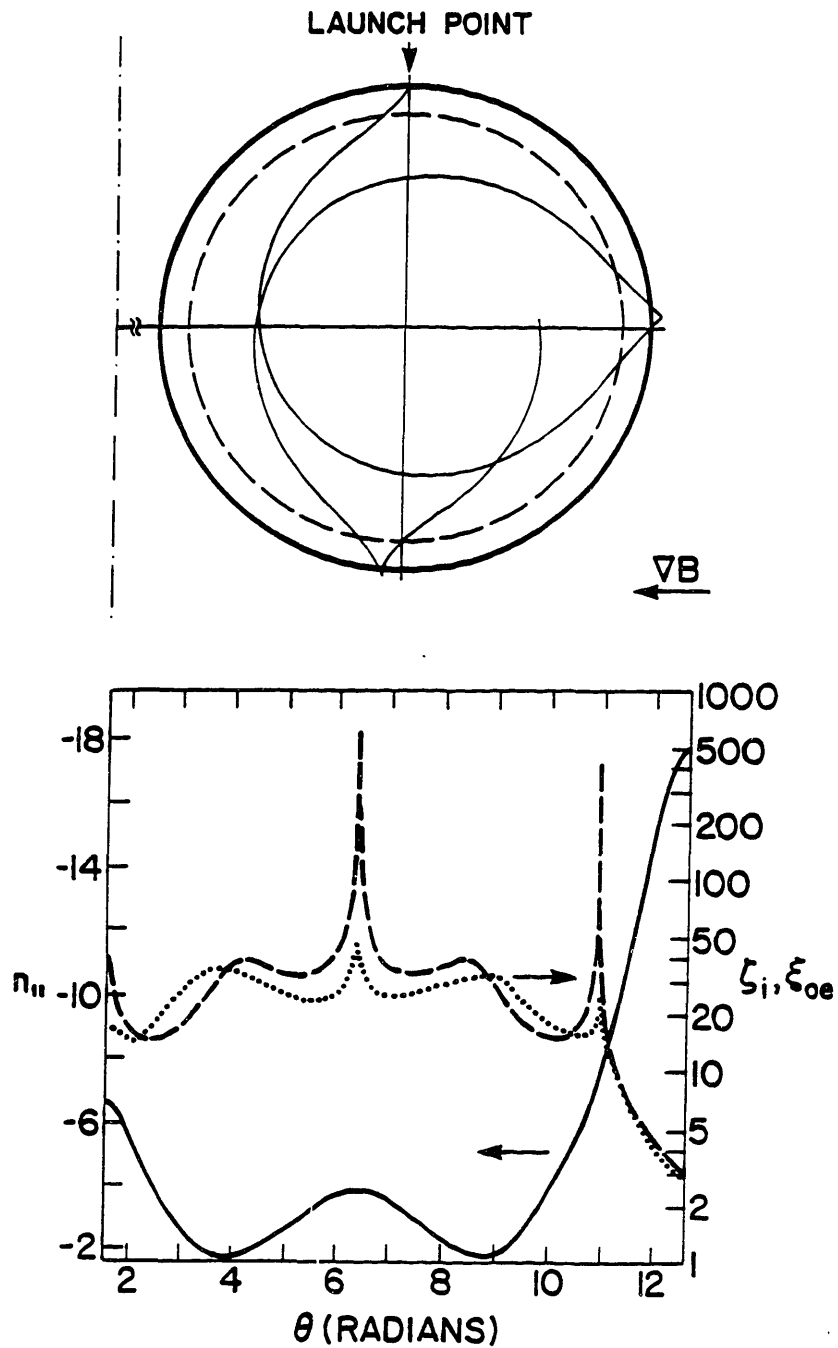


Figure 2.23. (a) Projection in the poloidal plane of the predicted path of the lower-hybrid wave. The plasma parameters are the same as in Fig. 2.1a and the initial $n_{||}$ is -6 . The wave is launched from the top of the plasma column ($\theta = 90^\circ$) toward the high field side. (b) Evolution of $n_{||}$ (solid line), ζ_i (dashed line), and ξ_{oe} (dotted line) along the poloidal trajectory of the ray.

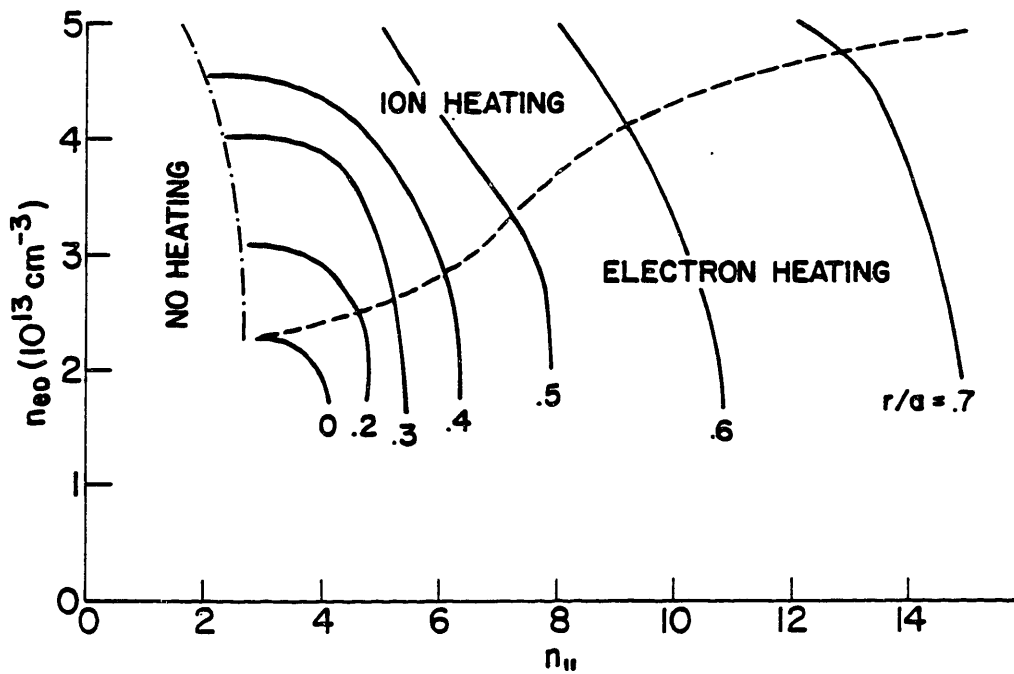


Figure 2.24. Contour plot of the damping radius (r/a) from toroidal ray-tracing analysis for waves with positive $n_{||}$ launched from the top of the torus, with the same plasma parameters as in Fig. 2.20.

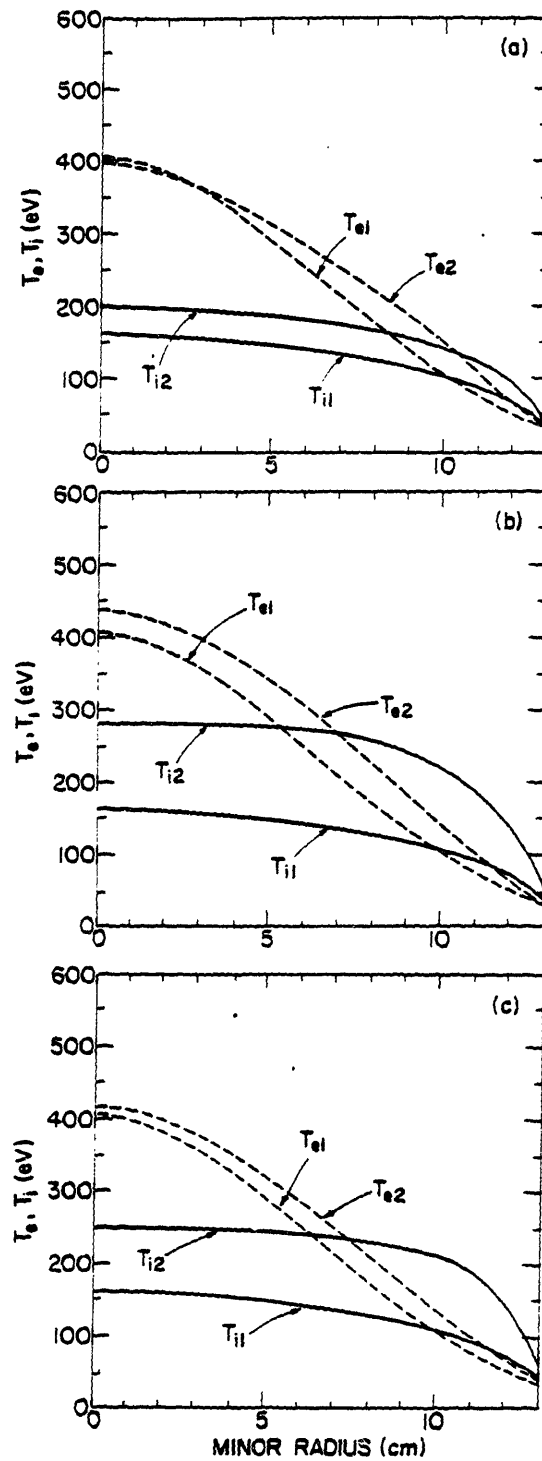


Figure 2.25. Transport code predictions of the electron and ion temperature profiles in Versator during rf heating with the top-launching antenna. T_{e1} and T_{i1} represent the initial electron and ion temperature profiles before the rf is turned on. T_{e2} and T_{i2} are the calculated profiles at the end of the 5 msec rf pulse. The rf power is 100 kW; the plasma parameters are given in the text. In (a), the relative phase between adjacent waveguides is $\Delta\phi = +90^\circ$; in (b), $\Delta\phi = -90^\circ$; and in (c), $\Delta\phi = 180^\circ$.

asymmetry with the sign of the waveguide phasing, based on the transport simulations employing the full spectrum of the grill. The most effective ion heating is predicted to occur when the grill is phased in the "wrong" direction, i.e. when most of the ray trajectories look similar to those for side-launching. The reason for this seemingly curious result is that the relatively high n_{\parallel} spectrum of this grill should give rise to electron heating when the toroidal upshift of n_{\parallel} is taken into account. Only when the spectrum is downshifted is electron Landau damping avoided, and the possibility of ion heating recovered.

2.7. Other Effects on Wave Propagation and Damping

In the final section of this chapter, we consider some possible effects of other phenomena on the lower-hybrid heating efficiency. Their relegation to the end is not indicative of their lack of importance, but rather to the difficulty of assessing their relation to the damping rates. In addition to toroidal effects, the evolution of the wave numbers may be influenced by the scattering of the lower-hybrid wave from drift wave density fluctuations in the plasma.^{73,74} In general, the frequency and parallel wave number of the low frequency fluctuations are negligible with respect to those of the lower-hybrid wave; hence ω and n_{\parallel} of the incident wave are considered to be conserved in the scattering process. Thus the perpendicular wave number n_{\perp} remains constant in magnitude but its direction may be rotated during scattering.

Knowledge of the density fluctuation level and the n_{\perp} -spectrum of the turbulence is needed for quantitative estimates of the effect of drift wave scattering of the lower-hybrid wave. On Versator, measurements of these quantities have been performed, albeit at plasma densities lower than that required for ion heating,⁵⁵ and the results are applied in the ray tracing code to determine the possible effect of the turbulence. In the few cases considered, the drift-wave scattering allows first-pass absorption of the side-launched lower-hybrid wave for all densities considered above $4 \times 10^{12} \text{ cm.}^{-3}$ Moreover, efficient ion heating is predicted at densities in cases for which only electron heating is predicted without scattering being taken into account. The reason for the improved damping efficiency due to drift wave scattering is the following: with the introduction of random variations in the direction of n_{\perp} , the shift of n_{θ} to negative values is reduced, thereby preventing the strong downshift of n_{\parallel} which is responsible for inefficient damping. However, whether or not such scattering actually occurs in the experiment is unknown.

Non-linear effects, namely parametric decay, may also play a significant role in the heating of the plasma. Heating due to parametric decay near the lower-hybrid frequency has been clearly observed from the results of small experiments in linear machines,⁸⁸ and is often inferred to be the mechanism for the production of the fast ion tail and perhaps even bulk heating in lower-hybrid experiments on tokamaks.¹⁵ The difficulty in verifying the latter assertion arises from the inability to measure the decay location in the interior of the tokamak plasma with probes. Theoretical treatments^{42,43} show that for $\omega_{LH} < \omega < 2\omega_{LH}$ and $T_e \geq 3T_i$, non-resonant decay (non-linear Landau damping) into low frequency ion quasi-modes and lower-hybrid waves should

occur. The quasi-modes couple to the electron motion, and the lower-hybrid waves may damp on ions or electrons as described earlier. At the lower densities near the plasma edge ($\omega > 2\omega_{LH}$) and $T_e \simeq T_i$, resonant decay into ion cyclotron quasi-modes and ion cyclotron waves and cold lower-hybrid waves is favored. The cyclotron waves are predicted to damp on the ion distribution if $T_e \simeq T_i$. In general, parametric decay may have the effect of increasing the overall damping rate if pump waves with local n_{\parallel} too low for linear damping can decay to highly damped waves, but may also cause lower heating efficiencies if the non-linear absorption occurs near the plasma edge. Both these aspects of damping of decay waves have been used to justify observations of lower-hybrid ion heating on JFT-2.^{28,40,41} As mentioned in Chapter 1, the heating efficiency in that experiment was correlated with the edge electron temperature, with higher ion temperature increases reported for higher edge temperatures. In that study, the onset of parametric decay was blamed for the variable efficiency: if parametric decay near the edge is responsible for absorbing a significant fraction of the lower-hybrid wave power, then better wave penetration should occur in plasmas with higher edge temperatures because of the increase in the power threshold for parametric decay with increasing electron temperature.⁴³ However, assessments of this sort may still be somewhat speculative because the decay location is unknown, and we will not attempt to relate in a quantitative way the measured parametric decay spectra to theoretical heating rates. Fortunately, such estimates may be possible in the near future on the Alcator C lower-hybrid experiment in which the sideband of the lower-hybrid pump wave has recently been detected by CO₂ laser scattering.⁸⁹ Further comments on parametric decay will be made with the presentation of the results.

In general, the application of lower-hybrid wave theory to the Versator heating experiment shows that the expected heating efficiency may not be high, as the plasma parameters cannot be adjusted to ensure damping of the wave at the plasma center. Ion heating taking place well off-axis ($r/a \gtrsim 0.5$) is expected to be especially inefficient because of orbit losses of fast perpendicular ions. Though launching from the top of the plasma column holds promise with regard to better radial penetration, the possibility of achieving central ion heating may still be limited because of strong absorption on electrons due to the available n_{\parallel} spectrum.

3. Linear Theory of Lower-Hybrid Wave Coupling

In this chapter, we discuss the theory of lower-hybrid wave coupling to the edge plasma using the cold plasma model of wave propagation introduced in Section 2.1 of the last chapter. The calculated coupling efficiency of the phased waveguide array antenna, or grill, is reviewed.^{6,7} The theory of grill coupling with a simple edge plasma model has been formulated by Brambilla and incorporated into a computer code^{7,90}. In this chapter, the general method of calculating the coupling efficiency of lower-hybrid waves to the plasma is discussed, and the principles of the coupling code are outlined. Modifications of the coupling theory suggested by the difference between the experimental conditions at the waveguide mouth and the plasma model used in previous calculations are made and their effects are assessed. The n_{\parallel} spectra of the two antennas used in this experiment are computed with the use of this code. The coupling behavior of the side-launching four-waveguide grill is also calculated, and will be compared with experimental antenna reflectivity measurements in Chapter 5.

3.1. General Theory of Antenna-Plasma Wave Coupling

The coupling problem is one of matching the wave impedance of the launching structure to that of the lower-hybrid wave in the edge plasma. The Cartesian coordinate system of Fig. 3.1 is used to describe the geometry of the problem. The antenna face lies in the y - z plane with the short sides of the waveguides parallel to the toroidal field of the tokamak. The plasma density increases in the x -direction. In the conventional (r, θ, ϕ) geometry of the tokamak, the x -direction corresponds to the $-r$, or negative radial direction, the y -direction to the θ , or poloidal direction, and the z -direction to the ϕ , or toroidal direction. The waveguide height is h , and the guide width is b . The y and z components of the rf electric and magnetic fields, E and B , must be continuous in the y - z plane which, for the purpose of analysis, separates the antenna from the plasma.

In the low density regime ($0 < \omega_{pe} \ll \omega_{ce}$) appropriate to the coupling problem, the dispersion relation Eq. (2.4) can be simplified. Specifically, $K_{zz} \simeq 1$ in this regime, and if $(n_{\parallel}^2 - 1)$ is of order 1 or greater, then $\beta \simeq -K_{zz}(n_{\parallel}^2 - 1)$ and the dispersion relation Eq. (2.4) can be written as

$$n_{\perp}^4 - n_{\perp}^2 K_{zz}(n_{\parallel}^2 - 1) + K_{zz} \left[(n_{\parallel}^2 - 1)^2 - K_{zy}^2 \right] = 0. \quad (3.1)$$

The inequality (2.6) is valid if $(n_{\parallel}^2 - 1)^2 \gg |K_{zy}^2/K_{zz}|$, or if

$$n_{\parallel}^2 - 1 \gg \frac{\omega_{pe}}{\omega_{ce}}, \quad (3.2)$$

which is easily satisfied in the edge plasma unless $|n_{\parallel}| \approx 1$. Accordingly, the solutions of the dispersion relation Eq. (3.1) are well separated in the limit (3.2), and are¹²

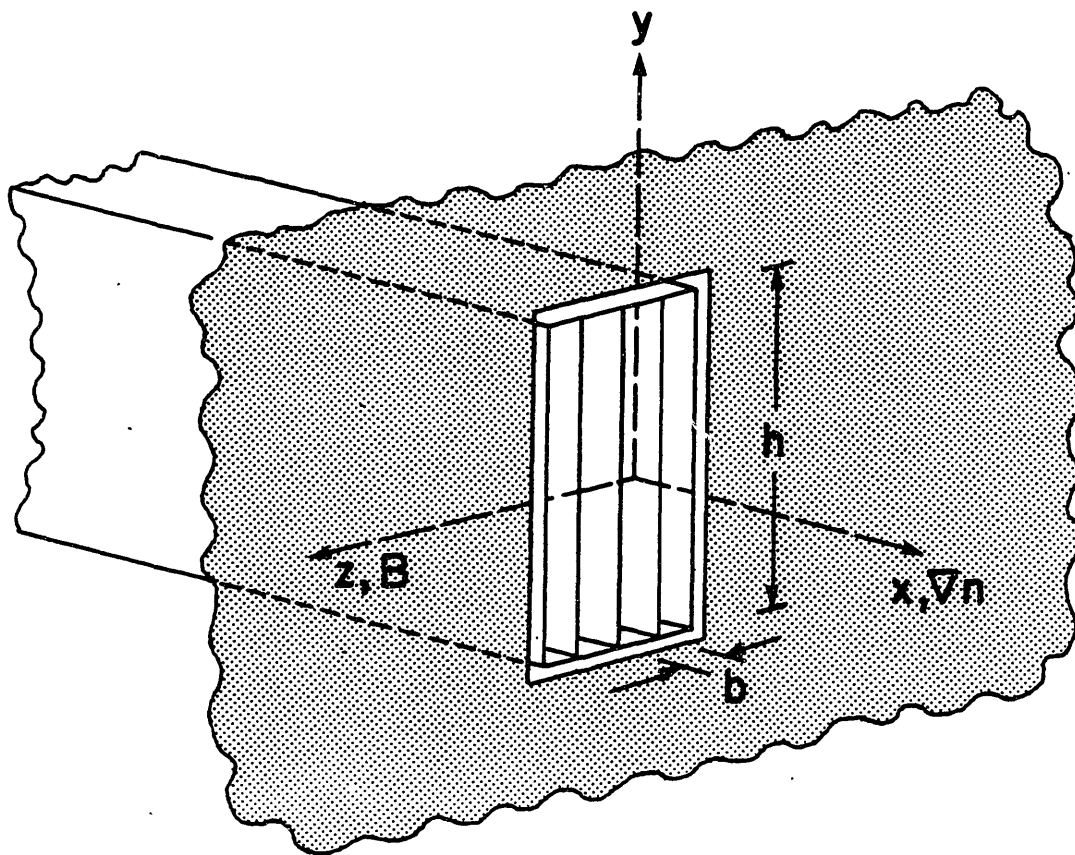


Figure 3.1. Coordinate system of the grill mouth located near the tokamak vessel wall.

$$n_{\perp s}^2 \simeq -K_{zz}(n_{\parallel}^2 - 1) \quad (3.3a)$$

$$n_{\perp f}^2 \simeq -(n_{\parallel}^2 - 1) + \frac{K_{xy}^2}{(n_{\parallel}^2 - 1)}. \quad (3.3b)$$

Assuming that the launching structure excites a wave with a finite wavelength in the z -direction but with no spatial variation in the y -direction ($n_y = 0$), it can be shown from direct substitution into Eq. (2.3) that the electric field polarization of the slow wave is predominantly in the z -direction and that of the fast wave is in the y -direction. Thus if the launcher excites only electric fields in the z -direction, only the slow wave will be generated at the plasma edge and, if the accessibility condition of Eq. (2.10) is valid, the wave will remain a slow wave in its propagation through the plasma. As the slow wave branch is the one which experiences the resonance near $\omega = \omega_{LH}$, the antenna is designed to couple to this mode. Regarding the antenna-plasma coupling problem then, only the slow wave equation is considered in solving for the plasma fields E_z and B_y . According to Eq. (3.3a), slow waves with $|n_{\parallel}| \leq 1$ are evanescent everywhere for $\omega < \omega_{pe}$. On the other hand, waves with $|n_{\parallel}| > 1$ are only cut off in the relatively thin region $\omega \geq \omega_{pe}$. The width of this evanescent layer in large part determines the coupling efficiency of slow waves to the plasma. However, we note that if the inequality (3.2) is not satisfied, the solutions of Eqs. (3.3) are not distinct from one another, and coupling to the fast wave can occur. If a substantial fraction of the launched power spectrum is represented by n_{\parallel} values near 1, the coupling to the fast wave may be significant, and the antenna reflectivity will not be well-predicted by the following slow wave coupling model.⁹¹

The general wave equation (2.1) must be used to solve for the electric and magnetic fields in the inhomogeneous edge plasma. The wave equation for the slow wave is obtained by setting E_y and n_y to zero:⁹²

$$(n_{\parallel}^2 - K_{xx})E_x + i\frac{cn_{\parallel}}{\omega}\frac{\partial}{\partial x}E_z = 0 \quad (3.4a)$$

$$-i\frac{cn_{\parallel}}{\omega}\frac{\partial}{\partial x}E_x + \left(\frac{c^2}{\omega^2}\frac{\partial^2}{\partial x^2} + K_{zz}\right)E_z = 0. \quad (3.4b)$$

Eliminating E_x gives

$$\frac{\partial^2 E_z}{\partial x^2} + \frac{n_{\parallel}^2}{K_{xx}(n_{\parallel}^2 - K_{xx})}\frac{\partial K_{xx}}{\partial x}\frac{\partial E_z}{\partial x} - \frac{\omega^2 K_{zz}}{c^2 K_{xx}}(n_{\parallel}^2 - K_{xx})E_z = 0. \quad (3.5)$$

Except for $K_{zz} = 0$, the second term is small compared to the third and is neglected.

As illustrated in Fig. 3.2, we postulate a density step and a linear density gradient in front of the waveguides:

$$n(x) = n_o + n_c(x/L), \quad (3.6)$$

where n_o is the density at the waveguide mouth, n_c is the cutoff density, $m_e \omega^2 / 4\pi e^2 = 8 \times 10^9 \text{ cm}^{-3}$ for a frequency of 800 MHz, L is the density scale length, and the location of the grill face corresponds to $x = 0$. Also shown in Fig. 3.2 is a density ramp with density gradient n_c/d inside the waveguide. At present, the effect of the waveguide plasma on the coupling is neglected, but will be discussed later.

Incorporating Eq. (3.6) and the approximation $K_{xx} \simeq 1$ into Eq. (3.5) gives

$$\frac{\partial^2 E_z}{\partial x^2} + \frac{\omega^2(n_{\parallel}^2 - 1)}{c^2 L} (L(\mu - 1) + x) E_z = 0 \quad (3.7)$$

where we define μ to be the ratio of the density at the waveguide mouth to the cutoff density, n_o/n_c . Making the substitution

$$u = -\left(\frac{\omega^2(n_{\parallel}^2 - 1)}{c^2 L}\right)^{\frac{1}{3}} (L(\mu - 1) + x) \quad (3.8)$$

allows Eq. (3.18) to be rewritten as

$$\frac{\partial^2 E_z}{\partial u^2} - u E_z = 0 \quad (3.9)$$

The solutions to Eq. (3.9) are the Airy functions. The particular linear combination of the two solutions that we choose is dependent on the far-field radiation condition: from Eq. (3.3a), the oscillatory solution is chosen for $|n_{\parallel}| > 1$, and the evanescent one is chosen for $|n_{\parallel}| < 1$. Because the lower-hybrid wave is a backward wave in the direction perpendicular to the magnetic field, the outgoing asymptotic solution should be proportional to $e^{-ik_{\perp}x}$. For this discussion, we will consider only the propagating solution, as the four-waveguide grill should preferentially launch waves with $|n_{\parallel}| > 1$. However, the coupling calculations performed by the computer code make use of both the propagating and evanescent solutions to Eq. (3.9) over the full range of n_{\parallel} 's $-\infty < n_{\parallel} < \infty$.

The propagating solution to Eq. (3.9) is

$$E_z(u) = -iAi(u) + Bi(u), \quad (3.10)$$

where Ai and Bi are the Airy functions of the first and second type. The rf magnetic field in the plasma is obtained from Faraday's law:

$$i\frac{\omega}{c} B_y = i\frac{\omega n_{\parallel}}{c} E_x - \frac{\partial E_x}{\partial x}. \quad (3.11)$$

Substituting for E_x from Eq. (3.4a) gives

$$B_y = -i\frac{c}{\omega(n_{\parallel}^2 - 1)} \frac{\partial E_z}{\partial x}, \quad (3.12)$$

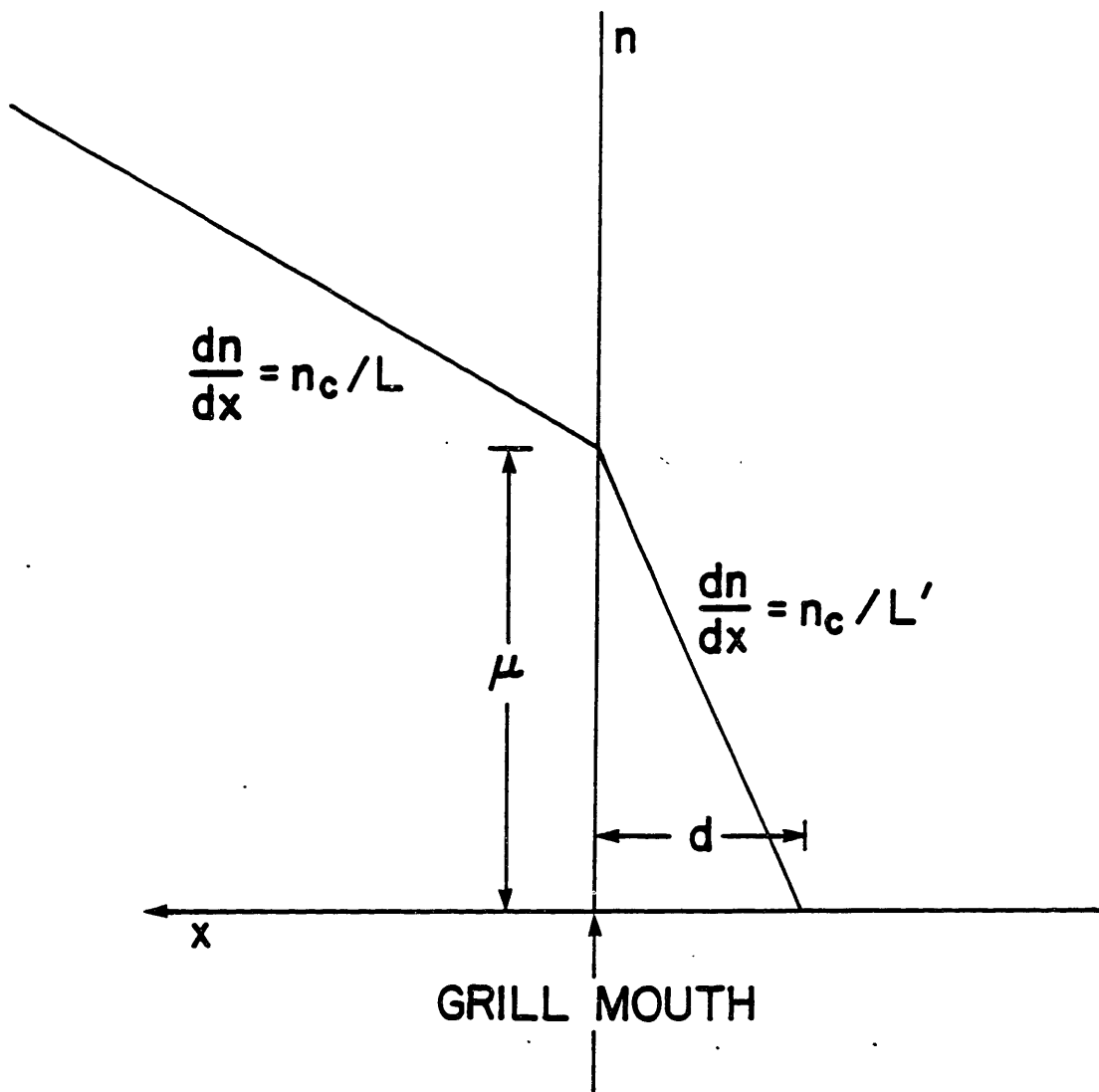


Figure 3.2. Idealized density behavior near the grill mouth. L represents the plasma density scale length in front of the waveguides, and L' is the density scale length inside the waveguides.

or, switching variables from x to u ,

$$B_y(u) = i \frac{c}{\omega(n_{\parallel}^2 - 1)} \left[\frac{\omega^2 (n_{\parallel}^2 - 1)}{c^2 L} \right]^{\frac{1}{2}} \left(-i \frac{\partial A_i(u)}{\partial u} + \frac{\partial B_i(u)}{\partial u} \right). \quad (3.13)$$

The procedure for solving the coupling problem is the matching of the plasma wave fields of Eqs. (3.10) and (3.13) to the waveguide antenna fields at the antenna face $x = 0$:

$$\begin{aligned} E_x(u_o) &= E_{zi}(0) + E_{zr}(0) \\ B_y(u_o) &= B_{yi}(0) - B_{yr}(0) \end{aligned} \quad (3.14)$$

where from Eq. (3.8),

$$u_o = u(x = 0)$$

and $E_{zi}(x)$ and $B_{yi}(x)$ are the incident electric and magnetic fields imposed by the antenna, and $E_{zr}(x)$ and $B_{yr}(x)$ are the reflected fields of the antenna. The field reflection coefficient $[E_{zr}(0)/E_{zi}(0)]$ is

$$\Gamma = \frac{(Z_p/Z_o) - 1}{(Z_p/Z_o) + 1} \quad (3.15)$$

where

$$Z_p = \frac{E_x(u)}{B_y(u)} \quad (3.16)$$

is defined to be the wave impedance of the plasma and

$$Z_o = \frac{E_{zi}(x)}{B_{yi}(x)} \quad (3.17)$$

is the wave impedance of the antenna. Defining $Z_p/Z_o = |Z|e^{i\phi}$, we find that the power reflection coefficient, $|\Gamma|^2$, can be minimized for $|Z| = 1$, $-\frac{\pi}{2} < \phi < \frac{\pi}{2}$.

3.2. The Brambilla Coupling Code

The numerical computations of the Brambilla rf coupling code perform the matching of the transverse electric and magnetic fields, and provide calculated predictions of the antenna reflectivity and the inward-propagating power spectrum of n_{\parallel} . The process by which this is accomplished is described in detail in Ref. 7. The waveguide launcher is modeled by a set of infinitely high parallel plate waveguides adjacent to one another. The antenna fields, both incident and reflected, are superpositions of the normal modes of the waveguides. In general, both propagating and evanescent modes of the guides are considered, with the number of evanescent modes limited to 3 or 4, depending on the desired accuracy of the calculation. Following the notation of Brambilla,⁷ we write the waveguide fields as

$$\begin{aligned}
E_z^{wg}(x, z) &= \sum_{p=1}^N e^{i\phi_p} \Theta_p(z) \left[\sum_{n=0}^{\infty} (\alpha_{np} e^{ik_n x} + \beta_{np} e^{-ik_n x}) \cos \frac{n\pi(z-z_p)}{b} \right] \\
B_y^{wg}(x, z) &= \sum_{p=1}^N e^{i\phi_p} \Theta_p(z) \left[\sum_{n=0}^{\infty} -\frac{\omega}{ck_n} (\alpha_{np} e^{ik_n x} + \beta_{np} e^{-ik_n x}) \cos \frac{n\pi(z-z_p)}{b} \right] \\
E_x^{wg}(x, z) &= -i \frac{c}{\omega} \frac{\partial B_y^{wg}}{\partial z}
\end{aligned} \tag{3.18}$$

where p is the waveguide number, z_p is the z -coordinate of the edge of the p th waveguide, and ϕ_p is the phase factor associated with the p th waveguide. The function $\Theta_p(z)$ is a "window" operator: it is equal to 1 for $z_p \leq z \leq z_p + b$ and 0 elsewhere. The sum over the n modes includes both propagating and evanescent ones. The coefficients α_{np} and β_{np} are the amplitudes of the incident and reflected n th mode fields in the p th waveguide, respectively. The waveguide wave vector of the n th mode is

$$k_n = \sqrt{\frac{\omega^2}{c^2} - \frac{n^2 \pi^2}{b^2}}. \tag{3.19}$$

Because of the assumption of infinitely high waveguides, there is no spatial variation of the fields in the y -direction; hence there are no m modes. Since coupling to the fast wave is neglected, only modes with $E_y = 0$ are included in the analysis. These are the TEM mode (corresponding to the TE_{10} fundamental mode in rectangular waveguide) and the evanescent TM modes. The incident wave is assumed to be in the fundamental TE_{10} mode ($\alpha_{np} = 0$ for $n \neq 0$). The forward and reflected waveguide fields at the grill mouth are Fourier-analyzed in n_{\parallel} -space and matched to generalized vacuum fields

$$E_z(x, z) = [\sigma(n_{\parallel}) e^{ik_{\perp} x} + \rho(n_{\parallel}) e^{-ik_{\perp} x}] e^{i(\omega/c)n_{\parallel} z} \tag{3.20a}$$

$$B_y(x, z) = \frac{i}{\sqrt{n_{\parallel}^2 - 1}} [\sigma(n_{\parallel}) e^{ik_{\perp} x} - \rho(n_{\parallel}) e^{-ik_{\perp} x}] e^{i(\omega/c)n_{\parallel} z} \tag{3.20b}$$

in front of the grill. Here, $\sigma(n_{\parallel})$ is the coefficient corresponding to the field incident on the plasma and $\rho(n_{\parallel})$ the coefficient for the reflected field from the plasma. For a given n_{\parallel} , the field reflectivity of the plasma is $Y(n_{\parallel}) = \rho(n_{\parallel})/\sigma(n_{\parallel})$. The vacuum region in front of the grill is employed as a mathematical convenience, and is usually assumed to have zero width. The vacuum wave fields are matched to the plasma fields of Eqs. (3.10) and (3.13). With the matching of the wave fields at the plasma-vacuum and vacuum-grill interfaces, the solution of the coupling problem is complete and the unknown quantities $\sigma(n_{\parallel})$, $\rho(n_{\parallel})$, and β_{np} are determined. The reflectivity of the p th waveguide is $|\beta_{0p}^2|/|\alpha_{0p}^2|$. The n_{\parallel} spectrum of the rf power launched into the plasma is obtained from the Poynting flux in the x -direction at the plasma-vacuum boundary:

$$\begin{aligned}
S(n_{\parallel}) &= -\frac{c}{8\pi} \text{Re}(E_z B_y^*) \\
&= \frac{c}{4\pi} \frac{|\sigma(n_{\parallel})|^2}{\sqrt{n_{\parallel}^2 - 1}} \text{Im} Y(n_{\parallel})
\end{aligned} \tag{3.21}$$

where the expressions Eqs. (3.20) for the vacuum fields have been used.

Several modifications to this program were made in the course of this work. Based on Langmuir probe measurements presented in Chapter 4, the density at the waveguide mouth was found to be variable, ranging from a fraction of the cutoff density to over 100 times that, depending primarily on the radial location of the grill. As discussed previously, the plasma model incorporates a linear density gradient perpendicular to the face of the antenna. In the original version of the code,^{5,7} the edge density was chosen such that $\omega = \omega_{pe}$, or $\mu = 1$, at the waveguide mouth with the density gradient being a variable parameter. The possibility of a finite density at the waveguide mouth had been considered in early formulations of the problem, but not implemented because a faulty analytic approach suggested that the coupling would be poor if $\omega_{pe} > \omega$ at the grill mouth.⁵ Subsequent formulations introduced an adjustable density step at the waveguide mouth,^{93,94} and we have added this feature to our code.

Since the actual grill is constructed of rectangular waveguides rather than parallel plates, we have also considered some aspects of finite waveguide height in our calculations. The use of rectangular guides in the model changes the coupling description in several ways. First, the electric field of the fundamental mode of the waveguide exhibits a y -dependence: E_z is proportional to $\cos(\pi y/h)$, where the antenna midplane is located at $y = 0$. Hence the antenna launches a spectrum which is finite in n_y . However, the waveguide height must be at least one-half of a free space wavelength if the fundamental mode is not to be cut off. The minimum wavelength of the fundamental mode in the y -direction is the free space wavelength; thus the fundamental mode preferentially couples to plasma waves with $|n_y| \leq 1$. The qualitative effect of a small but finite value of n_y on the coupling efficiency may be estimated in the following way. The coupling efficiency should be inversely related to the width of the evanescent region at the plasma edge. The cutoff density for slow waves is obtained by setting $n_z^2 = 0$ in Eq. (3.3a):

$$\frac{\omega_{pe}^2}{\omega^2} = 1 + \frac{n_y^2}{n_{||}^2 - 1}. \quad (3.22)$$

Except for values of $|n_{||}|$ near 1, the cutoff density is not much greater than if $n_y = 0$. Hence the inclusion of finite n_y should have little effect on the antenna reflectivity.

Secondly, the electric fields for the evanescent modes have y -components, and if we continue to neglect coupling to the fast wave, the TE_{1n} modes must be included to ensure that $E_y = 0$ everywhere at the guide mouth. However, because of the relative strengths of the y and z -components of the TM_{1n} and TE_{1n} modes, the contribution of the evanescent TE modes to the slow wave coupling is slight. The ratio of the y -component of the TM_{1n} mode to that of the TE_{1n} mode is

$$\frac{E_y(TM)}{E_y(TE)} = \frac{E_o(TM)}{E_o(TE)} \left(\frac{b}{nh} \right) \sqrt{1 - (c\omega/\pi h)^2} \ll 1$$

while the same ratio for the z -components is

$$\frac{E_z(TM)}{E_z(TE)} = -\frac{E_o(TM)}{E_o(TE)} \left(\frac{nh}{b}\right) \sqrt{1 - (c\omega/\pi h)^2} \gg 1$$

Thus only a small $E_o(TE)$ field is needed to cancel the y -component of the corresponding TM mode. The contribution of the TE_{1n} mode to the z -component of the electric field is a factor of $(b/nh)^2$ smaller than that of the TM_{1n} mode; hence the evanescent TE modes contribute little to the matching of the E_z fields at the waveguide mouth. Consequently, only the evanescent TM modes need to be considered in addition to the fundamental TE mode.

Lastly and most importantly, the wave impedance for finite height waveguides is different than for parallel plates. The impedance of a TE mode in an evacuated waveguide is $Z_{TE} = -ck_{mn}/\omega$ while the impedance of a TM mode is $Z_{TM} = -\omega/ck_{mn}$, where k_{mn} is the wave vector of the m th rectangular waveguide mode:

$$k_{mn} = \sqrt{\left(\frac{\omega}{c}\right)^2 - \left(\frac{m\pi}{h}\right)^2 - \left(\frac{n\pi}{b}\right)^2}. \quad (3.23)$$

These changes are included in the code for both the fundamental TE_{10} and evanescent TM_{1n} modes. We will analytically show later that the value of the waveguide impedance significantly affects the edge density and density gradients required for good coupling.

3.3. Calculated n_{\parallel} Power Spectra

The computer-code predictions of the n_{\parallel} spectra of the Versator grills are plotted in Figs. 3.3 and 3.4. The calculated n_{\parallel} power spectra for the four-waveguide side-launching antenna is shown in Fig. 3.3 for two different assumed edge density conditions: (a) $\mu = 10$, $\nabla n = 5.3 \times 10^{11} \text{ cm.}^{-4}$; and (b) $\mu = 1$, $\nabla n = 5.3 \times 10^{10} \text{ cm.}^{-4}$. The spectra are plotted for the relative phase angle between waveguides $\Delta\phi = 0^\circ$, 90° , and 180° . The individual waveguides of this antenna have a width of 2.45 cm. Expectedly, the spectra for $\Delta\phi = 0^\circ$ and 180° are symmetric in n_{\parallel} . The spectrum for $\Delta\phi = 180^\circ$ exhibits a peak at $n_{\parallel} = 5.5$ corresponding to two parallel wavelengths across the width of the grill. For this phase, 91% of the power is carried by waves with $n_{\parallel} > 3$; hence in our experiment, the accessibility condition Eq. (2.10) is well satisfied for the bulk of the launched power. A significant portion of the computed spectrum for $\Delta\phi = 0^\circ$ is represented by n_{\parallel} values close to 1. As discussed in the argument following Eqs. (3.3), we expect coupling to the fast wave to be important for low phase angles such as this, and the actual slow wave spectrum and antenna reflectivity may be different than that predicted by the above theory. However, heating experiments are usually performed using higher phase angles because of the need to satisfy the accessibility condition; hence the problem of fast wave coupling is not believed to have practical implications in our experiment. For $\Delta\phi = 90^\circ$ in the high edge density case of Fig. 3.3a, the spectrum is asymmetric with the fundamental peak at $n_{\parallel} = 2.5$. Approximately 70% of the power is directed in the positive n_{\parallel} direction for this relative phase. The dominant or representative n_{\parallel}

value of each power spectrum is largely dependent on the relative phase between waveguides, whereas the sensitivity of the details of the spectra to the density at the grill mouth is relatively weak. At the higher edge density, the spectral components with high n_{\parallel} values are somewhat enhanced relative to those at the lower density. That this should be true is evident from Eq. (3.3a), which indicates that high n_{\parallel} waves suffer stronger attenuation in the evanescent edge region than waves of low n_{\parallel} .

In Fig. 3.4 the n_{\parallel} spectrum of the four-waveguide top-launching grill is plotted for the same phase angles and edge density conditions as in Fig. 3.3a. The waveguide width of this grill is 1.0 cm. Consequently, the power spectrum of this grill is characterized by higher n_{\parallel} values than that of the side-launcher.

3.4. Analytic Solutions of the Coupling Problem

To provide physical insight into the code predictions of the antenna reflectivity, the conditions for optimum coupling can be estimated analytically for a number of limiting cases in which the plasma fields are matched directly to generalized antenna fields of impedance Z_o . For this analytic treatment, only the fundamental TE_{10} waveguide mode is considered; therefore from Eqs. (3.17) and (3.23), the antenna impedance is simply

$$Z_o = -[1 - (c\pi/\omega h)^2]^{-\frac{1}{2}}. \quad (3.24)$$

By comparison, $Z_o = 1$ for parallel plate waveguides. The cases considered are: $|u_o| \gg 1$ with $u_o < 0$; $|u_o| < 1$; and $|u_o| \gg 1$ with $u_o > 0$, where u is given by Eq. (3.8).

The case of $|u_o| \gg 1$ and $u_o < 0$, which is valid for $n_{\parallel}^2 \gg 1$ and $\mu \gg 1$, corresponds to the presence of an overdense plasma at the grill mouth. The appropriate asymptotic expansions for the Airy function solutions are⁹⁵

$$\begin{aligned} -iAi(u_o) + Bi(u_o) &= \pi^{-\frac{1}{2}}(-u_o)^{-\frac{1}{2}} \exp\left(-i\left[\frac{2}{3}(-u_o)^{\frac{3}{2}} + \frac{\pi}{4}\right]\right) \\ -i\frac{dAi(u_o)}{du} + \frac{dBi(u_o)}{du} &= i\pi^{-\frac{1}{2}}(-u_o)^{\frac{1}{2}} \exp\left(-i\left[\frac{2}{3}(-u_o)^{\frac{3}{2}} + \frac{\pi}{4}\right]\right). \end{aligned} \quad (3.25)$$

This approximation embodies an assumption of WKB validity at the grill mouth as the above solutions are propagating modes. In this limit, the plasma wave impedance obtained from Eqs. (3.10), (3.13), and (3.16) is

$$Z_p \simeq -\left[\frac{(n_{\parallel}^2 - 1)}{(\mu - 1)}\right]^{\frac{1}{2}}. \quad (3.26)$$

In the high density approximation the quantity Z_p/Z_o is real and positive, and hence by the argument following Eq. (3.17), optimal coupling is predicted for $Z_p/Z_o = 1$, or for

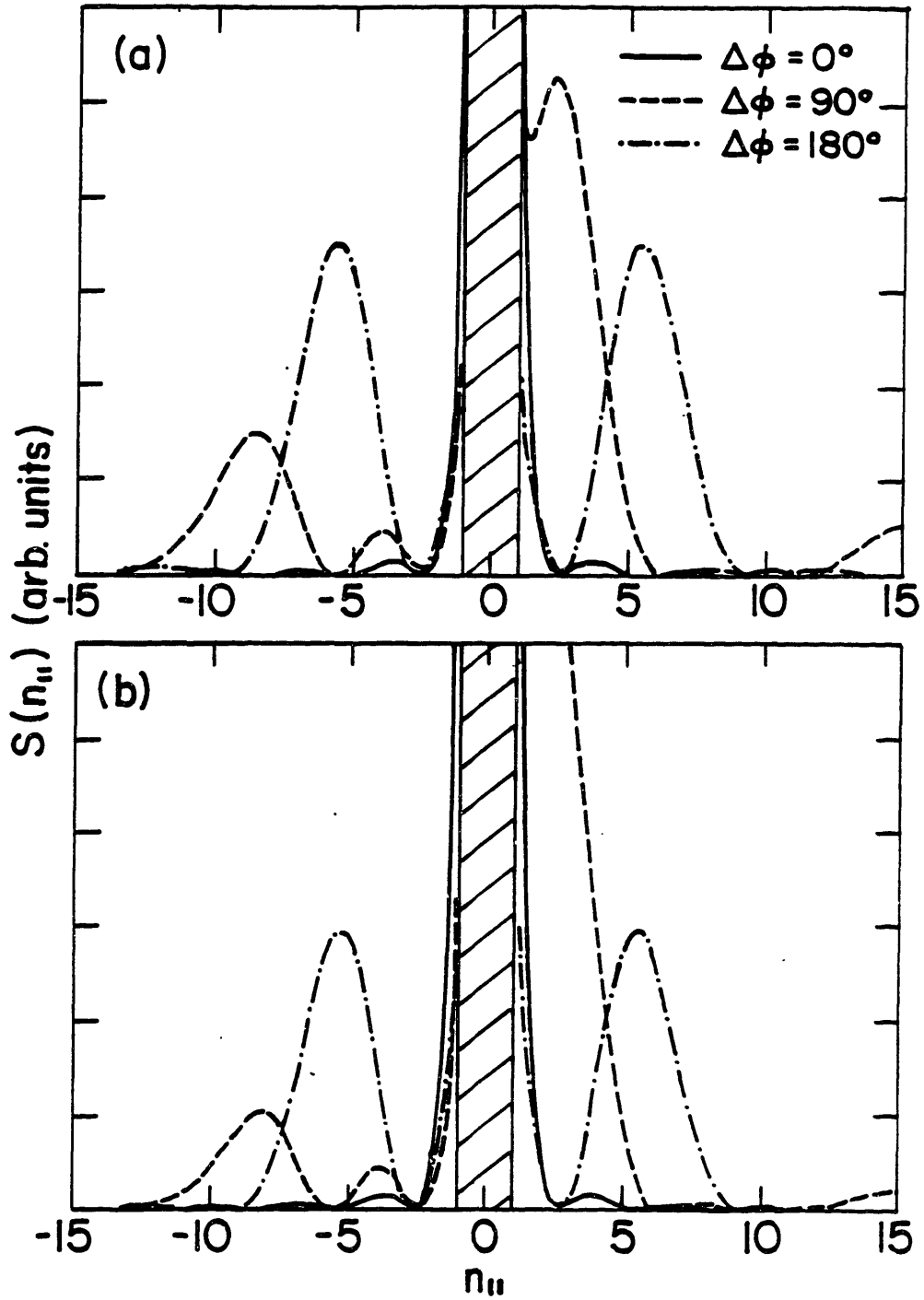


Figure 3.3. Calculated $n_{||}$ spectra of the side-launching four-waveguide grill for $\Delta\phi = 0^\circ$, 90° , and 180° at (a) $\mu = 10$, $\nabla n = 5.3 \times 10^{11} \text{ cm}^{-4}$; and (b) $\mu = 1$, $\nabla n = 5.3 \times 10^{10} \text{ cm}^{-4}$.

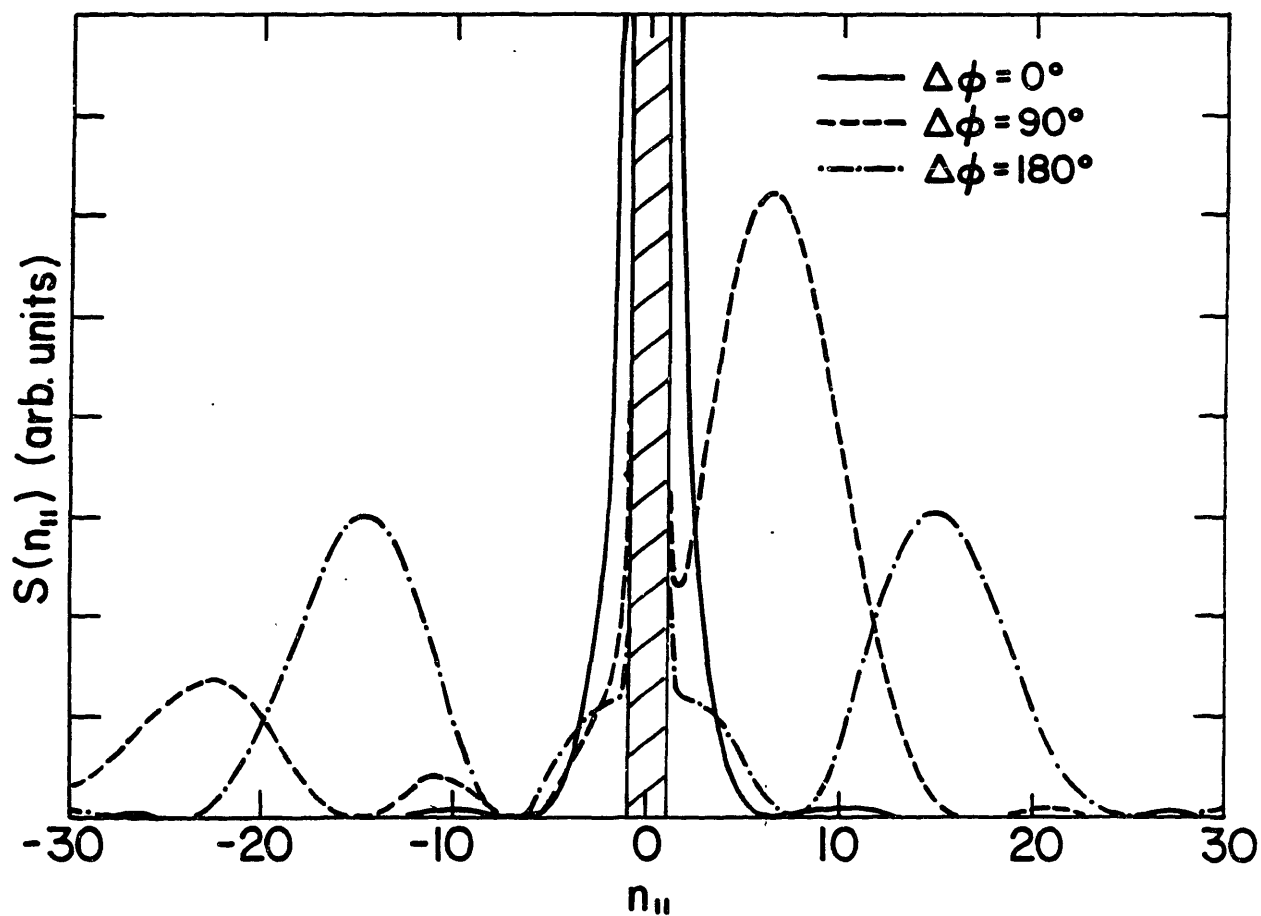


Figure 3.4. Calculated $n_{||}$ spectra of the top-launching four-waveguide grill for the same edge density conditions as Fig. 3.3a.

$$\mu = 1 + [1 - (c\pi/\omega h)^2](n_{\parallel}^2 - 1). \quad (3.27)$$

Clearly, the dependence of the minimum reflectivity condition on the launched n_{\parallel} spectrum is strong. For the Versator antenna dimensions, Eq. (3.27) may be rewritten as $\mu = 0.6 + 0.4 n_{\parallel}^2$. The density at the grill mouth required for good coupling is significantly reduced by the finite height of the waveguide. The reduction is a factor of roughly 2.5 in our case. The optimal density increases with n_{\parallel}^2 ; thus we expect the grill position for best coupling at $\Delta\phi = 180^\circ$ to be at a higher density than for lower phase angles between waveguides. For $\Delta\phi = 180^\circ$, the n_{\parallel} corresponding to the peak of the spectrum is approximately 5.5; hence best coupling in this instance is predicted for a 13 times overdense plasma at the grill mouth.

The original Brambilla theory⁷ was performed in the limit of $|u_o| \ll 1$ corresponding to $\mu \simeq 1$. In this limit, we use the series expansions for the Airy functions, keeping only the lowest order terms:⁹⁵

$$\begin{aligned} -iAi(u_o) + Bi(u_o) &\simeq 2 \frac{3^{-\frac{1}{3}}}{\Gamma(2/3)} e^{-i\pi/6} \\ -i \frac{dAi(u_o)}{du} + \frac{dBi(u_o)}{du} &\simeq 2 \frac{3^{-\frac{1}{3}}}{\Gamma(4/3)} e^{\pi/6}, \end{aligned} \quad (3.28)$$

where Γ is the Gamma function. The plasma impedance is then

$$Z_p = -\frac{\Gamma(\frac{4}{3})}{\Gamma(\frac{2}{3})} (9\omega L/c)^{\frac{1}{3}} (n_{\parallel}^2 - 1)^{\frac{1}{3}} e^{-i\pi/6}. \quad (3.29)$$

Again, the reflection coefficient is minimized for $|Z_p/Z_o| = 1$, or for

$$\begin{aligned} \frac{dn}{dx} = \frac{n_c}{L} &= \left[\frac{\Gamma(4/3)}{\Gamma(2/3)} \right]^3 (9\omega n_c/c) [1 - (c\pi/\omega h)^2]^{\frac{1}{3}} (n_{\parallel}^2 - 1)^2 \\ &\simeq 8.7 \times 10^8 n_{\parallel}^4 \text{ cm}^{-4} \end{aligned} \quad (3.30)$$

The density gradient required for good coupling in this approximation is strongly dependent on the value of n_{\parallel} .

For the final case of $u_o > 0$; $|u_o| \gg 1$ (grill density near zero and shallow density gradients), the asymptotic expansions of the Bi and dBi/du functions are the dominant terms in the expressions for the plasma fields:⁹⁵

$$\begin{aligned} -iAi(u_o) + Bi(u_o) &\simeq \pi^{-\frac{1}{2}} u_o^{\frac{1}{2}} \exp\left(\frac{2}{3} u^{\frac{3}{2}}\right) \\ -i \frac{dAi(u_o)}{du} + \frac{dBi(u_o)}{du} &\simeq \pi^{-\frac{1}{2}} u_o^{-\frac{1}{2}} \exp\left(\frac{2}{3} u^{\frac{3}{2}}\right). \end{aligned} \quad (3.31)$$

The plasma impedance is

$$Z_p \simeq -i(n_{\parallel}^2 - 1)^{\frac{1}{2}}. \quad (3.32)$$

In this limit, the antenna is totally reflective because of the purely reactive impedance. In consideration of all three limits, the best coupling should be achieved in the first for which the grill mouth is situated in an overdense plasma.

3.5. Further Modifications of the Plasma Model

In addition to a variable density at the waveguide mouth, we have also considered the ramifications of other differences between the idealized density profile of the Brambilla model and the measured profiles. As described in Chapter 5, the experimental density profile at the plasma edge is better represented by an exponential than a linear profile. Furthermore, measurements indicate a tenuous but finite plasma to be present inside the waveguides, whereas the model assumes the waveguides to be totally evacuated. We now address these two differences analytically, and show that in most cases the predicted changes in the previously-described coupling calculations are likely to be small.

3.5.1. Exponential Density Gradient

Regarding the exponential density gradient, an analytic solution for the electric field in the plasma can be found for exponential profiles in the same manner as for linear profiles. We let the density profile be represented by

$$n(x) = n_o \exp(x/\lambda) \quad (3.33)$$

where λ is the exponential density scale length. The wave equation analogous to Eq. (3.7) is

$$\frac{\partial^2 E_z}{\partial x^2} + \frac{\omega^2}{c^2}(n_{\parallel}^2 - 1)(\mu e^{x/\lambda} - 1)E_z = 0. \quad (3.34)$$

By transforming the variable x to g such that

$$g = 2\frac{\omega\lambda}{c}\sqrt{\mu(n_{\parallel}^2 - 1)}e^{x/2\lambda}, \quad (3.35)$$

Eq. (3.34) can be rewritten as Bessel's equation:

$$\frac{\partial^2 E_z}{\partial g^2} + \frac{1}{g}\frac{\partial E_z}{\partial g} + \left(1 - \frac{\nu^2}{g^2}\right)E_z = 0 \quad (3.36)$$

where $\nu = 2(\omega\lambda/c)\sqrt{n_{\parallel}^2 - 1}$. The oscillatory solutions of Eq. (3.36) are the Hankel functions of order ν . The Hankel function of the second kind has the required asymptotic dependence e^{-ig} ; thus the solution of Eq. (3.36) corresponding to the solution for the linear density gradient, Eq. (3.10) is

$$E_z(g) = H_{\nu}^{(2)}(g). \quad (3.37)$$

A similar solution for the electrostatic wave in an exponential density profile has been obtained by Bellan and Porkolab.⁹⁶ As before, the rf magnetic field is calculated with the use of Eq. (3.11):

$$B_y = -i\sqrt{n_{\parallel}^2 - 1} \left[H_{\nu}^{(2)}(g) - \sqrt{\mu} e^{x/2\lambda} H_{\nu+1}^{(2)}(g) \right]. \quad (3.38)$$

The wave impedance at $x = 0$ is then

$$Z_p = i\sqrt{n_{\parallel}^2 - 1} \left[1 - \sqrt{\mu} H_{\nu+1}^{(2)}(g_0) / H_{\nu}^{(2)}(g_0) \right]^{-1}. \quad (3.39)$$

In the high density limit ($g \gg 1$), the asymptotic expansion for the quotient of Hankel functions in the above equation is simply $e^{i\pi/2}$, and the impedance becomes

$$Z_p = - \left[\frac{n_{\parallel}^2 - 1}{\mu + 1} \right]^{\frac{1}{2}} \exp(i \tan^{-1} \mu^{-1/2}). \quad (3.40)$$

Consequently, optimal coupling should occur for

$$\mu = -1 + [1 - (\pi c / \omega h)^2] (n_{\parallel}^2 - 1) \quad (3.41)$$

or for a numerical value of only 2 less than that for the optimal coupling in a linear gradient (see Eq. 3.27). In this limit, the coupling behavior for the two density profiles is similar. However, we note that the difference may prove to be significant for low n_{\parallel} grills designed for coupling to reactor-type plasmas.

At lower densities, the density gradient generally plays a stronger role in the coupling, as evidenced by Eq. (3.29). The effect of the density gradient on the coupling is localized to the narrow region in front of the grill in which WKB is invalid, i.e., for

$$\left| \frac{dk_x}{dx} \right| > k_x^2, \quad (3.42)$$

or using the dispersion relation Eq. (3.3a) with an exponential density profile,

$$\Delta x \leq 2\lambda \ln \left(2\omega\lambda / c [\mu(n_{\parallel}^2 - 1)]^{\frac{1}{2}} \right)^{-1} \quad (3.43)$$

where Δx is the thickness of the coupling region defined by Eq. (3.42). This coupling region for our parameters is several millimeters thick. Given a measured exponential density scale length of 0.2 cm. (see Chapter 5), the effective linear density gradient over this region can be several times the linear gradient at the grill mouth. Consequently, for grill positions which are located in an underdense plasma, we have increased the linear density gradient at the antenna mouth supplied to the rf coupling code. The new value is the average linear gradient over the coupling region specified in Eq. (3.43). For overdense plasmas, the thickness of the layer is small, and as the coupling in this limit is strongly dependent on the value of the density at the grill mouth rather than the density gradient, no correction to the linear gradient is made for these cases. For completeness, Hankel function expansions could replace the Airy functions used in the code; however, since the expected change in the coupling results is small, no such improvement has yet been made.

3.5.2. Finite Plasma Density Within the Waveguides

Plasma penetration into the waveguide is illustrated in Fig. 3.2. In general, the plasma diffusing into the waveguide should lead to an increase in overall antenna reflectivity since fundamental mode propagation in the waveguide is cut off at a density corresponding to

$$\frac{\omega_{pe}^2}{\omega^2} = 1 - \left(\frac{c\pi}{\omega h}\right)^2 \quad (3.44)$$

or at $n = 3.2 \times 10^9 \text{ cm}^{-3}$ for the Versator grill. However, for a thin evanescent layer in the waveguides, most of the power should tunnel through.

The method of calculating the additional reflectivity due to the plasma in the waveguide is similar to that for the edge plasma-waveguide interface, except that the matching problem needs only to be solved in a single waveguide. The solutions for the waveguide vacuum fields Eqs. (3.18) are joined to the solutions for the thin plasma ramp in the waveguide. As before, the density inside the waveguide is assumed to be a linear function of position. For the sake of simplicity, we consider only the fundamental TE mode with waveguide wave vector k_{10} (see Eq. 3.23). The transverse vacuum waveguide fields at $x = 0$ are

$$\begin{aligned} E_z^{wg}(x=0) &= \alpha_0 e^{ik_{10}x} + \beta_0 e^{-ik_{10}x} \\ B_y^{wg}(x=0) &= -\frac{ck_{10}}{\omega}(\alpha_0 e^{ik_{10}x} - \beta_0 e^{-ik_{10}x}), \end{aligned} \quad (3.45)$$

and at $x = -d$;

$$\begin{aligned} E_z^{wg}(x < -d) &= \alpha_- e^{ik_{10}x} + \beta_- e^{-ik_{10}x} \\ B_y^{wg}(x < -d) &= -\frac{ck_{10}}{\omega}(\alpha_- e^{ik_{10}x} - \beta_- e^{-ik_{10}x}), \end{aligned} \quad (3.46)$$

where the "o" subscript denotes the coefficients for the waveguide fields at $x = 0$, and the "-" subscript for those at negative x for $x < -d$. The length of the finite density ramp inside the waveguide is d . As before, the solutions for the fields in the density ramp inside the waveguide are the Airy functions:

$$\begin{aligned} E_z^r &= C_1 Ai(u') + C_2 Bi(u') \\ B_y^r &= i \frac{c(k_{10}L)^{\frac{2}{3}}}{\omega L} \left[C_1 \frac{\partial Ai(u')}{\partial u'} + C_2 \frac{\partial Bi(u')}{\partial u'} \right] \end{aligned} \quad (3.47)$$

where $u' = -(k_{10}L)^{\frac{2}{3}}[1 - \mu - x/L]$, and C_1 and C_2 are coefficients determined by the boundary conditions at $x = 0$ and $x = -d = -\mu L$. Matching the impedances at $x = 0$ and $x = -d$ gives:

$$-\frac{\omega}{ck_{10}} \left(\frac{\alpha_o + \beta_o}{\alpha_o - \beta_o} \right) = -i \frac{\omega L}{c(k_{10}L)^{\frac{2}{3}}} \left(\frac{Ai(u'_o) + (C_2/C_1)Bi(u'_o)}{\partial Ai(u'_o)/\partial u' + (C_2/C_1)\partial Bi(u'_o)/\partial u'} \right) \quad (3.48a)$$

$$-\frac{\omega}{ck_{10}} \left(\frac{\alpha_- + \beta_- e^{2ik_{10}d}}{\alpha_- - \beta_- e^{2ik_{10}d}} \right) = -i \frac{\omega L}{c(k_{10}L)^{\frac{2}{3}}} \left(\frac{Ai(u'_{-d}) + (C_2/C_1)Bi(u'_{-d})}{\partial Ai(u'_{-d})/\partial u' + (C_2/C_1)\partial Bi(u'_{-d})/\partial u'} \right). \quad (3.48b)$$

We can solve the first equation for C_2/C_1 , and substitute into the second to find β_-/α_- , the field reflectivity of the waveguide. We can easily estimate the effect on the coupling for $|u'_o| \ll 1$, or for $\mu < 5$. In this case, we use the series approximations Eqs. (3.28) for the Airy functions, keeping only the first order terms in u'_o . Then Eq. (3.48a) is subtracted from Eq. (3.48b), giving the simple result:

$$\frac{\omega}{ck_{10}} \left[\frac{1 + \beta_o/\alpha_o}{1 - \beta_o/\alpha_o} - \frac{1 + (\beta_-/\alpha_-)e^{2ik_{10}d}}{1 - (\beta_-/\alpha_-)e^{2ik_{10}d}} \right] = i \frac{\omega L}{c(k_{10}L)^{\frac{2}{3}}} = i \frac{\mu\omega L}{c}. \quad (3.49)$$

Denoting $\Gamma = \beta/\alpha$ to be the field reflectivity and rearranging terms we obtain

$$\Gamma_- = \left[\frac{\left(\frac{1+\Gamma_o}{1-\Gamma_o} \right) - 1 - i\mu k_{10}L}{\left(\frac{1+\Gamma_o}{1-\Gamma_o} \right) + 1 - i\mu k_{10}L} \right] e^{-2ik_{10}d}. \quad (3.50)$$

The inherent power reflectivity of the plasma layer, i.e. $\Gamma_o = 0$, is

$$|\Gamma_-|^2 \simeq \left(\frac{\mu k_{10}L}{2} \right)^2 \quad (3.51)$$

For typical parameters ($\mu = 5, k_{10} = .1 \text{ cm}^{-1}, L = .2 \text{ cm}$) this value is less than 1%, and the plasma in the waveguide should have little effect on the coupling when the grill mouth is located in a mildly overdense plasma. For this reason, and because of the computer time and memory space required for this additional inversion, the effect of plasma in the waveguides has not been included in the numerical coupling calculations.

3.6. Conclusion

Regarding the predicted reflectivity of the Versator antenna, we see from the analytic arguments made above that the existence of optimal coupling conditions, i.e. minimum reflectivity, provides a relationship between the parallel wave number of the plasma wave to the density near the waveguide mouth. In general, the coupling behavior is found to be dependent on both the density gradient and the absolute density at the grill mouth. Consequently, we defer the specific theoretical treatment of the coupling efficiency of the Versator grill to Chapter 4 following the presentation of the edge density measurements. However, we note that the experimental coupling is qualitatively expected to be best in the highly overdense edge plasma regime because the plasma impedance is purely real in this limit.

4. Versator II Lower-Hybrid Heating Experimental Set-Up

The Versator II tokamak and related power supplies and plasma diagnostics were designed and assembled by the staff and students of this laboratory. Detailed descriptions of the device may be found elsewhere, chiefly in the Ph.D. theses of former graduate students.^{54–57} The present chapter is a review of the operating characteristics of this tokamak and a descriptive summary of the diagnostics related to the ion heating experiment. The 800 MHz rf system is also described with particular emphasis placed on the lower-hybrid antenna. For reference, the basic parameters of the Versator plasma and rf system are summarized in Table 1 in Chapter 1.

4.1. The Tokamak

The tokamak vacuum vessel is constructed of type 304 electropolished stainless steel. The chamber, separable into two halves, is square (30×30 cm.) in cross-section with a 40.5 cm. major radius of the chamber axis. The electrical break to prevent induction of toroidal currents in the chamber wall is made by the elastomer O-rings sealing the joints between the two halves of the vacuum vessel. The chamber is evacuated by a single turbo-molecular pump operating through a LN₂ cold trap. Discharge cleaning of the vacuum vessel with a 15 kW, 25 KHz oscillator is often performed to reduce the gas load of the chamber walls, with water vapor and methane being the gases predominantly released in this process. No baking of the vacuum chamber is performed, with the exception of occasional heating of Langmuir probe drives or the lower-hybrid antenna to a temperature of about 150°C with electrical heating tapes. Titanium sublimation on the vacuum vessel wall has been employed during the last several years for the purpose of obtaining a plasma more free of impurities. Up to 50% of the wall is accessible to Ti-coating from the getter ball. The base pressure of the vacuum chamber is typically 2×10^{-7} Torr, and can drop to as low as 8×10^{-8} Torr following titanium gettering.

Limiters of various materials are used on Versator; radially movable, electrically floating limiters of molybdenum are usually present in the vacuum vessel, and stainless steel limiters are often directly mounted on the chamber walls. The purpose of the latter ones is either to protect probe tips or other delicate apparatus situated near the outer edge of the plasma, or to reduce the density in front of the lower-hybrid antenna for the purpose of improving rf coupling. The latter point will be discussed in the next chapter. The positions and widths of the stainless steel limiters were changed frequently over the duration of these experiments. Usually the limiters were placed so as to define a plasma minor radius of 13 cm., giving the plasma an aspect ratio of 3.1.

The magnets of the toroidal (TF), ohmic heating (OH), and vertical (VF) field systems are all capacitor bank-fed. The 700 kJ TF power supply provides a current pulse with a 15 msec rise time and 90 msec L/R decay time. The maximum field is approximately 15.5 kG on axis, but the temporal decay of the TF current limits the maximum field during the plasma discharge to about 14.5 kG. The OH banks store an energy of 120 kJ and provide a positive inductive voltage on

the plasma loop for a duration of 30–35 msec through an air-core transformer. The 5 kJ vertical field system is programmed by trial-and-error to provide an adequate plasma equilibrium near the center of the chamber over most of the duration of the discharge.

Hydrogen is the working gas of our experiments as the lower-hybrid accessibility criterion (Eq. 2.10) is not satisfied for any other gas. The gas can be introduced into the chamber by a bleed valve such that the chamber fill pressure is $0.8\text{--}1.2 \times 10^{-4}$ Torr, or as is usually the case, by puffing gas into the chamber at a pre-programmable time-dependent rate through a fast piezo-electric valve. A maximum line-averaged density of $\bar{n}_e = 1\text{--}1.5 \times 10^{13}$ cm.⁻³ is usually obtained with the constant fill pressure method; therefore, additional gas puffing is essential to obtain the densities of $\bar{n}_e = 2\text{--}3 \times 10^{13}$ cm.⁻³ required for the ion heating experiment.

Breakdown of the plasma is achieved with the use of the previously-mentioned oscillator triggered 10 msec before the start of the OH pulse. Pre-ionization during the oscillator phase of the breakdown is assisted by thermionic electron emission from heated filaments located near the chamber wall. The plasma discharges for the ion heating experiments have a typical duration of 25–35 msec. The gross plasma parameters are usually reproducible from shot-to-shot over a series of discharges on a given day. The plasma parameters evolve over a long run (≤ 150 shots) as the temperature of the vacuum vessel rises. Without corrections by the operator, the average plasma density of a discharge typically increases while the plasma current decreases, indicating that the impurity content of the plasma increases over the course of a run. The spectroscopic line intensity of the light impurity atoms (oxygen and carbon) and the bolometric signal also increase gradually over a long run.

4.2. Plasma Diagnostics

The locations of the diagnostics and the lower-hybrid antennas are shown in the schematic of the Versator vacuum vessel in Fig. 4.1. The direction of the plasma current and the toroidal magnetic field are also indicated. The plasma current and magnet currents are measured with Rogowski coils. The loop voltage is measured inductively with a four-turn toroidal coil, one coil at each corner of the square vacuum chamber.

4.2.1. VUV Spectroscopy

The major diagnostic devices for the ion heating experiments are the vacuum ultraviolet (VUV) spectrometer⁹⁷ and the charge-exchange (CX) neutral energy analyzer,⁹⁸ both of which are used to measure ion temperature. The VUV system resolves neutral and partially ionized atomic line emissions over the wavelength range 1150–3200 Å. In particular, emissions from O VII (1623 Å), N VI (1897Å), C V(2271Å), O V(2781 Å), and C III(2297 Å) are usually monitored. The wavelength resolution of the instrument (0.5 Å) is such that the Doppler widths of the above lines can be measured to infer temperatures for those impurity species. The collisional coupling between protons and impurities is much higher than between protons and electrons.⁹⁹

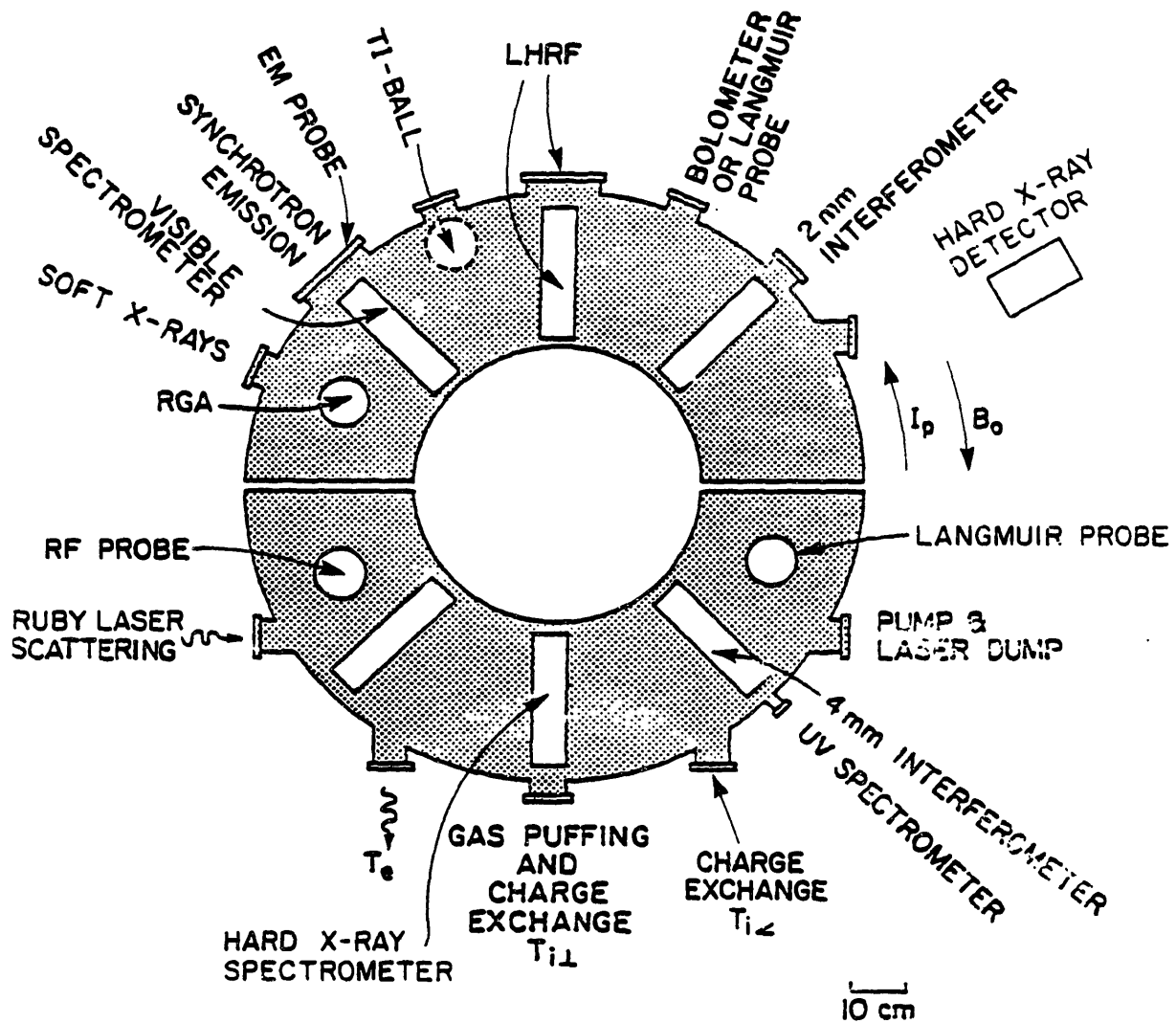


Figure 4.1. Diagram of the Versator vacuum vessel viewed from the top. The locations of the side and top ports used for lower-hybrid injection are indicated, as are the positions of the diagnostic instruments.

$$\frac{\nu_{pI}}{\nu_{ep}} \approx \frac{(m_p/m_I)^{1/2} Z_I^2}{(m_e/m_p)^{1/2}} = \frac{m_p}{(m_e m_I)^{1/2}} Z_I^2 \gg 1 \quad (4.1)$$

where $\nu_{\alpha\beta}$ is the collision frequency for thermal equilibration between the species α and β . In ohmic discharges, both the impurities and protons are heated at comparable rates by collisions with electrons. Likewise, in rf-heated discharges the impurities and bulk protons should also be heated at similar rates by fast protons (see Eq. 2.41). Because the heating rates of the proton and impurity populations are not very different and their equilibration times is short, the impurity temperature is considered to be a good measure of the local proton temperature, hereafter referred to as simply the ion temperature. Furthermore, the inferred temperature is assumed to be a reliable measure of the bulk ion temperature since emission from the lowest velocity impurity ions in the distribution contribute most to the measurement of the spectroscopic line width. Moreover, the phase velocity of the lower-hybrid wave should never reach low enough values for resonant interaction between the wave and the impurity ions; hence the impurity velocity distribution should not significantly deviate from a Maxwellian distribution. The viewing chord of the VUV spectrometer is along a major radius on the midplane. Spatial resolution is obtained by relating a particular ionization state to the local electron temperature from profile measurements. For instance, the impurity states O VII and N VI with respective ionization energies of 739 and 552 eV are assumed to exist only in the plasma center. Consequently, the ion temperature obtained from these lines is a measurement of the central ion temperature. The location of the C V species of ionization energy 392 eV is assumed to be 5–8 cm. off the axis.

The entire width of a spectroscopic line may be scanned by the spectrometer several times in one shot with the use of a vibrating MgF₂ plate. However, the ion temperature evolution during rf heating takes place on a time scale of 1–2 msec, which is beyond the time resolution of the above method. Therefore, the spectroscopic line shape is usually compiled over a sequence of 10–15 shots with the spectrometer wavelength changed between shots.

4.2.2. Charge-Exchange Analysis

Use of the CX spectrometer provides a measure of the energy spectrum of escaping neutral hydrogen atoms over the range 0.3–4.0 keV. Hydrogen atoms of these energies are produced by the resonant charge-exchange process,



whereby a neutral atom donates an electron to a proton without a significant transfer of kinetic energy. The neutral atom, which has an energy characteristic of the hot plasma, escapes the plasma. Reionization of the neutral before escaping is not likely to occur if

$$\bar{n}_e a \ll \frac{v_0}{(\sigma v_e)_i + (n_i/n_e)(\sigma v_i)_{CX}} \quad (4.3)$$

where $\langle \sigma v_e \rangle_i$ is the velocity-averaged electron impact ionization cross-section for atomic hydrogen and $\langle \sigma v_i \rangle_{CX}$ is the corresponding cross-section for charge-exchange. Both have about the same value of $3-4 \times 10^{-8}$ cm³/sec for electron and ion temperatures typical of the Versator plasma, and the above inequality is reasonably well satisfied for neutral energies above 500 eV. Hence most charge-exchange neutrals with energies greater than this leave the plasma. Some of the escaping atoms pass through the evacuated beam line of the charge-exchange analyzer into an N_2 gas cell in which a small fraction of the incident atoms are stripped of their electrons by the transfer ionization process. Energy separation of the protons is performed by an electrostatic parallel plate analyzer. The ions are detected by electron multipliers; output pulses are height-discriminated to reduce background noise, and converted to digital TTL-level pulses which are then averaged to obtain an analog count-rate. Though designed for 8-channel operation, the analyzer was usually operated with only a single channel because of electrical cross-talk between channels. Consequently, ion energy spectra were compiled on a shot-by-shot basis with the plate voltage of the electrostatic analyzer changed between shots. From the measured count-rates and knowledge of the energy dependence of the charge-exchange cross-section and stripping cell efficiency, the energy distribution of the ions in the plasma can be inferred. Charge-exchange cross-sections and stripping cell efficiencies were obtained from published data,¹⁰⁰ while the analyzer ballistics were determined using a local ion source.¹⁰¹

Data analysis of the charge-exchange measurements is usually performed with the aid of a computer program implemented on the Versator data acquisition system. The procedure of the analysis is as follows. First, the analyzer noise is subtracted from the signal for a given energy. The noise is determined by the analyzer output when no voltage is present on the plate, and is believed to result from UV or secondary electron emission induced by neutral bombardment within the analyzer itself. Next, the signal is normalized by the application of the energy-dependent stripping cell efficiency and charge-exchange cross-section factors to give the relative number of ions in the plasma distribution at the given energy. With the compilation over many shots of ion count-rate signals at different energies, the ion energy spectrum is obtained. In a Maxwellian distribution, the number of ions in an energy range $d\mathcal{E}$ is

$$dN = K \mathcal{E}^{1/2} \exp(-\mathcal{E}/T_i) d\mathcal{E} \quad (4.4)$$

where K is a constant. Consequently, a plot of $\ln \left[\sqrt{\mathcal{E}} (dN/d\mathcal{E}) \right]$ versus \mathcal{E} yields a straight line with slope $-T_i^{-1}$ for a Maxwellian distribution of temperature T_i .

The interpretation of the charge-exchange measurements is complicated by the fact that the detected neutral flux is a chord-averaged quantity. The Versator charge-exchange analyzer views the plasma through a central chord. The neutral hydrogen density profile in the plasma is not known, though on physical grounds it is likely to be several orders of magnitude higher at the plasma edge than at the center. The local charge-exchange neutral production rate in the energy

range $d\mathcal{E}$ is

$$\frac{\partial N}{\partial t} d\mathcal{E} = n_o n_i \sigma_{CX}(\mathcal{E}) v_i(\mathcal{E}) f_i(\mathcal{E}) d\mathcal{E} \quad (4.5)$$

where n_o is the neutral hydrogen density, σ_{CX} is the cross-section for the charge-exchange reaction, $v_i = \sqrt{2\mathcal{E}/m_i}$ is the ion energy, and $f_i(\mathcal{E})$ is the ion energy distribution. Because the neutral density is highest at the plasma periphery, the neutral flux at low energies should be dominated by emission from the edge. Consequently, the ion temperature of the hottest plasma in the viewing chord of the instrument must be inferred from the slope of the ion energy spectrum of the fastest ions ($v_i \gg v_{thi}$), or typically between 500 and 1000 eV for Versator ion temperatures. Because the ion temperature is highest on axis for Maxwellian ion distributions, the charge-exchange analyzer provides a measure of the central ion temperatures. The value obtained from this procedure is in reasonable agreement ($\pm 15\%$) with VUV temperature measurements of the central impurity species.

An additional complication in the interpretation of the charge-exchange data is that small-angle scattering of the stripped ions from the beam line in the stripping cell of the analyzer is more severe for the lower energy ions than the higher energy ones.¹⁰² As our particular stripping cell is uncalibrated for overall efficiency of the conversion of neutrals entering the cell to ions entering the electrostatic analyzer, the true ion distribution at low energy ($\mathcal{E} \leq 500\text{eV}$) is not believed to be accurately measured by charge-exchange analysis.

In the lower-hybrid heating experiments, rf injection usually gives rise to an energetic tail in the ion distribution, which is detected by charge-exchange. As discussed in Chapter 2, the radial location of the tail cannot be unambiguously determined on theoretical grounds. The assumption used in inferring the central temperature of the thermal plasma, namely that the most energetic ions in the plasma are located in the center, is generally not valid for use in estimating the tail density and energy because the location of the fast ion tail is not known. Because the Versator charge-exchange analyzer is not capable of performing a radial scan of the plasma column, the origin of the fast neutral flux during rf heating cannot be spatially resolved by this measurement. More will be said on this subject in Chapter 6.

During this experiment, the charge-exchange analyzer was operated in two orientations with respect to the toroidal magnetic field. One orientation was near-perpendicular, with the beam line set at an angle of 6° away from the normal to the magnetic axis. Though the neutrals escaping at this angle result from charge-exchange with ions which are banana-trapped (for a pitch-angle of 6° , only those particles inside a minor radius of approximately 0.2 cm are circulating), the slight angle off the normal to the axis ensures that the sampled ions are not those that are ripple-trapped in the magnetic field minimum between TF coils. This small fraction of ions is expected to suffer poor confinement relative to the remainder of the distribution. The pitch angle defining this region is

$$\sin \theta = |v_{\parallel}/v| = \sqrt{\delta} \quad (4.6)$$

where δ is the magnetic field ripple defined in Chapter 2. For $\delta = 0.002$, $\theta = 2.6^\circ$; hence the charge-exchange analyzer is set at a larger angle than this to avoid measuring the ripple-trapped distribution.

The second orientation was at an angle of 45° with respect to the magnetic axis. As lower-hybrid heating is known to create perpendicular ion tails which are often poorly confined, measurement of the off-perpendicular ion energy spectrum provides an unambiguous estimate of the thermalization efficiency of the fast ion distribution. Accommodating this orientation required moving the analyzer to an adjacent angled port on the tokamak (see Fig. 4.1). In the course of these experiments, the instrument was moved from its usual near-perpendicular orientation to the 45° position for a period of several months.

4.2.3. Thomson Scattering, Soft X-ray Spectroscopy

Electron temperature measurements of the plasma were provided by two methods: Thomson scattering of ruby laser light by electrons,¹⁰³ and soft X-ray spectroscopy by pulse-height analysis from a Si(Li) detector.¹⁰⁴ Like Doppler-broadening of impurity lines for ion temperature measurements, Thomson scattering provides a reliable local value of the bulk electron temperature. Similarly, soft X-ray spectroscopy gives information on the non-Maxwellian nature of the electron distribution function as charge-exchange analysis does for ions, but it is also subject to some of the same difficulties of interpretation of bulk temperature from spectra with non-thermal features. Electron temperature measurements were not routinely made during ion heating experiments, but enough data was collected to provide a good characterization of the electron temperatures and profiles for high density plasmas in Versator.

4.2.4. Microwave Interferometry

The electron density of the plasma was measured by single-pass microwave interferometry. A 75 GHz Zebra-stripe interferometer provided an unambiguous determination of the line-averaged density along a vertical chord through the plasma.¹⁰⁵ At densities $\bar{n}_e \approx 2 \times 10^{13} \text{ cm}^{-3}$ the 139 GHz EIO source for the microwave scattering diagnostic was usually set up as an interferometer to supplement the information obtained from the lower frequency one, as the signal from the latter was often difficult to interpret at high density because of the large number of fringes. The density profile was measured on a few occasions by moving the viewing chord of the 75 GHz system to different radial locations, keeping the position of the 139 GHz interferometer horns fixed for shot-to-shot reference. A profile could not be obtained above a density of $\bar{n}_e \approx 2 \times 10^{13} \text{ cm}^{-3}$ as the refraction of the 75 GHz wave for chord positions between the plasma center and edge led to too much transmission loss. Therefore, the only density profile measurements obtained from microwave interferometry were performed at densities lower than those at which most of the ion heating work was done. However, relative measurements of electron density obtained during

Thomson scattering temperature profile measurements at $\bar{n}_e = 3 \times 10^{13} \text{ cm.}^{-3}$ confirmed that the density profile at high plasma densities is similar to that at lower densities.

4.2.5. Probes

The properties of the edge plasma in the shadow of the limiter were measured with electric probes. Langmuir probes provided measurements of the local plasma density and electron temperature, while high frequency fluctuations were detected with rf probes. Both types of probes are mounted on radially-movable probe drives originally constructed at Princeton Plasma Physics Laboratory and were modified for use on Versator. The electrical feedthrough is standard 50 ohm semi-rigid copper coaxial cable in which the vacuum seal is made by the tightly fitting teflon insulation in the approximately 30 cm. length of coaxial line. Only one failure of such an "unguaranteed" seal occurred during the course of this study.

Construction of probe tips varied according to their intended use. All are single-tipped. The center conductor is either tungsten, molybdenum, or tantalum wire ranging from 0.010" to 0.025" in diameter. The outer conductor is stainless steel, and is insulated from the wire by a thin tube of alumina ceramic. The outer conductor is surrounded by another ceramic tube to electrically shield the outer conductor from the plasma. The outer ceramic is protected by an electrically floating stainless steel tube, as the ceramic was often found to shatter when directly exposed to the plasma.

The inner and outer coaxial conductors are soldered to a standard 0.085" female SMA connector which attaches to its mate on the semi-rigid coaxial feedthrough described above. The probe tips for rf fluctuation measurements were constructed to have a 50 ohm impedance so that they were matched to the rest of the transmission line. The dimensions of these tips and the method of measuring their impedance are given in Appendix C. The rf probe tips used in the experiment have a measured VSWR of less than 1.3 over the frequency range 0–1 GHz. The frequency spectrum of the high frequency signals were measured with a Tektronix 7L12 spectrum analyzer.

Langmuir probe tips were constructed of less specific dimensions since high frequency response was not required for the density and temperature measurements. The extension of the exposed center conductor in the radial direction was typically 0.1–0.3 cm., which is of the same order of magnitude as the density gradient scale length of 0.2–1.5 cm (see Chapter 5). The exposed tips were either straight, L-, or T-shaped with the cross bar of the latter two configurations oriented perpendicular to the magnetic field. The physical dimensions of the tip must be known for ion density measurements, and were usually measured with the use of an optical comparator. Probe measurements were only made in the region between the limiter radius and the wall, as exposure to the runaway electron flux inside the limiter radius usually resulted in the destruction of the probe tip.

4.2.6. Bolometer

Knowledge of the behavior of the total radiative and neutral emission of the Versator plasma is obtained with the use of a fast-response pyroelectric bolometer. The bolometer views the plasma from the outer major radius through a collimator such that the width of the viewing area at the plasma major radius extends approximately 2 cm. in the radial direction and 4 cm. in the toroidal direction. The line-of-sight of the bolometer may be rotated with respect to the midplane such that emission from the entire plasma cross-section may be collected. If the measured line-averaged emission profiles in the upper and lower halves of the plasma are symmetric, and the emissivity is assumed to be poloidally symmetric, then the profiles may be Abel-inverted to obtain the local power emissivity both with and without the presence of rf power.

A pyroelectric detector was selected as the bolometric transducer because of its fast response time and the simplicity of the measurement technique.¹⁰⁶ The lithium tantalate detector chip mounted on a base with electrodes was supplied by Eltec Instruments, Inc. The face of the detector exposed to the plasma was coated with an organic black paint to provide broad spectral response. Though the spectral response of this device was not measured, the known performance of similar black coatings suggests that the sensitivity of the bolometric to incident radiation is flat in the spectral range from infrared to soft X-ray.

The pyroelectric detector produces a current which is proportional to the rate of change of the temperature of the chip, or to the absorbed thermal power. For an incident power pulse duration less than the thermal relaxation time of the detector (the time required for the chip to thermally equilibrate with its surroundings), the output current is thus a direct measure of the incident power. The measured thermal decay time of our detector is approximately 80–120 msec; hence the above criterion is satisfied for Versator plasma durations. Because the detector is a high impedance device ($Z \approx 10^{10}\Omega$), a FET preamplifier is employed to convert the current signal to a voltage, which is then amplified by conventional operational amplifiers. The FET preamp is located just to the outside of the bolometric vacuum flange approximately 3 cm. from the detector so as to minimize electrical pick-up on the weak detected signal. The detector itself is situated in vacuum at the end of a collimating tube extending 50 cm. from the outer wall of the chamber.

The bolometer response was calibrated with a 2 mW He-Ne laser focused on the detector through an optical chopping wheel. The radiant output of the laser was measured with a calibrated, commercial pyroelectric detector and also with a radiant energy meter. The sensitivity of the detector was determined 1.2 $\mu\text{A}/\text{Watt}$, or with the FET preamplifier assembly, 1.5 kV/Watt. The response time of the instrument was 0.2–0.3 msec.

As the output signal of the pyroelectric chip is a small current, the detector operation must be kept free of charge collection effects, e.g. secondary electron emission induced by neutral or UV bombardment. Consequently, the side of the chip facing the plasma was grounded so that any charge loss or build-up caused by bombardment should contribute little to the measured current.

However, the effectiveness of this scheme has not been checked. Furthermore, during bolometric measurements of the plasma emission, the sensitivity of the bolometer was often observed to change over a series of many shots, particularly in the presence of rf injection into high density plasmas from which the charge-exchange neutral flux was enhanced. This curious problem is not believed to be related to the amplifier electronics, as the calibration procedure was occasionally repeated immediately following such a change in detector sensitivity, with the original calibration result being obtained. Instead, the problem may be caused by charge build-up on the detector itself, since pointing the bolometer away from a strongly emissive region of the plasma, or even electrically shorting the two electrodes of the detector itself, has been found to permit the return of the bolometer sensitivity to what is believed to be its bench-calibrated value. The upshot of this discussion is the following: the absolute response of the bolometer is questionable because of the slow variation in its sensitivity when exposed to emission from the plasma. By use of the methods described above to reduce the degradation of the instrument sensitivity, and randomly varying the angle of the bolometer with respect to the midplane, one can obtain the relative bolometric emission profile. However, the quantitative value of the power emission is not reliable. We also note that the ratio of the absorption coefficient of particulate energy to that for radiant energy is unknown. We have assumed the two to be identical, but this may not be a valid assumption.

4.3. Density and Temperature Profiles; Z_{eff}

In concluding this chapter, we show typical plasma parameters of the discharges in which the ion heating experiments were performed. The evolution of the plasma current, loop voltage and line-averaged density are shown in Fig. 4.2. Radial profiles of the electron density and electron and ion temperatures are shown in Figs. 4.3–4.6. The density profile of Fig. 4.3 was obtained by Abel-inversion of the 75 GHz microwave interferometer data collected at 6 radial locations. The central line-averaged density was $\bar{n}_e = 1.3 \times 10^{13} \text{ cm}^{-3}$. The Thomson scattering electron temperature and density profiles⁵⁷ shown in Fig. 4.4 were measured for $\bar{n}_e = 3 \times 10^{13} \text{ cm}^{-3}$. The impurity ion temperature profile¹⁰⁷ obtained during the same run is depicted in Fig. 4.5. A soft X-ray electron temperature profile¹⁰⁸ has been performed at $\bar{n}_e = 1.5 \times 10^{13} \text{ cm}^{-3}$ and is shown in Fig. 4.6.

The density profile is represented reasonably well by a parabola, or by a Gaussian profile with a half-width of about 9.7 cm. The former representation is used in the theoretical modelling in Chapter 2 and in the power balance calculations of Chapter 5. The ion temperature can be fitted to a Gaussian profile of half-width 10.5 cm. The electron temperature profile may be represented by the function

$$T_e(r) = T_{e0} \left[1 + \left(\frac{r}{7.5 \text{ cm.}} \right)^2 \right]^{3/2} \quad (4.7)$$

which will be employed in the power balance calculations of Chapter 6. Near the plasma axis, the electron temperature profile may be fitted to a Gaussian with a half-width of $\lambda_{te} \approx 7.5 \text{ cm.}$

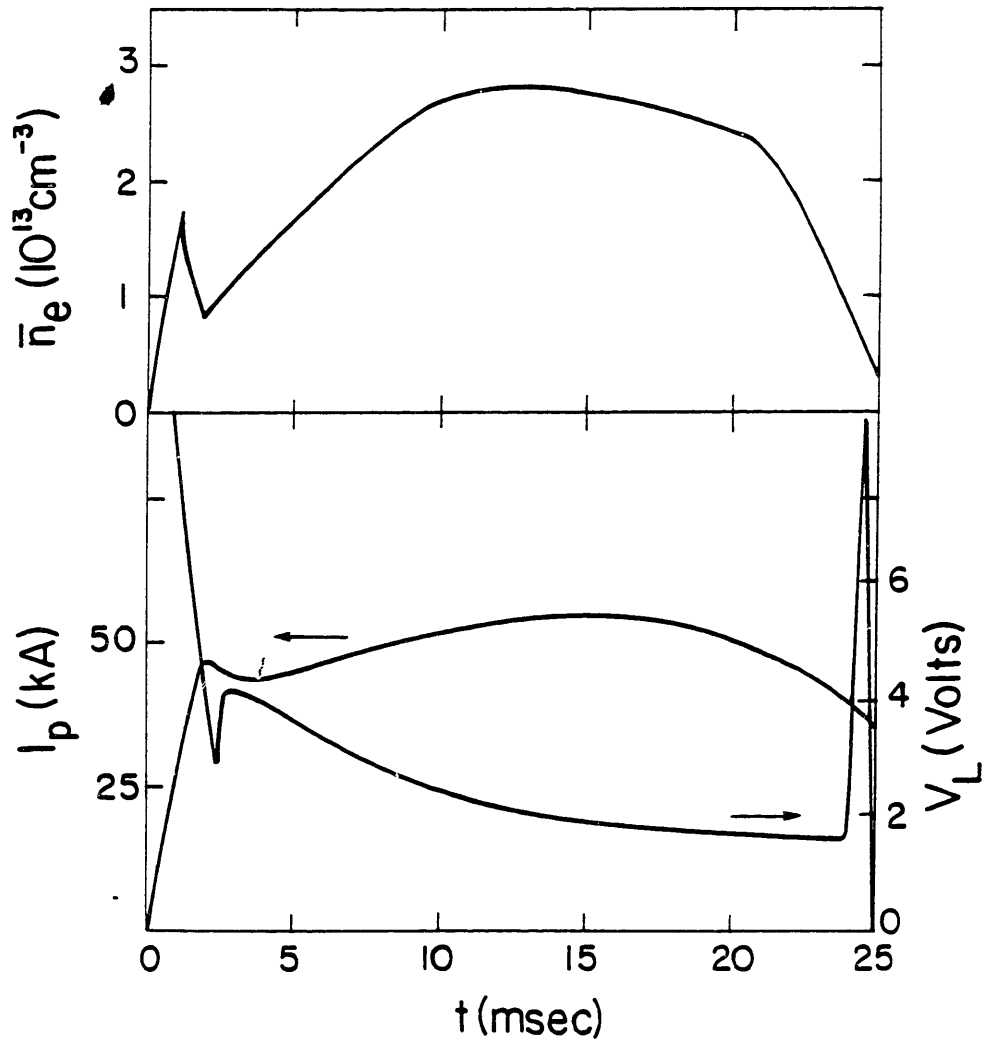


Figure 4.2. Temporal evolution of the line-averaged electron density, plasma current, and loop voltage during a typical discharge used in the ion heating studies.

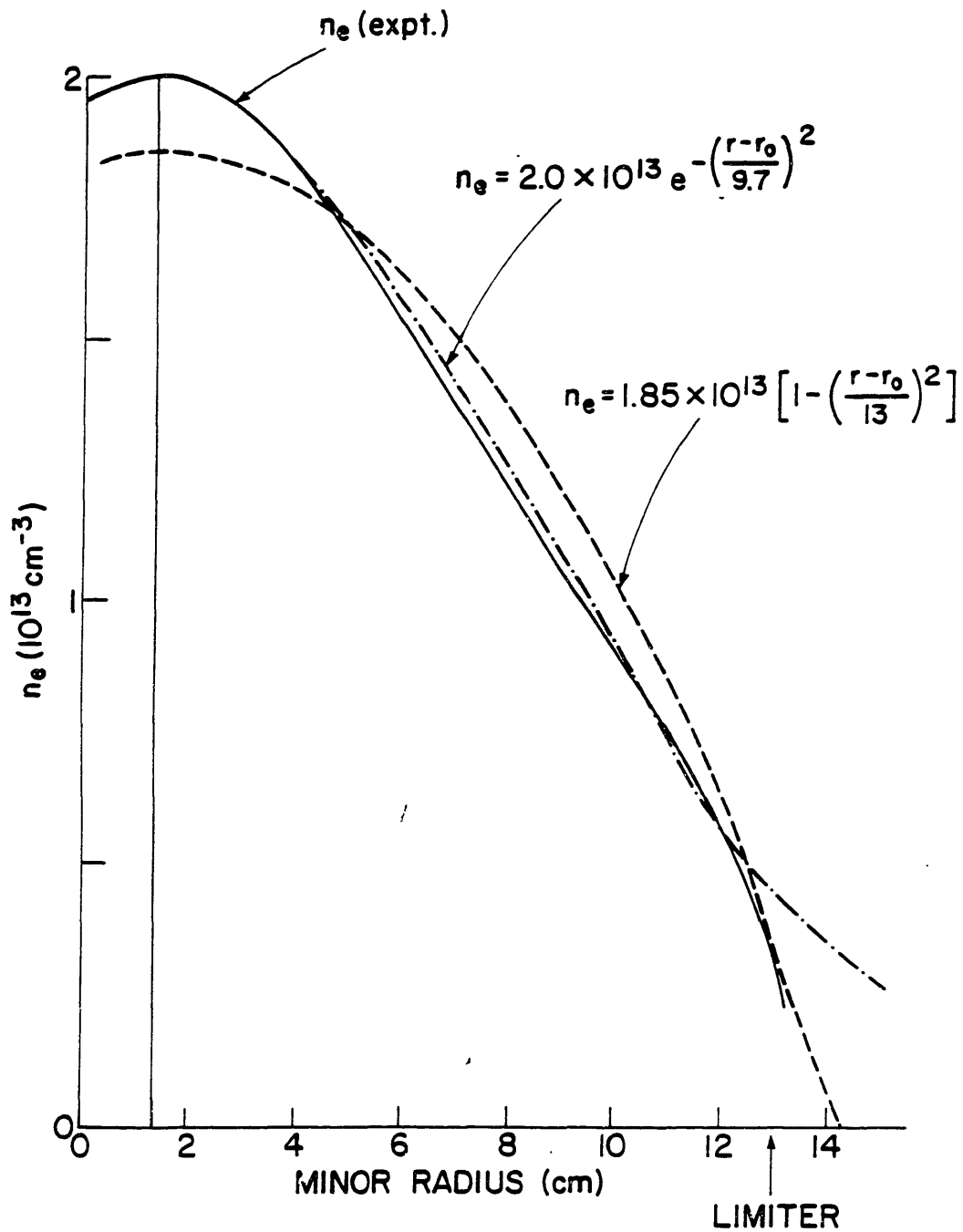


Figure 4.3. Electron density profile measured by 75 GHz interferometry (solid line) for $\bar{n}_e = 1.3 \times 10^{13} \text{ cm}^{-3}$. The dashed and dash-dot lines are analytic representations of the data.

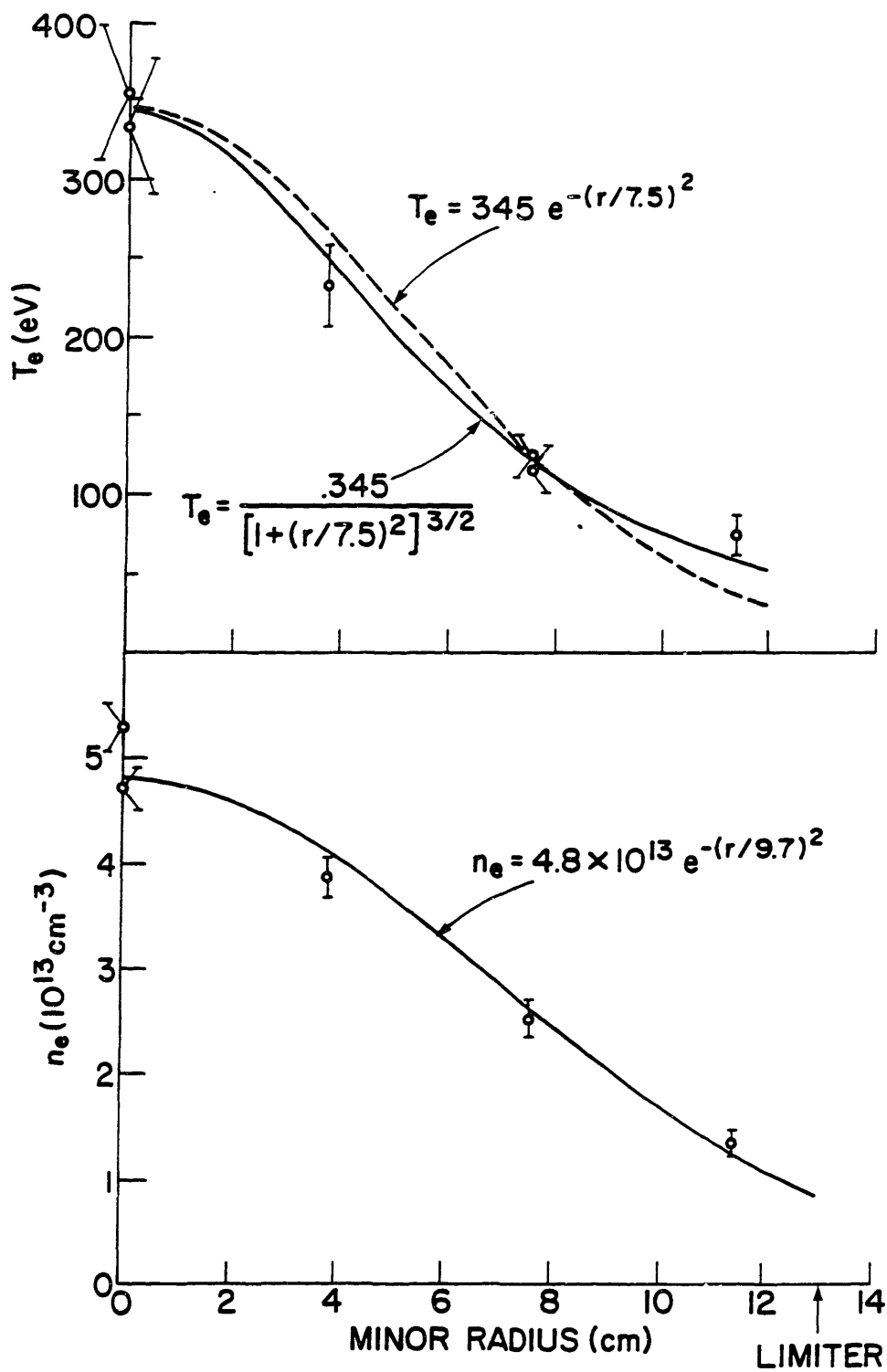


Figure 4.4. Electron temperature and density profiles measured by Thomson scattering for $\bar{n}_e = 3.2 \times 10^{13} \text{ cm}^{-3}$. The curves are analytic profiles fitted to the data.

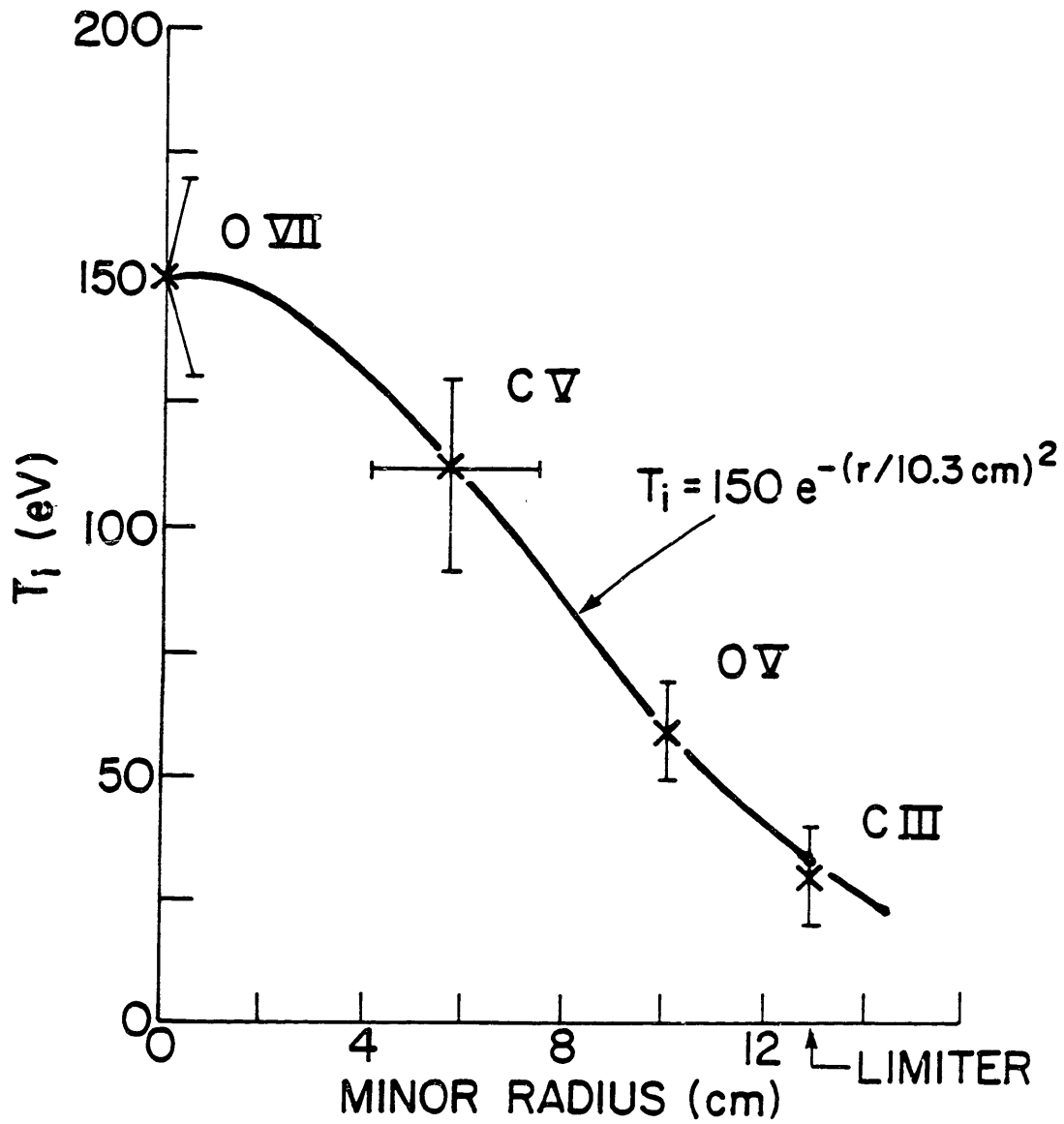


Figure 4.5. Ion temperature profile inferred from chord-averaged Doppler broadening measurements of the O VII, C V, O V, and C III impurity lines using the electron temperature profile illustrated in Fig. 4.4. The ion and electron temperature measurements were performed during the same run.

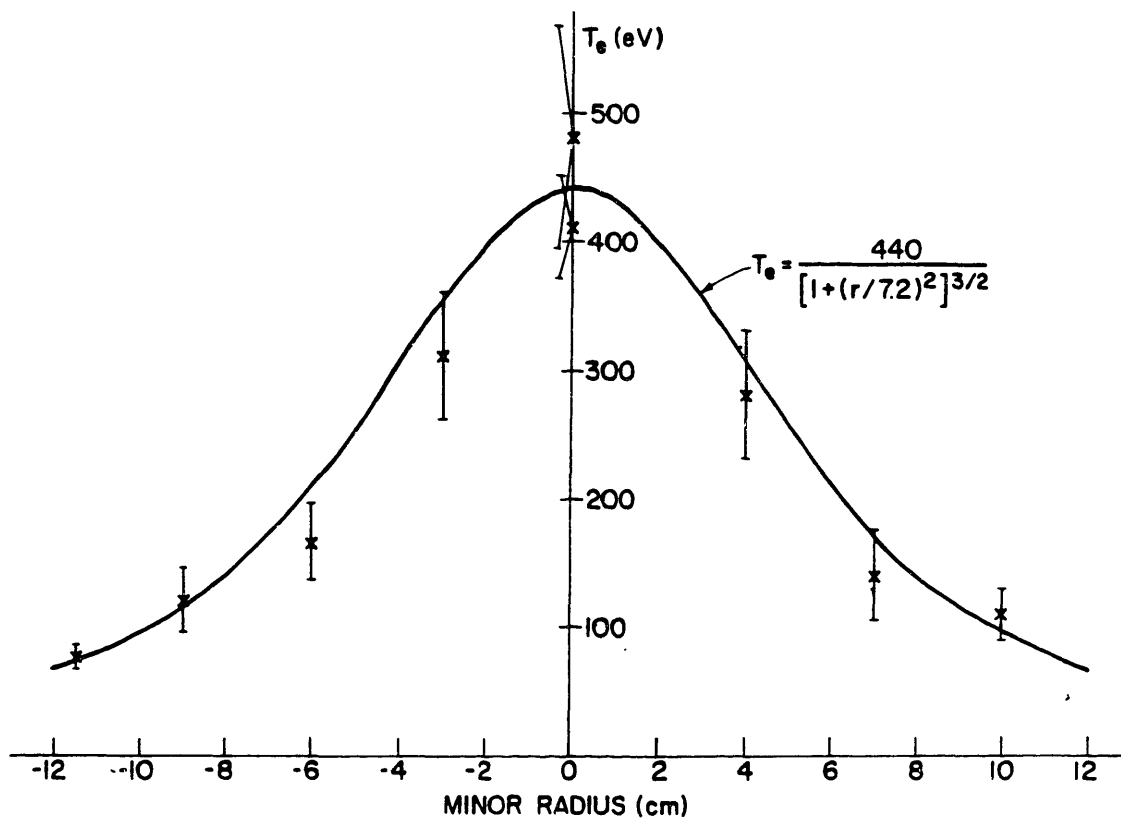


Figure 4.6. Electron temperature profile obtained by soft X-ray spectroscopy at $\bar{n}_e = 1.5 \times 10^{13} \text{ cm}^{-3}$

The importance of the relative impurity content of the plasma with regard to the ion heating experiment has been pointed out in Chapter 2. The effective ionic charge, Z_{eff} , can be estimated from the electrical resistance of the plasma and the temperature profile. The input power is equated with the ohmic losses:

$$P_{OH} = 4\pi^2 R_o \int_0^a \eta_{\parallel} J_{\parallel}^2 r dr \quad (4.8)$$

where ν_{\parallel} is the resistivity in the direction parallel to the magnetic field, and J_{\parallel} is the current density. Neglecting neoclassical effects, the resistivity is¹⁰⁹

$$\eta_{\parallel}(r) = 1.1 \times 10^{-2} \ln \Lambda G(Z_{eff}) T_e(r)^{-3/2} \quad (\Omega\text{-cm}) \quad (4.9)$$

where T_e is in eV and

$$G(Z_{eff}) = \frac{Z_{eff}(2.67 + Z_{eff})}{3.4(1.13 + Z_{eff})}. \quad (4.10)$$

Assuming Z_{eff} and the ohmic electric field to be constant with minor radius, and taking a Gaussian electron temperature profile, we obtain

$$G(Z_{eff}) = \frac{V_l}{I_p} \frac{\lambda_{te}^2 T_{eo}^{3/2}}{3(1.1 \times 10^{-2}) R_o \ln \Lambda} \quad (4.11)$$

where I_p is the peak "steady-state" plasma current, and V_l is the loop voltage at the current peak. The central electron temperature measured by Thomson scattering at high plasma densities ($\bar{n}_e = 2.5\text{--}3.2 \times 10^{13} \text{ cm.}^{-3}$) has been observed to vary from 350 to 440 eV for $I_p = 55\text{--}60$ kA and $V_l = 1.8\text{--}2.2$ V. Substituting the extreme values of V_l and T_{eo} into Eq. (4.11) and taking $\lambda_{te} = 7.5$ cm. and $\ln \Lambda = 15$, we calculate Z_{eff} to be 1.3–2.6. The effect of banana-trapping of a fraction of the electron population may reduce this estimate of Z_{eff} somewhat. For most of our calculations, we take $Z_{eff} = 2$.

4.4. The 800 MHz Rf System

The rf system for the lower-hybrid experiments consists of a high-voltage power supply, an rf source and high power amplifier, a transmission and power splitting network, a phased-array waveguide antenna, and an rf power and phase measurement detection system. A schematic of the entire system is shown in Fig. 4.7 With the exception of the power splitting network and the antenna, the system was designed and built at PPPL, and is on loan from that laboratory. The system is outlined here, with details relevant to this particular experiment being highlighted.

At the heart of the rf system is a single Varian type VA-955B klystron driven at 800 MHz by a TTL pulse-modulated source of controllable power level. The klystron itself is powered by a 60 kV, 10 μ F capacitor bank charged by a 100 kV, 18 mA DC power supply. The voltage on the klystron is regulated by a type 4CX35000 high-voltage tetrode switch tube. The klystron voltage

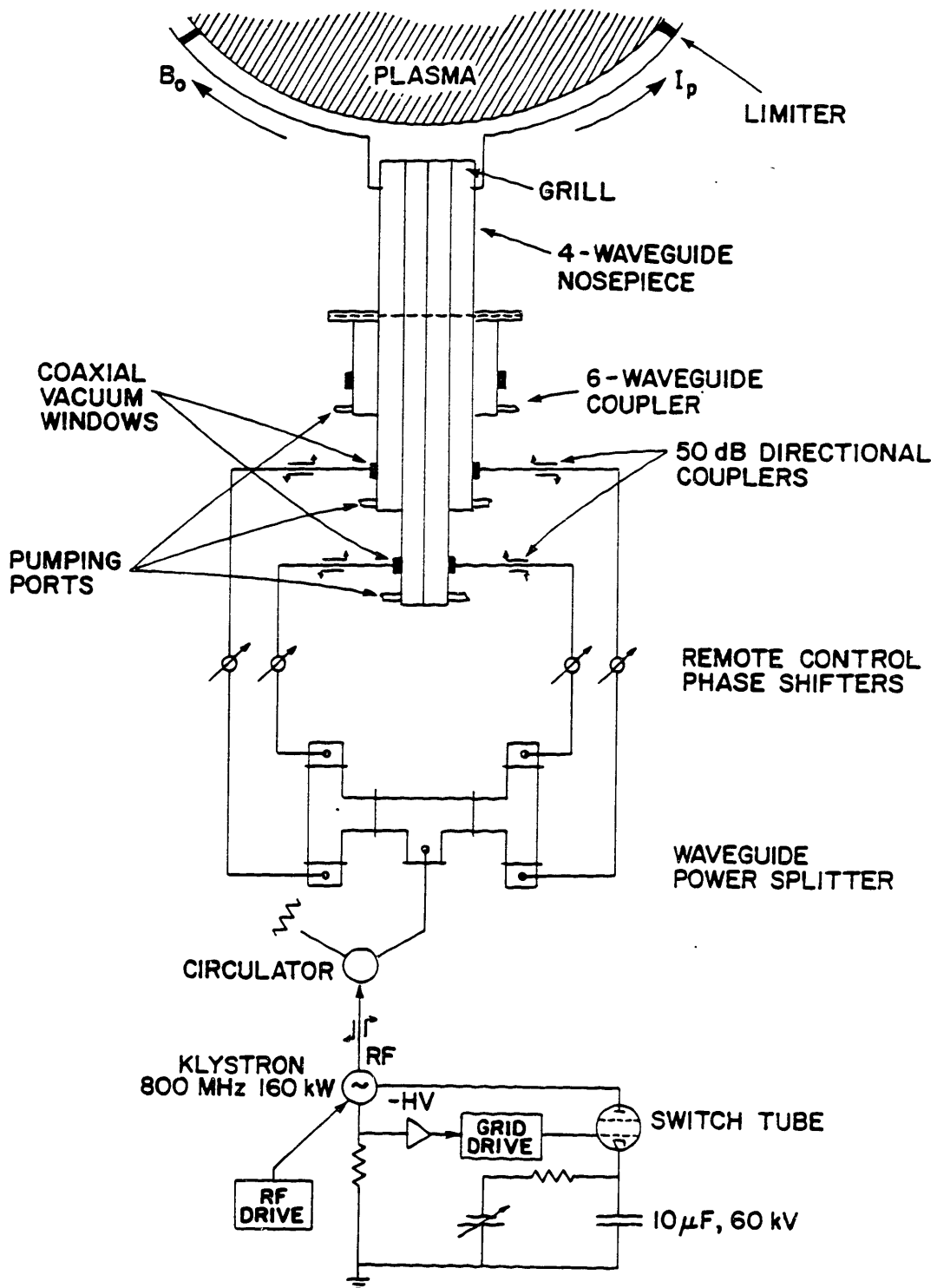


Figure 4.7. Schematic of the rf system, showing the high power klystron, transmission and power-splitting network, and the waveguide antenna.

is controlled by the amplitude of the grid voltage on the switch tube. The size of grid voltage pulse is also user-controllable and is feedback-regulated by the measured beam current of the klystron. Thus the rf output power may be regulated by either the level of the rf drive power to the tube or by the voltage on the klystron. The maximum measured output power of this klystron is approximately 160 kW. At this power, the maximum pulse length at constant power is approximately 10 msec, limited by the present capacitor bank energy.

The rf output power of the klystron is directed through 50 ohm, 3.125" diameter copper coaxial line to a high power ferrite core circulator and thence to a set of waveguide-T power splitters which divide the power into four approximately equal parts. Each fraction is returned to 1.875" diameter coaxial conductor and routed through a calibrated phase shifter, a bi-directional couple for monitoring forward and reflected power, a coaxial ceramic window assembly, and then coupled into a waveguide of the antenna with an E-type coupler.

The rf vacuum window section is comprised of a commercial coaxial window structure which is electron-beam welded to a transitional coaxial piece with a copper inner conductor and stainless steel outer conductor. To the other end of this coaxial section is welded a standard Varian-type 2.75" diameter vacuum flange. The vacuum flange is bolted to the waveguide antenna feed, and the copper gasket vacuum seal provides electrical continuity of the outer conductor. The welds on the interior of the coaxial transition are polished to a smooth finish and the inside of the copper gasket is rounded to reduce the chance of rf breakdown in this section. Arcing in this transition piece was a frequent occurrence before attention was directed to the interior finish.

Several different waveguide antennas have been used in the lower-hybrid experiments on Versator. A waveguide array with interchangeable four and six-waveguide nosepieces centered on the midplane launches lower-hybrid waves from the outer major radius. The nosepiece is the section of the antenna closest to the plasma. In separate and more recent experiments, a four-waveguide grill has been used to inject lower-hybrid waves from the top of the torus.¹¹⁰

The dimensions of the four-waveguide side-launching antenna are a guide width of 2.45 cm., guide septum width of 0.6 cm., and a height of 24.2 cm. The antenna system extends approximately 2 meters radially from the outer wall of the tokamak vacuum vessel. The $n_{||}$ spectrum of this grill for several different phasings has been shown previously in Fig. 3.3. The waveguide width of the six-guide nosepiece is 0.8 cm. and the septum width is 0.15 cm. The higher $n_{||}$ spectrum launched by this grill is believed to be suitable for electron heating.

The entire side-launching antenna is constructed of type 304 stainless steel. Additional pumping of the grill volume is possible via a vacuum manifold on the antenna, though it was found in practice that the extra pumping had no effect on breakdown behavior at high power. The ends of the waveguide walls at the grill mouth have been rounded to reduce the likelihood of arcing at that location. The side-launching grill is movable in the radial direction with respect

to the chamber wall. The grill position is chosen for optimal coupling of rf power to the plasma, as discussed in the next chapter.

The dimensions of the four-waveguide top-launching grill are a waveguide width of 1.0 cm., septum width of 0.16 cm., and guide height of 20.8 cm. The calculated $n_{||}$ spectrum of this grill has been shown in Fig. 3.4. The present version of this antenna is also constructed of type 304 stainless steel, though a titanium nosepiece was employed in the initial experiments with this grill. The position of the top-launching grill mouth relative to the tokamak vessel wall is determined by the width of spacer flanges between the antenna flange and the tokamak vessel port. The spacers may be changed during vacuum breaks.

For monitoring the antenna operation and coupling behavior, the rf signals from the reflectometers in each of the four or six channels are directed to a detection assembly inside an rf-shielded box. The detector for each channel has the capability of measuring absolute power and absolute phase (relative to a local oscillator which is provided by the same source as that for the drive signal to the klystron). Thus the forward power and reflectivity in each waveguide may be measured along with forward and reflected phase. Knowledge of the forward phase is required to set the relative phase between waveguides to the desired value. In practice, the phase angle between waveguides is adjusted once to a common angle, e.g. 0° , using the phase detection network, and the settings of the motor-driven mechanical phase shifters needed to achieve this phase angle are noted. The phase delay of the shifters versus setting is known. During heating experiments, the relative phase angle can be set by remotely adjusting the phase-shifters to previously calibrated positions. As discussed in the next chapter, monitoring the reflected phase is useful in detecting the onset of rf breakdown in the waveguides.

After detection, the forward and reflected power signals are directed through a chain of amplifiers to the Versator data acquisition system. The DC output voltage versus input power for each rf detector has been calibrated a number of times during the course of this experiment. The overall gain of the series of amplifiers is calibrated by a square voltage pulse of known amplitude fed into the amplifier chain immediately following the rf detector output. During heating experiments, the calibration pulse for each channel is triggered approximately 10 msec before the rf pulse and is stored with the rest of the data. A data analysis program has been written in which the voltages of the rectified and amplified rf pulses are normalized by the calibration pulse voltages, and the input rf powers to the detectors are calculated using analytic representations of the individual detector calibration curves stored in the computer memory. Application of the known reflectometer coupling coefficients completes the measurement of the forward and reflected power measurement in each waveguide.

The klystron is protected from high power faults by a standard set of fault detection circuits. To protect the antenna system against internal arcs in the waveguides or near the surface of the windows, an electronic arc detector was built and installed. This instrument shuts off the klystron

in the event of a high reflection coefficient in any waveguide of the antenna, which is often indicative of a fault. The final version of this device on our system was based on the design of the Alcator C arc detector,¹¹¹ and has proven to be successful in minimizing damage from rf breakdown in the grill.

For the ion heating experiments, both the four-waveguide side-launching and top-launching antennas were used. The majority of the experiments have been performed with the former.

5. Experimental Results: Rf Coupling and Antenna Conditioning

The importance of the n_{\parallel} spectrum of the lower-hybrid waves to the expected heating behavior has been discussed in Chapter 2. Because of the accessibility criterion (2.10) and, in the case of ion heating, the necessity of avoiding electron Landau damping, the preferred range of n_{\parallel} for the Versator experiment was determined to be $3 < n_{\parallel} < 8$, roughly. As in most other lower-hybrid heating experiments, the grill-type of antenna is used because it efficiently couples rf power to lower-hybrid waves with $|n_{\parallel}| > 1$, and by virtue of its all-metal construction, it has the additional benefit of reducing possible contamination of the plasma. The computational method developed by Brambilla for predicting the coupling efficiency (antenna transmissivity) and n_{\parallel} power spectrum of the grill has also been described in Chapter 3. In general, the calculated values of antenna reflectivity and n_{\parallel} spectrum are interrelated (see, e.g. Eqs. 3.27 and 3.30). Ideally, both quantities should experimentally be determined and compared with the predictions of the Brambilla theory: unfortunately, measurement of the n_{\parallel} spectrum is difficult. Nonetheless, if reasonable agreement between the theoretical and experimental coupling efficiencies can be demonstrated, we may be justified in assuming that the launched n_{\parallel} spectrum is adequately described by the Brambilla theory. Consequently, we compare in the first part of this chapter the antenna reflectivity measurements of our experimental work to the predictions of the modified Brambilla code described in Chapter 3. As knowledge of the edge density and density gradient is required for application of the coupling theory, the experimental density measurements at the plasma edge are presented first.

Though in theory the grill represents an efficient means of coupling rf power into the plasma, considerable attention to preparation of the waveguide surfaces and *in vacuo* conditioning are usually needed to permit reliable transmission of power through the evacuated waveguides to occur. In the latter part of this chapter, the problems of high-power operation ($P_{rf} > 10$ kW) of the grill and our methods of solving them are discussed.

5.1. Edge Density Measurements

The plasma density near the waveguide mouth was measured with Langmuir probes inserted through the nosepiece of the four-waveguide grill (see Fig. 5.1). These probes, one in an inner guide and the other in an outer one, were movable with respect to the grill mouth; thus the density gradient as well as the absolute value of the density at the grill mouth could be measured in the absence of rf injection. The advantage of this technique is that the density is measured in the precise location required for the comparison between experimental and computed results, rather than at an adjacent port. Unfortunately, because this arrangement necessitated the removal of the rest of rf antenna system, the local density and the rf coupling could not be recorded simultaneously. However, with another Langmuir probe located 22° toroidally from the grill port, the edge density was monitored during both the rf coupling and the grill density measurement runs to confirm that the edge density was similar for both cases.

The probe current-voltage characteristic yielded values of ion density n_i and electron temperature T_e using two means of analysis: the numerical calculations of Laframboise for a cylindrical probe in an unmagnetized plasma,¹¹² and a simple plane probe theory.¹¹³ The latter may be justified in that $\rho_{ce} \ll r_p$ and $\rho_{ci} \approx r_p$, where r_p is the probe radius. In general, the densities obtained using plane probe theory are about 5 times higher than those obtained using the Laframboise method. We will return to this point later. Unless otherwise noted, the Langmuir probe data presented in this section were reduced using an iterative procedure based on Laframboise's calculations.

Density gradient measurements are presented for the two limiter configurations shown in Fig. 5.1. Initial rf coupling experiments into a plasma with no radial limiters showed the antenna reflectivity to be high when the grill mouth was located at the major radius of the outer wall of the tokamak. The reflectivity was measured to decrease continuously as the grill was retracted up to 3.5 cm. outward from this position, indicating that the edge plasma density was too high to achieve a minimum in reflectivity near the tokamak vessel wall. Consequently, a pair of radial limiters was placed near to the waveguide port to reduce the local density. These vertical limiters were first placed 2 cm. toroidally to each side of the waveguide port on the outboard wall. Because the calculated lower-hybrid ray trajectories from the grill were later found to intercept the limiters in this position, the limiters were later moved to a circumferential position of approximately 55 cm. to each side of the grill port. The density measurements in front of the waveguides for both limiter positions are shown in Fig. 5.2. The density profiles are seen to be roughly exponential. For the case of the limiters placed near the waveguide port, the exponential fit is good from the inner edge of the limiter to the waveguide mouth. The density scale length λ , defined by

$$n_i(x) = n_i(0)e^{x/\lambda} \quad (5.1)$$

is 0.3–0.5 cm. For the latter case, the profile exhibits a change in slope near the radius of the wall-grill port junction. Between the inner edge of the limiter and the wall radius, the density scale length is $\lambda \simeq 1.2$ cm; inside the waveguide port, with the grill retracted, we find $\lambda \simeq 0.2$ cm. The electron temperature profiles for both cases are shown in Fig. 5.3. The temperature is 20–30 eV just outside the limiter radius and 4–5 eV inside the grill port. A break in the temperature profile for the second limiter position is also evident from the data.

The measured density profiles are consistent with a model of the edge plasma in which the density gradient is determined in part by the flux of particles along the field lines. This assertion is justified by arguments presented in Appendix D. The point to be made is that the estimated edge diffusion coefficients based on the measured density and temperature profiles are reasonably consistent with Bohm diffusion values, which also corroborates similar findings on other tokamaks.^{114,115} With this justification, we can estimate with some confidence the edge density profile in regions where the density is not measured (e.g., well inside the waveguides or at other toroidal locations). Moreover, the coupling results, at least in their relation to the density profile,

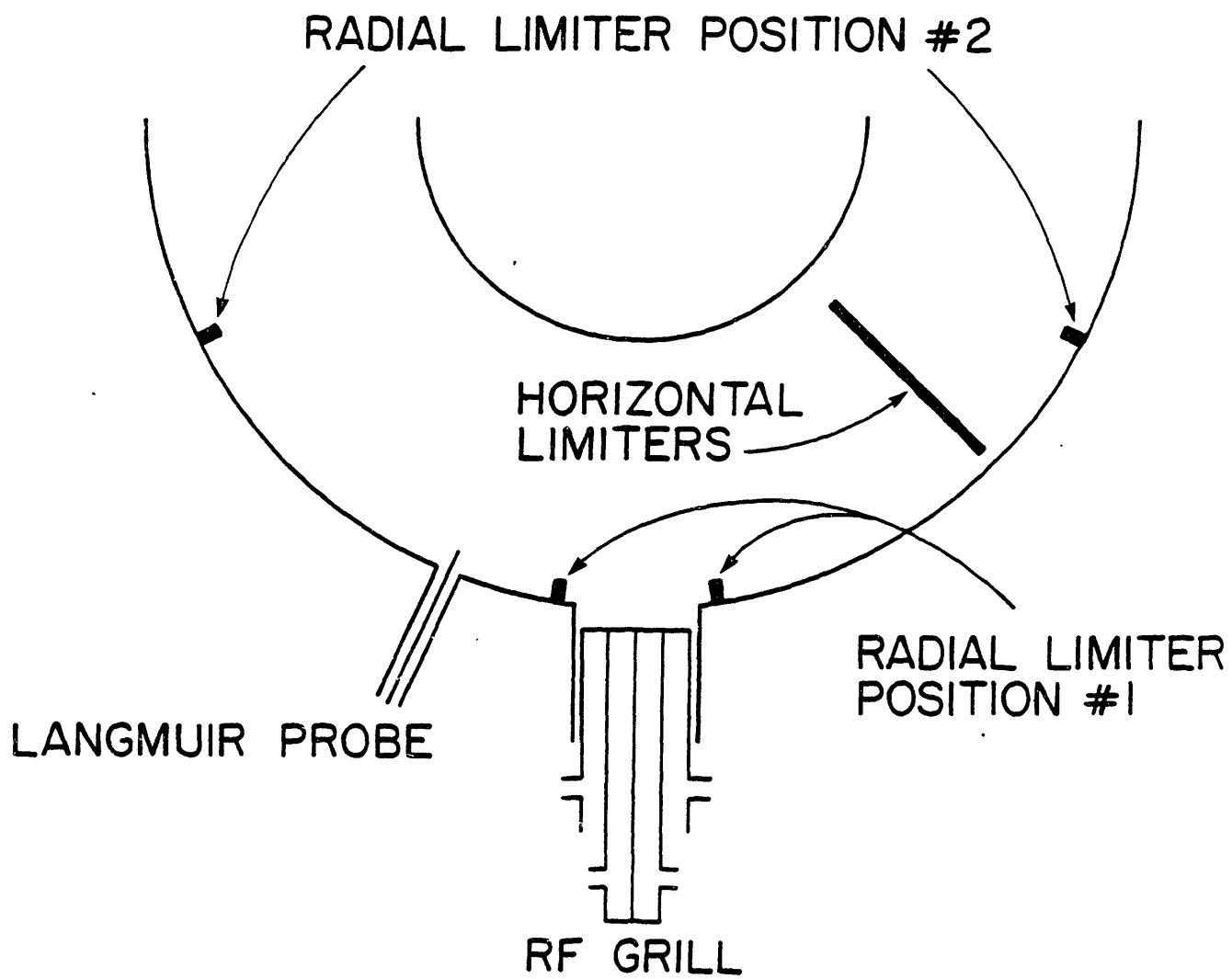


Figure 5.1. Limiter and Langmuir probe configuration for the coupling experiments.

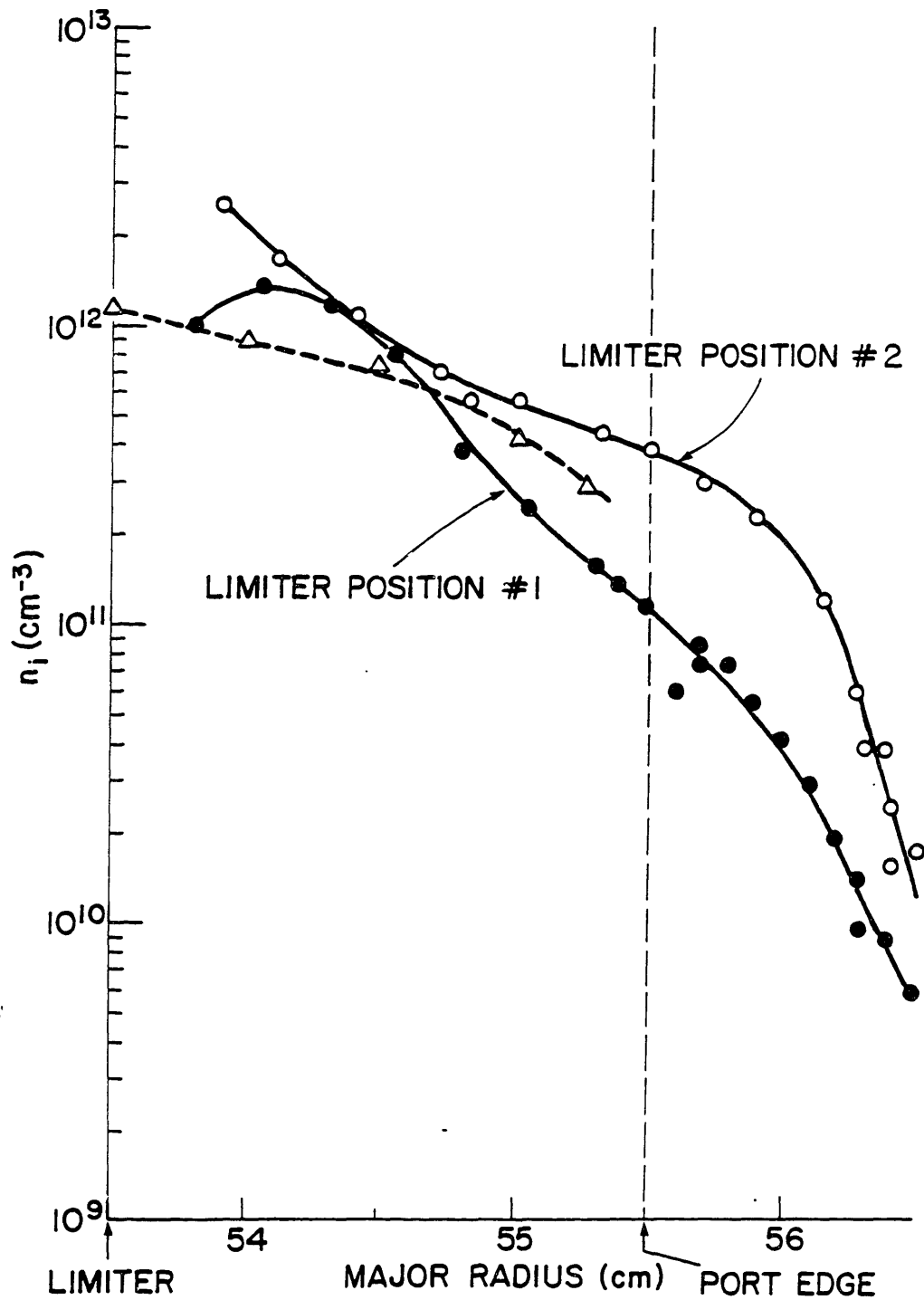


Figure 5.2. Edge density profiles in front of the grill. The solid lines indicate the measurements made directly in front of the grill, and the dashed line shows the density profile measured with the probe 22° toroidally away from the antenna.

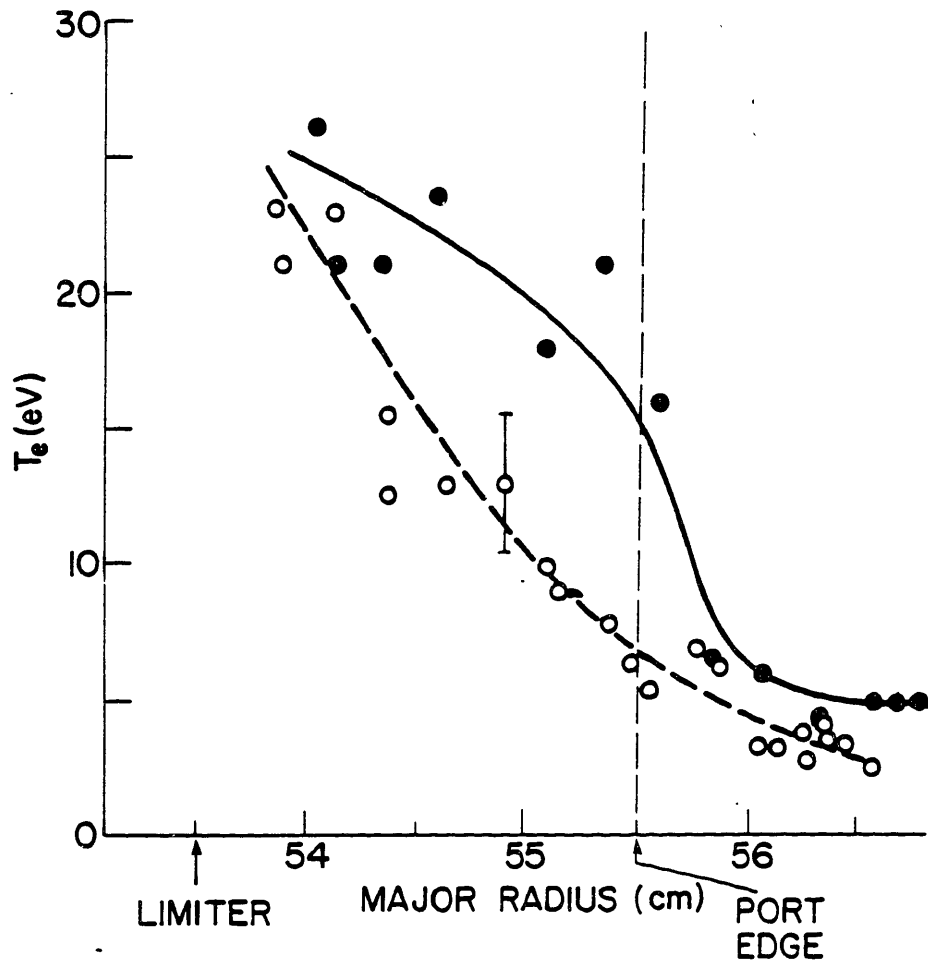


Figure 5.3. Edge electron temperature profiles in front of the grill. The dashed line indicates the temperature for the first limiter position, the solid line for the second.

are general in that the edge density profiles near the waveguide grill are understood and are in agreement with similar measurements from other tokamaks.

The validity of the unmagnetized plasma approximation in the measurement of the plasma density may be assessed from the electron temperature profile. Referring to Fig. 5.3, we note that because of the low electron temperature near the waveguide mouth, the ion Larmor radius, assuming $T_i \leq T_e$, is comparable to the probe radius at this location:

$$\begin{aligned} \rho_{ci} &= \frac{c}{eB} (m_i T_i)^{\frac{1}{2}} = 1.3 \times 10^{-2} \sqrt{T_i (\text{eV})} \quad (\text{cm}) \\ &\approx r_p \geq 0.03 \text{ cm.} \end{aligned} \quad (5.2)$$

Therefore, for probe measurements performed well outside the limiter radius, magnetized plasma effects may become important in interpreting the probe data. Consequently, in this region, we employ a simple plane probe theory in which the effective probe area is taken to be the cross-sectional area perpendicular to the magnetic field. This is the highly magnetized plasma limit. The collected ion current is then

$$I_{sat} = 2n_i r_p l_p \sqrt{T_e / m_i} \quad (5.3)$$

where l_p is the probe length.

The plasma density values given by this approximation are about a factor of five higher than those obtained using the Laframboise method. The comparison is shown in Fig. 5.4 for a typical density profile. The density at the limiter given by the plane probe method is about 10^{13} cm^{-3} which would appear to be too high as the line-averaged density for these discharges is probably $1.5 \pm 0.5 \times 10^{13} \text{ cm}^{-3}$. Since the temperature is high ($T_e = 30 \text{ eV}$) at this location, according to Eq. (5.2) plane probe theory is no longer valid, and the true density should be intermediate between the two limits. An attempt to measure the density unambiguously using the resonance cone method¹¹⁶ was made in which one probe was used as a launching antenna and another as a receiver, but the strong plasma noise, steep density gradients, and temporal variation of the edge density during the discharge prevented reliable measurements. Lacking corroborating data, we have assumed a more accurate density measurement is given by plane probe theory when the probe is located in the low-temperature plasma of the grill port. The Laframboise method is used to provide a density measurement for the probe located near the limiter radius.

Other observations regarding the measured density profiles are the following: first, the density is not constant in the z -direction, but is constant along the toroidal field. As shown in Fig. 5.5, the density in front of the inner guide is 1.5 to 4 times that in front of the outer guide, depending on the local density scale length. The effect of this variation in density across the grill mouth on the coupling efficiency has not been calculated in detail. However, based on the toroidal curvature and the value of k_{\perp} from the local dispersion relation, Eq. (3.3a), the phase retardation of the outer guides relative to the inner ones is less than 3° as long as the density at the grill mouth is low

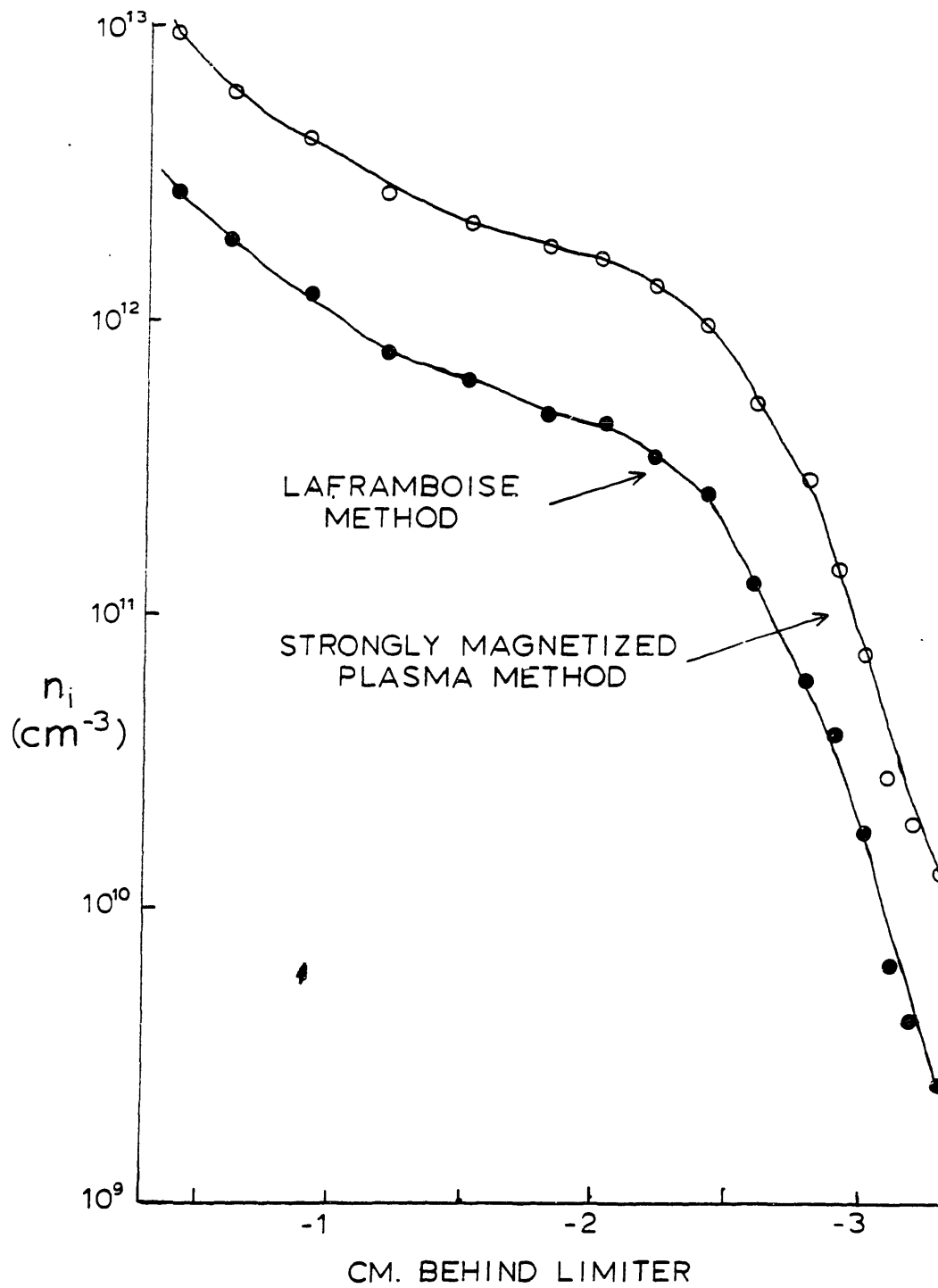


Figure 5.4. Comparison of edge densities obtained with different techniques of reducing the Langmuir probe data. The lower curve results from use of the Laframboise method, the upper from plane probe theory.

($\omega_{pe}^2/\omega^2 \leq 10$). Thus the spectrum should not be significantly affected by the plasma curvature. Since the measured reflectivity is not a strong function of the density gradient, as we shall see in next section, the coupling efficiency is likely to be determined by merely an average value of the density gradient across the grill mouth. Secondly, as also indicated in Fig. 5.5, the measured density within the waveguides themselves is finite. The density scale length inside the guides is 0.1–0.2 cm. in the first several millimeters inside the guides; farther inside, the plasma is too tenuous for accurate probe measurements, and the narrow waveguides may allow the flux tubes sampled by the probes to be depleted (though in principle the density could be estimated from Eq. D.4). As discussed in Chapter 3, the effect of plasma in the waveguide can be estimated, and for mildly overdense plasmas is found to be negligible.

5.2. Comparison of Calculated and Experimental Rf Coupling Results

To compare the experimental coupling efficiency to the values predicted by the calculations described in Chapter 3, measurements of the grill reflectivity, along with those of the density profile in front of the grill mouth, were carried out early in the course of this work. During most of these tests, the incident rf power was deliberately limited to less than two kilowatts to avoid the problem of rf breakdown in the waveguides and the possible effect of pondermotive modulation of the density gradient in front of the grill. The reflectivity measurements were performed using the calibrated rf detection system described in Chapter 4. Sufficient rf shielding was provided to ensure that rf leakage into the detector box was negligible. With adequate shielding, the unwanted rf pickup on the detectors was reduced to 20–25 dB below the signal level.

Coupling measurements were performed with the four-waveguide side-launching grill for both limiter positions described earlier. Figure 5.6 shows the measured grill reflectivity for the relative phase angles $\Delta\phi = 0^\circ$, 90° , and 180° for the two limiter positions. For $\Delta\phi = 90^\circ$ and 180° , the grill mouth location for the best coupling for the second limiter position is approximately one cm. radially outward from the optimally coupled grill position for the first limiter location. Given that the density decreases from the limiter edge with a steeper gradient for the case of the first limiter than for the second, the difference in the coupling between the two cases supports the general premise of the theory that the coupling is determined by the plasma density at the waveguide mouth. We note that the reflectivity minimum for $\Delta\phi = 90^\circ$ occurs at a lower density than for $\Delta\phi = 180^\circ$; this is explained well by Eq. (3.27), given that the power spectrum for the 90° phasing is characterized by lower values of n_{\parallel} (roughly a factor of 1/2) than that for the 180° phasing. According to Eq. (3.33), the optimal coupling locations for the two phases should be separated by a distance $\Delta x \simeq \lambda \ln(4) \approx 0.3 - 0.7$ cm, which is not inconsistent with results shown in Fig. 5.6. The reflectivity for $\Delta\phi = 0^\circ$ (low n_{\parallel}) is high, as expected.

Using the modified Brambilla code described in Chapter 3, we obtain reasonably good agreement between the coupling data and the calculated results for the grill locations closest to the plasma surface. The measured and calculated coupling results for the second limiter position

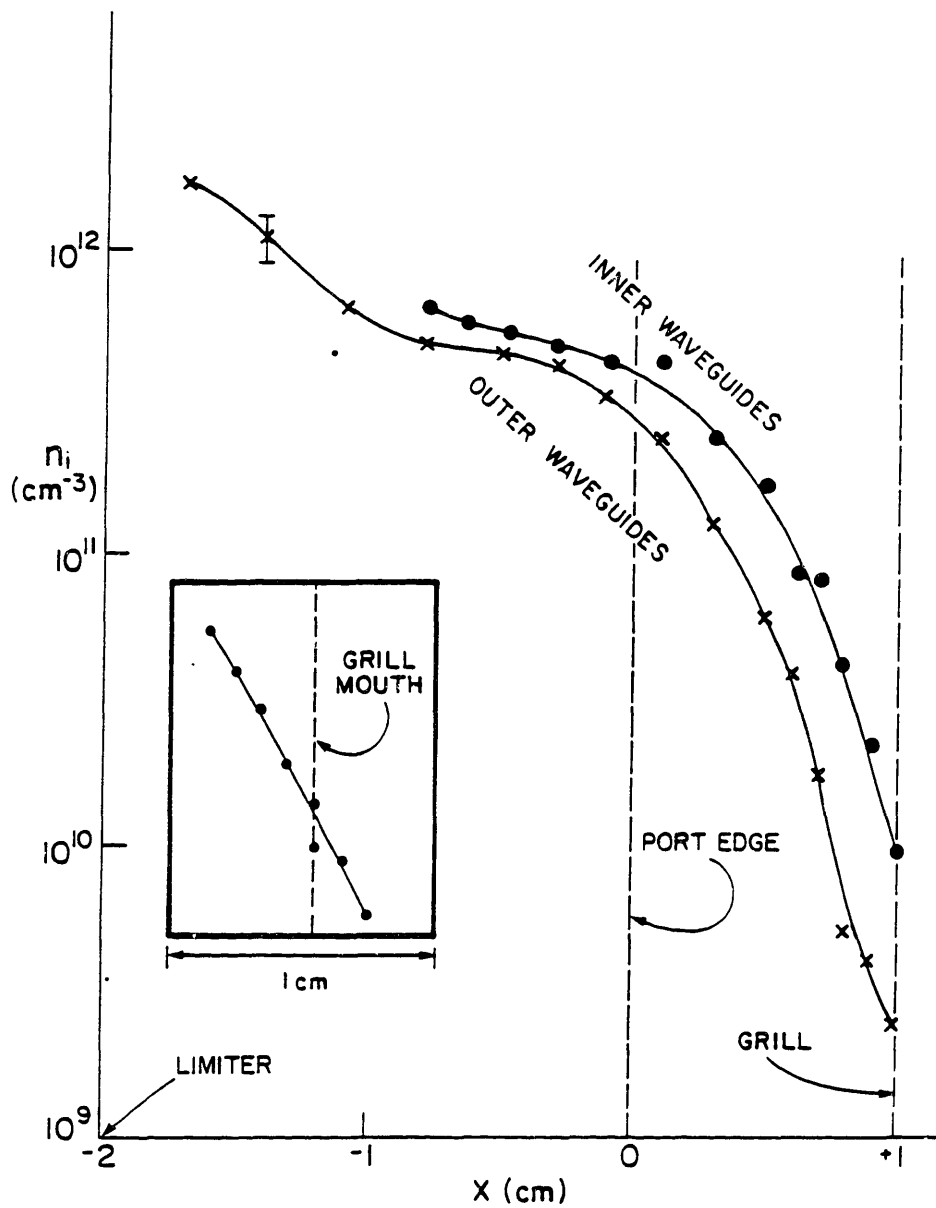


Figure 5.5. Density profiles in front of an inner and outer waveguide of the four-waveguide grill. The horizontal axis is in units measured relative to the face of the grill. The inset shows the measured density inside one of the waveguides. The vertical axis for the insert is the same as for the larger figure.

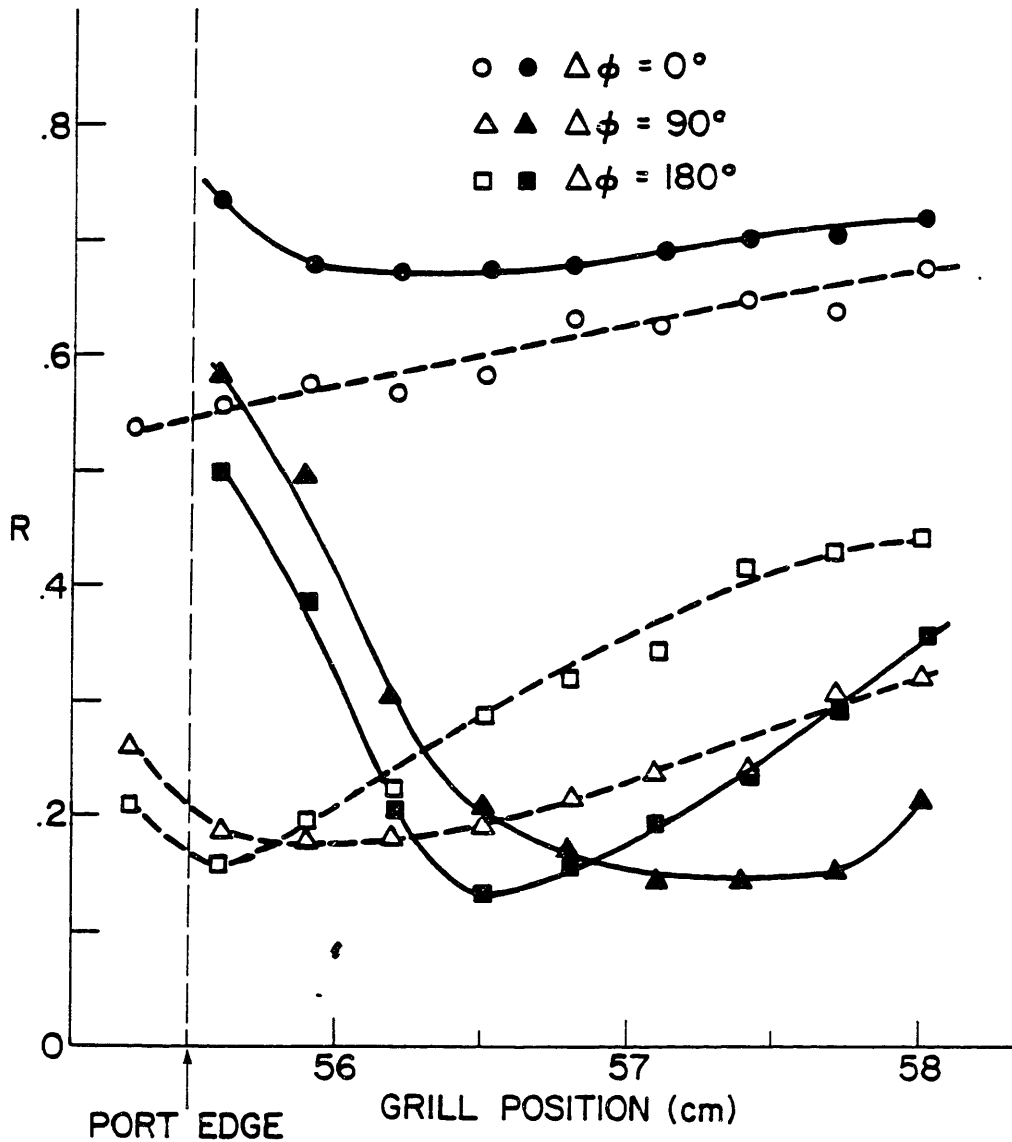


Figure 5.6. Measured total grill reflectivity as a function of grill position (in major radius) for the two limiter positions and relative phase between waveguides $\Delta\phi = 0^\circ$ (circles), 90° (triangles), and 180° (squares). Open symbols represent the data for the first limiter position, solid symbols for the second. The plasma density increases to the left in the illustration. The juncture of the antenna port wall and the outer wall of the tokamak vessel is indicated.

are compared in Fig. 5.7. The densities and density gradients used in the model are obtained from the measured probe data which have been reduced using plane probe theory for the reasons given earlier. The location of the measured reflectivity minima for $\Delta\phi = 90^\circ$ and 180° correspond well to those obtained from the code. Both the actual and calculated coupling coefficients increase as the grill is moved further toward the plasma from this location, with the theoretical values being somewhat lower than the experimental ones over this range. For the grill retracted more than one centimeter inside the port, the correspondence between the experimental and theoretical values is poor, with the experimental reflectivities being lower for $\Delta\phi = 90^\circ$ and 180° and higher for $\Delta\phi = 0^\circ$ than the predicted values.

The calculated and experimental reflectivities for the individual guides for the three phases are plotted in Figs. 5.8–5.11. For $\Delta\phi = 180^\circ$ (see Fig. 5.8), the measured reflectivities are roughly symmetric as expected, with the outer guides generally exhibiting higher reflectivities than the inner ones over most of the grill position range. Again, there is qualitative agreement between this finding and the experimental results for the grill located one centimeter or less inside the port; we see the outer guides are predicted to be more reflective than the inner ones when the grill is located in an overdense plasma.

The measured individual reflectivities for $\Delta\phi = 90^\circ$ (see Figs. 5.9 and 5.10) are more difficult to generalize, but the notable feature of the coupling is the high reflectivity of the "downstream" waveguide (the outer waveguide on the side of the grill in the direction of the traveling wave spectrum generated by the asymmetric phasing). As the grill is pushed into the plasma, the reflectivity of the other outer waveguide increases from 2.5% , the lowest of all four guides, to a value just under that of the opposite outer waveguide. As in the case of $\Delta\phi = 180^\circ$, the individual guide reflectivities for $\Delta\phi = 90^\circ$ also show qualitative similarities with the measured values for the grill situated close to the port edge, with the correlation becoming worse for antenna locations farther into the port. The experimental minimum for this phasing extends over larger span of grill positions than does the calculated minimum.

For a relative phasing of 0° between waveguides, there is little correspondence between the code predictions and the experimental results (see Fig. 5.11). The average calculated reflectivity decreases monotonically from 90% to 35% as the grill is retracted into the port, whereas the measured reflectivity remains high for all grill locations tried. Also, the inner guides are calculated to be typically 10–30% more reflective than the outer guides while the measurements indicate the outer guides to be 1.5–3 times as reflective as the inner ones.

The symmetry of the measured inner and outer guide reflectivities is not as pronounced for this phase as for $\Delta\phi = 180^\circ$. The poorer symmetry of the 0° case cannot be explained by errors in setting the relative phase between guides; a numerical test using the Brambilla code shows that a small change in several of the waveguide phasings reduces the symmetry of the reflectivity for $\Delta\phi = 180^\circ$ to a greater extent than for $\Delta\phi = 0^\circ$. However, because the spectrum for the latter

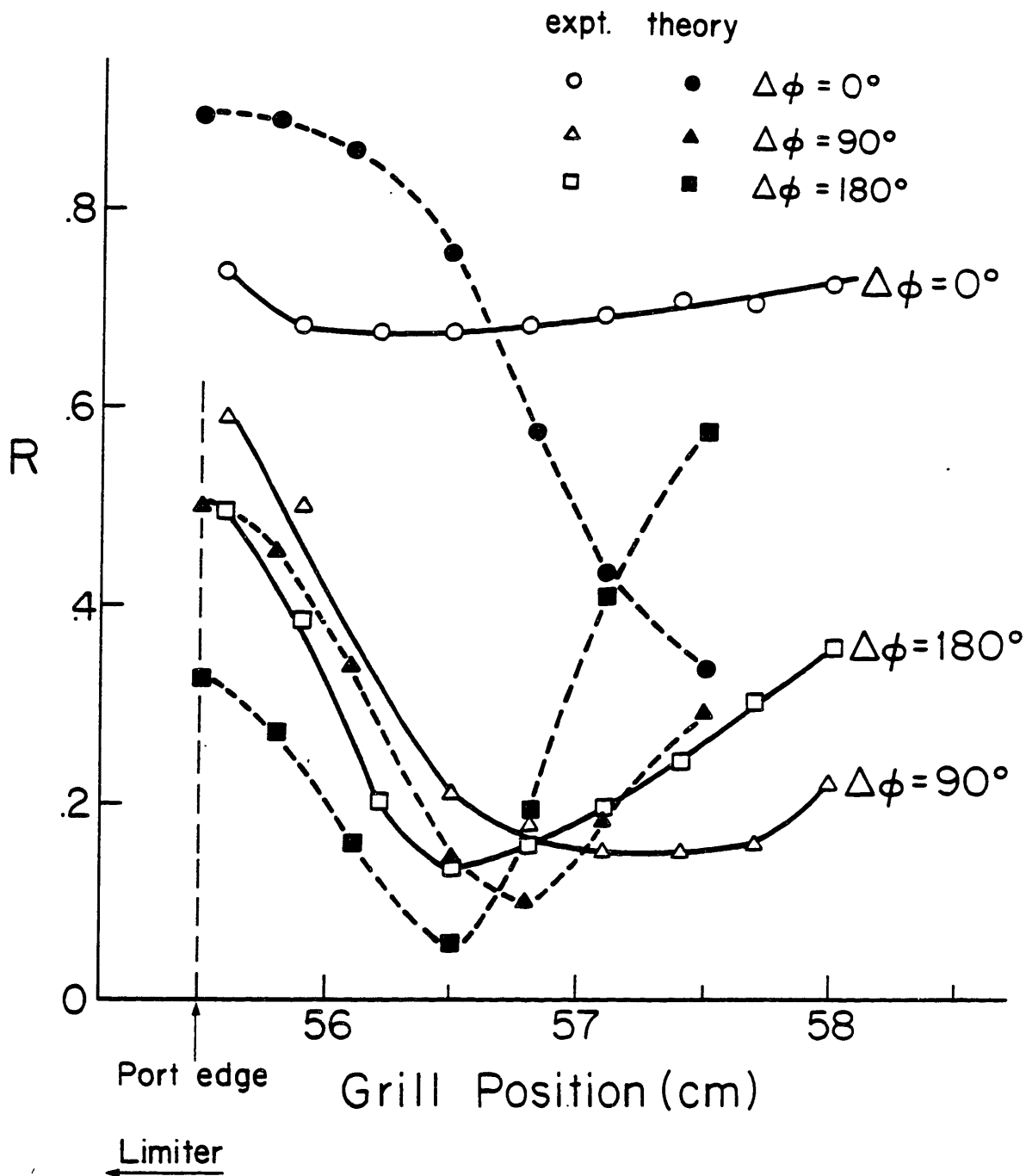


Figure 5.7. Comparison of the calculated and experimental antenna reflectivity versus grill position for the second limiter location. The theoretical values are indicated by dashed lines and closed symbols, the measured ones by solid lines and open symbols. Circles denote the case of $\Delta\phi = 0^\circ$, triangles the case of $\Delta\phi = 90^\circ$, and squares the case of $\Delta\phi = 180^\circ$. For $\Delta\phi = 180^\circ$, the theoretical reflectivity minimum occurs at $\mu = 10$. The limiter is located at a major radius of 53.5 cm.

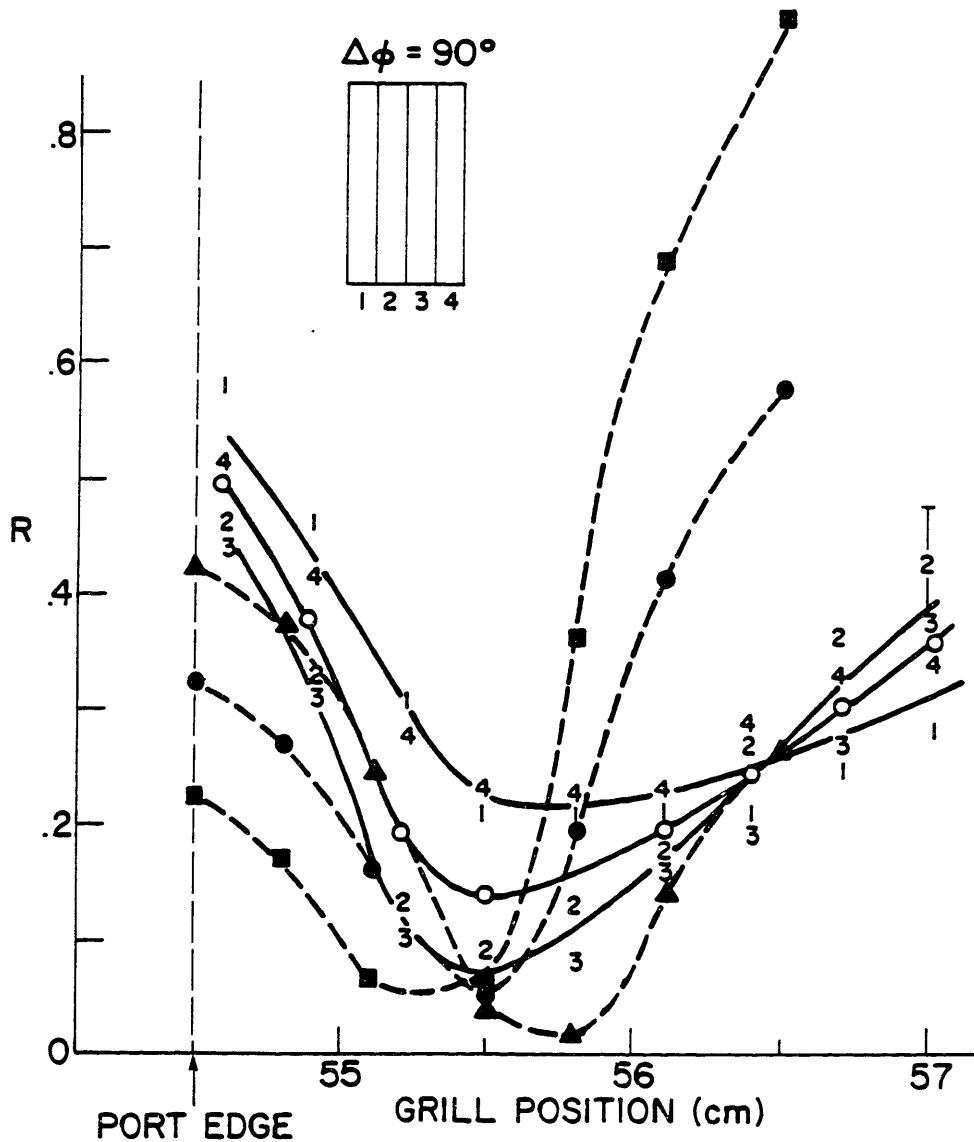


Figure 5.8. Comparison of experimental and theoretical relectivities for individual waveguides for the case $\Delta\phi = 180^\circ$. Dashed lines are the calculated values; solid lines experimental. The numbers referring to the data points are guide numbers: 1 and 4 are the outer guides; 2 and 3 the inner ones. Open circles denote the measured overall grill relectivity, closed circles the theoretical total grill relectivity. The calculated relectivity of the inner waveguides is indicated by closed squares, and that of the outer guides by closed triangles.

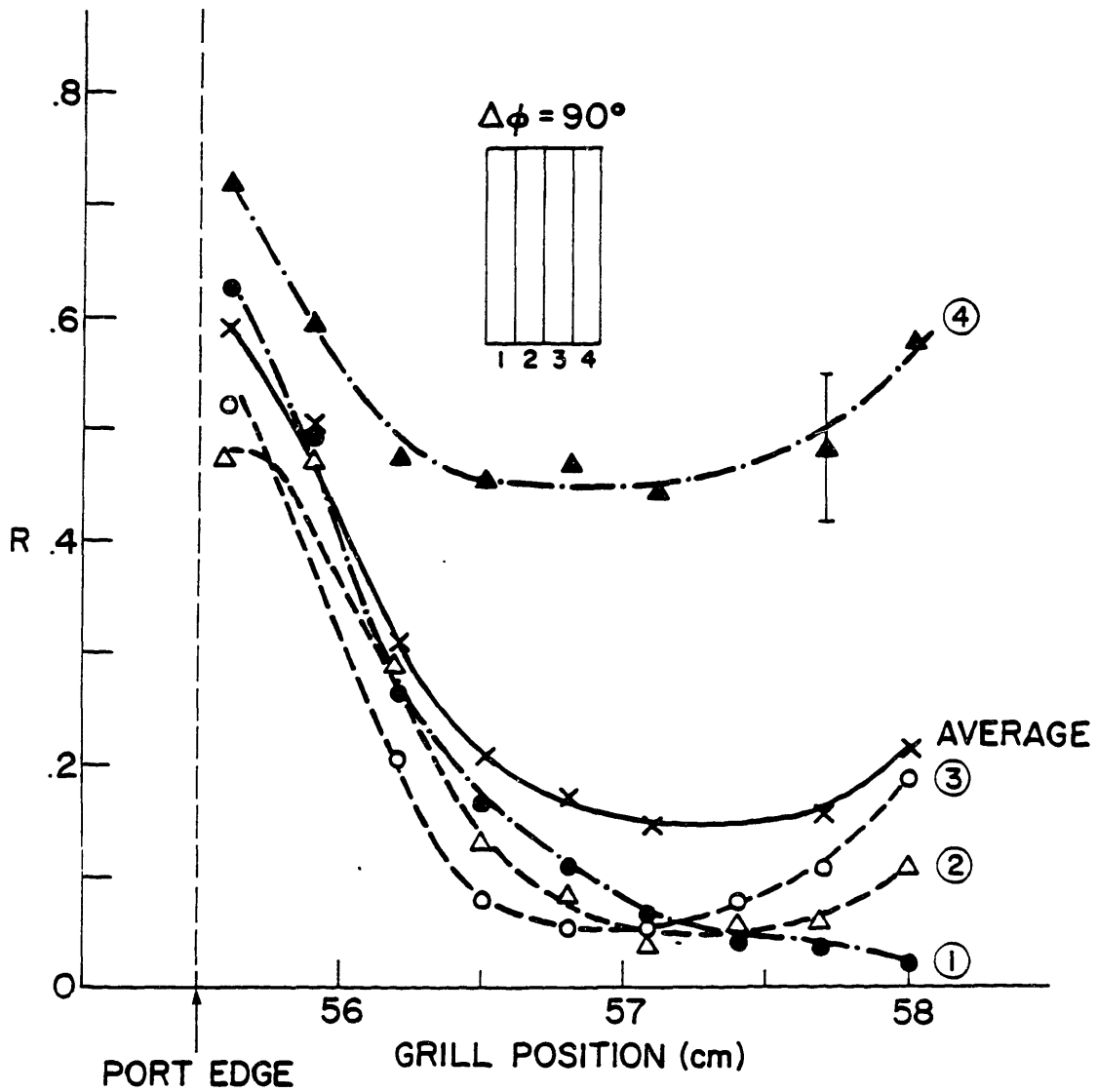


Figure 5.9. Experimental reflectivities for individual waveguides; $\Delta\phi = 90^\circ$. The reflectivities of the inner guides (2 and 3) are shown with dashed lines and open symbols. The reflectivities of the outer guides (1 and 4) are shown with dot-dash lines and closed symbols. The total reflectivity is denoted by x's and a solid line.

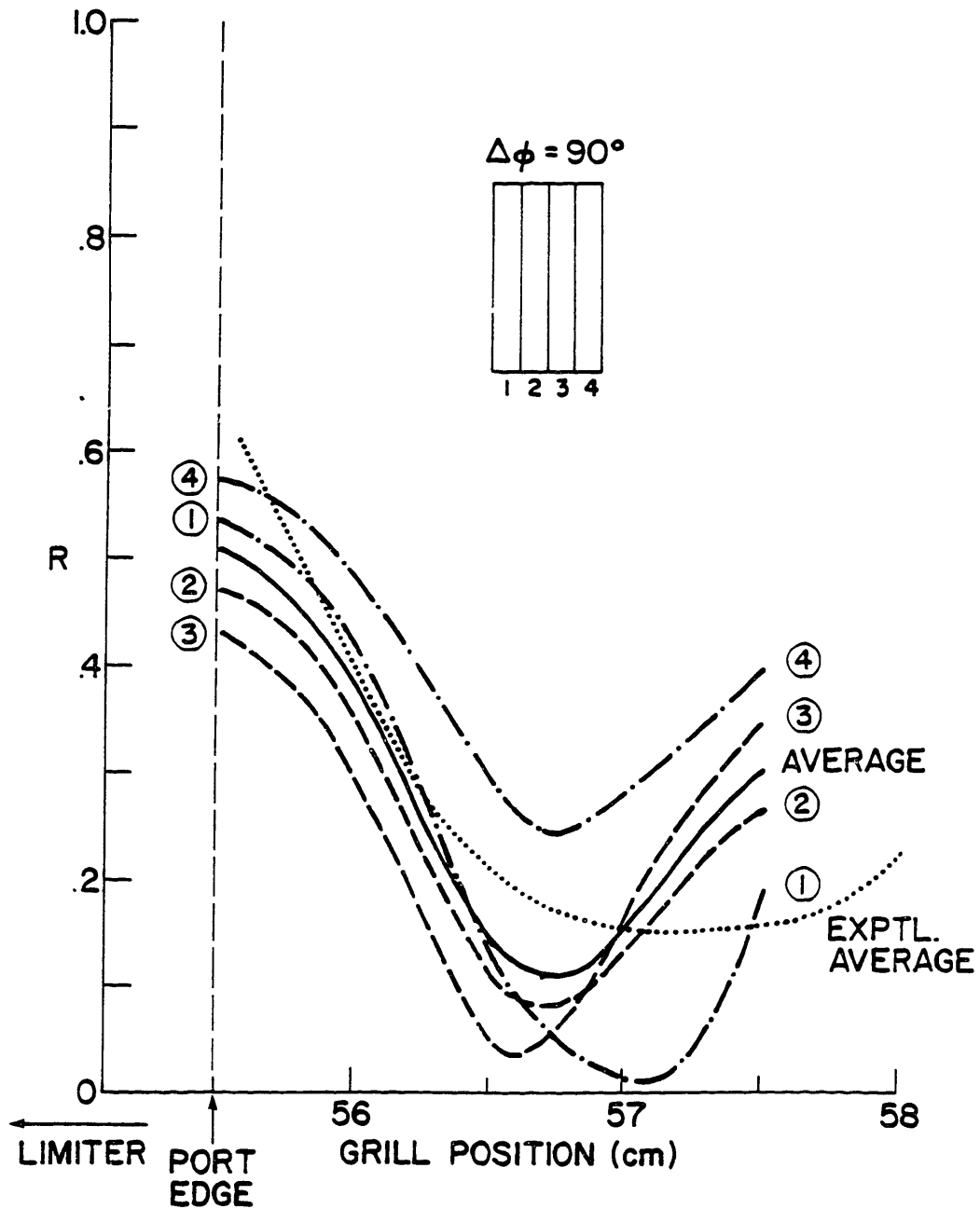


Figure 5.10. Calculated reflectivities for individual waveguides; $\Delta\phi = 90^\circ$. The measured total reflectivity from the previous figure is shown with a dotted line.

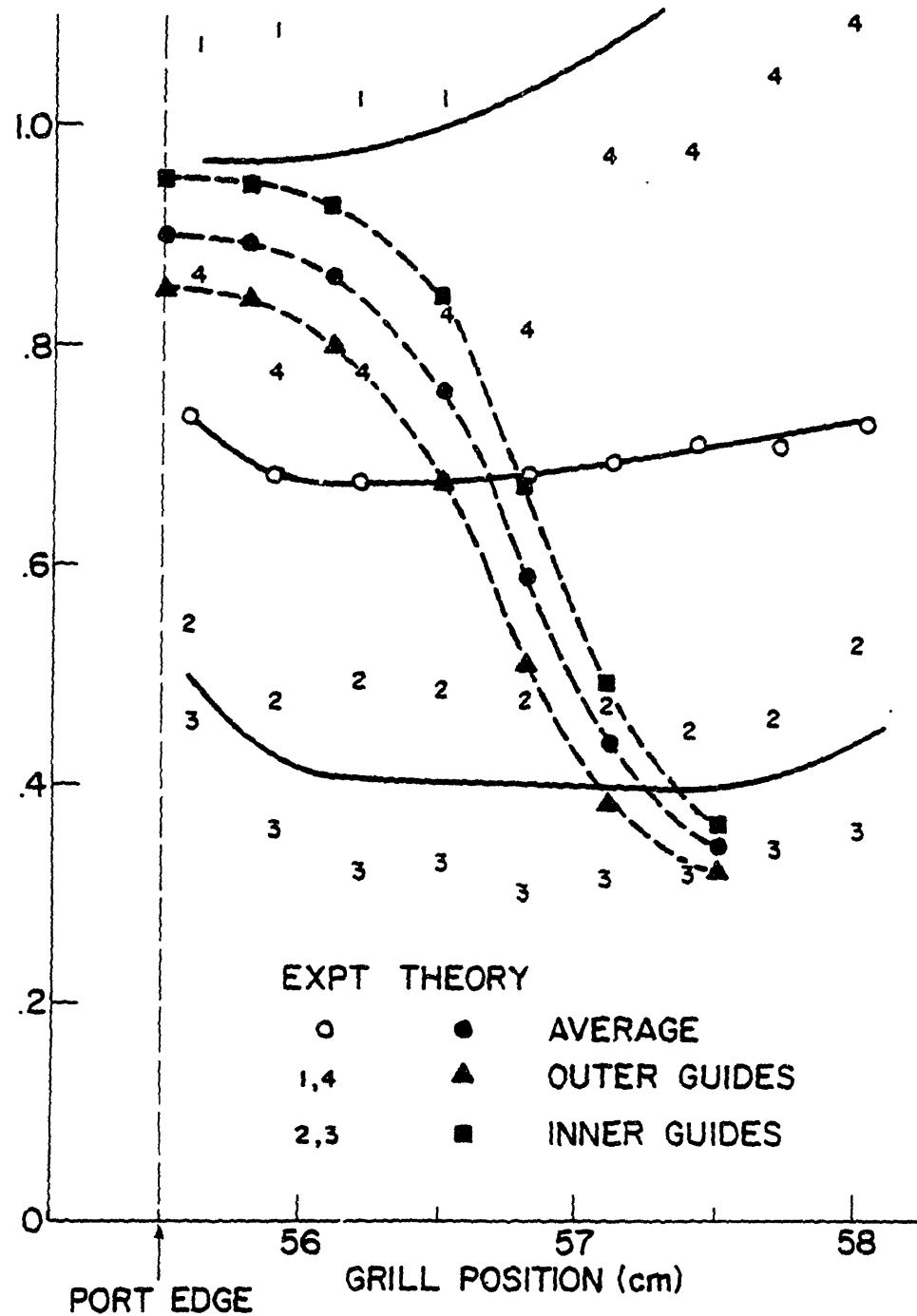


Figure 5.11. Comparison of experimental and individual guide reflectivities for $\Delta\phi = 0^\circ$. The calculated values are shown with dashed lines and solid symbols and the measured ones are shown with solid lines. Circles denote the total reflectivity. The calculated reflectivities of the inner waveguides are represented by squares, while those of the outer waveguides are represented by triangles. The measured reflectivities of individual guides are denoted by their guide number.

case consists largely of inaccessible surface waves, the coupling may be more affected by local port geometry than for the former phasing, possibly giving rise to more asymmetric coupling behavior.

The measured overall reflectivity as a function of phase angle for several different grill positions is plotted in Fig. 5.12. The results show the expected symmetry about $\Delta\phi = 0^\circ$, and indicate that good coupling ($R \leq 0.15$) can be achieved for $90^\circ \leq \Delta\phi \leq 180^\circ$.

The most likely reason for the observed differences between the calculations and the experimental values is the proximity of the port walls to the waveguide grill. Recall that the Brambilla theory assumes the waveguides to be imbedded in a conducting wall. The worst correspondence is seen for grill locations inside the port. It is expected that reflections from the port wall could modify the coupling behavior. In particular, the presence of a reflecting wall close to the outer guides is likely to enhance the reflectivity of the outer guides over the inner ones. However, it is unclear from this simple explanation why the overall reflectivity of the grill for $\Delta\phi = 90^\circ$ and 180° would be lower than calculated, as is the case of the experimental values.

The lack of agreement is most severe for $\Delta\phi = 0^\circ$, which suggests that the lower n_{\parallel} values are more affected by considerations of local geometry and fast wave coupling than the higher ones. It is conceivable that the poorer correspondence between theory and experiment for this phasing as opposed to $\Delta\phi = 180^\circ$ and 90° is indicative of the problem of fast wave coupling to waves of low n_{\parallel} discussed in Chapter 3. We recall that the Brambilla theory for slow wave coupling is not strictly applicable to waves with values of n_{\parallel} near 1; hence it is not surprising that the coupling predictions for this phase do not agree with the experimental results. Moreover, waves with $n_{\parallel} < 1$ are evanescent in the plasma for $\omega_{pe} > \omega$; however, near the edge where $\omega_{pe} = \omega$, the coupling of such waves to the surface plasma may be strongly influenced by the details of the launching structure and its environs.

The calculated n_{\parallel} power spectra of the side-launching four-waveguide grill has been shown in Fig. 3.3 for $\Delta\phi = 0^\circ, 90^\circ, \text{ and } 180^\circ$. An experiment was considered in which the n_{\parallel} spectrum would be measured interferometrically with the use of a pair of movable rf probes in front of the grill mouth; however, the dominant n_{\perp} contribution to the wave number ($n_{\perp} \approx (\omega_{pe}/\omega)n_{\parallel} \geq n_{\parallel}$ near the plasma edge) makes a reliable determination of n_{\parallel} very difficult, and the idea was dropped. Consequently, no direct measurement of the launched n_{\parallel} spectrum has been made to compare with the above predictions. As the n_{\parallel} spectrum is largely determined by the relative phasing of the grill and only to a lesser extent by the coupling efficiency, we conclude nonetheless that the launched spectrum must be similar to the calculated one, especially for the higher phase angles for which qualitative agreement between the experimental and theoretical reflectivities is relatively good.

In summary, it is evident that the coupling model developed by Brambilla and modified by the inclusion of more realistic edge plasma conditions, provides an adequate description of

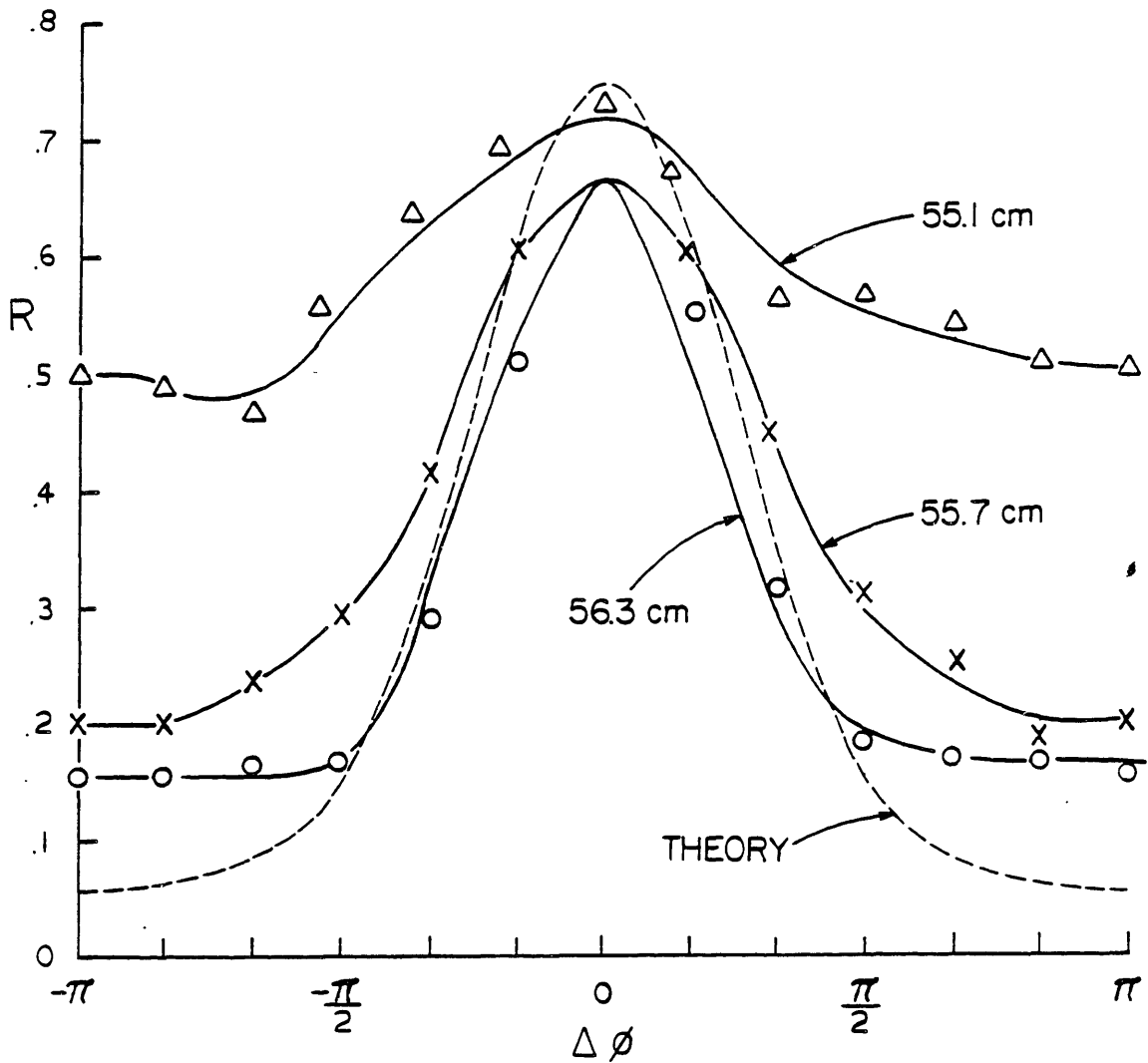


Figure 5.12. Measured grill reflectivity versus phase angle between waveguides for several different grill positions. Also displayed is the calculated grill reflectivity for $\mu = 10$, $\nabla n = 5.3 \times 10^{11}$ cm^{-1} .

the actual coupling results in which the launched power spectrum is characterized by $n_{\parallel} \gg 1$. There is little agreement, however, between the predicted coupling and the experimental results when the grill is retracted well into the port where indeed the theory is not expected to be valid. In addition, we note that measurements of the edge density, which are critical to quantitative comparisons between theory and experiment, were not unambiguous because of the choice of the model for reducing the Langmuir probe data. Nonetheless, the experimental data reproduce the basic features of the theory in that an optimal coupling position was found to exist and that the optimal coupling location varied in the expected manner with $\Delta\phi$. Within uncertainties imposed by the density measurements, the location and magnitude of the measured reflectivity minima are well predicted by the model.

Because the coupling for different phase angles is explicable by the model, we have confidence that the calculated power spectrum also represents the launched spectrum fairly. The achievement of efficient coupling ($R < 0.15$) in these initial experiments at low power levels is a prerequisite to high power heating studies. The other requirement for this end is the reliable operation of the antenna at high levels of incident power, which is the subject of the remainder of this chapter.

5.3. High Power Operation of the Grill

Although good rf coupling was obtained at low incident rf power, the coupling efficiency, in general, was not maintained as the rf power was raised into the multi-kilowatt range. Rf breakdown in the evacuated portion of the grill, occurring in several different forms, was found to be responsible for the high power coupling results. The breakdown is detrimental to the transmissivity of the grill and sometimes damages the antenna itself. Such problems appear to be endemic to waveguide couplers in which all or part of the antenna is open to the vacuum chamber, which must be the case unless the vacuum window seals are made near the mouth of the waveguides. Other experiments have reported similar difficulties with their antennas,^{31,38,117,118} and the elimination of these breakdown problems is a major concern for most experimental projects in this field.

In the Versator antenna systems, two types of breakdown are distinguished. The first is characterized by sudden ($\Delta t \lesssim 10 \mu\text{sec}$) changes, usually increases, in individual waveguide reflectivities. This breakdown is associated with arcing in the waveguides: either a series arc between two sections of a waveguide wall which have a poor electrical contact between them, as in the joint between the nosepiece and transition coupler; or more commonly an arc across the waveguide or coaxial transition pieces. On the first grill with the teflon window, the arcing occurred across the window itself at a power level of 15–20 kW per guide, coating the window with metal. In the later antenna systems, arcing often took place between the inner and outer conductors of the coaxial transitions in which the average power density is approximately six times that in the waveguide. The initial fabrication of these pieces in which a commercial window assembly is welded to a standard vacuum flange left a groove approximately 1.5 mm. wide and several mm.

deep in the inner surface of the outer conductor. Examination of subsequently-formed arc tracks showed that arcing was initiated at these grooves. Blackening of the ceramic windows, presumably due to metallic deposits, was often noted after substantial arcing had occurred; however, gentle sandblasting of the window surface could remove these deposits with no apparent degradation of the high power performance of the windows. Midway through the heating experiments, the outer conductors of the transition pieces were rebuilt to eliminate the grooves. Furthermore, a more reliable arc detector was constructed to better protect the antenna system in the event of a fault. With these improvements, arcing was eliminated.

The more common occurrences of breakdown are related to plasma formation within the evacuated waveguides, both during operation into vacuum and the tokamak plasma. Unlike arcs, the plasma generated during the rf pulse does not damage the antenna; however, power transmission of the grill is reduced by the presence of this waveguide plasma. Furthermore, the formation of this plasma is difficult to eliminate. As a result, it constituted one of the major obstacles of the experiment. The rest of this chapter discusses this problem and its solution.

The formation of plasma in the waveguides is inferred from the variation in the reflected power and phase during the rf pulse.¹¹⁹ The grill is processed in vacuum ($P \leq 5 \times 10^{-7}$ Torr) with short rf pulses; pulse durations of 0.5 ms. and repetition rates of one per second are typically used. For a newly-installed grill, conditioning effects become apparent at a total incident power level of about 10 kW ($E_z(\text{peak}) \simeq 300$ V/cm). The reflected power pulses are observed to change over a several hundred microsecond time scale; shifts in the reflected phase on the order of 180° also take place. Gas is evolved during these pulses. These effects usually disappear after sufficient conditioning, and the power may be incrementally raised until the problem recurs, whereupon the process is repeated until the maximum available incident power of about 110 kW is reached. The conditioning time required is considerably reduced by vacuum-baking the grill for 8 hours at 400° C (higher temperatures may stress fabricated antenna components). After such heat treating and installation of the baked grill on the tokamak, processing to the 100 kW level necessitates only 10–15 hours, while previous conditioning of the unbaked waveguides for well over 40 hours had not sufficiently prepared the surfaces to permit operation at this power level. The vacuum baking releases gases absorbed in the surface of the stainless steel waveguides which must otherwise outgas in the tokamak at lower temperatures. The baking temperature must be sufficiently high to significantly reduce the gas load. Heating the emplaced grill on the tokamak to 150° C with heater tapes has little effect on the conditioning behavior.

The performance of the antenna when operating into vacuum, as measured by the power level at which reflected phase shifts are noted, is altered with the ambient neutral gas pressure and applied magnetic fields. Figure 5.13 shows the incident rf power that can be attained without phase shift as a function of neutral hydrogen fill pressure. At a fill pressure of 10^{-4} Torr, the rf power is reduced by 30% relative to that achieved at 3.6×10^{-6} Torr. As shown in Fig. 5.14, the presence

of small magnetic fields in the grill is also leads to plasma formation at power thresholds below the unmagnetized case. A magnetic field with a strength near or below the cyclotron resonant value of 286 gauss is generated by passing a small current through the toroidal field coils. The orientation of this field is parallel to the rf electric field in the guide. The threshold for rf breakdown decreases with increasing field; for a field of 300 gauss at the waveguide mouth, the allowable power level is 25% below that obtained with no field.

Nonetheless, with sufficient conditioning in vacuum, the antenna may be processed up to the available power limit of approximately 110 kW ($E_z(\text{peak}) = 1.1 \text{ kV/cm}$). However, when rf power is applied to the magnetically-confined tokamak plasma, rf breakdown recurs at power levels much lower than that reached in vacuum conditioning. Above a typical total incident power level of 30 kW, reflected phase shifts occur in all four waveguides. Shown in Fig. 5.15 is the reflected phase shift and the total reflected power versus incident power in one of the waveguides. The phase shifts in the negative direction during the first several hundred microseconds of the rf pulse and reaches a steady state for the remainder of the pulse. The amount of phase shift increases with increasing power above the threshold level. Concurrently, the overall antenna reflectivity decreases during the rf pulse. At an incident power level of 57 kW, the grill reflectivity is reduced to 55% of its low power value, and the net reflected phase shift is -230° . Above this power level, the reflected power pulses become very irregular and phase shifts can no longer be measured.

As mentioned earlier, the phase shift and reflectivity changes are attributed to plasma formed in the waveguides. If the entire measured phase shift is due to the dielectric effect of the plasma created in the waveguide, and if the plasma forms along the entire length of the waveguide, then the plasma density inferred from the phase shift measurement is $1 \times 10^9 \text{ cm.}^{-3}$ for an incident power level of 57 kW. This density is close to the waveguide cutoff density of $3 \times 10^9 \text{ cm.}^{-3}$. Though the antenna reflectivity typically decreases with the onset of plasma formation, the transmissivity of the grill apparently decreases as well. The power detected by rf probes in the edge plasma show decreases of 1–3 dB over the pulse duration at power levels above the threshold for plasma formation. In an experiment in which rf power was fed into a single waveguide, the fraction of incident power coupled to an adjacent waveguide was observed to decrease with increasing power above the threshold level as depicted in Fig. 5.16. Typically, measured transmissivity reductions of 50–60% were obtained for an rf power of 20 kW/guide, in rough agreement with the probe measurements (the coupling and probe measurements were performed with different grills, however). Moreover, the effect of the rf on the tokamak plasma, as determined by the temperature for the fast ion tail generated by the rf, diminishes with increasing rf power above the threshold for plasma formation. Apparently, rf power is absorbed in the waveguide plasma, making this breakdown phenomenon deleterious to the rf heating efficiency.

5.4. Interpretation of the Rf Breakdown Problem

The plasma formation during the rf pulse is believed to arise from electron-stimulated

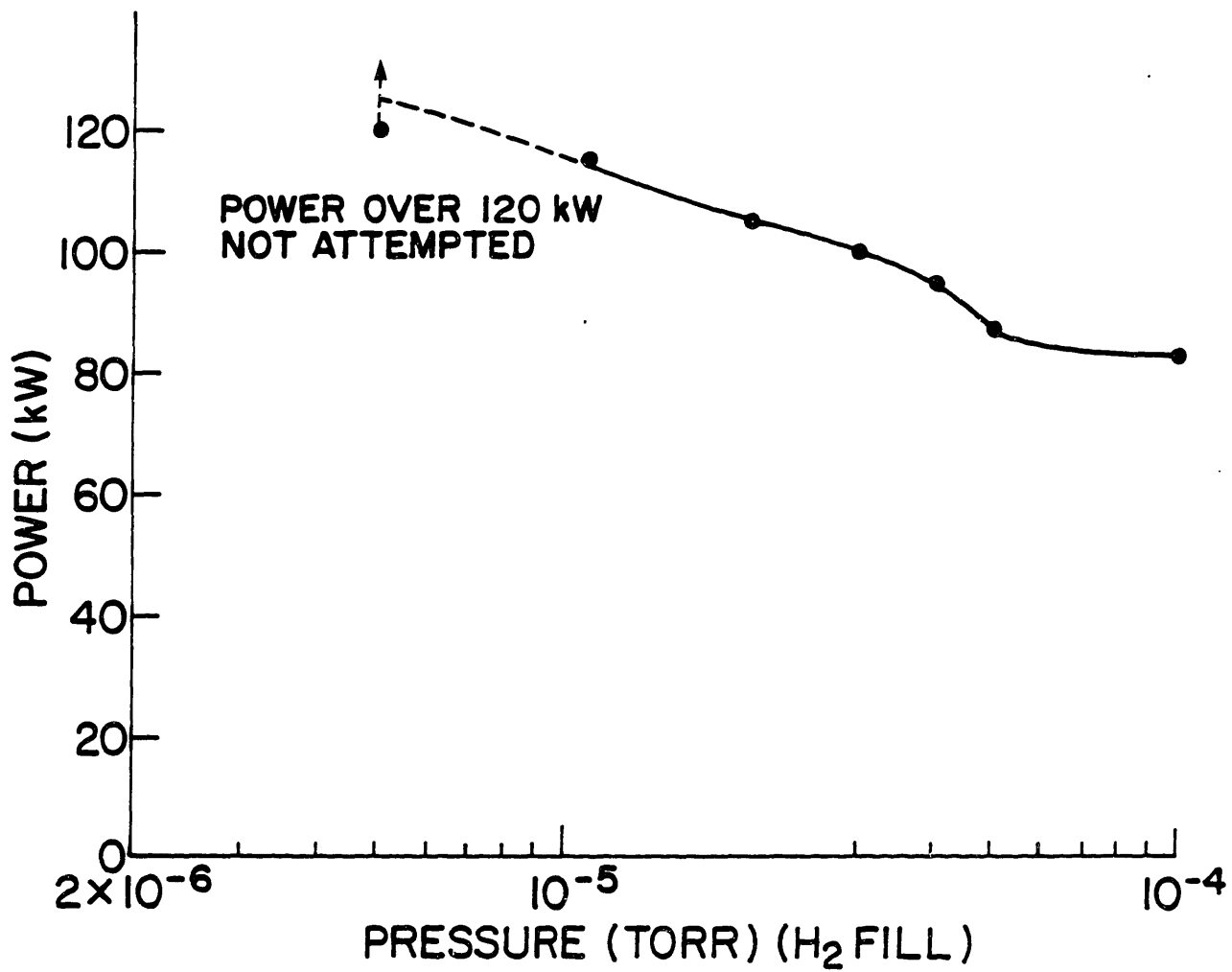


Figure 5.13. Maximum rf power achievable without breakdown versus neutral hydrogen fill pressure.

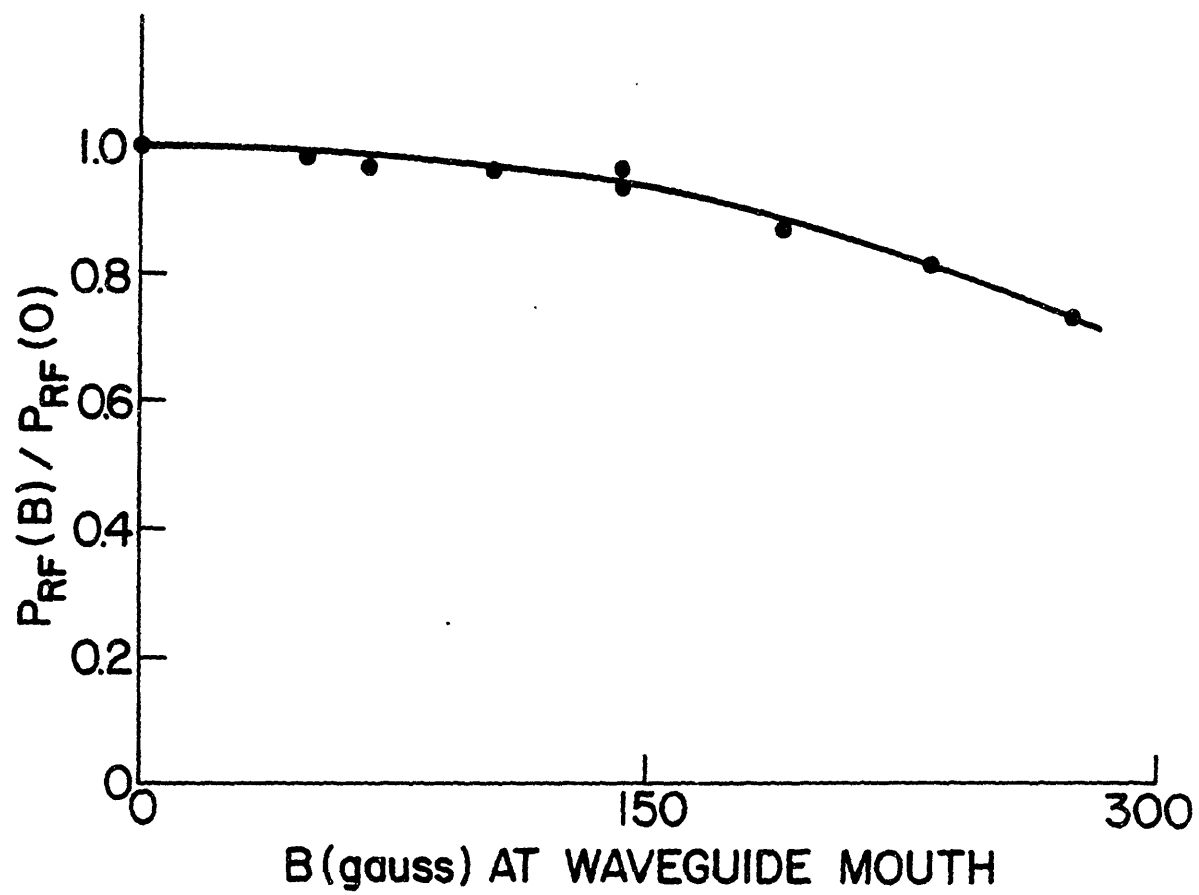


Figure 5.14. Maximum rf power achievable *in vacuo* versus applied magnetic field at the grill mouth.

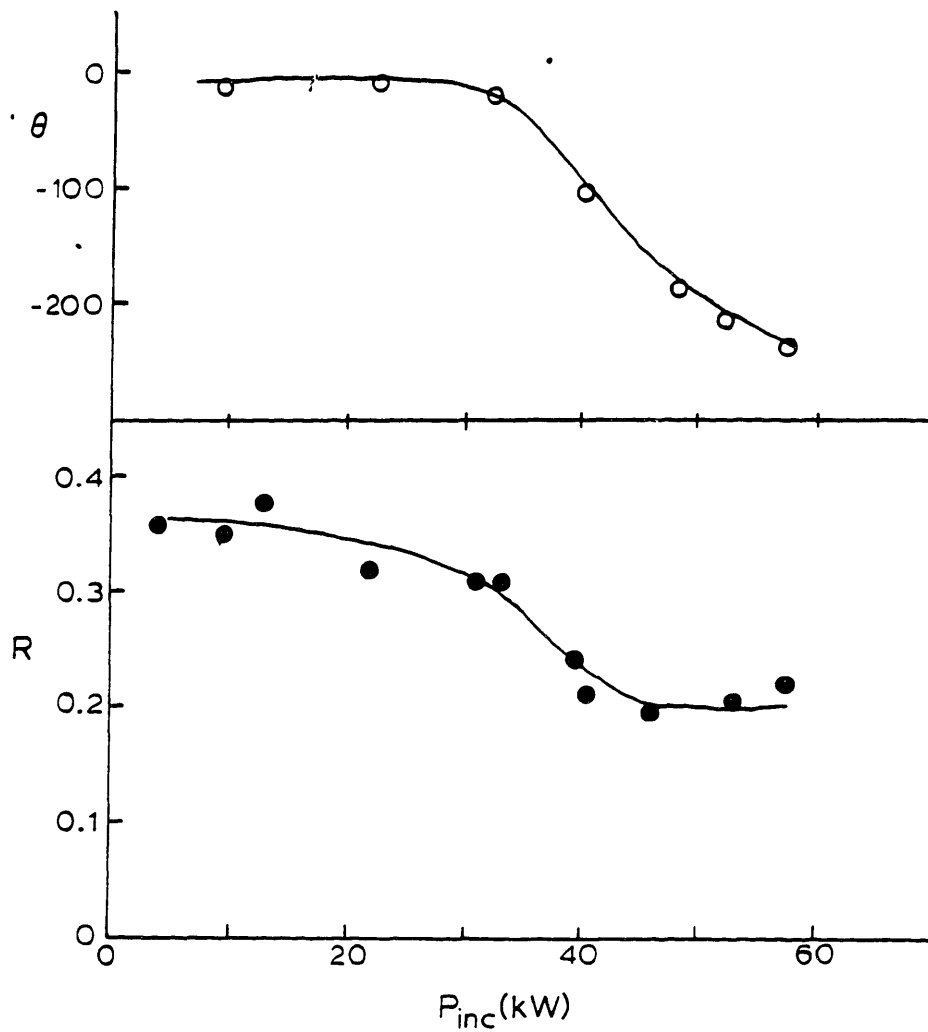


Figure 5.15. Reflected phase shift and grill reflectivity versus incident power for rf injection into a tokamak plasma.

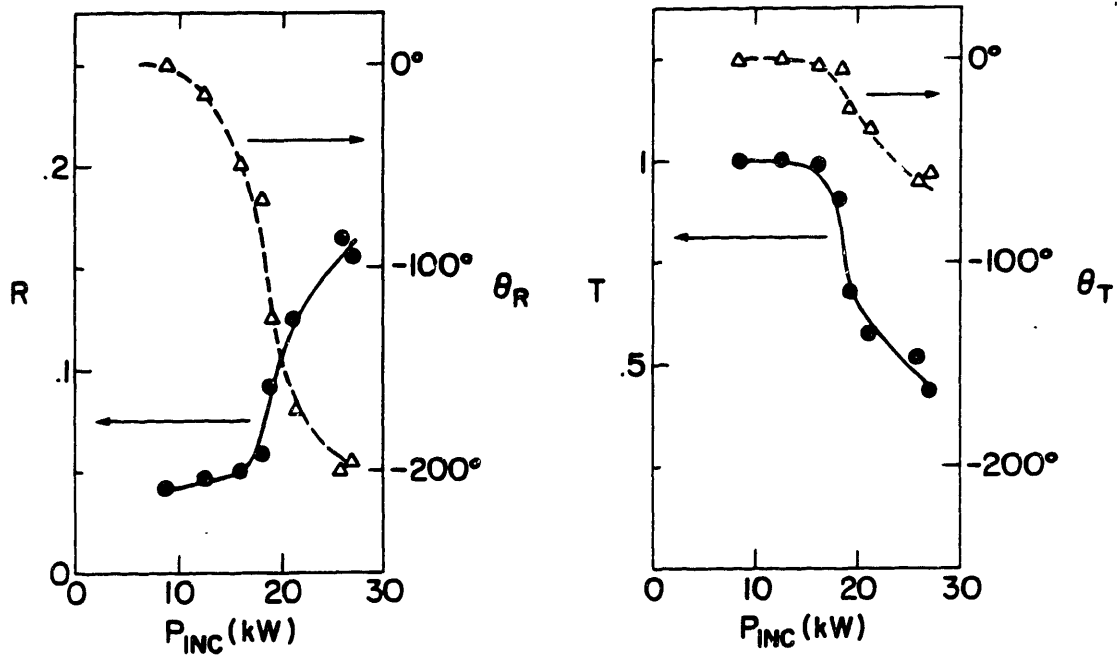


Figure 5.16. Single waveguide breakdown test. The left-hand figure shows the reflection coefficient and phase shift in the fed waveguide; the right-hand figure depicts the transmissivity and phase shift of the transmitted power as measured by the rf power coupled into the adjacent guides.

desorption (ESD) of contaminants on the waveguide walls. Contributing effects are electron multiplication via secondary electron emission (SEE) and ionization of the residual neutral gas in the waveguides. During rf injection into the tokamak plasma, the presence of electron cyclotron resonance in the guides enhances the plasma formation because electrons gain energy above their maximum rf oscillatory energy, increasing the magnitude of both SEE and ESD.

The source of electrons to initiate the breakdown is the waveguide wall. If the secondary electron emission (δ) coefficient of the wall is greater than one, as is usually the case for most metals without extensive surface cleaning, electron multiplication will occur as electrons accelerated in the electric field strike the wall with a maximum energy

$$\mathcal{E}_i = \frac{e^2 E_{rf}^2}{2m\omega^2} \quad (5.4)$$

or about 1.4 eV/kW-guide for the Versator four-waveguide side-launching grill. This does not include the effect of the magnetic field, which will be discussed shortly. As the secondary electron emission coefficient is an increasing function of electron impact energy up to 400–500 eV for all impact angles relative to the waveguide surface,¹²⁰ SEE increases with incident power for the entire range of rf power available in this experiment. The electric field threshold at which electron loading effects begin may be determined by the multipactor phenomenon.¹²¹ The multipactor process requires the existence a secondary electron emission coefficient greater than one and resonant electron trajectories; that is, secondary electrons that are emitted with the proper phase relationship to the rf field such that they strike the opposite wall with their maximum oscillatory velocity. Multipacting modes are characterized by the number of half-cycles completed by an electron in the rf field before impact. The fundamental 1/2 cycle mode has been experimentally identified in early multipactor work,¹²² while higher order modes are not clearly delineated as such. The breakdown field in these experiments was dependent on wall cleanliness, and higher mode structure was not always identifiable. For the Versator four-waveguide grill, the onset of resonant multipactor is predicted to occur at an electric field of 300 V/cm, or about 2 kW/guide¹²¹, and should represent a high order ($> 11/2$) mode. Indeed, reflected phase shifts are observed at or near this power level when a new grill is conditioned in vacuum; however, the phase shifts disappear with continued processing, and the rf power may be raised. The phase shift does not exhibit apparent mode structure as a function of power. In general, above the threshold for plasma formation, the phase shift increases monotonically with power. For our frequency and grill width, however, the theoretical multipactor modes overlap, and one would not expect mode structure in the data even if high order resonant multipactor is present. Nonetheless, since the rf power level may be safely raised above the low threshold for breakdown predicted by multipactor theory, either the multipacting limit is raised by the reduction of the SEE coefficient because of rf conditioning, or multipacting alone is not responsible for the observed plasma formation. Though the former is likely to be true, as will be argued shortly, the latter is also plausible since the measured electron

densities in the waveguides are higher than what one would expect if the density is limited by space-charge effects, i.e., if the electron plasma created by electron multiplication is not neutralized by the presence of ions. If an electrostatic field in the guide is calculated under the assumption of constant electron density,¹¹⁸ then resonant multipactor is inhibited for an electron density of

$$n_e \simeq \frac{E_{rf}^2}{\pi m \omega^2 b^2}, \quad (5.5)$$

or $n_e \simeq 1 \times 10^6 \text{ cm.}^{-3} \times P_{rf}(\text{kW/guide})$.

This estimate is derived by calculating the energy a secondary electron requires to reach the center of the waveguide assuming its maximum energy is its oscillatory energy in the rf electric field. For typical powers of 10–20 kW per guide, the space-charge limited density is much lower than the measured density, either during vacuum conditioning or injection into the tokamak plasma. Multipactor effects, or more generally electron multiplication via the secondary electron emission process, are most likely responsible for initiating this discharge, but the magnitude of the observed plasma formation is higher than can be explained by resonant multipactor alone. Ionization of neutral gas, either on the guide wall or in the guides themselves, must be invoked to explain the measured plasma densities in the waveguides. We recall that the breakdown electric field is lowered by increasing the neutral gas fill pressure, suggesting that ionization of neutrals is the dominant source of the plasma. At the highest fill pressure, the electron-neutral collision length ($\gtrsim 100 \text{ cm.}$) is much larger than the guide width, making direct ionization of the gas unlikely. However, earlier studies have produced evidence of similar rf discharges, or plasmoids, in which the electron-neutral collision length is much larger than the dimension of the cavity.¹²¹ Plasmoids in cavities have been shown to attenuate rf power levels by 10–20 dB,¹²¹ and may be responsible for the similar phenomena observed in our waveguides.

With regard to the noted effectiveness of baking the grill prior to its installation on the tokamak, it is well known that vacuum-baking of metals generally reduces the source of the gas which is believed to give rise to plasma formation. As a result, the ESD efficiency of such heat-treated metals is decreased. In particular, the drop in ESD efficiency is strongly dependent on the bakeout temperature: the ESD coefficient for hydrogen is reduced more than an order of magnitude by a 400° C bakeout compared to a 150° C bake or no heat treatment at all.¹²³ Qualitatively, our conditioning results following vacuum-baking are in agreement with this data.

We turn now to a discussion of the source of this gas and the beneficial effect of rf conditioning. According to surface physics studies, the improvement in high power operation with rf processing is believed to result from polymerization of a hydrocarbon layer on the metallic surface of the waveguides.^{124–126} The hydrocarbons may come from pump oil residue and gases desorbed from the tokamak wall by discharge cleaning. We note that the partial pressures of water vapor and methane are observed to increase to several times their initial value during discharge cleaning. Electron impact during rf conditioning is known to desorb hydrogen gas and hydrogen

ions from this hydrocarbon layer to leave a several monolayer thick carbon polymer residue with unsaturated bonds. At impact energies near 100 eV, typical for rf conditioning, electrons are inefficient in desorbing contaminants other than hydrogen;¹²⁷ thus rf processing is not believed to cleanse the waveguide surface of all contaminants (metallic oxides, water vapor, and hydrocarbons) so as to leave a relatively pure metal surface. Rather, the carbon polymer surface produced by rf conditioning provides a high cross-section for absorption of the kinetic energy of secondary electrons emitted from the metal and contaminant gases underneath the layer. Up to 50% of the secondary electrons from the metal are possibly absorbed in the polymer.¹²⁶ At temperatures of 300° K, however, the polymer is known to be unstable. Exposure to air or other contaminants can destroy the polymer structure of the layer, necessitating reconditioning.

Our observations are also consistent with this picture. During rf conditioning of the Versator grill, hydrogen gas is evolved,¹²⁸ as measured by residual gas analysis. Moreover, we also note that extensive conditioning must be repeated following vacuum breaks. In addition, the "clean" grill must be processed for approximately one hour prior to high power experimental runs, indicating that some of the effect of earlier conditioning is lost after many hours. We remark that whatever additional procedures are used, rf conditioning remains a necessary prerequisite to reliable high power antenna operation, suggesting that polymerization of the waveguide surface is the most important requirement for reduction of rf breakdown in the waveguides.

The lower breakdown threshold observed when injecting rf into the tokamak plasma is largely attributed to the effect of the tokamak magnetic field in the waveguide. In particular, the cyclotron resonance region is present in the evacuated portion of the waveguide, located approximately 45 cm. from the outboard wall of the tokamak. The magnetic field, calculated from the currents in the magnets and from the plasma current, is oriented mostly parallel to the rf electric field in the 40 cm. length of guide closest to the plasma and is mostly perpendicular (in the vertical direction) to the rf field at larger major radii within the antenna. At cyclotron resonance, the angle between the magnetic and electric fields is approximately 10°.

Cyclotron resonance may be expected to have a detrimental effect on rf power transmission. At or near the resonance, electrons will gain energy at the expense of the rf electric field. The power absorbed per unit volume is

$$P = \frac{\nu \omega_{pe}^2}{8\pi \omega^2} \left[E_z^2 \left(\frac{\omega^2}{\omega^2 + \nu^2} \right) + \frac{1}{2} E_{\perp}^2 \left(\frac{\omega^2}{(\omega - \omega_{ce})^2 + \nu^2} + \frac{\omega^2}{(\omega + \omega_{ce})^2 + \nu^2} \right) \right], \quad (5.6)$$

where E_z and E_{\perp} are the components of the rf electric field parallel and perpendicular to the local magnetic field, and ν is the electron-wall collision frequency (this being the largest collision frequency). The average energy with which an electron strikes the wall is

$$\mathcal{E}_c = \frac{e^2 E^2}{2m\omega^2} \left[\frac{\cos^2 \alpha}{(1 + \nu^2/\omega^2)} + \frac{\sin^2 \alpha}{2} \left(\frac{1}{(1 - \omega_{ce}/\omega)^2 + \nu^2/\omega^2} + \frac{1}{(1 + \omega_{ce}/\omega)^2 + \nu^2/\omega^2} \right) \right] \quad (5.7)$$

where α is the angle between the electric and magnetic fields. In Fig. 5.17 is plotted the calculated impact energy versus ω_{ce}/ω for our grill parameters assuming an incident power of 10 kW/guide. The impact energies for two angles (10° and 90°) are plotted for a plausible electron-wall collision frequency of $5 \times 10^7 \text{ sec}^{-1}$ which represents a 4 eV drift energy (typical energy for SEE) for an electron traversing the waveguide width. The calculated impact energy is increased by orders of magnitude due to cyclotron resonance, though of course this value is strongly dependent on the assumed collision frequency. To confirm that larger electron impact energies should give rise to increases in the amount of SEE and ESD, the processes believed responsible for plasma formation, we reproduce from the literature the measured SEE coefficient and ESD efficiency as a function of electron impact energy. Shown in Fig. 5.18, both quantities are increasing functions of energy over the range in which we are interested for this experiment, indicating that rf breakdown should indeed be more pronounced for the higher electron impact energies near cyclotron resonance.

We can estimate the power absorbed in the waveguide by evaluating Eq. (5.6) with the above collision frequency and assuming the plasma density in the waveguides to be a constant and equal to $n_e = 1 \times 10^9 \text{ cm}^{-3}$ as given by the phase shift measurement described earlier. For $P_{rf} = 57 \text{ kW}$, we have $E_z = 540 \text{ V/cm}$, and we calculate an absorbed power of approximately 2 kW, where we have taken the resonance layer to extend 4 cm. in the radial, or x -direction. This estimate is an order of magnitude lower than the power needed to explain the observed drop in the transmissivity of the grill. The discrepancy may result from the assumed value of the collision frequency ν , which has been chosen somewhat arbitrarily. We have also assumed the plasma density to be uniform inside the waveguides; in fact, it is likely to be highest near the resonant layer, where the local power absorption rate is a maximum. In short, it appears plausible that a significant fraction of the incident power could be absorbed in the waveguide plasma, though because of the uncertainties involved in the the estimate, this claim cannot be conclusively verified.

Off-resonance magnetic fields may also affect the high power operation of the waveguides. As shown earlier, a small ($\omega_{ce} < \omega$) magnetic field oriented parallel to the electric field reduces the threshold electric field for breakdown in vacuum. In this case, the magnetic field serves to confine the electron along its parallel trajectory, enhancing the usual resonant multipactor effect by reducing the electron loss rate (the rate at which electrons drift up or down out of the region of maximum electric field). Perpendicular magnetic fields could also lead to enhanced plasma formation. The component of the field perpendicular to the rf electric field will cause the electrons to strike the wall at an angle off the normal, which also significantly increases the secondary electron yield (see Fig. 5.18). On the other hand, perpendicular magnetic fields may serve to reduce plasma formation by altering the electron trajectories to make the requirements for resonant

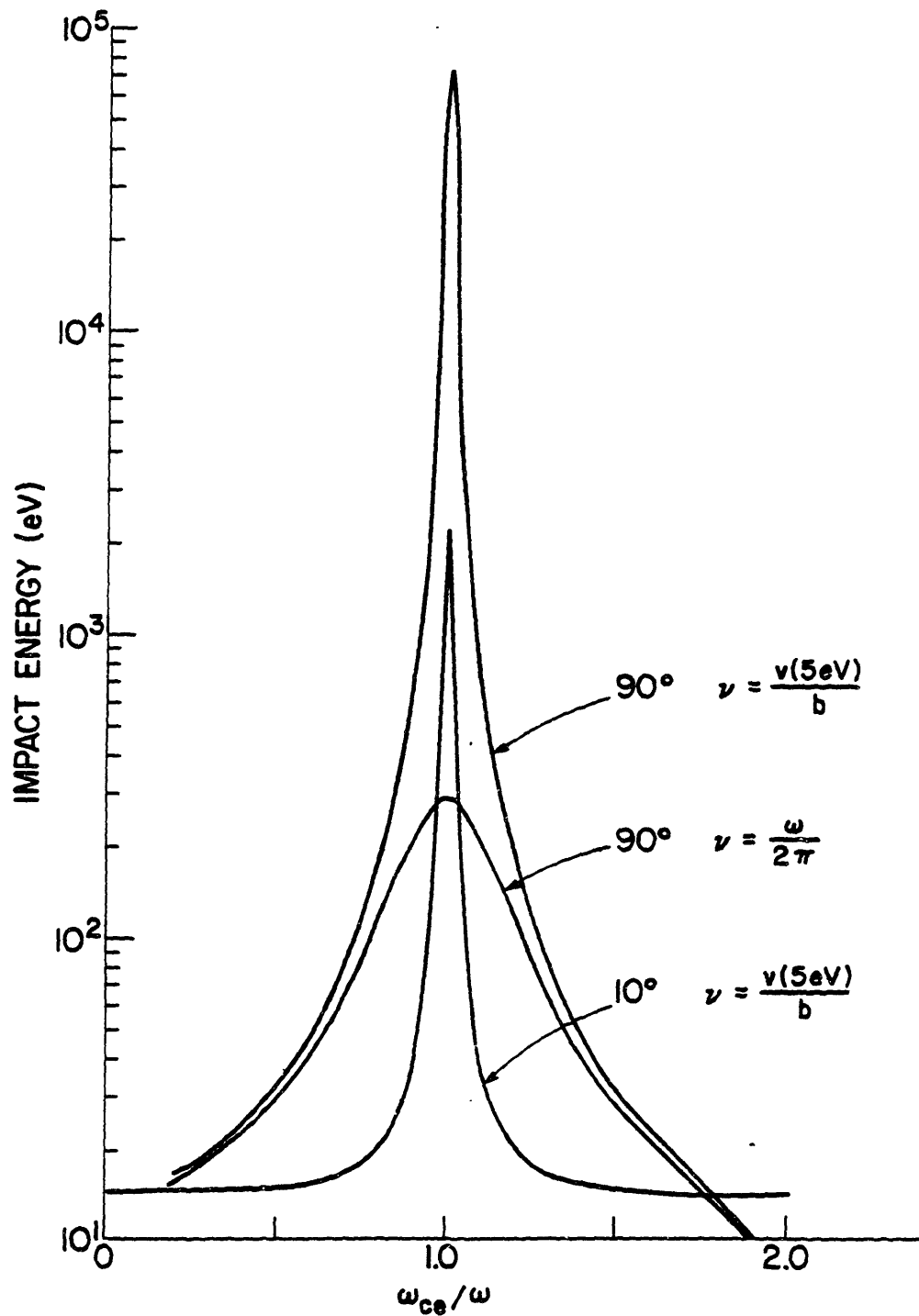


Figure 5.17. Calculated electron impact energy versus magnetic field. The angles indicated are those between the magnetic field and the rf electric field. The impact energy for two nominal electron-wall collision frequencies are also depicted.

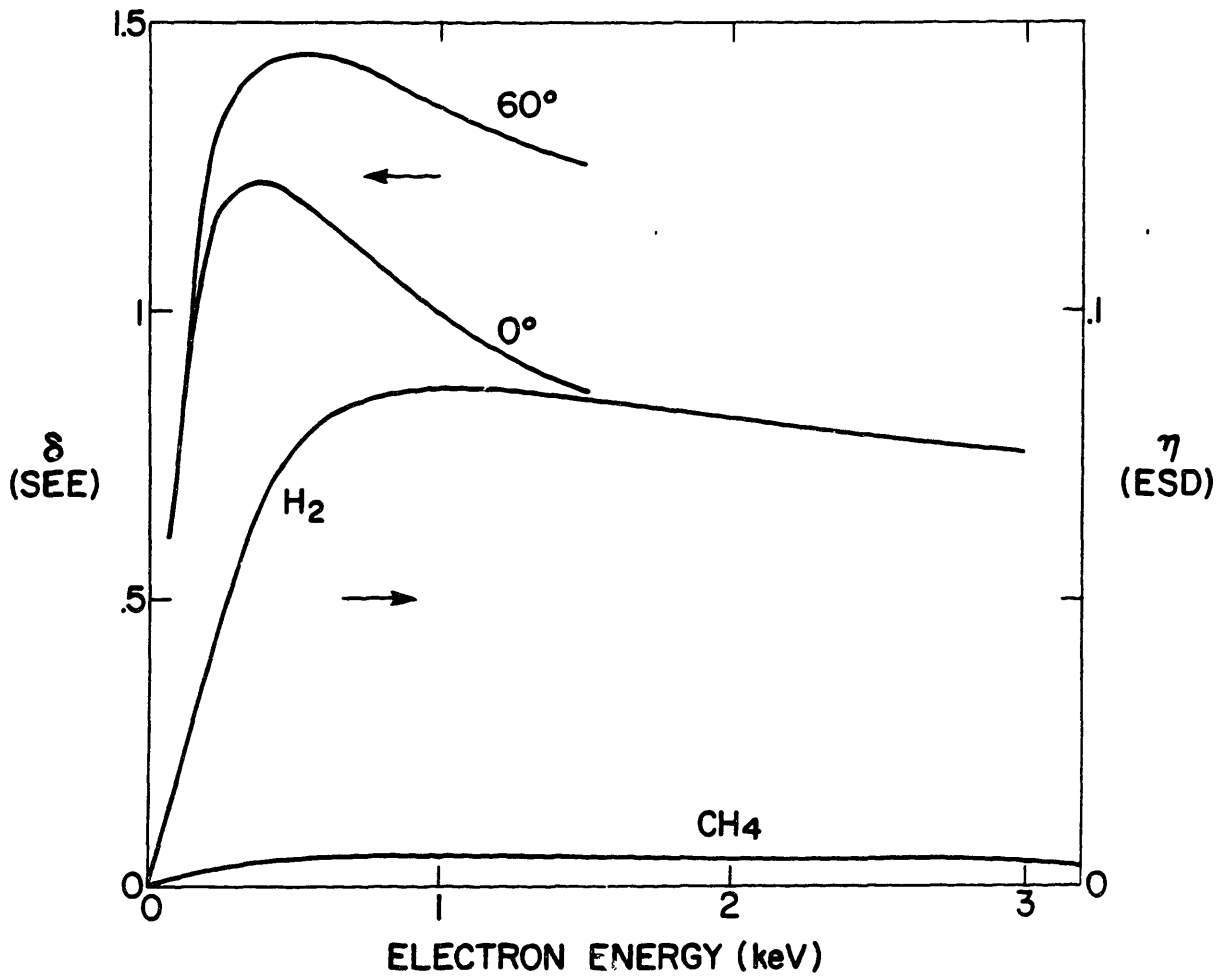


Figure 5.18. SEE coefficient for two angles of incidence on stainless steel cleaned by argon sputtering¹²⁰, and ESD coefficient for hydrogen and methane on stainless steel vacuum-baked at 325° C¹²³.

multipactor more severe,¹²⁹ and by preventing charged particle drift across the waveguide. The size of the Larmor orbit in the direction parallel to the electric field is

$$\rho_{\parallel} = \frac{eE_{\perp}}{m(\omega_{ce}^2 - \omega^2)} \left(\frac{\omega}{\omega_{ce}} \right). \quad (5.8)$$

Above a field of 15 gauss for an rf power of 10 kW/guide, the average electron orbit will not span the waveguide unless the field is near cyclotron resonance. For magnetic fields higher than the above threshold, the plasma will be restricted to the region near the waveguide walls. In the Versator grill, the cyclotron resonant layer is in a region in which the electric and magnetic fields are nearly parallel, hence this postulated confinement effect is not applicable at that location where breakdown should be most severe.

We conclude that electron multiplication by SEE provides a source of electrons which generates free hydrogen gas and ions from the surface hydrocarbon layer by ESD. This layer becomes polymerized by this desorption process and is absorbent to secondary electrons escaping from the metal, lowering the overall secondary electron emission coefficient below one and halting plasma formation. Breakdown occurs at lower incident power levels when rf is launched into plasma because cyclotron resonance has the effect of increasing the energy with which an electron strikes the wall. Also, electron trajectories in the magnetic field can intersect the wall at a grazing angle for which the secondary emission coefficient is higher than for normal incidence.

5.5. Improvements in Antenna Performance

Attempts to reduce rf breakdown in the guides during the more severe electron loading conditions of tokamak operation proceeded along two lines: reducing the secondary electron emission coefficient of the wall surface to below unity; and eliminating cyclotron resonance within the evacuated portion of the waveguide to reduce electron impact energies.

Reduction of the secondary electron emission coefficient was first tried by sublimating titanium on the waveguide mouth prior to tokamak shots. Pure titanium metal is known to have a secondary electron emission coefficient of less than one, and its application was hoped to be beneficial in reducing electron multiplication. However, the power threshold for plasma formation was only increased by 30% at most with the use of this method. Because the improvement was slight (possibly because titanium could not be deposited on the interior of the guides *in situ*) and the method was cumbersome, the procedure was discontinued. A solid titanium nosepiece was constructed for use on the four-waveguide top-launching antenna. Successful conditioning in vacuum was never achieved with this grill, and operation into plasma was also poor. We believe the titanium, well known as an efficient pump for many gases, was saturated with gas. This had the effect of raising the coefficient above one,¹³⁰ eliminating its potential benefits for our application.

Recently, the inner surfaces of the top-launching antenna (all stainless steel) were coated with carbon, again with the object of reducing the SEE coefficient. The method used was identical

to the one for the P.I.T grill,¹³¹ with the exception that the waveguide walls of the Versator antenna were not mechanically polished or electropolished prior to carbon coating. The procedure in our case consisted of the following: the waveguides were degreased using standard solvents, then filled with a 50/50 mixture of Glyptal and xylene. The xylene serves as a thinner for the Glyptal, a carbon-rich, electrically insulating varnish. The mixture was drained out, leaving a smooth coat of the varnish which was allowed to air-dry overnight. The coated antenna pieces were then vacuum-baked for one hour at 400° C to pyrolyze the coating. Measurements at PPPL of similar heat-treated coatings on stainless steel show the composition to be 96% carbon and its thickness to be approximately 300 Å. The measured values of the maximum SEE coefficient following argon sputter cleaning are $\delta_{max} = .88$ at an impact energy of 250 eV for normal incidence and $\delta_{max} = 1.4$ for 300 eV incident electrons for an impact angle of 60° from the normal¹²⁰. The corresponding values for stainless steel are, from the same reference, $\delta_{max} = 1.2$ at 375 eV for normal incidence and $\delta_{max} = 1.45$ at 460 eV for a 60° incidence angle. For most of the impact angles tested, the carbon surface exhibits lower SEE coefficients than the bare stainless steel, although the extensive sputter cleaning of the samples just prior to the measurements is not representative of the preparation the waveguide surfaces receive.

Following the carbon treatment, the Versator antenna was rf conditioned after emplacement on the tokamak. With approximately 20 hours of processing, incident rf power levels of up to 120 kW in vacuum were attained with no reflected phase shifts other than sudden, small (< 15°) shifts occurring at intermediate power for which we have no conclusive explanation as yet. After firing the rf into many tokamak discharges, during which breakdown was often observed, the incident rf power level could be raised to 120 kW, representing a peak electric field strength of 2.8 kV/cm. and an average power density of 1.4 kW/cm.² Due to the unusual location of the antenna atop the plasma column, the calculated ambient magnetic field is above the cyclotron resonant value almost everywhere in the evacuated portion of the waveguides. Curiously, the antenna operation was adversely affected by discharge cleaning of the tokamak. Following as little as 15 minutes of discharge cleaning, the threshold for rf breakdown is lowered to 5–8 kW. Up to 20 hours of reconditioning are required to regain the previously-obtained performance. Neither filling the chamber with hydrogen gas nor titanium gettering the tokamak was observed to have such a drastic effect on the grill operation. As with the case of the stainless steel side-launching antenna, recovery of high power performance following a vacuum break requires substantial rf processing; however, the dramatic negative effect of discharge cleaning appears to be peculiar to the carbonized grill. Nonetheless, when sufficiently conditioned, the carbon coating permits rf injection at the maximum power level presently available to this experiment.

The second general method, that of eliminating cyclotron resonance within the waveguides, was tested on the side-launching grill with the use of an auxiliary magnetic field generated by copper coils wrapped around the antenna structure so as to produce a predominantly vertical field in the region of the guides (see Fig. 5.19). This particular orientation was chosen so as to add

to the ambient vertical field due to the OH and VF magnets, and to provide possible magnetic insulation between the waveguides walls as discussed earlier. This auxiliary field coil was placed in series with the TF magnets, and the current varied either by changing the toroidal field current or by placing a water-cooled stainless steel shunt in parallel with the waveguide magnet.

The coupling results as a function of incident power are shown in Figs. 5.20 and 5.21 for several different values of the coil current. For a current of 14.6 kA, the calculated magnetic field (shown in Fig. 5.22) is 450 Gauss on the axis of the axis of the waveguide grill and is at least 25% above the cyclotron resonace value everywhere in the evacuated volume of the waveguide. The field is primarily toroidal (parallel to the rf electric field) near the waveguide mouth regardless of whether or not the auxiliary field is applied, and primarily vertical (perpendicular to the rf field) at larger major radii. For this current setting, the reflected phase exhibits no shift during the rf pulse and the reflectivity remains constant from 30 to 100 kW incident power. For lower waveguide coil currents, the magnetic field is less than or roughly equal to the cyclotron resonant value somewhere in the waveguide volume. In these cases, the reflected phase exhibits shifts above an incident power level of 30 kW, although the maximum phase shift is only 50° at an incident power of 75 kW. The phase shift is independent of magnetic field strength over the 35% variation of the magnetic field for these lower coil current experiments. The overall antenna reflectivity drops by 25% above the 30 kW threshold. In these four-waveguide tests, the maximum output of the rf source limits the incident power density to 0.42 kW/cm^2 . Consequently the rf system was modified to feed all the available rf power to one waveguide to determine at what power level, if any, the magnetic suppression of plasma formation fails. The results of the single-waveguide experiment are depicted in Fig. 5.23. For no current in the coil, breakdown occurred at an incident power level of 10 kW/guide. The higher power threshold for the onset of phase shifts in the single-waveguide experiments is explained by the higher reflection coefficient in that experiment. For a coil current of 25 kA (600 Gauss on the waveguide axis) up to 56 kW incident power (0.94 kW/cm^2) was injected with no significant change in the reflected phase or power. Above this level, arcing in the coaxial window section took place. As this problem is unrelated to plasma formation (it has since been corrected, as mentioned earlier), magnetic suppression of breakdown is likely to prove effective above a power density of 1 kW/cm^2 .

5.6. Discussion of Antenna Improvements

The presence of the auxiliary magnetic field clearly improves the power handling capability of the antenna. This improvement is accomplished by the reduction of cyclotron-enhanced ESD and SEE in the waveguides. We have shown in Eq. (5.7) that electron impact energies are increased by cyclotron effects. Without the auxiliary field, the electrons can gain approximately 2 keV before striking the wall, while with the breakdown suppression field applied such that $\omega_{ce}/\omega = 1.25\text{--}1.5$ and $\mathbf{E}_{rf} \perp \mathbf{B}$, the electrons have an energy of only 30–70 eV for an incident power level of 10 kW/guide. Nonetheless, this latter range of impact energies is 2–5 times higher than that possible

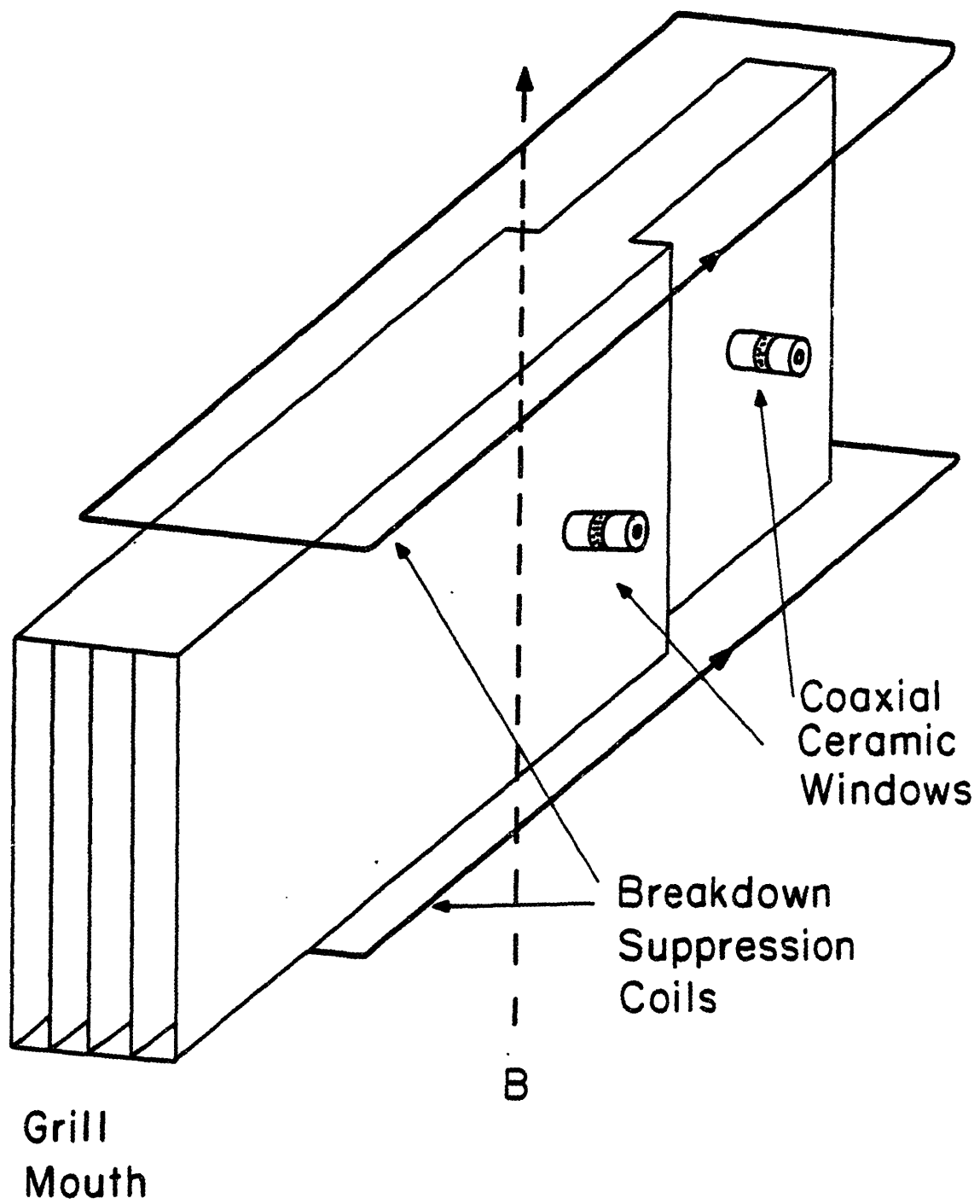


Figure 5.19. Illustration of the magnetized grill. The additional magnetic field is mainly in the vertical direction.

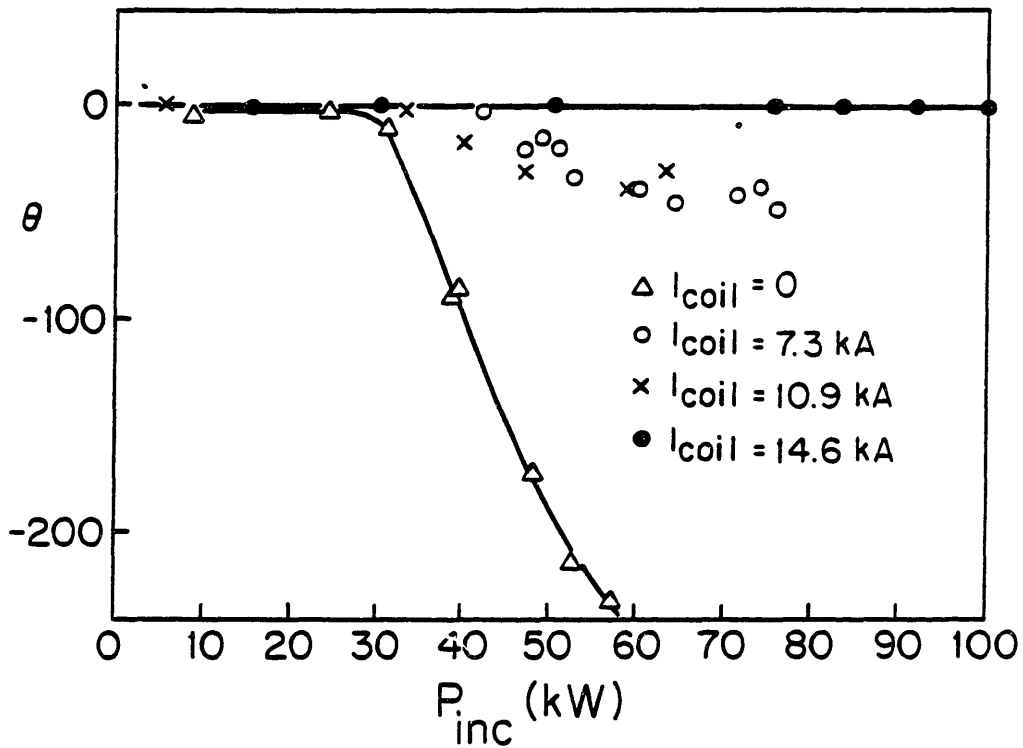


Figure 5.20. Reflected phase shift in one of the waveguides versus incident power for several values of the waveguide coil current. For the coil current of 14.6 kA, the magnetic field is above the cyclotron resonant value everywhere in the waveguides.

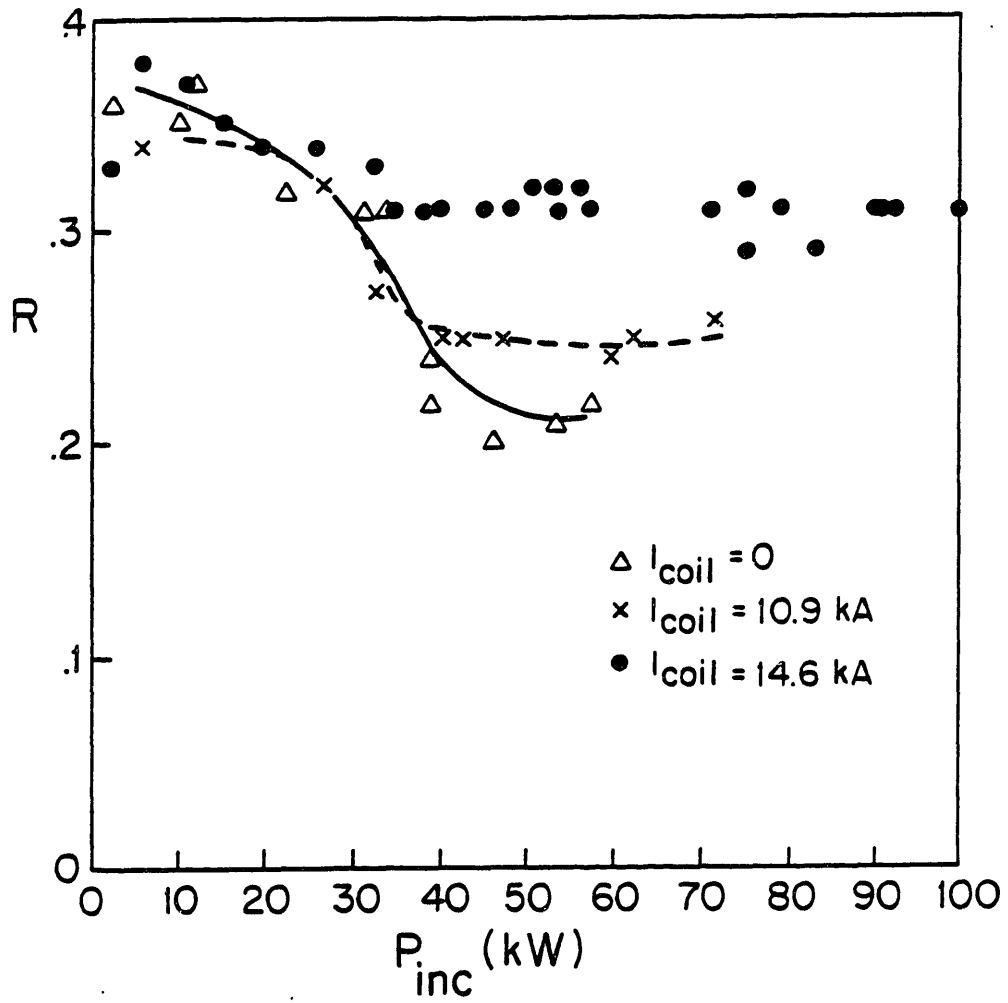


Figure 5.21. Grill reflectivity versus incident power for several values of the coil current

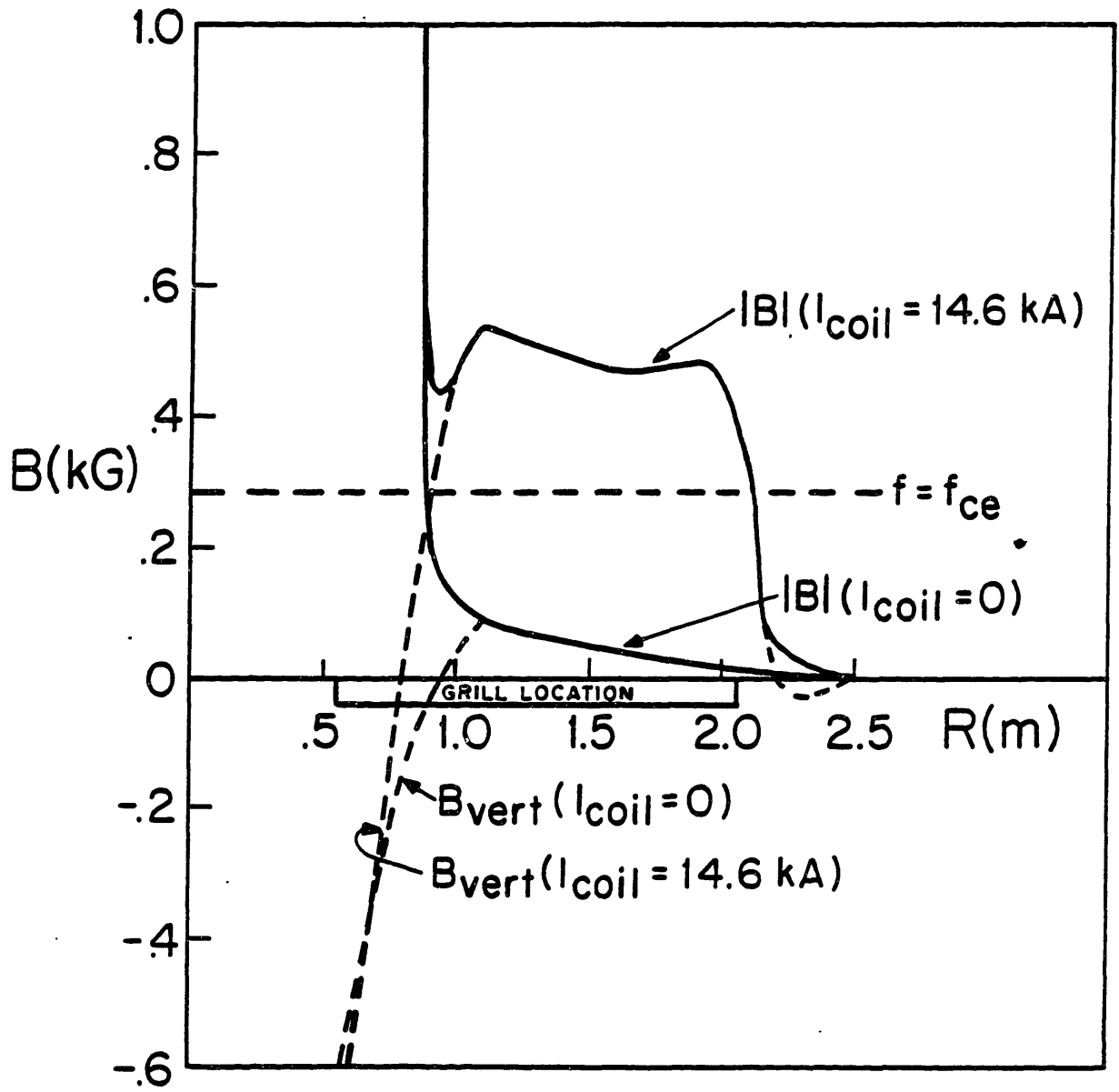


Figure 5.22. Calculated values of $|B|$ and $B_{vertical}$ versus major radius in the region of the grill.

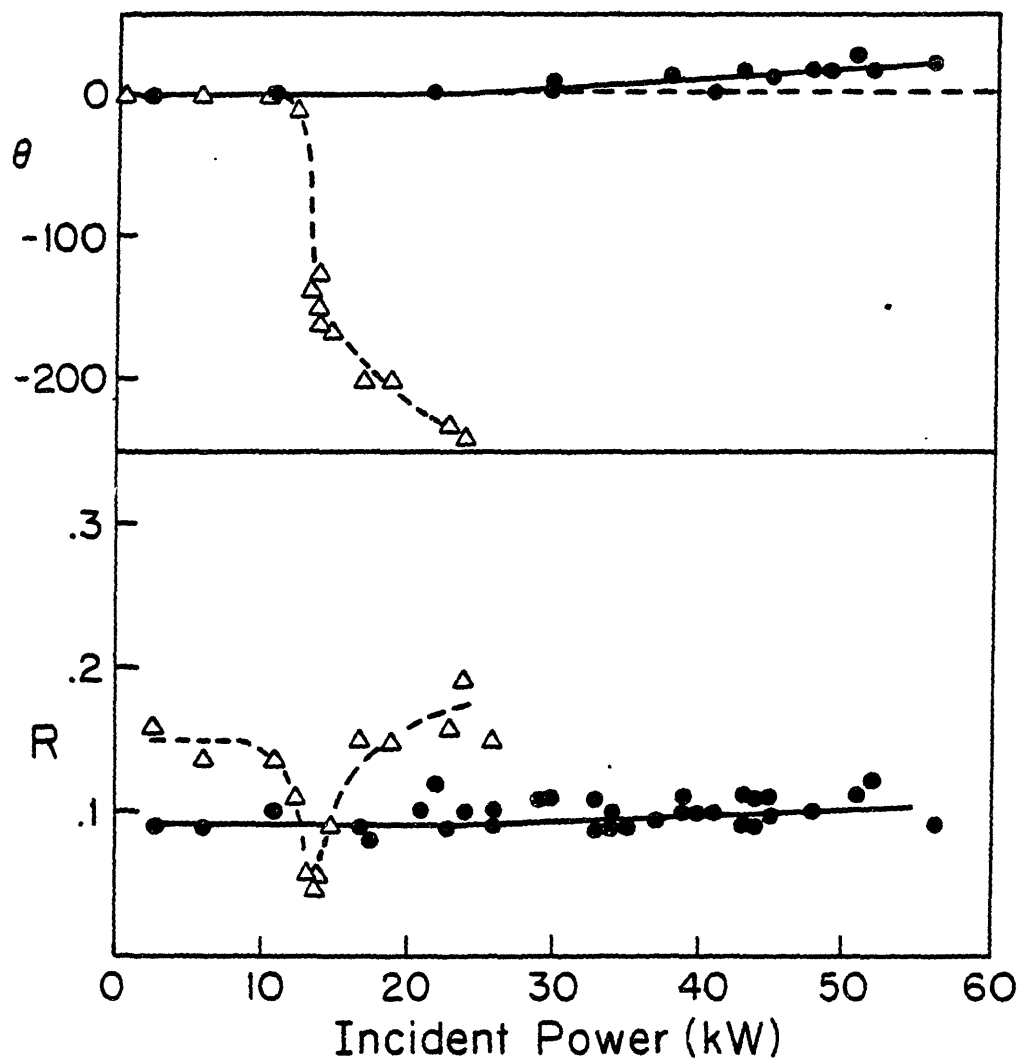


Figure 5.23. Reflectivity and reflected phase shift versus incident power; single waveguide fed. Open triangles denote the case of no auxiliary field; closed circles for a coil current of 25 kA.

during rf conditioning at the same incident power, explaining why the grill must be conditioned with a number of rf pulses into the tokamak plasma even with the auxiliary field in use.

These typical impact energies are dependent on the assumed collision frequency, especially for $\omega_{ce}/\omega \simeq 1$. For $E_{rf} \perp B$, one might expect the effective collision frequency to be much higher than the one postulated earlier since electrons emitted from the wall cannot drift away from it. The collision frequency would then be on the order of the rf frequency. The impact energy for this case is also plotted in Fig. 5.17, showing that the electron energy, even at cyclotron resonance, can be an order of magnitude lower than for the case of E nearly parallel to B in which the power absorbed by the electron is less, but its estimated collision time is longer.

Confinement of energetic electrons is also invoked to explain the beneficial effect of the auxiliary field. Since in the absence of the auxiliary magnetic field, the tokamak residual field B is nearly parallel to E near cyclotron resonance, electrons are free to drift across the waveguide. With the auxiliary field applied, electrons are restricted to the volume near the wall ($\rho_{ce} \lesssim 0.2$ cm. for $\mathcal{E}_e = 500$ eV) and drift in the vertical direction. Since the electric field decreases as $\cos(\pi y/h)$ away from the guide axis, the average electron impact energy is thus reduced. Moreover, as the effective electron-wall collision frequency is conceivably higher for electrons near the wall, electron impact energies for perpendicular magnetic fields are below that for no applied auxiliary field. The confinement of electrons explains the reduction of rf breakdown for supplemental fields of intermediate strength for which cyclotron resonance still exists in the waveguides. Plasma formation still takes place, but not to the extent as in the no-field case. We note, however, that confinement is probably not the major reason for the elimination of breakdown. In the section of waveguide nearest to the antenna, the magnetic field remains parallel to the electric field even with the application of the auxiliary field; therefore electrons in this region are free to drift across the waveguide. That rf breakdown does not occur indicates that these electrons are not energetic enough to cause electron multiplication.

The effect of surface coatings on the rf breakdown threshold is less well understood, though the lowering of the SEE coefficient of the waveguide surface is the most likely explanation. The clean carbon-coated surface indeed exhibits a lower SEE coefficient than does stainless steel, based on the measurements cited earlier. This is distinct from the properties of the carbon polymer formed by rf conditioning which acts as an absorber of secondary electrons. Graphite surfaces are also known to have low sorption coefficients for CO and H₂;¹³² therefore ESD may be reduced in the carbonized waveguides. It is not known, however, if the pyrolyzed varnish forms a graphite surface. Nor is it known if the carbon polymerization is as effective or stable on the carbon surface as it is on stainless steel. The effect of contamination by discharge cleaning is much more severe with the carbon-coated waveguides than for stainless steel, suggesting that the carbon polymerization is not as stable for the former as for the latter. Nonetheless, the carbon coating is predicted to have a lower SEE coefficient than stainless steel, which is probably responsible for

the improved performance.

6. Experimental Results: Rf Heating

In this chapter, the major experimental results of this study are presented and discussed. First, the measurements of ion heating obtained with the use of the four-waveguide side-launching grill are described. The results of electron heating experiments are also presented. Next, similar though less extensive measurements are presented for the ion heating experiments in which the four-waveguide top-launching antenna was employed. Finally, an empirical power balance of the plasma is performed for the purpose of obtaining an estimate of the overall rf heating efficiency. The relationship of the experimental results to one another, and to the qualitative theoretical predictions of chapter 2 are discussed, and the possible interpretations of the measurements in this study are stated.

6.1. Lower-Hybrid Heating with the Side-Launching Antenna

The heating experiments described in this section were performed with the use of the four waveguide grill located on the midplane of the tokamak. Described in detail in Chapters 3 and 4, the grill is calculated to launch an $n_{||}$ spectrum peaked at $n_{||} = 5.5$ with a FWHM $\Delta n_{||} \approx 3$ for $\Delta\phi = 180^\circ$. With some run-to-run variation, effects of rf injection on the ion distribution are noted for the density range $\bar{n}_e = 1.1\text{--}3.2 \times 10^{13} \text{ cm.}^{-3}$ and for a magnetic field of 12–15 kG. The upper density value is the operational density limit of Versator, and is not necessarily a physical bound for the interaction of lower-hybrid waves with the ion population.

6.1.1. Perpendicular Charge-Exchange Measurements

In the above density band, a high energy ion tail is formed during the rf pulse, as measured by near-perpendicular charge-exchange analysis. As mentioned in Chapter 1, this tail is a ubiquitous feature of all lower-hybrid ion heating experiments. A typical energy spectrum is shown in Fig. 6.1. For this case, the transmitted rf power was 75 kW and the relative phase between adjacent waveguides was $\Delta\phi = 180^\circ$. The plasma density was $\bar{n}_e = 2.2 \times 10^{13} \text{ cm.}^{-3}$

The experimental ion distribution is seen to be characterized by three parameters: the Maxwellian temperature of the bulk distribution, the effective Maxwellian temperature of the tail, and the intercept energy of the bulk and tail distributions. For the case illustrated in Fig. 6.1, the tail temperature is 1.4 keV and the intercept energy is approximately 1.2 keV. The bulk temperature is 105 eV without rf, and is indicated to be 25 eV higher during rf injection. As discussed later, this small decrease in the slope of the low energy spectrum is also consistent with the tail extending to lower energies than 1.2 keV, and may not represent a true temperature rise.

The measured tail temperature varies linearly with the applied rf power, as shown in Fig. 6.2. This power scan was performed in conjunction with rf breakdown tests (described in Chapter 5); the curve of reflectivity versus power shows that plasma formation in the waveguides occurs at a threshold power of 40–60 kW. The onset of plasma formation is believed to be responsible for

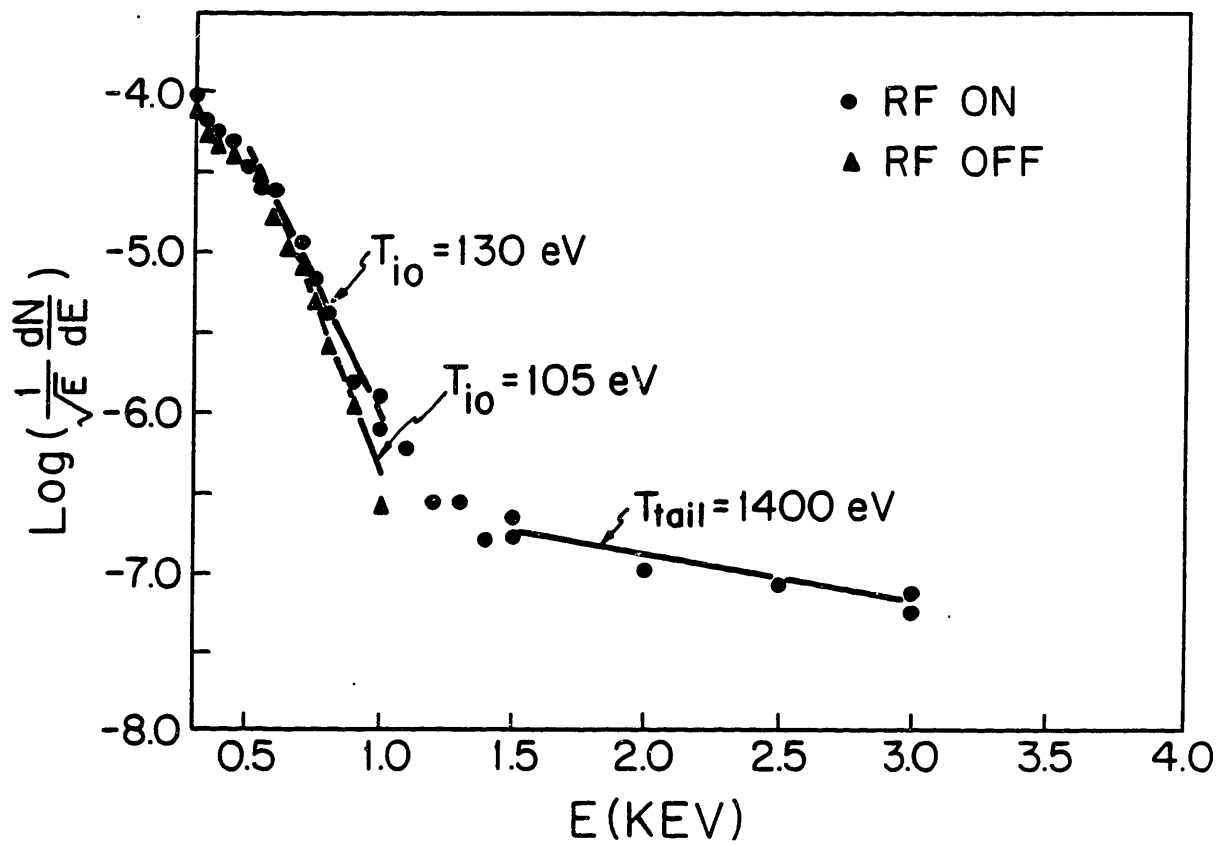


Figure 6.1. Perpendicular charge-exchange neutral energy spectrum for $P_{rf} = 75 \text{ kW}$, $\Delta\phi = 180^\circ$, $\bar{n}_e = 2.2 \times 10^{13} \text{ cm}^{-3}$, $B_0 = 14 \text{ kG}$.

the apparent saturation of the tail temperature, rather than a process occurring within the plasma itself. If breakdown is neglected, the tail temperature is measured to be a linear function of rf power, with an apparent intercept energy of 120–135 eV if we extrapolate to $P_{rf}=0$. The central ion temperature in this experiment was approximately 100 eV.

The amplitude of the parametric sideband decay wave is also shown in Fig. 6.2. Described more fully in Section 6.1.5, the parametric decay spectrum is always observed in conjunction with an enhancement of the fast neutral flux. Plotted in Fig. 6.2 is the amplitude of the first lower sideband of the incident lower-hybrid pump wave which is separated from the pump by 17 MHz, corresponding to the ion cyclotron frequency near the outer major radius. The onset of parametric decay appears to exhibit a threshold near $P_{rf} \approx 14$ kW; the decay wave strength also increases with rf power.

The lifetime of the perpendicular tail is found to be short compared to an energy confinement time. In all experiments in which the high-energy charge-exchange counts were digitally tallied or displayed directly on a fast oscilloscope, the maximum fast ion lifetime was estimated to be 100–150 μ sec following the end of the rf pulse. This observation is in agreement with measurements from the other lower-hybrid experiments discussed in Chapter 1.

In Fig. 6.3 is plotted the variation in ion tail temperature versus line-averaged density for $\Delta\phi = 180^\circ$ and constant toroidal field. Despite some scatter in the data, the results indicate a generally decreasing trend of tail temperature with density. Because the neutral flux measurement is a chord-averaged one, it is possible that the value of the tail temperature obtained from these measurements may not represent a local tail temperature, i.e. one that can be compared to the theoretical prediction of Karney (see Eq. 2.46). Nonetheless, it is clear from the data that the count-rate of higher energy ions in the tail is enhanced relative to the lower ones at the lower plasma densities. This result is consistent with the fact that the phase velocity of the wave, and hence the resonant energy of the ion, is typically higher in lower density plasmas. This is explicitly illustrated in Fig. 2.8, in which the predicted resonant ion energy at the damping location is a decreasing function of density for a given $n_{||}$. Furthermore, we note from Fig. 2.10 that the tail temperature is also expected to decrease with increasing plasma density. Thus the behavior of the measured tail temperature with variation in density is in general agreement with the theoretical predictions.

The increase in the fast neutral flux during injection of rf power appears to be relatively insensitive to the waveguide phasing. In Fig. 6.4, the count-rate of 900 eV ions during rf injection, again normalized to transmitted power, is plotted versus $\Delta\phi$. The toroidal field is 12.5 kG. The relative ion count rate for $\Delta\phi = 0^\circ$ is as high or perhaps greater than that for $\Delta\phi = 90^\circ$ and 180° . Within experimental error, the normalized tail temperatures are identical for $\Delta\phi = 0^\circ$, 90° , and 180° . This phase independence suggests that parametric decay at the surface may be responsible for the ion tail. Alternatively, the launched $n_{||}$ spectrum may be sufficiently scrambled

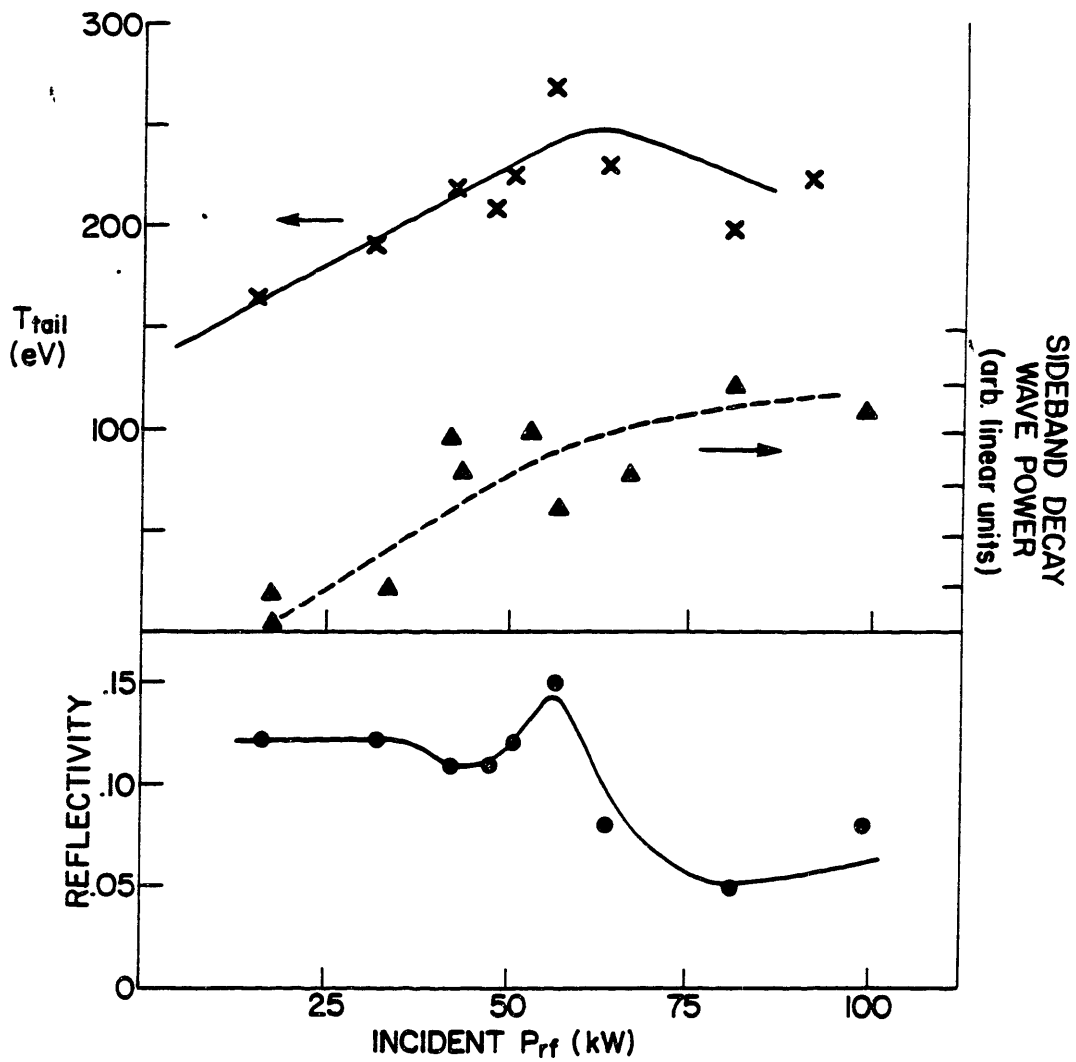


Figure 6.2. Cha. π -exchange tail temperature, grill reflectivity, and relative strength of parametric decay sideband versus incident power for $\bar{n}_e = 2.5 \times 10^{13} \text{ cm}^{-3}$.

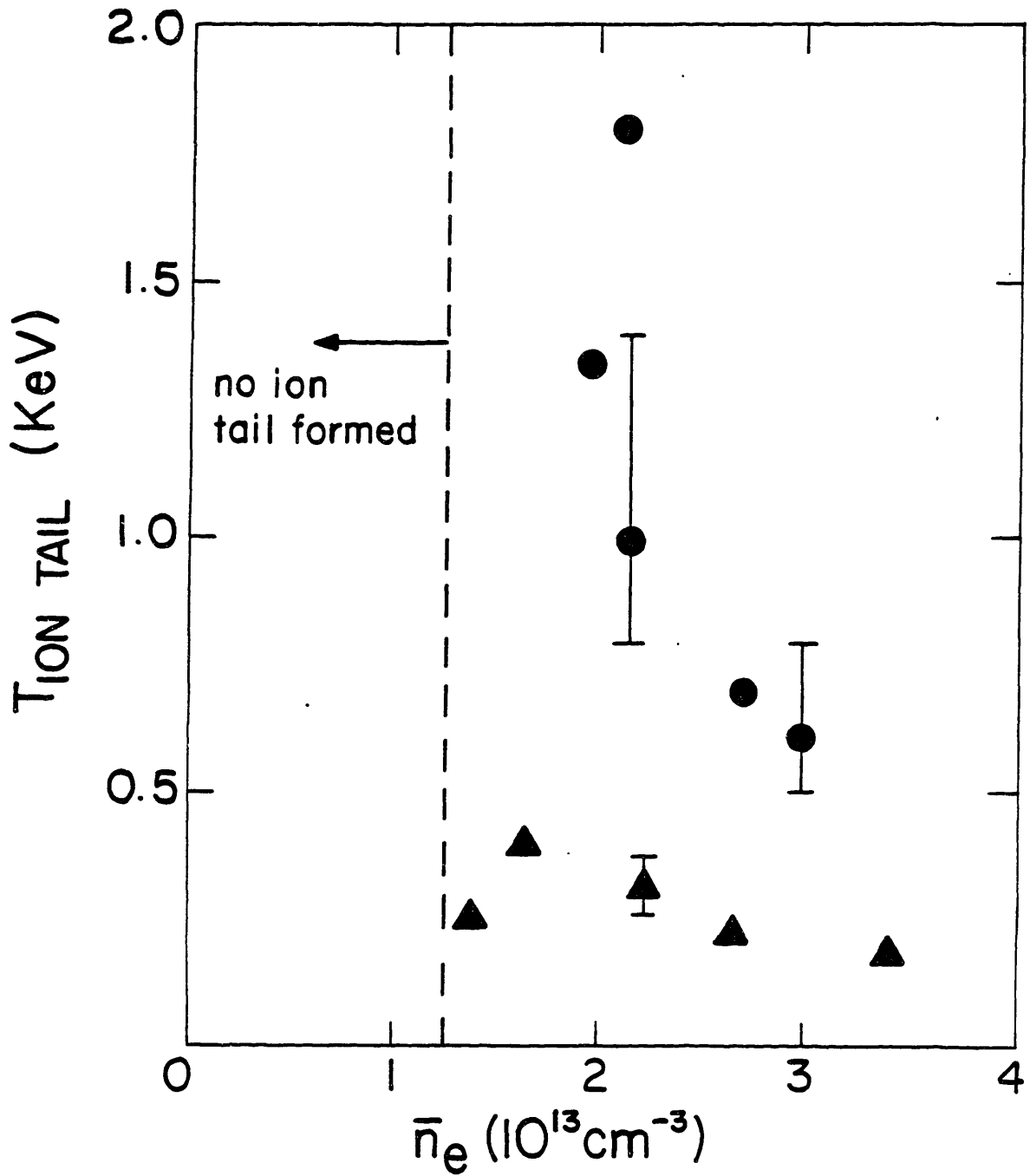


Figure 6.3. Charge-exchange tail temperature versus line-averaged density for $B_0 = 14 \text{ kG}$.

by toroidal effects and/or drift wave scattering such that the final spectrum is unrelated to the initial one. The damping behavior of the lower-hybrid wave in the toroidal model has been shown previously in Fig. 2.18; for $n_{\parallel} \lesssim 6$, the damping location is not well-defined and does not exhibit a clear variation with the launched n_{\parallel} , i.e. $\Delta\phi$.

The increase in the fast ion count-rate during rf heating exhibits a threshold with the strength of the toroidal magnetic field, as depicted in Fig. 6.5. The threshold field of 10.9 kG for the given density of $\bar{n}_e = 1.8 \times 10^{13} \text{ cm}^{-3}$ ($\omega/\omega_{LH}(0) \simeq 1.6$, where $\omega_{LH}(0)$ is the central lower-hybrid frequency) corresponds to a minimum n_{\parallel} of 10 for a mode conversion layer to exist in the plasma. Most of the power launched by the side-launching grill is calculated to lie in the range $|n_{\parallel}| \leq 8$ (see Fig. 3.3); hence the threshold may be explicable in terms of the available n_{\parallel} spectrum of the grill. However, the predicted variation of n_{\parallel} induced by toroidal effects make this interpretation less clear. Furthermore, if the ion tail results from the damping of parametric decay waves near the plasma edge, the condition of having a mode conversion layer in the plasma is irrelevant. However, we note that parametric decay of the pump wave is observed both above and below the threshold field for fast ion production; therefore its relationship to the magnetic field threshold for the onset of the ion tail in this case is somewhat uncertain.

In principle, changes in the central bulk temperature of the ion distribution during rf heating can be inferred from that portion of the charge-exchange spectrum below the bulk/tail intercept energy. However, this approach is subject to error for the following reason. Because the charge exchange analyzer views a chord of the plasma, the neutral flux from the high energy tail, which may be located anywhere along the minor radius, adds to the flux from the thermal ion distribution in the core to give a measured spectrum like that illustrated in Fig. 6.6. If the tail is generated off-axis and joins to an ion distribution of lower temperature, the true bulk/tail intercept energy is lower than the apparent value from Fig. 6.6. For example, if the wave damping takes place about 10 cm. off-axis such that the absorption occurs where the ion temperature is only 50 eV, then by the criterion of Eq. (2.37) the bulk/tail intercept energy should be approximately 450 eV or greater. Consequently, the measured charge-exchange spectrum above the energy of 450 eV would be sum of the thermal contribution from the center and the fast tail. The average slope of the spectrum between 450 eV and the apparent junction of the bulk and tail distributions would give a temperature larger than the true central ion temperature.

The problem may be resolved in two ways, neither one being totally satisfactory. In the first, the tail is assumed to extend to lower energies than the apparent intercept energy, and is subtracted from the total charge-exchange flux. Alternatively, the bulk temperature can be measured over an energy span well below the apparent intercept energy. The weakness in the first technique is that one does not know the true low energy boundary of the tail. The second method is also subject to error, since the energy range over which the measurement is made is small and the apparent temperature measurement may be confused by emission of neutrals from colder regions

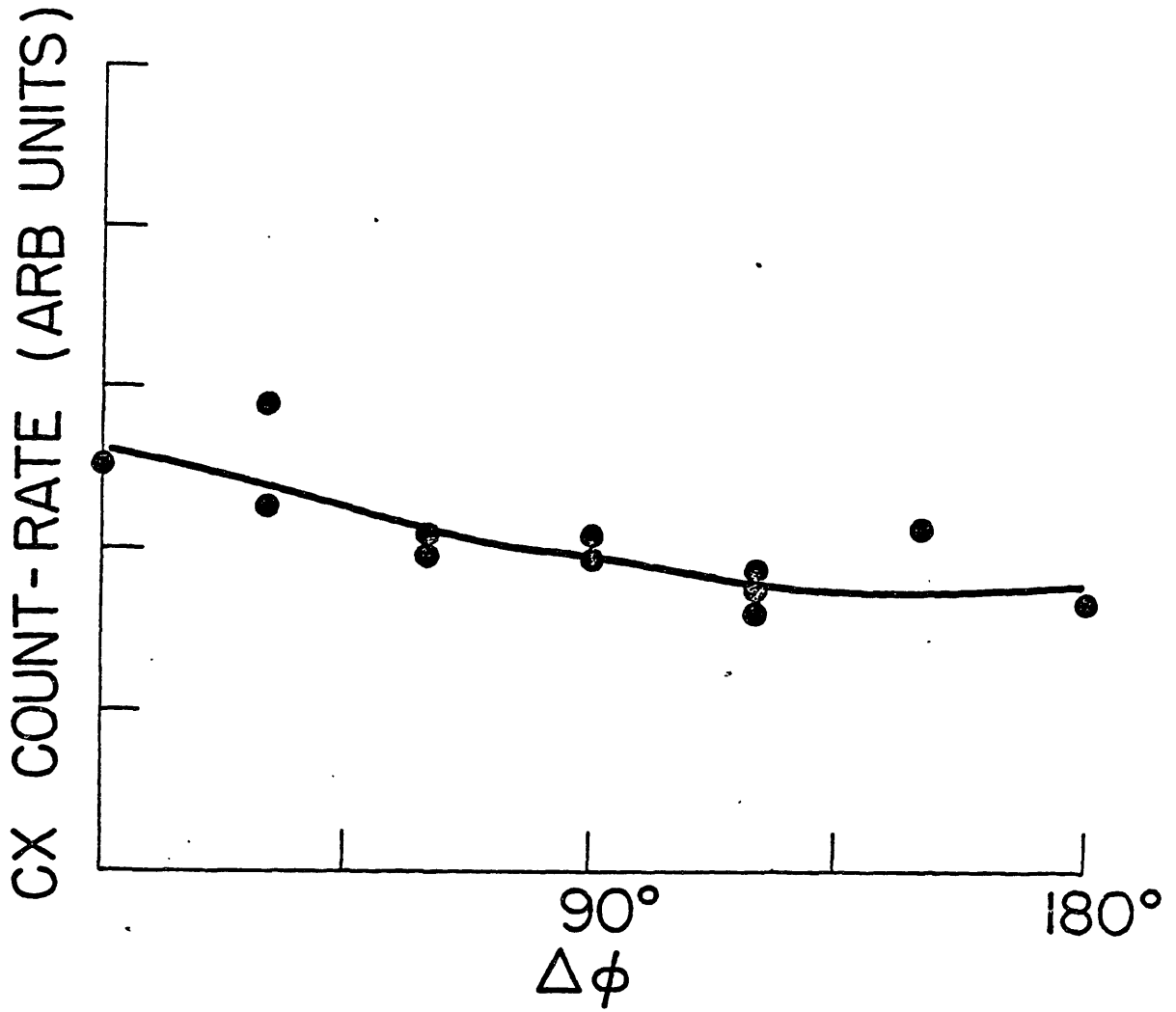


Figure 6.4. Count-rate of 900 eV ions, divided by the transmitted power, versus $\Delta\phi$ for $\bar{n}_e = 2.0 \times 10^{13} \text{ cm}^{-3}$, $B_0 = 12.5 \text{ kG}$.

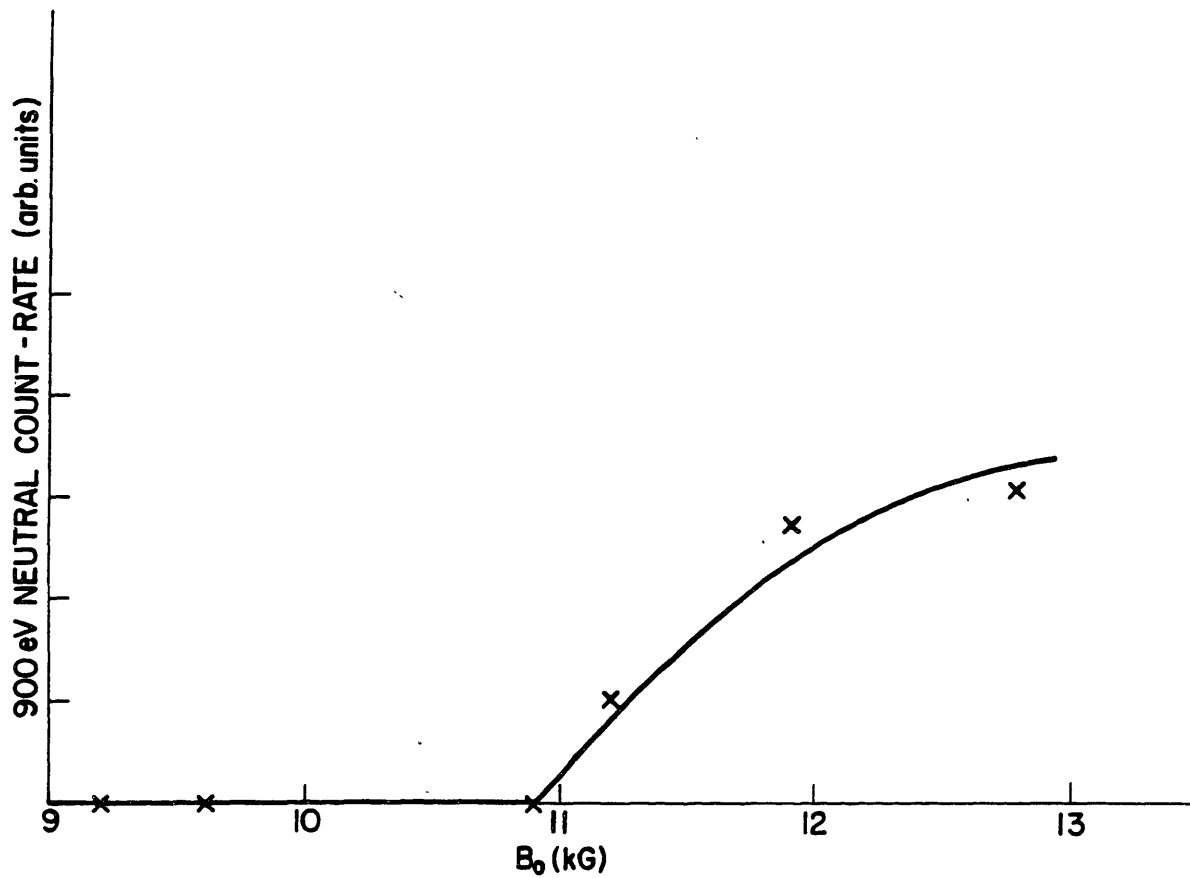


Figure 6.5. Count-rate of 900 eV ions versus toroidal field for $\bar{n}_e \approx 1.8 \times 10^{13} \text{ cm}^{-3}$.

of the plasma. For the charge-exchange spectrum illustrated in Fig. 6.6 , the transmitted power is 50 kW, the density is $\bar{n}_e = 2.6 \times 10^{13} \text{ cm}^{-3}$ and $\Delta\phi = 90^\circ$. The central temperature is approximately 150 eV prior to rf injection. Depending on the energy range selected for the analysis, the measured-bulk temperature can range from 140 to 185 eV during rf injection. In short, it is difficult to obtain a reliable measurement of the bulk ion temperature from charge-exchange analysis with the presence of the perpendicular tail in the spectrum.

With an assumption made regarding the location of the detected ion tail, the maximum collisional absorption rate of the tail on the bulk can be estimated from Eq. (2.57). First, let us assume that for the case illustrated in Fig. 6.6, the observed ion tail is located near the center of the plasma. With the central temperature of 150 eV and a bulk/tail intercept energy of 1.2 keV, the damping criterion Eq. (2.37) is approximately satisfied. Taking $T_i = 700 \text{ eV}$ and $n_i = 3.9 \times 10^{13} \text{ cm}^{-3}$ along with the above values for the central ion temperature and intercept energy, we find that the central collisional heating rate is only about 9 mW/cm.³ For comparison, the central heating rate of the ions due to collisions with electrons is given by

$$P_{ei} = n_{eo} \nu_{ei} (T_{eo} - T_{io}) \quad (6.1)$$

where ν_{ei} is the collisional frequency for thermal equilibration between electrons and ions,⁹⁹

$$\nu_{ei} = 3.6 \times 10^{-37} \frac{\sqrt{m_e}}{m_p} \ln \Lambda \frac{n_e}{T_e^{3/2}} \left[1 - \frac{n_I Z_I}{n_e} \left(1 - \frac{Z_I}{A_I} \right) \right], \quad (6.2)$$

where all symbols are in CGS units. For the central parameters $T_{eo} = 400 \text{ eV}$, $T_{io} = 150 \text{ eV}$, $n_{eo} = 4 \times 10^{13} \text{ cm}^{-3}$ and assumed impurity values $n_I/n_e = 0.04$, $Z_I = 5$, and $A_I = 16$ (oxygen), the local value of P_{ei} is $3.4 \times 10^2 \text{ mW/cm}^3$ or almost 40 times the maximum heating rate due to the fast ions, assuming they exist in the center. Thus the bulk heating effect of this tail should be small. The collisional slowing-down time of this tail evaluated from Eq. (2.58) is 2.0 msec, which is about an order of magnitude larger than the observed loss time of the tail. For comparison, we also calculate the charge-exchange time and the perpendicular scattering time of fast ions at the center. The average time for an ion to undergo charge-exchange,

$$\tau_{cx} \approx (n_o \sigma_{cx} v_i)^{-1}, \quad (6.3)$$

can only be as low as 0.1 to 1 msec for a 1.5 keV ion if n_o is the range 10^{10} – 10^{11} cm^{-3} which is unlikely to be true at the plasma center, but may be a plausible value for the edge region. The perpendicular scattering time of fast ions is calculated from the collision frequency for transverse diffusion:

$$\tau_{i\perp} = \nu_{i\perp}^{-1} = \frac{1.2 \times 10^{-3} [\mathcal{E}_i(\text{keV})]^{3/2}}{n_e (10^{13} \text{ cm}^{-3}) Z_{eff}}, \quad (6.4)$$

which is about 270 μsec for 1.5 keV ions. Consequently, isotropization of the tail should occur at a greater rate than collisional absorption if the tail is indeed confined, and the bulk heating

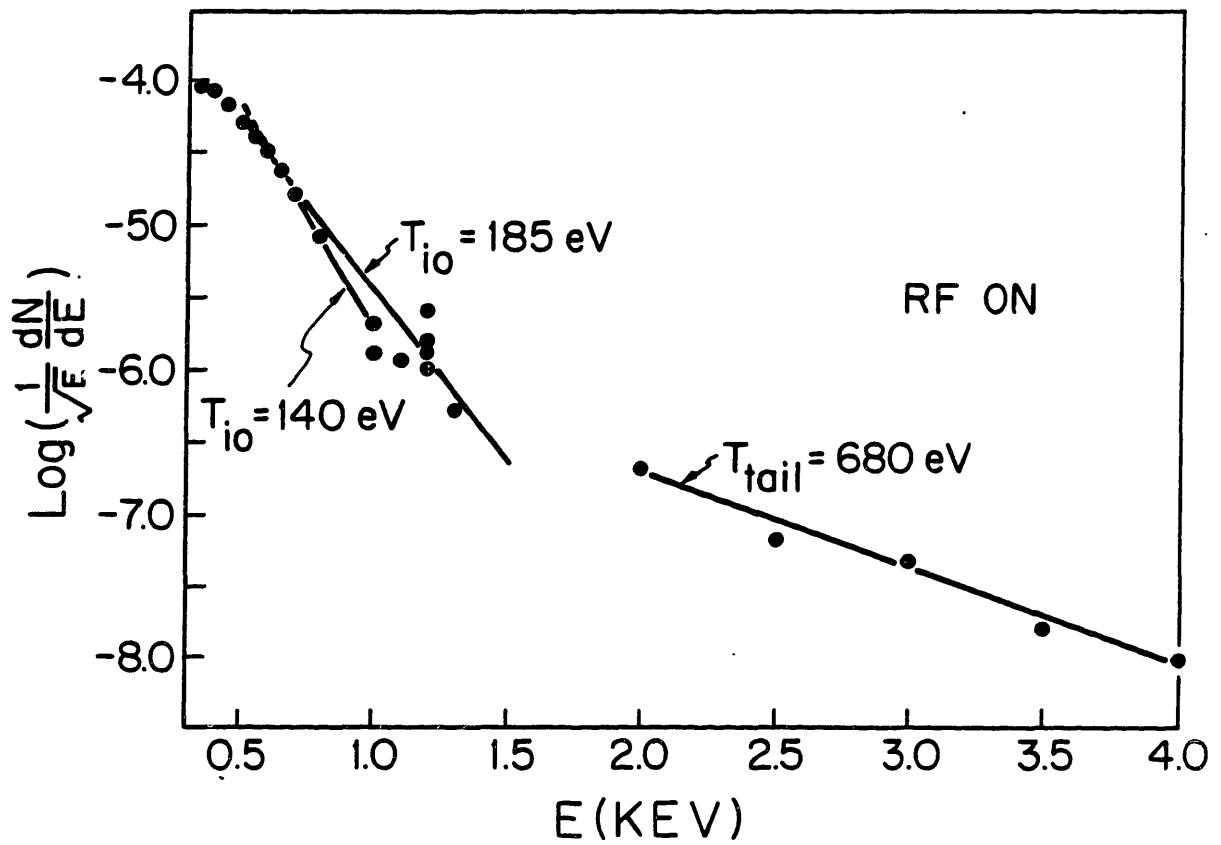


Figure 6.6. Charge-exchange spectrum for $P_{rf} = 50 \text{ kW}$, $\Delta\phi = 90^\circ$, $\bar{n}_e = 2.6 \times 10^{13} \text{ cm}^{-3}$, $B_0 = 14 \text{ kG}$.

rate may be somewhat larger than the value calculated above. If significant isotropization occurs, however, a tail with off-perpendicular orientations should also be present. Experiments which have been performed in this study to detect such a tail are described later. Without invoking such a mechanism, we reiterate that the amount of power deposited by the tail in the central bulk ion distribution should have an insignificant effect on the ion temperature.

The rate of absorption of rf energy, or the power flow to the tail, may be calculated from Eqs. (2.54) and (2.55) where we again assume the tail to be present in the center of the discharge, and take the confinement time of the tail to be 100–200 μsec , based on the observed decay rate. We find for the above parameters that

$$P_t \geq 190\text{--}380 \text{ mW/cm}^3 \quad (6.5)$$

or if the power deposition is uniform, then the rf power absorbed inside a radius of 5 cm. is 4–8 kW, or 8–16% of the injected power.

For the reasons described above, the power absorption cannot be so readily calculated from the charge-exchange spectrum if the wave damping and ion tail formation takes place off the axis. A tail temperature and intercept energy at low ion energies would have to be assumed. If we postulate the existence of a fast ion tail with a density of $n_t = 10^{11} \text{ cm.}^{-3}$ ($n_t \approx 0.0025 n_{i0}$) and temperature of $T_t = 1 \text{ keV}$ to exist in the outer half of the plasma ($6 \text{ cm.} \leq r/a \leq 13 \text{ cm.}$), then the absorbed power for the same empirical confinement times is 25–50 kW. Therefore it is possible that a large fraction of the total transmitted power could be deposited in the fast ion tail if it is present over the entire cross-section of the plasma. However, based on the above estimate of the maximum power absorption in the plasma center, less than 16% of the power is absorbed in the inner core ($r/a \leq 5 \text{ cm.}$).

6.1.2. VUV Doppler Broadening Measurements

For the reasons discussed in Chapter 3, VUV Doppler broadening provides a more reliable measure of ΔT_i for the bulk ion distribution during rf injection than does charge-exchange analysis. On Versator, we have observed increases in the bulk ion temperature over a range of densities which is narrow compared to that for ion tail formation. The evolution of the ion temperature is depicted in Fig. 6.7 for a net injected power of 50 kW at a line averaged density of $\bar{n}_e = 2.6 \times 10^{13} \text{ cm.}^{-3}$. Broadening of the O VII line indicates a temperature increase of 50 eV during rf injection, and the CV line, located approximately 7 cm. off-axis, also shows a rise in temperature. The charge-exchange spectra for this series of shots has been shown previously in Fig. 6.6. There is no decrease in the loop voltage. The density range over which bulk ion heating is measured is shown in Fig. 6.8, and extends from 2.4 to $2.8 \times 10^{13} \text{ cm.}^{-3}$. The value of $\omega/\omega_{LH}(0)$ in this density range is about 1.2 with the effect of impurities is included (we take $Z_{eff} = 2$).

The variation in the normalized temperature increase for the three waveguide phasings $\Delta\phi = 0^\circ, 90^\circ, \text{ and } 180^\circ$ is shown in Fig. 6.9. The apparent heating efficiency for $\Delta\phi = 0^\circ$ is lower

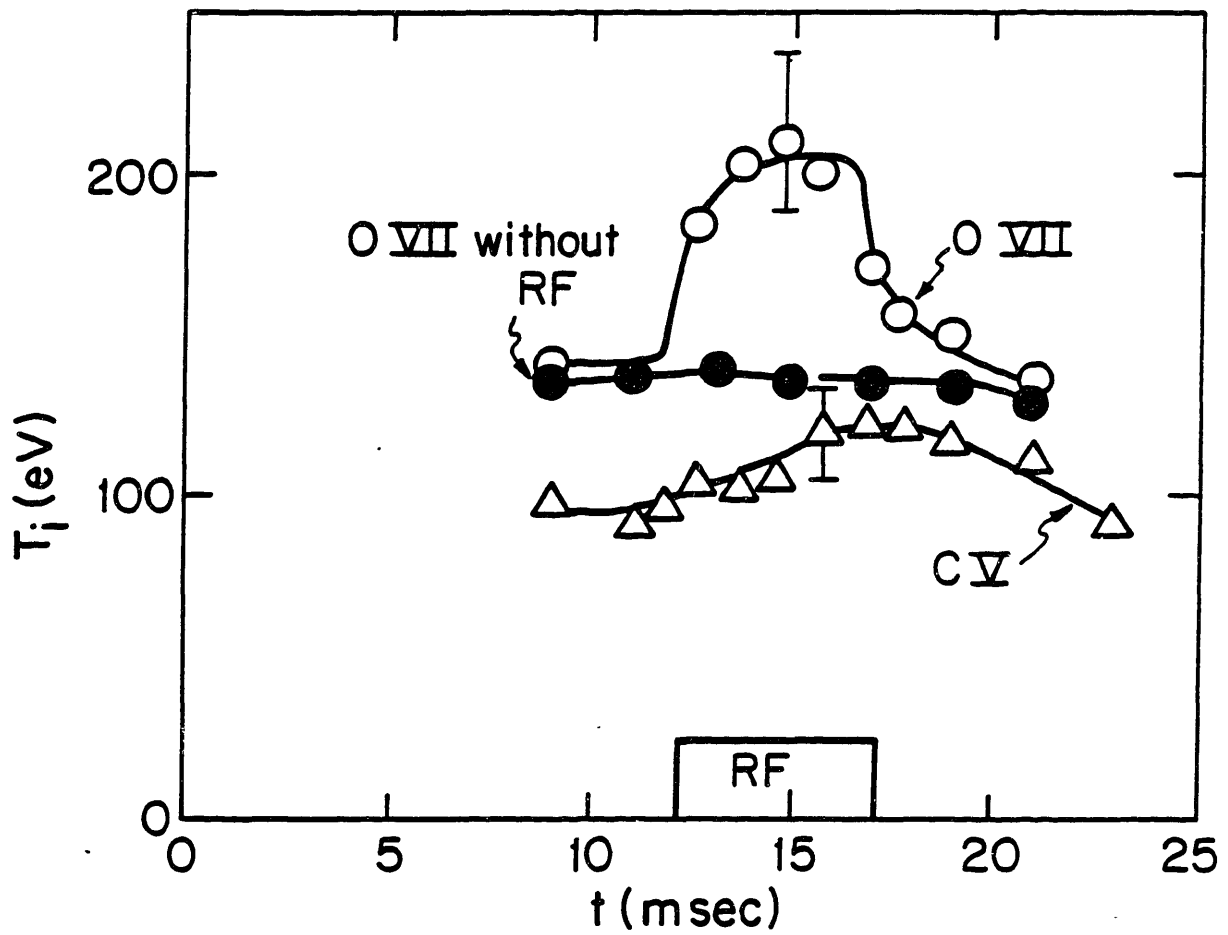


Figure 6.7. Temporal evolution of the ion temperature measured by Doppler broadening of the O VII and C V impurity lines for the same parameters as in Fig. 6.6.

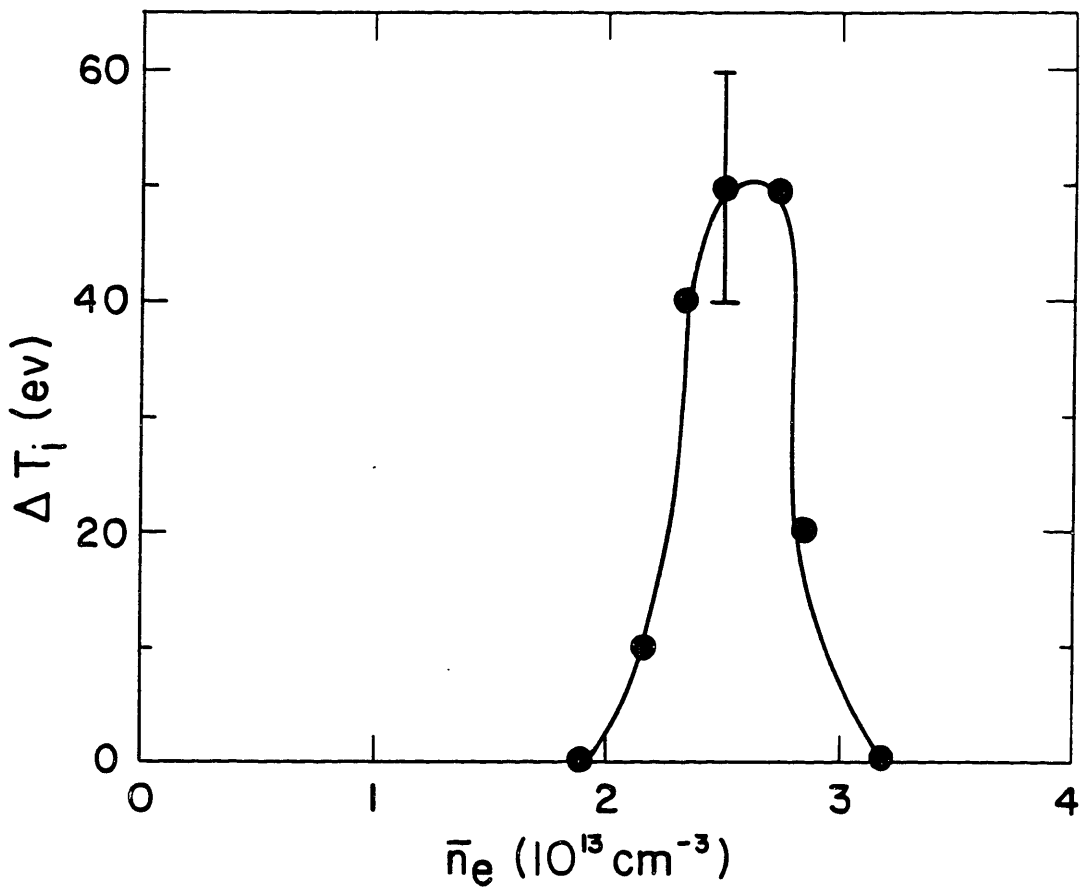


Figure 6.8. ΔT_{i0} measured by Doppler broadening, normalized to transmitted rf power of 50 kW, versus line-averaged density.

than for the other two phases, suggesting that the $n_{||}$ spectrum may be important in determining the heating effect. However, if the observed fast ion tail is responsible for the bulk heating, this finding is in apparent conflict with the phase independence of the fast ion tail strength illustrated in Fig. 6.5 The phase scan depicted here represents data collected in only one run, however, and later we have not been able to reproduce these results.

The overall brightness of the O VII line increases during the rf pulse as well as the line width. The VUV emission near the O VII central wavelength is plotted in Fig. 6.10 versus $(\Delta\lambda)^2$, where $\Delta\lambda$ is the number of Angstroms away from the peak of the line at λ_o . The ratio of the line intensity with rf to that without rf is denoted to be α , where

$$\alpha = \frac{I_2(\lambda_o)}{I_1(\lambda_o)}(T_2/T_1)^{1/2}, \quad (6.6)$$

where we have integrated over the line width. For the case illustrated in Fig. 6.10, $\alpha = 1.4$. In general, the line intensity of an impurity species I is proportional to the electron and the impurity species density and a factor g which depends on the electron temperature:

$$I_I \approx \int_{-a}^a n_e n_I g(T_e) dr \quad (6.7)$$

The integral across the plasma diameter reflects the fact that the measurement is a chordal line-average. Thus, the increase in impurity emission suggests that one or all of the following occurred during rf injection: the central electron temperature or density increased, the electron temperature profile broadened, or the concentration of oxygen impurity atoms increased. It is not likely that the electron or impurity density is the cause of the increased emission, for the line-averaged electron density drops during rf injection, as will be discussed in the next section. The increase in electron temperature required to change the emission by the measured value of 40% can be estimated from the excitation rate of the transition responsible for the 1623 Å emission of O VII. If the ion density and radial distribution is assumed to be constant or both cases, the above criterion is satisfied if the central electron temperature is increased from 400 to 480 eV and the profile shape remains the same, or if the central temperature is raised to 440 eV and the new temperature profile is flat inside a 5 cm. radius. Unless Z_{eff} increases, such a temperature increase may be unlikely in light of the fact that no loop voltage change is observed during rf injection. This point will be discussed further when the power balance calculations are presented at the end of this chapter.

The most puzzling result regarding the VUV Doppler broadening measurements of ion heating is that the increases in the temperature of the bulk ion distribution during rf injection are not consistently observed for the same plasma conditions. In fact, occasions on which ion heating is detected are fewer than those for which it is not when the plasma parameters are in the range over which the heating results shown in Fig. 6.8 were obtained. It could be argued that due to the low transmitted power ($P_{rf} \leq 50$ kW) of the experiments described thus far, the

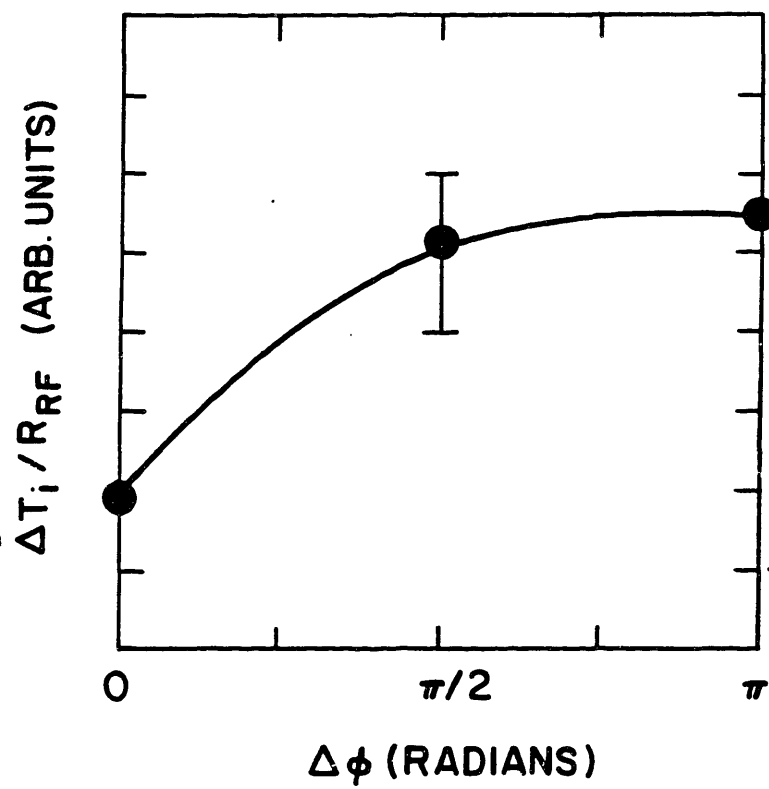


Figure 6.9. ΔT_{i_0} measured by Doppler broadening, normalized to a transmitted rf power of 50 kW, versus $\Delta\phi$.

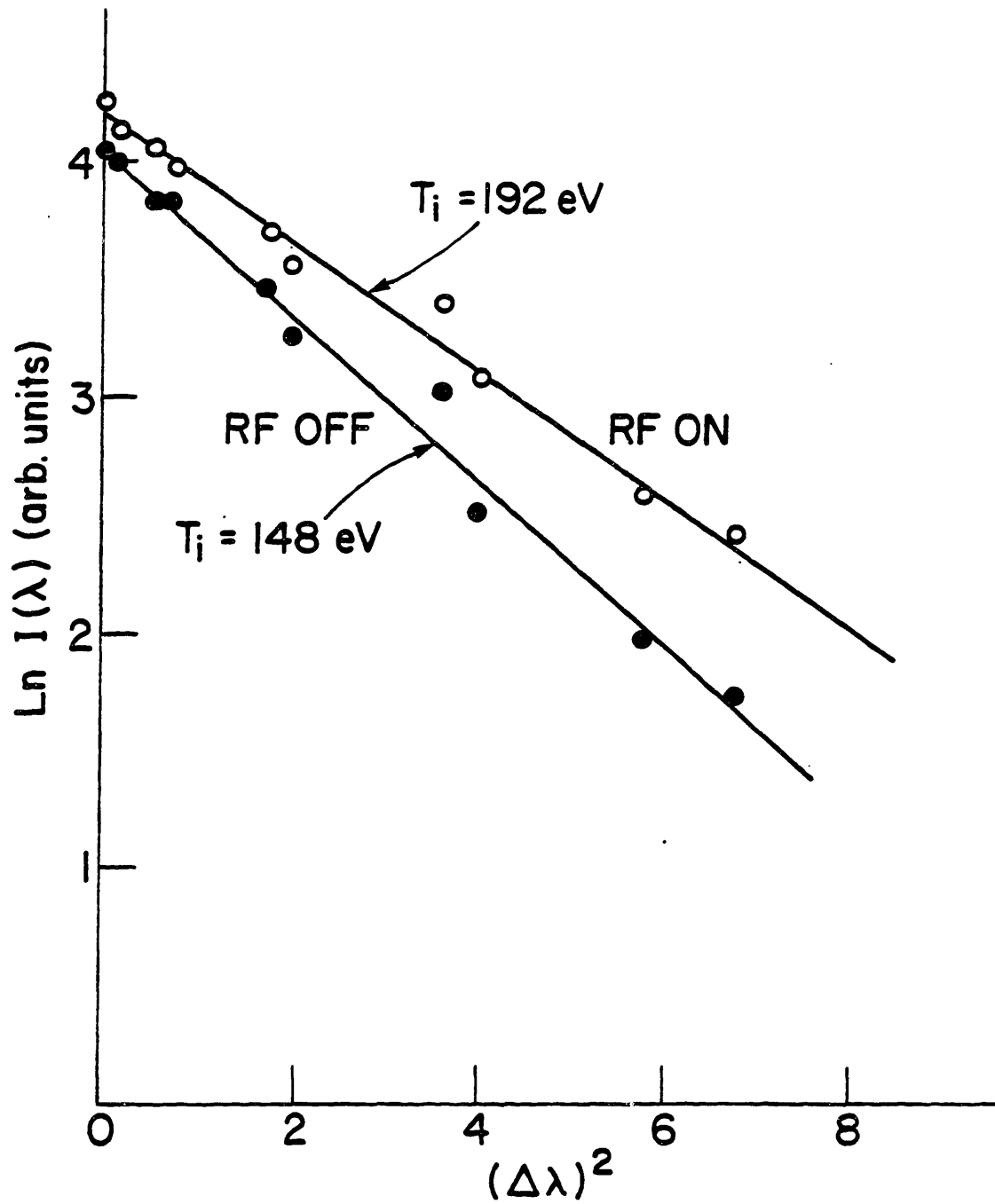


Figure 6.10. Intensity of the O VII 1623A line versus the square of the wavelength from the peak of the line, both with and without rf injection for $P_{rf} = 50 \text{ kW}$, $\bar{n}_e = 2.6 \times 10^{13} \text{ cm}^{-3}$

temperature increase is so small (50 eV maximum) that accurate assessments of ΔT_i are difficult to make. However, the observed heating extends beyond the error bars of the measurement itself. Furthermore, as a result of antenna improvements (see Chapter 5), the available net rf power was doubled to approximately 100 kW during the course of these studies and the higher input power should have provided a larger, more definitive temperature rise to compare with the case without rf injection. However, even in these high power experiments, no increase in the bulk ion temperature above $\Delta T_i = 30$ eV was ever recorded. This irreproducibility of the heating results will be further discussed in Section 6.1.6.

6.1.3. Density Variations During Rf Heating

In most cases, the line-averaged density was observed to change during rf injection. The sign of the density shifts appears to be related to the plasma cleanliness. In lower-hybrid heating experiments performed early in this study, the line-averaged density was observed to increase by up to 20% during rf injection; similar increases in the ion saturation current to a probe at the plasma edge were also noted. Titanium gettering was not employed in these runs. For discharges in which a portion of the wall was gettered prior to a set of shots, the density was noted to drop by up to 15% during the rf pulse (see Fig. 6.11). A significant density drop at the edge as measured by Langmuir probes was not routinely observed in these cases. Density decreases have been observed in plasmas of densities $\bar{n}_e \approx 1.3 \times 10^{13} \text{ cm}^{-3}$; below these densities, the density does not change, or may increase during rf injection. In a case where a high impurity level was known to exist (due to a small leak in the vessel), a density increase of 30% was observed during the rf pulse, in spite of gettering prior to the run. These measurements are similar to previous ones made during lower-hybrid ion heating experiments on the JFT-2 tokamak.^{30,52} The measurements suggest that the rf may increase the flux of particles to the wall, and the recycling rate, which is regulated by the cleanliness of the wall, determines whether the density increases or decreases during the rf pulse. The density range over which drops in the line-averaged density are observed during rf injection corresponds to that for fast ion production, and it is conceivable that the density changes are related to the poor high energy ion confinement discussed in Chapter 2. For heating experiments, any density decrease during rf was usually eliminated deliberately with an extra pre-programmed gas puff 1–2 msec. prior to rf injection.

6.1.4. Bolometry

The total radiated power from the plasma is detected by the pyroelectric bolometer described in Chapter 4. The bolometrically-measured power typically increases during rf injection concurrently with the fast neutral emission (see Fig. 6.12). Similar increases have also been measured by pyroelectric bolometry in other lower hybrid ion heating experiments.^{27,133} The line-averaged bolometric power is plotted versus chord height in Fig. 6.13 for two values of the plasma density. The radiated power is observed to increase with density. For both densities, the emission during rf injection is a factor of 2.5 larger than that without rf. At the lower density, the emission appears to

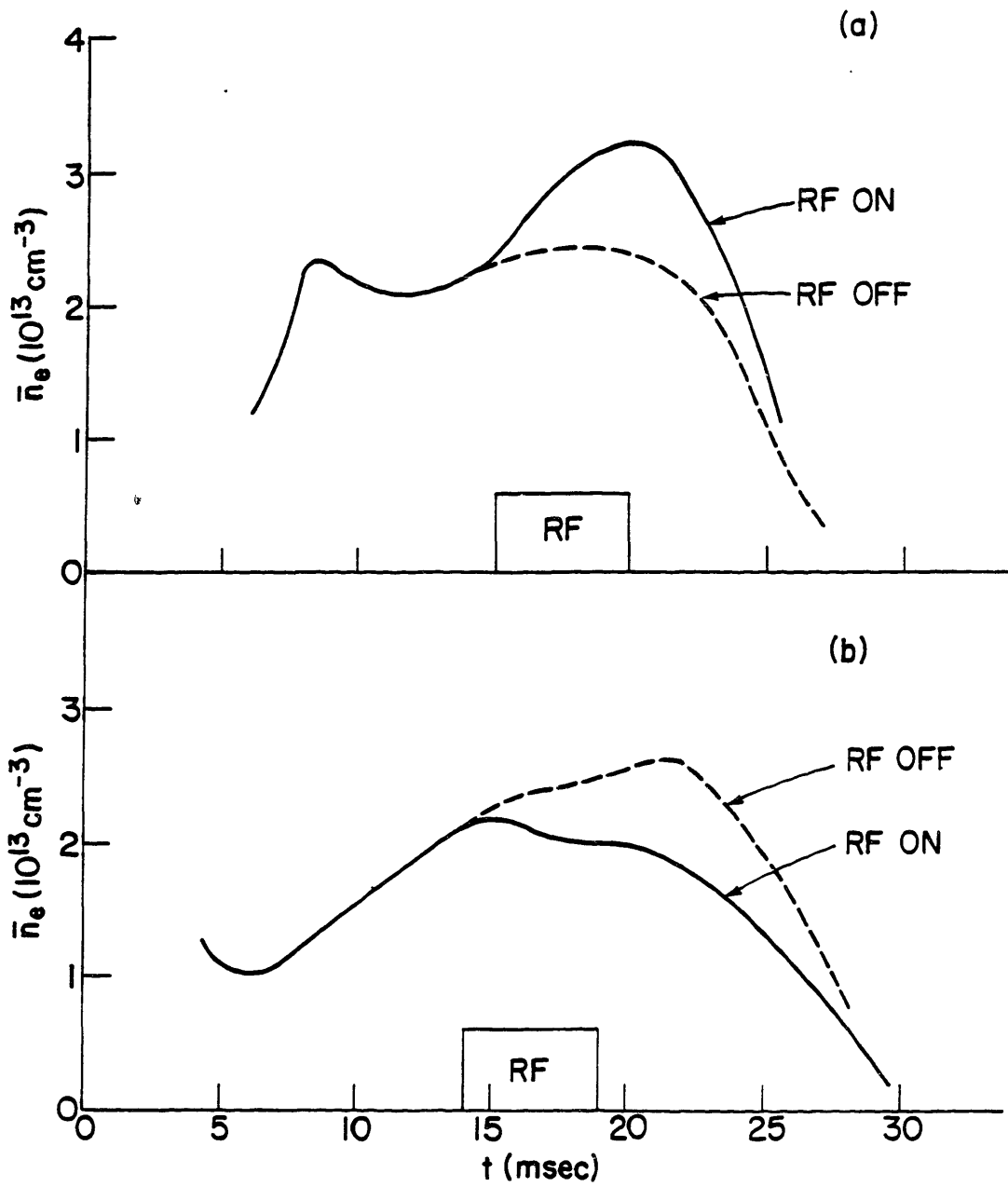


Figure 6.11. Temporal evolution of line-averaged density during rf pulse for: (a) ungettered discharges; and (b) gettered discharges.

be symmetric about the axis while at the higher density, the emission level is clearly larger in the bottom half of the plasma, both with and without rf. The direction of the asymmetry—whether the emission is greater in the upper or lower half of the torus—is not always the same in different runs (see Fig. 6.29). Up-down asymmetries in the bolometric emission and/or impurity radiation have been observed previously in other tokamaks.^{134,135} In-out poloidal asymmetries in the visible radiation from neutral hydrogen and O II have also been directly measured on Versator,¹³⁶ and a similar asymmetry in the bolometric emission on PLT has been inferred.¹³⁷ Neoclassical effects on impurity transport have been invoked to explain some of these effects,^{134,138} but asymmetric emission profiles are generally not well understood, and could conceivably be related to poloidally localized sources of hydrogen or impurities. On Versator, the gas puffer is located slightly above the midplane on the opposite side of the vacuum chamber from the bolometer, and is probably not responsible for the asymmetry. There is no obvious relationship between the asymmetry of the bolometric emission and the effect of the rf on the plasma.

The enhanced emission during rf, i.e. the total emission from which the emission in a shot without rf has been subtracted, is plotted versus chord height in Fig. 6.14a. At the higher density, the enhanced emission profile is broader than at the low density.

Abel inversions of the chord-averaged data can be used to deduce the relative value of the volume emissivity under the assumption of poloidal symmetry. This may be a valid assumption for the low density symmetric profile, but is not applicable to the high density profile shown in Fig. 6.13b. The inversions have been performed on both profiles, and the volume emissivities are plotted in Fig. 6.14b. For the case of the high density profile, we have inverted the top and bottom halves separately. This is unphysical, as the resultant emissivities do not match in the center; however, we can at least obtain a qualitative picture of the radial profile of the volume emissivity in the high density case to compare with that at the lower density. Because of the problems discussed earlier regarding the calibration and performance of the bolometer, we do not quote absolute emissivity results. However, the profiles themselves show that the enhanced emission during rf injection is not localized to the center of the discharge, and that the enhanced emissivity profile is broader in the high density plasma than in the lower density one.

Though the bolometric measurements do not provide knowledge of the constituents of the emission, i.e., the relative power in neutral particle emission compared to that in radiation, the coincidence and relative strengths of the bolometric and charge-exchange signals over a range of densities suggest that the increased energy flux results from neutral particle emission from the plasma. From bolometric measurements on other tokamaks, the major part of the power flux to the wall during ohmic discharges is believed to be impurity radiation in the ultraviolet.^{106,137} However, during rf injection in our experiments, the increase in bolometric emission is uncorrelated with any change in the spectroscopically-measured impurity line radiation from carbon or oxygen (though small increases in the latter have been observed on occasion, as discussed earlier). Although the

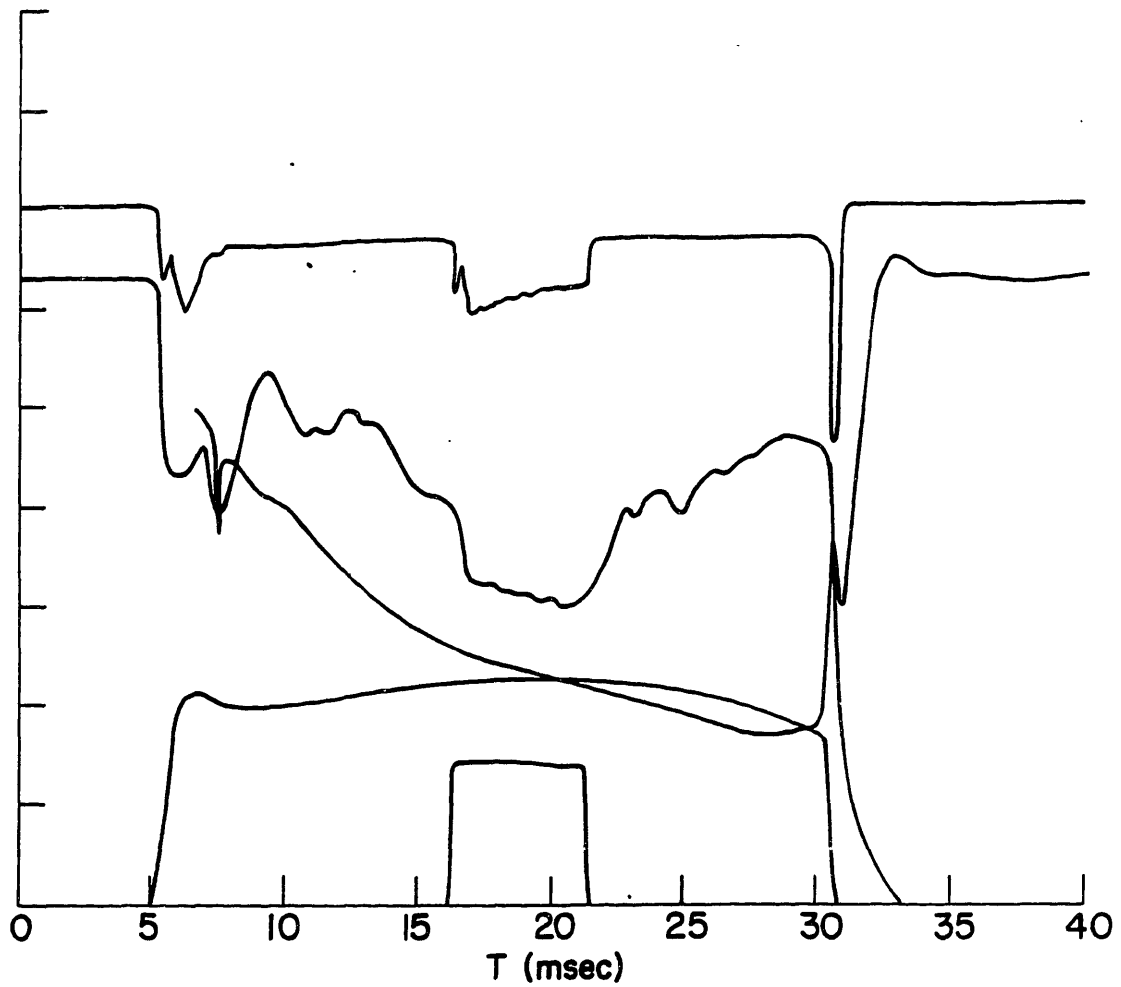


Figure 6.12. From top to bottom: bolometric emission (inverted), charge-exchange neutral flux (1100 eV, inverted), loop voltage (1 V/div.), plasma current (27 kA/div.), and rf power (60 kW) for $\bar{n}_e = 2.7 \times 10^{13} \text{ cm}^{-3}$

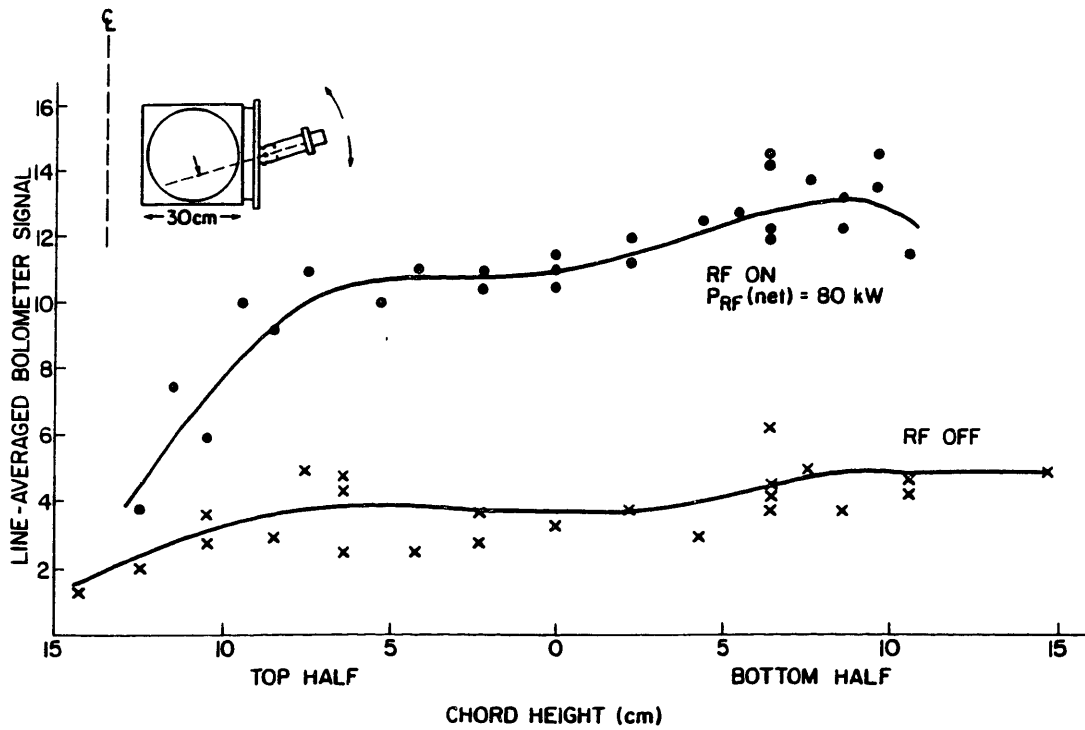
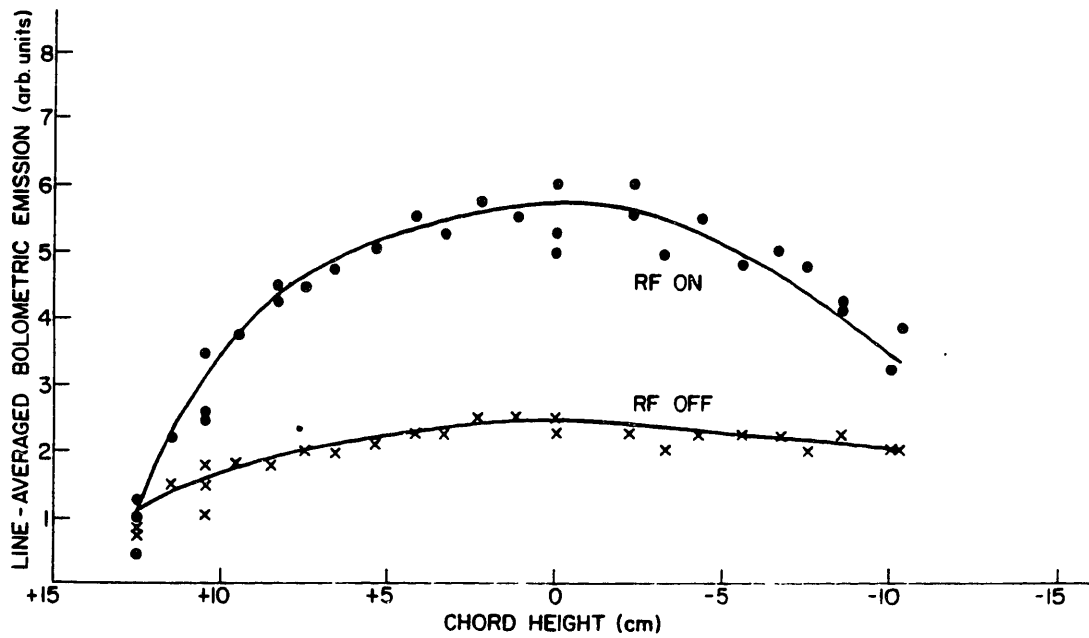


Figure 6.13. Line-averaged bolometric emission versus chord height for the cases of rf on ($P_{rf} = 80 \text{ kW}$) and rf off at: (a) $\bar{n}_e = 1.4 \times 10^{13} \text{ cm}^{-3}$ and (b) $\bar{n}_e = 2.2 \times 10^{13} \text{ cm}^{-3}$.

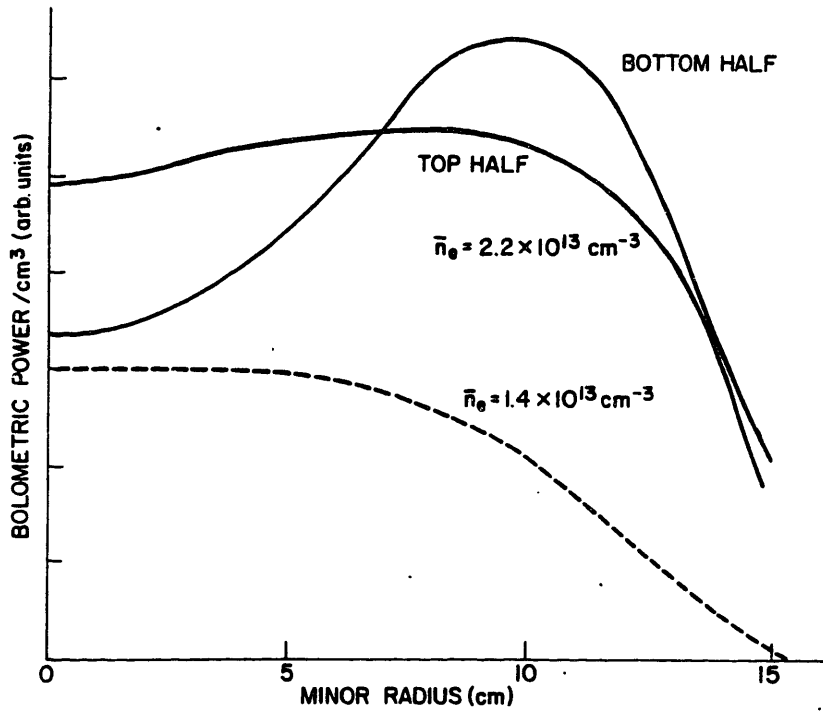
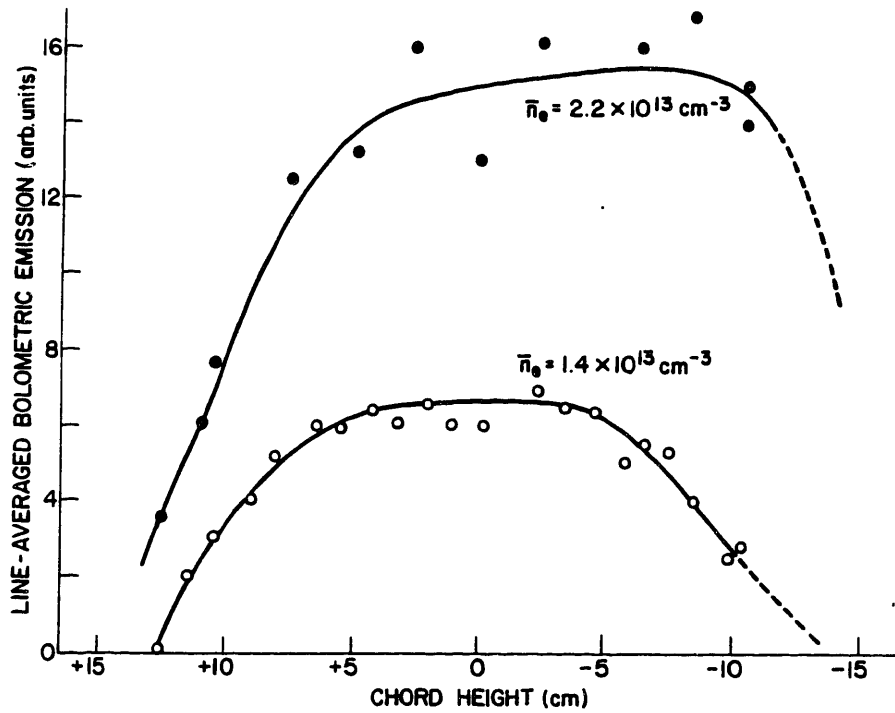


Figure 6.14. Enhanced bolometric emission profiles during rf (total minus ohmic) for the two cases illustrated in the previous figure: (a) line-averaged profiles versus chord height; and (b) Abel-inverted profiles of the local emissivity.

neutral hydrogen light was not monitored during the side-launching experiments because of rf pick-up in the visible monochrometer electronics, it is unlikely that there was an increase in the radiation from neutral hydrogen, since the density was usually noted to drop with rf injection in these experiments.

The emission of heavy impurities (Fe, Mo, or Ti) was also not monitored, and radiation from such ions is known to contribute significantly to the plasma power balance. However, the heavy impurity emission in the soft X-ray range of the spectrum did not increase during rf injection at densities above $\bar{n}_e \approx 2 \times 10^{13} \text{ cm.}^{-3}$ Furthermore, we note that the rise and decay times of the bolometric emission are several hundred microseconds or less, which is considerably shorter than an expected impurity confinement time.¹⁴¹ Therefore, though the enhanced emission appears to be from the center of the discharge, it is not ascribed to an influx of heavy impurities from the chamber wall.

If the increase in emission during rf is due to a rise in the charge-exchange neutral flux, the emission profile does not necessarily represent the lower-hybrid wave damping location because of the large banana orbits of the fast ions and the variation in the neutral hydrogen density. Rather, the profile shape indicates the extent of the volume in which the ions themselves are confined. The width of the high density profile enhancement during rf injection being greater than that at the lower density is consistent with the predicted outward shift of the wave damping location with increasing density. The Abel-inverted profiles for both densities are relatively broad, with characteristic half-widths on the order of half the plasma radius or greater. The profile of the net power emitted as a function of radius is even broader because of the increase in plasma volume per unit radius with minor radius. Consequently, the bolometric emission indicates that the ion tail is localized neither on axis nor at the edge. However, this conclusion is based on the assumption of symmetry of emission in the in-out orientation. The neutral hydrogen radiation from the Versator plasma has been shown to be highest from the region near the outer major radius on the midplane.¹³⁶ The reason for this anomaly is unknown, but may be related to the fact that two limiters were located on the outboard wall of the chamber during the side-launching experiments. Both the bolometer and the visible monochrometer were located near these limiters, and any local asymmetry in the neutral source introduced by the interaction of the plasma with the limiters may have affected the poloidal distribution of the visible and bolometric emission. If such was the case, then the region of the enhanced bolometric emission during rf would be farther off-axis than indicated by the profiles of Fig. 6.14. However, we have not experimentally checked the validity of this conjecture. If the fast ion location is indeed well represented by the profiles of Fig. 6.14 then it is plausible from the qualitative arguments of Chapter 2 that the ions would not exhibit good confinement. For this reason, and from a consideration of ion energy transport for off-axis heating, we might expect the heating efficiency to be low.

6.1.5. Parametric Decay

Measurements with rf probes at the plasma edge have revealed a broadening of the frequency spectrum near the 800 MHz pump frequency, and indicate other features in the spectrum below 800 MHz which are believed to be associated with parametric decay of the incident lower-hybrid wave. Significant frequency broadening of the spectrum is typically observed over the density band for ion tail formation, $\bar{n}_e \gtrsim 1.3 \times 10^{13} \text{ cm}^{-3}$. With electrostatic rf probes in the edge plasma, we have observed two types of spectra near the pump frequency during rf injection. In the first, the spectrum at 800 MHz is approximately 2 MHz wide at a power level 10 dB down from the peak of the pump, and exhibits lower sidebands at frequencies separated from the pump wave by multiples of 17 MHz, which corresponds to the ion cyclotron frequency near the antenna mouth. Similarly spaced peaks are also observed in the low frequency spectrum. Frequency matching of the decay and sideband waves is satisfied. An example is shown in Fig. 6.15. As noted in Chapter 1, this type of parametric decay has been observed in other lower-hybrid ion heating experiments on tokamaks. The pronounced peaks at the harmonics of the ion cyclotron frequency corresponding to the magnetic field at the outer edge of the plasma suggest that we have observed the decay of the incident lower-hybrid wave into cold lower-hybrid waves and either ion cyclotron quasi-modes or backward ion cyclotron waves. The general requirements for these decay process are that $5\omega_{LH}(\text{local}) \gtrsim \omega_o \gtrsim 2\omega_{LH}(\text{local})$ and $T_e \lesssim 3T_i$, where we denote the pump frequency to be ω_o .⁴³ This type of parametric decay was usually observed in early lower-hybrid heating experiments on Versator for which $I_p \leq 40 \text{ kA}$, $V_i \approx 2.5 \text{ V}$, $Z_{eff}(\text{est.}) \approx 4-5$, $T_{i0} \leq 100 \text{ eV}$. In these experiments, ion tail production was always observed concurrently with the appearance of the parametric decay spectrum. Near the low density threshold for these effects, both were observed to disappear simultaneously if the plasma was moved slightly inward or the density changed by a small fraction.

The parametric decay strength, as measured by the difference in power between the peak level of the first lower side band and the peak level of the pump wave, is plotted versus line-averaged density in Fig. 6.16 for these plasmas. Also plotted for reference is the charge-exchange tail temperature. Both exhibit the same density threshold for enhancement. The parametric decay strength versus incident rf power has been shown previously in Fig. 6.2; the apparent threshold power for the onset of decay was found to be $P_o \lesssim 14 \text{ kW}$. Similar findings were previously obtained in experiments on the ATC tokamak, in which a low density threshold for both parametric decay and ion tail formation was observed.¹⁵ We can estimate the convective threshold power for the decay of the pump wave into cold lower-hybrid waves and either ion cyclotron waves or quasi-modes. The ratio of the threshold power for resonant decay into the waves to that for non-resonant decay into the quasi-modes is obtained from Eqs. (43c) and (43d) of Ref. 43:

$$\frac{P_o(\text{res})}{P_o(\text{non-res})} \approx \frac{6\pi\omega_2^3 R v_{the}}{L_{o2}\omega_{LH}^2\omega_o\omega_{ci}} \left(\frac{\omega_2^2}{\omega_{LH}^2} - 1 \right)^{-1} \quad (6.8)$$

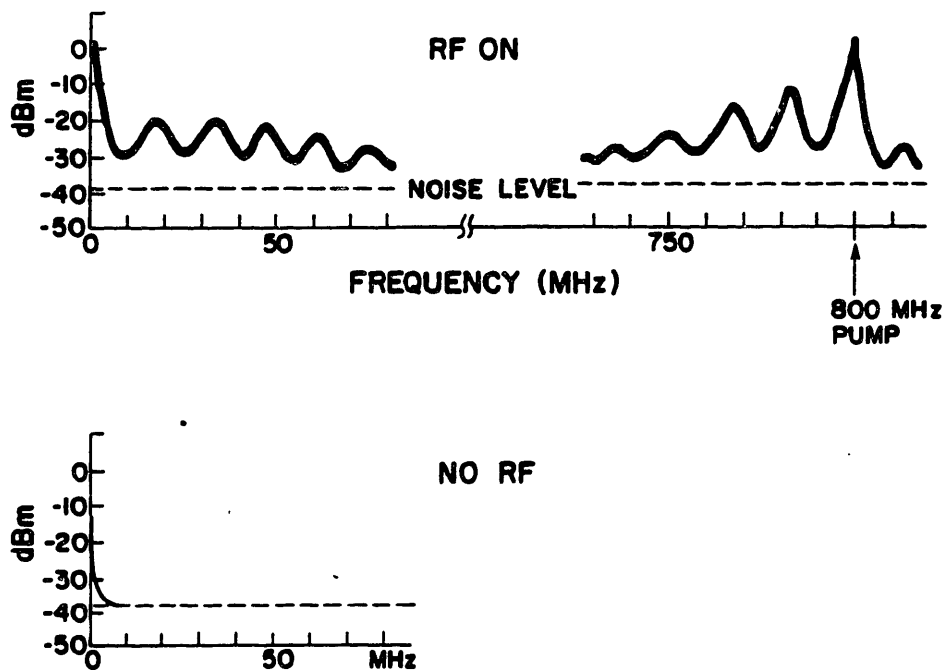


Figure 6.15. Parametric decay spectrum exhibiting low frequency decay waves near the ion cyclotron harmonics and matching high frequency pump wave sidebands. $P_{rf} = 30$ kW, $\bar{n}_e = 1.6 \times 10^{13}$ cm $^{-3}$. The dashed line indicates the noise level of the spectrum analyzer.

where $L_{oz} = 10$ cm. is the length of the grill in the z -direction and R is a numerical factor of order 0.5. The subscripts "o" and "2" refer to the pump and sideband, respectively. For plasma parameters typical of the outer layers ($r/a \approx 2/3$), we take $T_e = 100$ eV, $B_o = 11$ kG, and $\omega_2^2/\omega_{LH}^2 \approx 2.5$ to obtain

$$\frac{P_o(\text{res})}{P_o(\text{non-res})} \approx 10.$$

Therefore, we expect the decay into ion cyclotron quasi-modes to be predominant. The convective power threshold for this type of decay is given by Eq. (45) of Ref. 43:

$$P_o(\text{Watts}) = \frac{(3.8 \times 10^4) k_{o\parallel} L_{oy} C_s^3 B^2 \eta r \omega_{pi}^2 \left(\frac{\omega_o^2}{\omega_{LH}^2} - 1 \right)^{3/2}}{2\pi R n_{o\parallel} c \omega_2 \omega_o} \times \left| \frac{\omega_2^2}{\omega_{LH}^2} - 1 - \frac{3}{2} \frac{k^2 v_{the}^2}{\omega_2^2} \right| \quad (6.9)$$

where L_{oy} is the length of the grill in the poloidal, or y -direction, $C_s = \sqrt{T_e/m_i}$ is the ion sound speed, and $(\eta/\sqrt{2}) = (\omega_2/k_{\parallel 2} v_{the}) \gtrsim 3$. Substituting in values representative of the outer region of the Versator plasma ($r/a = 2/3$, $T_e = 100$ eV, $\omega_o^2/\omega_{LH}^2 \approx \omega_2^2/\omega_{LH}^2 = 2.5$, $\omega_{pi}^2/\omega_2^2 = 1.4$, $B = 11$ kG, $n_{\parallel} = 5$), we obtain a threshold of about 15 kW. For decay occurring near the limiter radius ($T_e \approx 30$ eV), the threshold is calculated to be only several kW. These low values are not inconsistent with the experimental value shown in Fig. 6.2.

As in other lower-hybrid heating experiments, it appears that the parametric decay may be responsible for the formation of the fast ion tail, either by ion cyclotron damping of the low frequency mode or by quasi-linear damping of the lower-hybrid sideband. The ion tail may be produced by damping of the parametric decay waves alone, or its strength may also be enhanced by damping of the pump wave itself on a "seed" ion tail in the manner illustrated in Figs. 2.11 and 2.12, in which the presence of an ion tail of modest density ($n_i \lesssim 0.01 n_i$) was shown to significantly increase the absorption of the lower-hybrid wave. Unfortunately, the radial location of the decay waves is not known in our experiment. The rf probe location for this set of measurements was on the midplane of the tokamak, 22.5° toroidally from the grill. The detected pump wave peak power was found to depend strongly on the relative phase between waveguides: the difference in amplitude of the pump wave was 13 dB between the cases of $\Delta\phi = +90^\circ$ and -90° . This asymmetric behavior is expected because of the travelling wave spectrum launched at this phasing (see Fig. 3.3) and has been confirmed by microwave scattering from the lower-hybrid wave in the edge plasma at a lower plasma density.⁵⁵ By contrast, the amplitudes of the lower sidebands are independent of the direction of the waveguide phasing, suggesting that the decay might not be occurring in the lower-hybrid field region near the plasma surface. On the other hand, the measured poor confinement of the ion tail in this experiment and others is consistent with the anomalous generation of an ion tail in the outer region of the plasma ($r/a \gtrsim 2/3$) where this type of parametric decay is expected to occur.

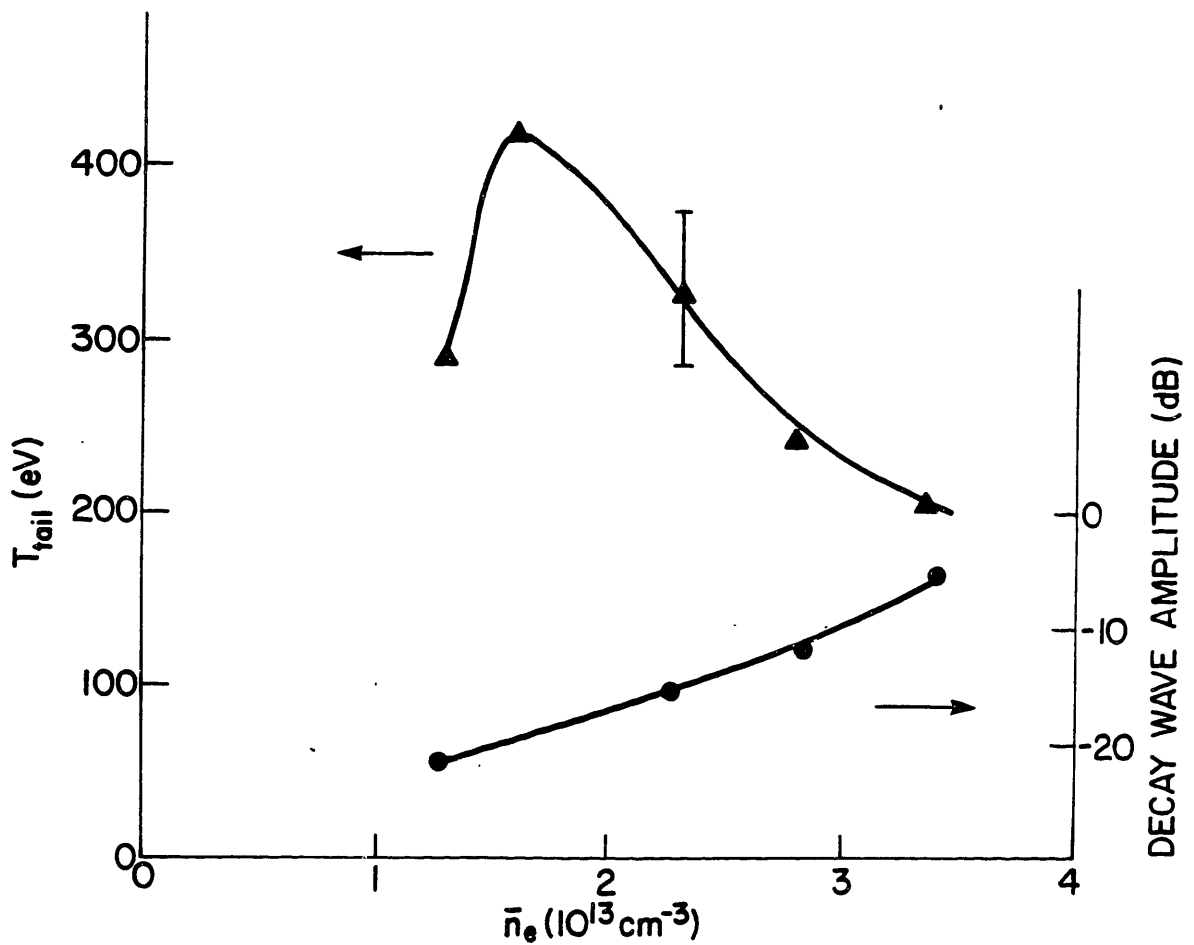


Figure 6.16. Relative strength of the first lower sideband versus line-averaged density for $P_{rf} \approx 30$ kW. Also shown is the charge-exchange tail temperature.

In more recent experiments in which most of the data presented in this chapter was taken, including the apparent ion heating inferred from VUV Doppler broadening measurements, a second type of parametric decay has also been observed. The decay is characterized by a broad spectrum extending from the pump frequency down to about 400 MHz (see Fig. 6.17a). The sideband plateau is approximately 30 to 40 dB below the pump in power, and the low frequency spectrum is comparable in power level to the sideband. Ion cyclotron harmonics are rarely observed, and if present at all, extend only a few dB above the broadband signal. In these experiments, the electromagnetic spectrum near the pump frequency was also measured with a loop antenna located directly outside a Pyrex window of the vacuum chamber (see Fig. 6.17b). The electromagnetic spectrum near the pump frequency is narrower than the electrostatic spectrum, and ion cyclotron peaks are more prominent. Furthermore, the spectrum is often characterized by a broad peak near 600 MHz. This feature is occasionally observed with the electrostatic probe, and in that case becomes more prominent relative to the background when the electrostatic probe is moved back from the plasma edge into a port. These facts indicate that the feature probably represents a long-wavelength electromagnetic mode. This electromagnetic peak has been observed previously in the JFT-2 lower-hybrid experiments, and is suggested to result from the non-linear decay of the electrostatic sidebands into electromagnetic whistler waves.⁴⁰ This type of decay is expected to occur only when further decay into lower-hybrid waves is impossible, i.e., where the sideband frequency is equal to the local lower hybrid frequency. For our plasma conditions, a lower hybrid frequency of 600 MHz corresponds to $n_e \simeq 2.1 \times 10^{13} \text{ cm}^{-3}$ which is present in the plasma during the ion heating experiments.

In the cases where the power dependence of the parametric decay has been measured, no clear power threshold (above 5 kW, at least) for the onset of the decay has been noted, and the features of the spectrum (low frequency and sideband plateau powers) are proportional to the transmitted rf power, as shown in Fig. 6.18.

No consistent variation in the decay spectrum is seen as the density is varied from $\bar{n}_e = 1.4$ to $3.2 \times 10^{13} \text{ cm}^{-3}$. In Fig. 6.19, we show the electrostatic and electromagnetic spectra measured in the same experimental run for the above two limits. Little difference between the two spectra is evident. (We remark that below a density of about $\bar{n}_e = 1.2 \times 10^{13} \text{ cm}^{-3}$ the spectrum near the pump frequency narrows dramatically with decreasing density). The lack of any change in the spectra is not surprising since the lower-hybrid frequency on axis in this density range only varies between 1.15 and 1.3 due to the low magnetic field. This fact suggests that the decay may be of the nonresonant type, i.e., decay into lower-hybrid waves (or ion plasma waves near the mode conversion layer) and ion quasi-modes.⁴³ The sideband frequency in this decay process is determined primarily by the local lower-hybrid frequency. The broad frequency spectrum of the decay wave suggests that the decay may be occurring near the mode conversion layer. If this is indeed the case, this type of parametric decay could lead to improved central heating efficiencies,⁴⁰ as opposed to parametric decay taking place at the edge which is believed to be a loss mechanism

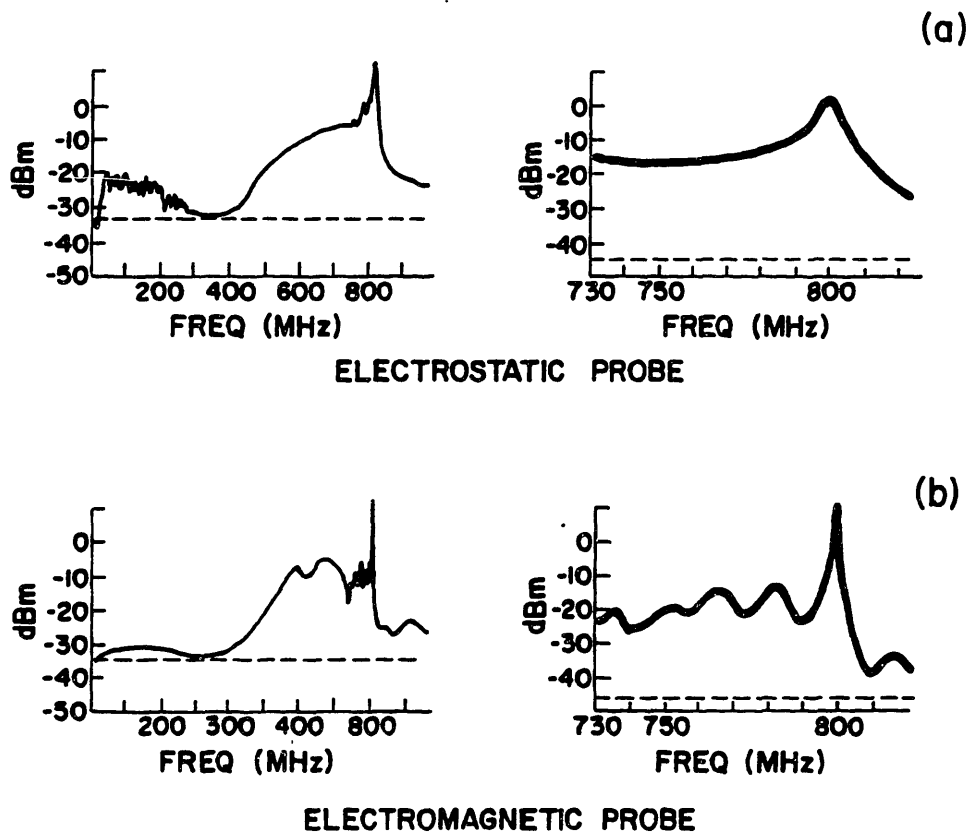


Figure 6.17. (a) Electrostatic and (b) electromagnetic decay wave spectra in "clean" plasma experiments at $\bar{n}_e = 2.4 \times 10^{13} \text{ cm}^{-3}$ and $P_{rf} = 65 \text{ kW}$. The full spectra from 0 to 800 MHz are shown in the left-hand diagrams, while the detailed spectra near the pump frequency are illustrated in the right-hand diagrams. The noise level of the analyzer in each diagram is indicated by the dashed line.

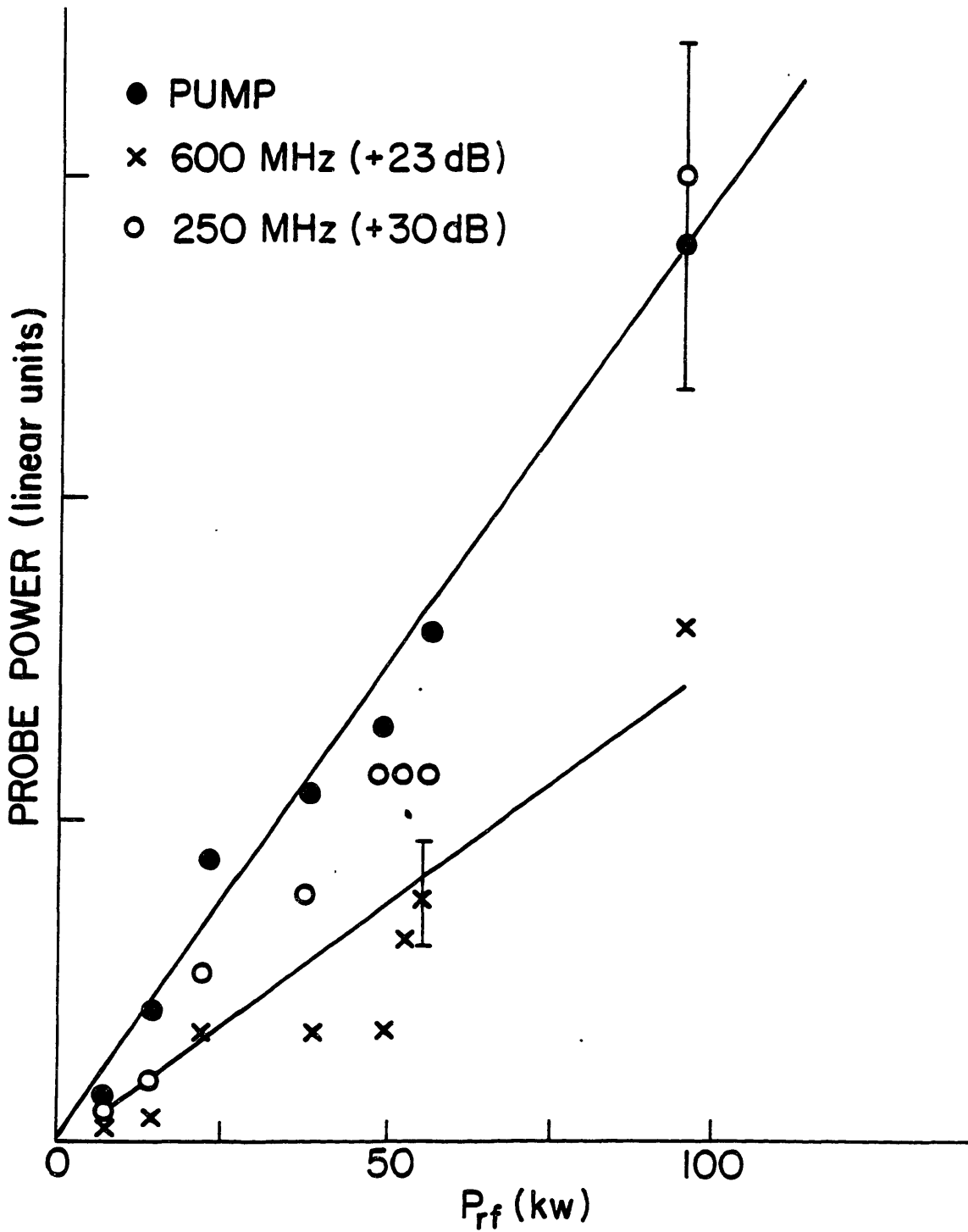


Figure 6.18. Variation of sideband power (600 MHz) and low frequency decay wave power (200 MHz) with transmitted rf power at $\bar{n}_e = 2.5 \times 10^{13} \text{ cm}^{-3}$

for the incoming pump wave. As before, parametric decay was always present when an ion tail was observed, but we did not carry out a quantitative comparison between the density thresholds of the two phenomena.

As before, we may compare the experimental threshold to the theoretical value for non-resonant decay near the mode conversion layer. The convective threshold for this decay is given by Eq. (46) of Ref. 43:

$$P_o(\text{Watts}) = \frac{(3.8 \times 10^4) g B^2 C_s^2 L_{oy} r}{n_{o\parallel} R k_{\perp}^2 c^2} \frac{L_{oz}}{a} \left(\frac{m_i}{m_e} \right)^{1/2} \frac{\omega_{pi}^2}{\omega_2^2} \left(\frac{\omega_o^2}{\omega_{LH}^2} - 1 \right)^{1/2} \times \left| \frac{\omega_2^2}{\omega_{LH}^2} - 1 - \frac{3k^2 v_{thi}^2}{\omega_2^2} \right| \quad (6.10)$$

where $g = k_{oz} L_{oz} / 2\pi \approx 1$. Following Ref. 43, we take

$$\frac{\omega_2^2}{\omega_{LH}^2} - 1 \approx \frac{3}{2} \frac{k^2 v_{thi}^2}{\omega_2^2}, \quad (6.11)$$

and choose $T_e = 300$ eV, $T_i = 120$ eV, $r/a = 0.3$, $\omega_o^2/\omega_{LH}^2 = 2$, $B_o = 14$ kG, and $\omega_{pi}^2/\omega_2^2 = 4$. The estimated threshold power is only 3 kW, which is not in disagreement with the measured value of < 5 kW, though we note that the uncertainties inherent in performing this calculation are large. In particular, we note that for the above estimate, the pump wave is assumed to propagate within a resonance cone. As discussed earlier, this may not be a valid model of wave propagation in a tokamak.

Spectral components at the second harmonic of the pump frequency are also present in the spectrum (see Fig. 6.20). These are not related to the weak harmonic generation of the klystron but apparently to a non-linear process in the plasma, such as the pump wave beating with itself. This behavior has been observed for ion acoustic waves in a linear device,¹⁴² and it has also been noted in a particle simulation of lower-hybrid wave propagation.⁶⁹ The relationship of the second harmonic generation to the heating process is unclear.

In conclusion, the decay of the pump wave generally appears to be correlated with the appearance of the fast neutral flux, and is very likely to be responsible for many of the effects described in the previous sections. For example, the lack of strong phase dependence of the fast ion count-rate during rf injection (see Fig. 6.4) may be explicable if the radius of wave damping is determined by the location of parametric decay rather than the linear processes described in Chapter 2. Unfortunately, neither the position of the parametric decay in the plasma nor the radial distribution of the fast ion tail are known. Such measurements should be made in future experiments to resolve the physical mechanism of lower-hybrid heating.

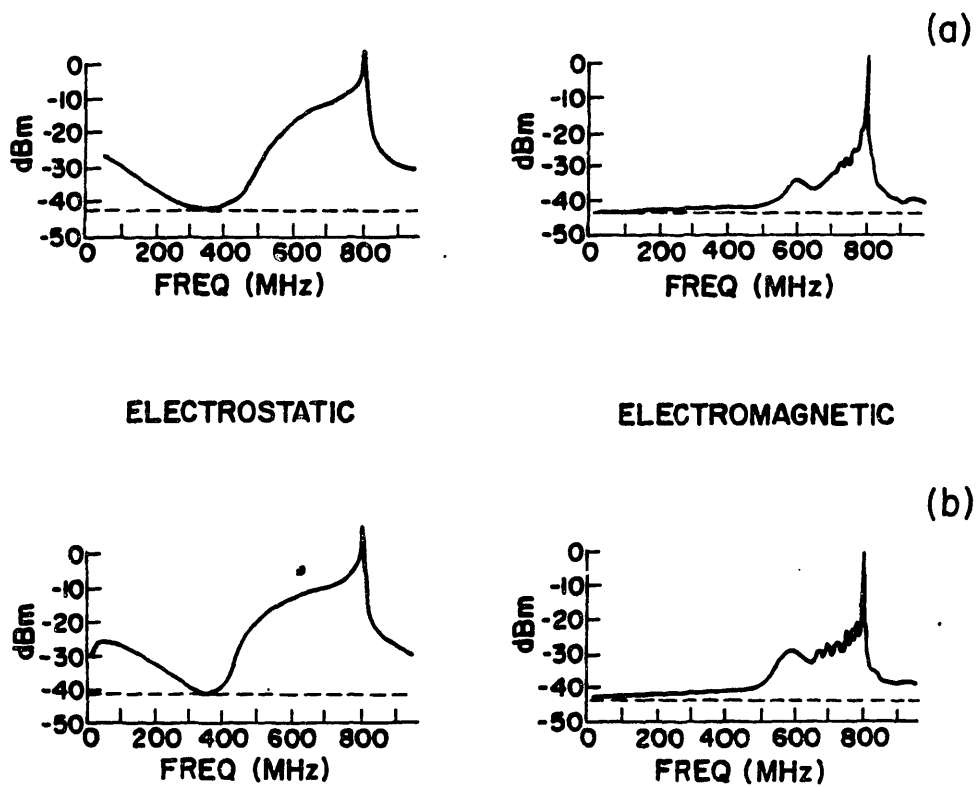


Figure 6.19. Electrostatic and electromagnetic decay spectra near the 800 MHz pump frequency for $P_{rf} = 60$ kW and (a) $\bar{n}_e = 1.4 \times 10^{13} \text{ cm}^{-3}$ and (b) $\bar{n}_e = 3.2 \times 10^{13} \text{ cm}^{-3}$. The noise level of the spectrum analyzer is indicated by the dashed line.

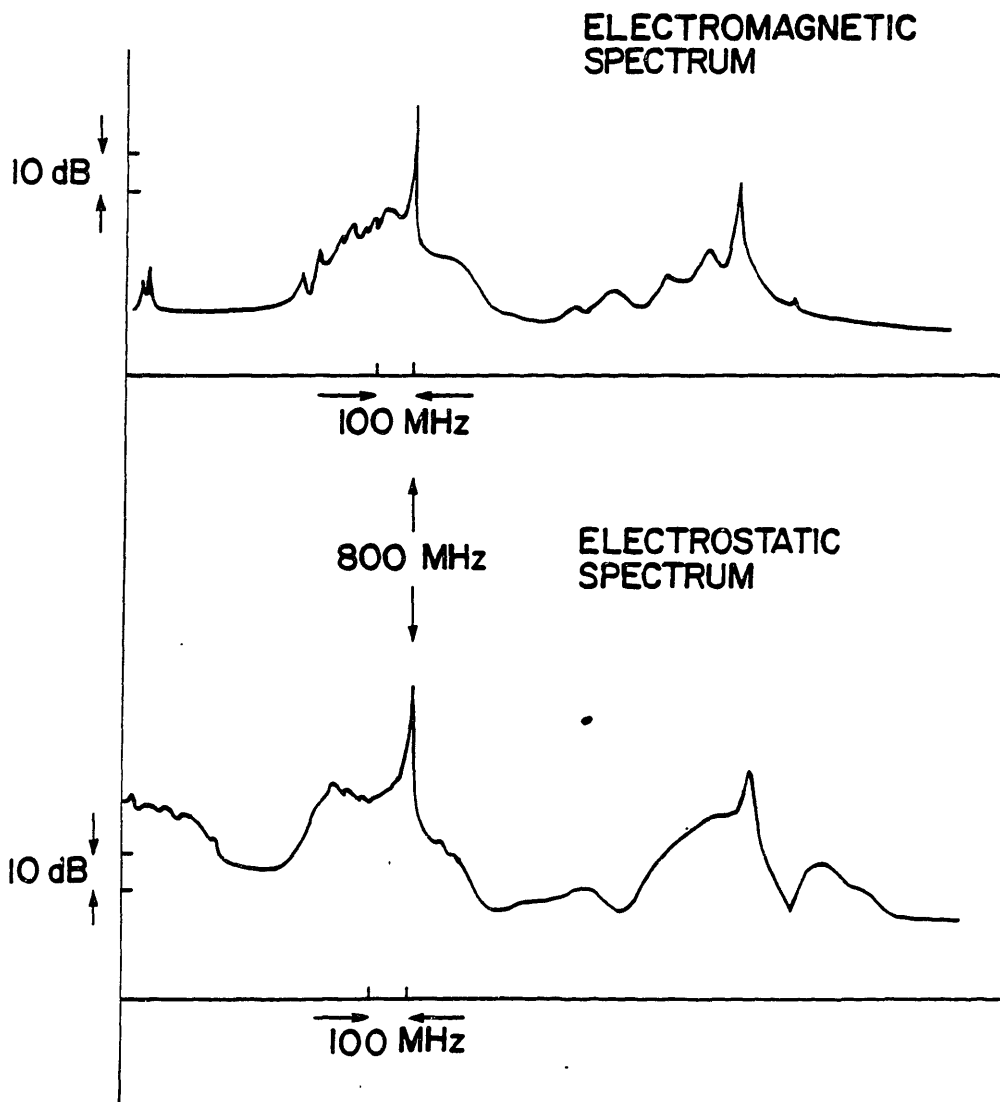


Figure 6.20. Electromagnetic and electrostatic decay spectra showing features at the second harmonic of the pump frequency. $P_{rf} = 100 \text{ kW}$, and $\bar{n}_e = 2.2 \times 10^{13} \text{ cm}^{-3}$

6.1.6. Off-Perpendicular Charge-Exchange Measurements

As discussed in Chapter 2, the energetic ions must be confined for a sufficient duration if thermalization of the tail is to occur. The time scale for thermalization is somewhat greater than for 90° scattering for collisions of fast protons on the background plasma,

$$\frac{\nu_{\perp}}{\nu_{\text{therm}}} \approx Z_{\text{eff}}. \quad (6.12)$$

Thus, if a significant ion tail oriented in the parallel direction is present during rf injection, one can conclude that thermalization of the fast ions is also taking place. As discussed in Chapter 1, parallel ion tails have been observed in a number of lower-hybrid heating experiments in which bulk heating is also reported. We have performed similar measurements for which the charge-exchange analyzer was moved from its near-perpendicular orientation to an adjacent port which allowed the sight-line of the analyzer to intersect the magnetic axis at an angle of 45° . In these experiments, no evidence of a parallel tail was obtained from the charge-exchange spectrum (see Fig. 6.21). On several runs, parallel charge-exchange analysis indicated a slight rise ($T_{i\parallel} \leq 20$ eV) in the apparent bulk temperature (with no tail on the spectrum) but VUV measurements showed no increase in the central impurity species temperature. Given that the charge-exchange measurements are typically recorded for ion energies in the range from 500 to 1500 eV, the apparent temperature increase probably represents a weak tail in the off-perpendicular ion distribution.

The charge-exchange analyzer in this off-perpendicular configuration detects ions moving counter to the plasma current direction. As the plasma current and toroidal field are in opposite direction on Versator, it is these particles which are most poorly confined. The pitch angle for the least well-confined ions has been calculated in Appendix B, and is plotted versus minimum orbit radius in Fig. 2.13. The value of the pitch angle is approximately 60° . Perpendicular ions accelerated by the rf must scatter through this region before being sampled by the off-perpendicular neutral analyzer. Consequently, this orientation of the analyzer provides a stringent test for isotropization of the tail ions. Observation of a tail would clearly indicate that good confinement of fast ions is possible and thermalization likely. The fact that such a tail is not observed does not necessarily preclude some isotropization of the tail in the co-moving direction, but certainly suggests that a loss region for fast particles is effective and that efficient heating is indeed unlikely, as predicted in Chapter 2. The lack of a parallel tail suggests that the rapid decay time of the perpendicular fast ion represents a "true" loss of ions in a time period shorter than the 90° scattering time. In the series of runs performed following the switch to the off-perpendicular neutral analyzer position, little ($\Delta T_{i\parallel} \leq 30$ eV) or no bulk heating was ever detected by VUV spectroscopy; this is in agreement with the charge-exchange results described above.

6.1.7. Variability of the Ion Heating Results

It was mentioned in Section 6.1.2 that the increases in the bulk ion temperature measured by Doppler broadening were found to be irreproducible and, in fact, were achieved only rarely. The

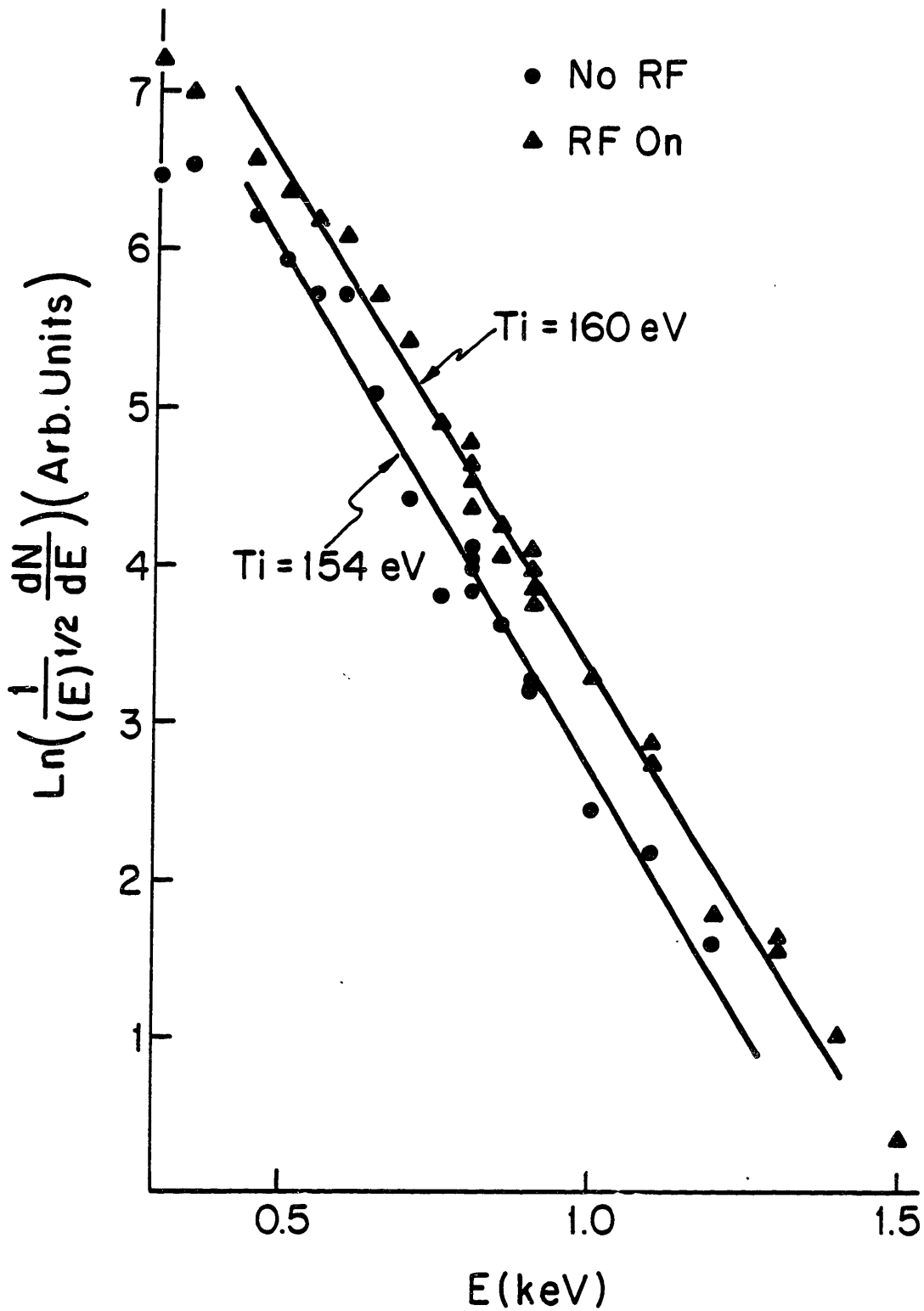


Figure 6.21. Charge-exchange tail at an orientation of 45° to the magnetic axis for the cases of $P_{rf} = 100 \text{ kW}$ and no rf at $\bar{n}_e = 2.5 \times 10^{13} \text{ cm}^{-3}$

attempt to achieve consistent results, or to understand the reason for the variability, has proven to be difficult and we have not obtained evidence for a conclusive explanation of the phenomenon.

Our investigation of this problem has centered on the edge properties of the plasma, specifically the electron temperature in the limiter shadow. Variations in the bulk heating efficiency by roughly a factor of 3 have been reported in lower-hybrid ion heating experiments on the JFT-2 tokamak.³⁰ In those studies, the heating efficiency depended on the electron temperature in the shadow of the limiter, with higher efficiencies being associated with larger edge temperatures. The level of parametric decay was also correlated with the edge temperature in those experiments, with the explanation that higher thresholds for parametric decay result from by higher local electron temperatures.⁴³ The decrease in heating efficiency is blamed upon loss of rf energy from the pump wave to the decay waves. As discussed in Section 2.6 of Chapter 2, the total collisional damping of the lower-hybrid wave can also be expected to vary significantly with the edge temperature since the wave trajectory traverses the edge region many times if toroidal effects on wave propagation are considered (see Figs. 2.15–2.19). Consequently, we have monitored the electron temperature with a Langmuir probe situated 0.5–1 cm. behind the edge of the limiter. The temperature at this location generally has been found to be 12–26 eV with no variation that can be correlated to the heating behavior of the plasma. For the heating data presented in Section 6.1.2, the edge electron temperature was measured to be 15 eV, near the lower end of the above range. No variation in the parametric decay spectrum is ascribed to the measured difference in the electron temperature, although the lack of strong features in our spectra make a comparison between different spectra somewhat qualitative.

At high plasma densities ($\bar{n}_e \geq 3 \times 10^{13} \text{ cm}^{-3}$), the plasma edge density and temperature have occasionally been observed to drop suddenly by a factor of 2–3 during the discharge, suggesting that the plasma column is unstable at these high densities and that the profiles have a tendency to contract. Little difference is noted between the parametric spectra obtained in the cases with and without contraction. In summary, we have not been able to relate the occurrence of an apparent ion temperature increase from Doppler broadening to specific ranges of edge temperature or strength of parametric decay.

Regarding collisional damping, we recall from Chapter 2 that the collisional damping should be strongest several centimeters inside the limiter radius. Electron temperatures are not routinely measured at this location; therefore, we cannot state with certainty that important temperature variations in this region did not occur over the course of these studies. An experiment was performed in which the NRL gyrotron (90 kW at 35 GHz)⁵⁶ was used in an attempt to heat the edge plasma by electron cyclotron resonance absorption. The toroidal field was set such that the cyclotron resonance (12.5 kG) lay approximately 7 cm. to the outside of the plasma axis. However, neither central nor edge electron heating was observed: according to Thomson scattering measurements, T_e at $r = 0$ remained at 450 ± 50 eV while T_e at $r = .88a$ remained at 80 ± 13

eV whether or not electron cyclotron or lower-hybrid waves were injected. Not surprisingly, no improvement in the ion heating efficiency was observed in this experiment.

In principle, variations in the impurity level of the plasma could give rise to different heating results. As discussed in Chapter 2, the impurity level can alter the propagation of the lower-hybrid wave, particularly with regard to the mode conversion density. The distribution of impurities in the plasma should also affect the electron temperature profile. It was mentioned earlier that the density often increases or decreases during rf injection, with the polarity of the shift determined by the suspected relative cleanliness of the vacuum vessel wall and/or the impurity content of the fill gas. We note that the apparent ion temperature increases have occurred only in cases in which the density is observed to drop during the rf pulse (without a correcting gas puff). However, on other occasions, we have obtained no measurable heating in plasmas of similar densities in which the density was also observed to decrease during rf injection; hence these observations may not be relevant to the issue of irreproducibility of heating. A deliberate attempt to change the plasma impurity level was made in which a set of heating experiments in gettered discharges was performed immediately following a set in ungettered discharges. The experiment did not prove to be fruitful as no heating was observed in either case. As expected, the plasma temperatures were lower in the gettered case, indicating that the gettered plasma was probably cleaner than the ungettered one. Therefore, we cannot conclude that the impurity content of the plasma has had a definite relationship to the observed heating behavior, although it is possible that rf injection may influence the influx of impurities in a variable manner.

Finally, we remark that moving the position of the grill with respect to the plasma, or changing the in-out equilibrium position of the plasma by a centimeter or two did not appear to have any beneficial effect on the heating efficiency. In conclusion, the question of the variation in the observed bulk heating has not been answered by the experimental data of this study. It is possible that subtle changes in the toroidal wave propagation path may be responsible for the irreproducibility of the ion heating. Further conjectures and suggestions for future work along this line will be put forth in the next chapter.

6.2. Electron Heating Experiments with the Side-Launching Antenna

A search for bulk electron heating has also been performed over the density range $\bar{n}_e = 1-3 \times 10^{13} \text{ cm}^{-3}$. Measurements of electron temperature were made with both Thomson scattering and soft X-ray spectroscopy. For $\bar{n}_e \leq 2.0 \times 10^{13} \text{ cm}^{-3}$ rf injection was observed to produce an energetic tail on the electron distribution, which was inferred from soft X-ray spectra. An example is shown in Fig. 6.22 for the case of $\bar{n}_e = 2.0 \times 10^{13} \text{ cm}^{-3}$, $P_{rf} = 100 \text{ kW}$ and $\Delta\phi = 180^\circ$. Before rf injection, there is only a small suprathermal electron tail present in the plasma. In the 5 msec period following the rf pulse, a relatively large electron tail is still present. However, no bulk heating of the electron distribution has been recorded at any plasma density in the above range. For discharges in the density span $\bar{n}_e = 1.0-2.6 \times 10^{13} \text{ cm}^{-3}$ into which

60–100 kW net rf power is injected, no significant change in the slope of the thermal part of the soft X-ray spectrum is observed. Thomson scattering experiments in plasmas with $\bar{n}_e = 2.5\text{--}3.0 \times 10^{13} \text{ cm.}^{-3}$ show that neither the central electron temperature nor the temperature profile is altered by rf injection. No increase in the overall hard X-ray flux was noted, and except at the lowest density of $\bar{n}_e = 1.0 \times 10^{13} \text{ cm.}^{-3}$ no change in the loop voltage took place during rf injection. In the low density experiment just mentioned, the loop voltage was sometimes observed to drop by a maximum of 10% during the rf pulse. The criterion for whether or not a loop voltage change occurred in this particular experiment was related to the plasma position: if the equilibrium position of the plasma on a particular shot lay to the inside of the normal equilibrium position on the chamber axis ($\Delta r \approx -2 \text{ cm.}$, typically), a loop voltage drop of the above magnitude was noted during the rf pulse, and an increase in the intensity of the metallic impurity lines of the soft x-ray spectra was also observed. The meaning of this last observation is not entirely clear, but the lack of any bulk heating suggests that the change in loop voltage is probably related to a current-drive or superthermal electron effect rather than plasma heating.⁴⁶

The density range for rf effects on the electron population and the lack of electron heating with rf injection are generally consistent with the cylindrical slab model predictions of Chapter 2. As shown in Fig. 2.7 and 3.3, the characteristic n_{\parallel} values of the four-waveguide grill are too low for significant electron Landau damping to occur. Absorption that does take place will be on high energy electrons ($\mathcal{E}_e(\text{res}) \approx 20 \text{ keV}$ for $n_{\parallel} = 5$). The slowing time of such electrons for $n_e = 3 \times 10^{13} \text{ cm.}^{-3}$ and $Z_{eff} \approx 2$ is about 0.4 msec. The fact that an electron tail persists for a length of time longer than the collision time suggests that the electron tail created by the rf is maintained by the ohmic heating electric field. The critical electron energy for runaway is found by setting the force due to the OH field equal to that of the collisional drag:

$$\dot{m}\nu_s v_e = eE_{OH} \quad (6.13)$$

where ν_s is the collision frequency for the slowing down of fast electrons,⁹⁹

$$\nu_s \approx 3.9 \times 10^{-6} n_e \ln \Lambda (2 + Z_{eff}) [\mathcal{E}_e (\text{eV})]^{-3/2} \quad (6.14)$$

For the parameters used just previously and $E_{OH} = 8 \times 10^{-3} \text{ V/cm.}$ ($V_l \approx 2 \text{ V}$) we find the electron runaway energy to be approximately 30 keV, or not much higher than the expected wave-particle resonant energy. Consequently, electron heating with the side-launching grill can be expected to be inefficient, since a significant fraction of the wave energy may be transferred to nearly collisionless electrons.

If toroidal ray tracing is taken into account, electron Landau damping can also occur, as illustrated in Fig. 2.18, but only at large minor radii. Electron heating in this case should also be inefficient. In conclusion, it is perhaps not surprising that our experiments have evidenced no significant electron heating.

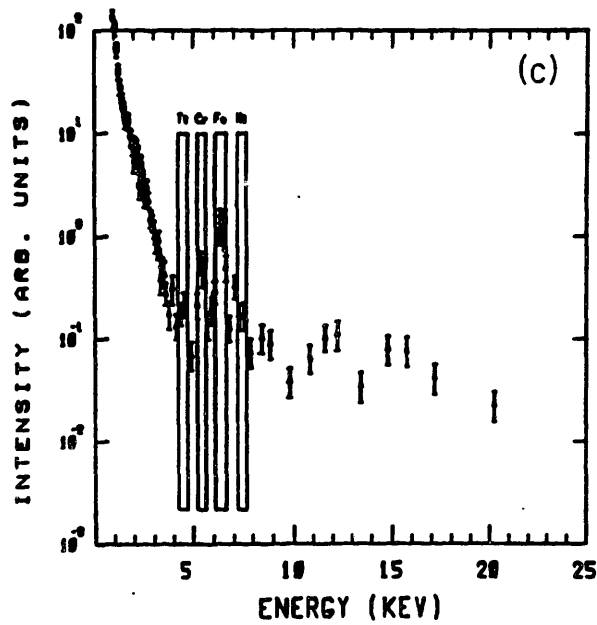
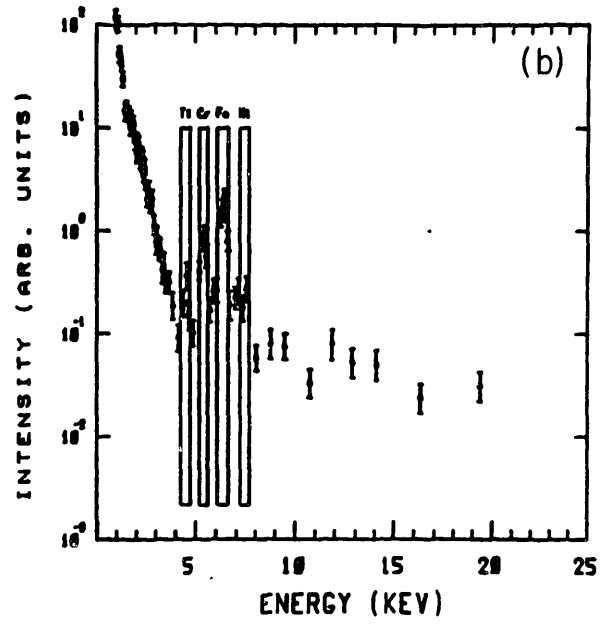
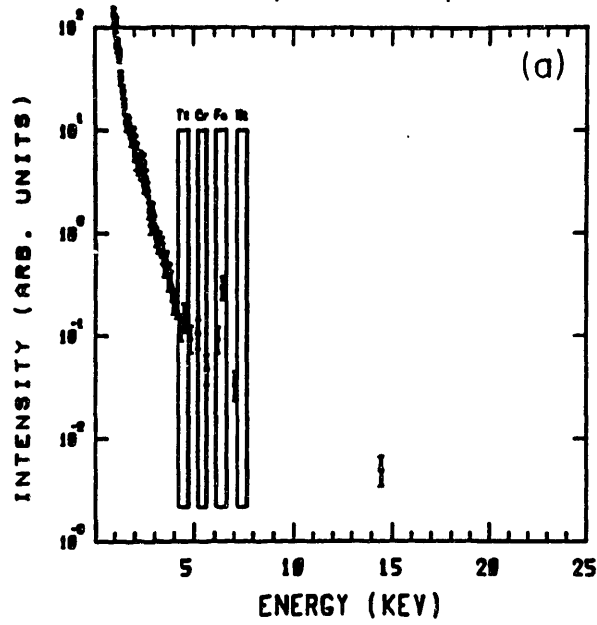


Figure 6.22. Soft X-ray spectra for the 5 msec. time periods (a) before; (b) during; and (c) after the rf pulse. $P_{rf} = 100$ kW, $\Delta\phi = 180^\circ$, $\bar{n}_e = 2.0 \times 10^{13}$ cm $^{-3}$. The vertical boxes in the diagrams enclose the spectral line emission peaks from (left to right) titanium, chromium, iron, and nickel.

6.3. Ion Heating Experiments using the Top-launching Antenna

The possibility of ion heating by lower-hybrid waves launched from the top of the torus has been investigated in a short set of experiments using the four-waveguide top-launching grill described in Chapters 2 and 3. The $n_{||}$ spectrum of this grill has been shown previously in Fig. 3.4, and is characterized by values of $n_{||} \leq 25$. The plasma conditions for these experiments were set to be similar to those for the side launching experiments described earlier in this chapter. The maximum transmitted rf power in these experiments was approximately 100 kW.

Over the density range of this study ($\bar{n}_e = 1.2\text{--}3.2 \times 10^{13} \text{ cm}^{-3}$) VUV Doppler broadening measurements showed no evidence of ion bulk heating at any density or at any radial location. The intensity of the O V line (located at $r \approx 10 \text{ cm.}$) was often observed to increase by up to 30% during rf injection over a wide density range, but the temperature of the species remained constant. The emission of other impurity species (O VII, C V, and C III) did not measurably change during the rf pulse.

On the other hand, the near-perpendicular neutral flux measured by charge-exchange showed a strong increase with rf injection. A comparison between the cases of rf on and rf off is shown in Fig. 6.23 for $P_{rf} = 100 \text{ kW}$, $\Delta\phi = 90^\circ$, $B_o = 14 \text{ kG}$, and $\bar{n}_e = 2.6 \times 10^{13} \text{ cm}^{-3}$. In contrast to the results for the side-launching antenna, the spectrum in the energy range 500–1000 eV exhibits a clear decrease in slope, suggesting that an apparent increase of 50 eV in the central ion temperature takes place during rf injection. This enhancement of the neutral flux at the lower energies is evident for all densities in the range $\bar{n}_e = 1.8\text{--}3.2 \times 10^{13} \text{ cm}^{-3}$. Below this density, an increase in neutral flux with rf injection was also observed, but charge-exchange spectra were not taken. The apparent increase in bulk temperature from perpendicular charge-exchange analysis is plotted versus line-averaged density in Fig. 6.24. The temperature rise above the initial central ion temperature is not a strong function of density. A fast ion tail is observed at high densities. At a density of $\bar{n}_e = 3.2 \times 10^{13} \text{ cm}^{-3}$ the tail temperature is approximately 400 eV, as illustrated in Fig. 6.25.

The apparent temperature increase is dependent on the relative phase between waveguides, with the maximum increase occurring at the lowest phase angles. The time evolution of the ion temperature inferred from perpendicular charge-exchange is shown in Fig. 6.26a for $\Delta\phi = \pm 90^\circ$ and 180° at $P_{rf} = 100 \text{ kW}$ and $\bar{n}_e = 2.6 \times 10^{13} \text{ cm}^{-3}$. For comparison, the central ion temperature measured by Doppler broadening of the O VII line during the same run is shown in Fig. 6.26b. Though no bulk heating is observed, the decrease in the slope of the charge-exchange spectrum varies with $\Delta\phi$, but is the same for $\Delta\phi = +90^\circ$ and $\Delta\phi = -90^\circ$. The value of $\Delta T_{i\perp}$ from charge-exchange measurements is plotted in Fig. 6.27 versus $\Delta\phi$. Plotted in Fig. 6.28 is a more detailed phase scan of the enhancement during rf of the 800 eV ion count-rate (total count-rate minus the count-rate during ohmic discharges). Both figures show a strong peaking of the neutral flux at the low phase angles. The relative flux is also symmetric with respect to the sign of the

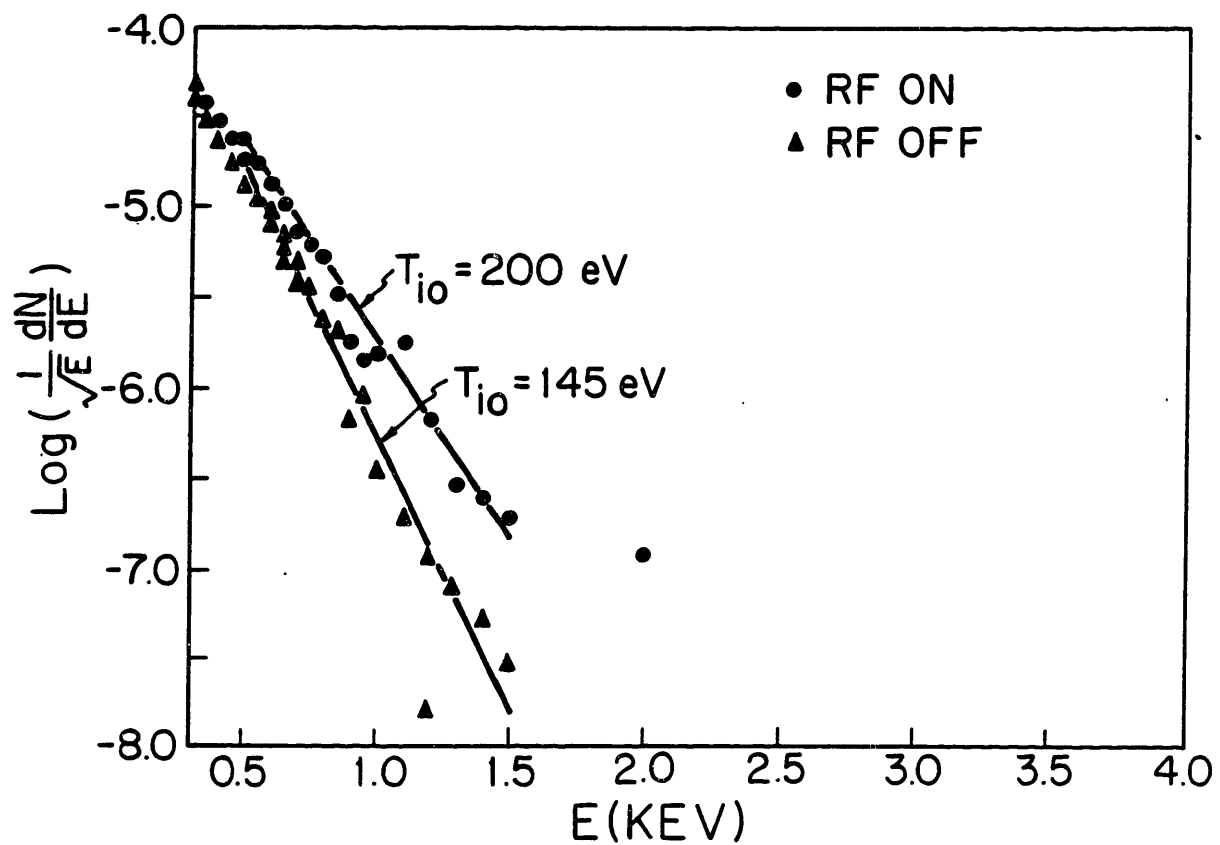


Figure 6.23. Perpendicular charge-exchange spectra during top-launching rf injection; $P_{rf} = 100$ kW, $\Delta\phi = 90^\circ$, $\bar{n}_e = 2.6 \times 10^{13} \text{ cm}^{-3}$, $B_0 = 14$ kG.

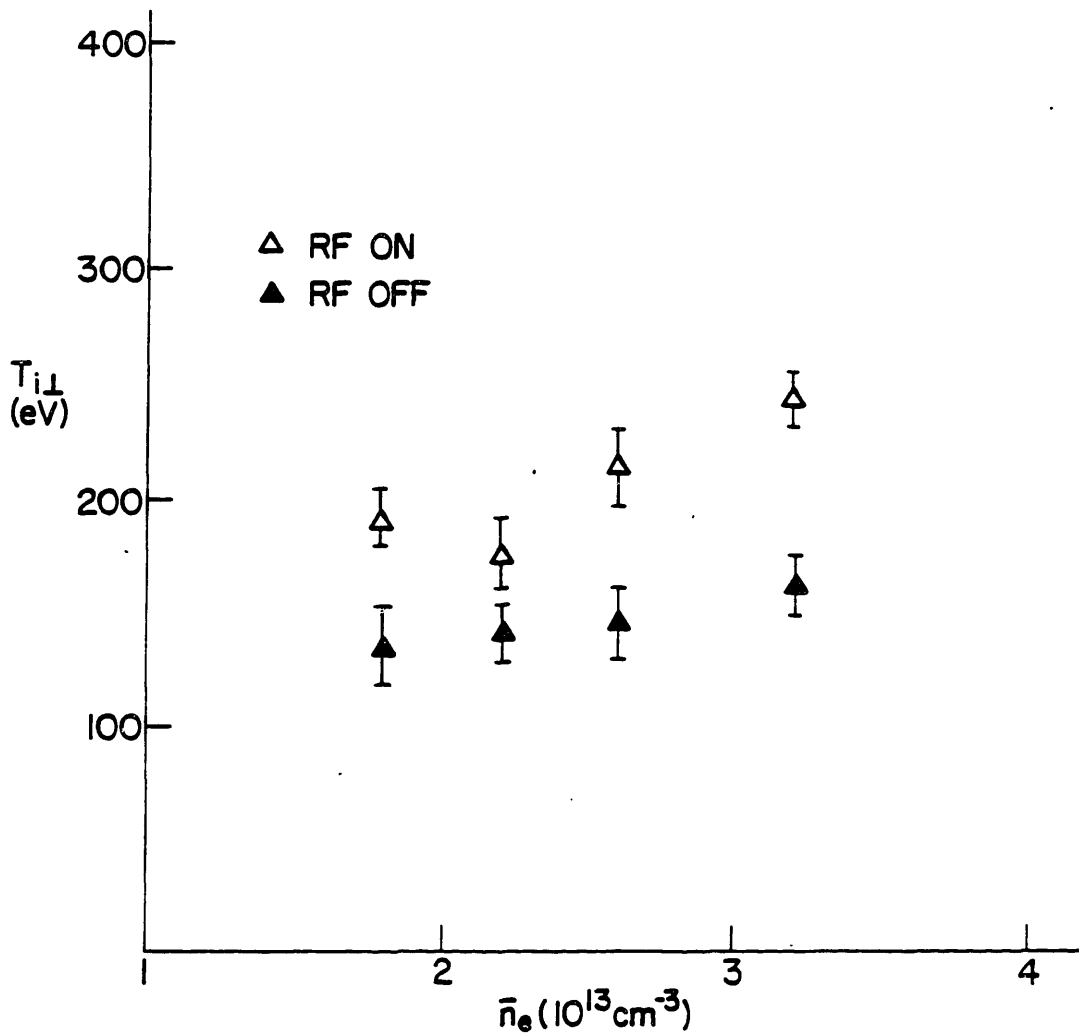


Figure 6.24. Central ion temperature inferred from perpendicular charge-exchange versus line-averaged density for $P_{rf} = 100$ kW.

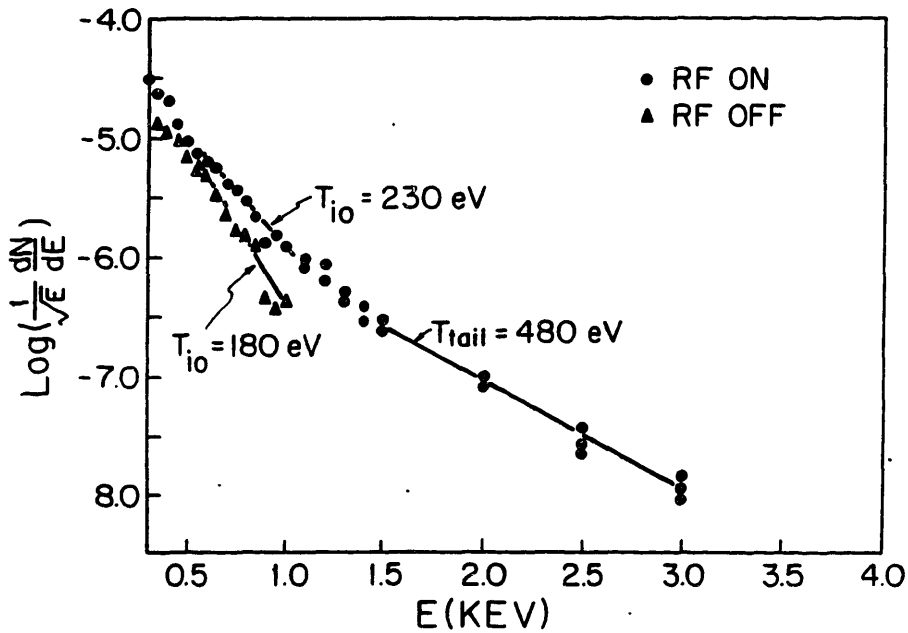
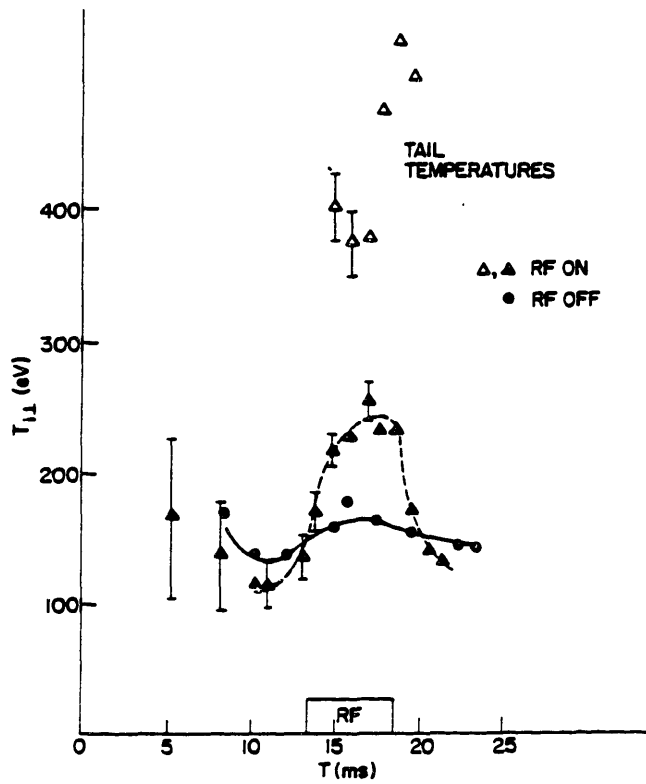


Figure 6.25. (a) Perpendicular charge-exchange spectrum for the same parameters as Fig. 6.23, except that $\bar{n}_e = 3.2 \times 10^{13} \text{ cm}^{-3}$ (b) Temporal evolution of apparent temperature increase and tail temperature for the above case.

waveguide phase. This result is unexpected in light of the arguments made in Section 2.6 of Chapter 2, in which lower-hybrid wave propagation was found to be very different for waves launched from the top with identical values of $|n_{\parallel}|$ but different sign.

The apparent ion temperature increase indicated by charge-exchange analysis is not believed to represent an actual increase in bulk temperature, but most likely results from a tail created in the ion distribution near the edge of the plasma. As in the case of heating with the side-launching antenna, the estimated decay time of the neutral flux enhancement was no more than 200 μsec , based on direct observation of the detected pulses on a fast time scale following the termination of the rf pulse. Furthermore, the lack of any increase in the ion temperatures inferred from VUV Doppler broadening indeed suggests that ion heating did not occur in this set of experiments.

The line-averaged bolometric emission is plotted versus chord height in Fig. 6.29 for the conditions $\bar{n}_e = 2.4 \times 10^{13} \text{ cm}^{-3}$, $P_{rf} = 85 \text{ kW}$, and $\Delta\phi = 45^\circ$. The profile is strongly asymmetric with the larger amount of radiation being emitted from the upper half of the plasma column, which is opposite from the case of the earlier side-launching experiments in which the radiation was stronger from the lower half of the plasma. The emission during rf is enhanced by only a factor of 1.2 in these top launching experiments. As shown in Fig. 6.30, the increase in bolometric emission during rf injection is only weakly dependent on the relative phase between waveguides.

As with the bolometric measurements described in Section 6.1.4, the emission profile is more symmetric at lower plasma densities. At line-averaged densities $\bar{n}_e \leq 1 \times 10^{13} \text{ cm}^{-3}$ the profile of bolometric emission was measured to be symmetric about the axis of the plasma.¹⁴³ At these low densities, there is no increase in emission with rf injection.

For this set of experiments, the density remained constant or increased slightly ($\Delta\bar{n}_e/\bar{n}_e < 10\%$) during the rf pulse relative to shots with no rf injection. The H_α and H_β light detected by a visible monochromator viewing the bottom limiter from the top of the plasma column was observed to increase during the rf pulse by 5–10%, independent of the waveguide phasing. The rise in the light level indicates an increase in ionization at the plasma edge, possibly by an increase in recycling due to energetic ion or neutral bombardment of the wall, and is consistent with the observation of a small density increase during the rf pulse.

No attempt has been made to investigate the possibility of electron heating in high power experiments with the top launching antenna. In the studies described above, however, no change in loop voltage with rf injection was ever observed in the given density range $\bar{n}_e = 1.2\text{--}3.2 \times 10^{13} \text{ cm}^{-3}$. Therefore, it is unlikely that significant bulk electron heating took place in these experiments.

6.3.1. Interpretation of the Top Launching Experiments

Though no measurable ion heating was observed in these top-launching experiments, the results are of interest because of their differences from the side-launching observations, particularly

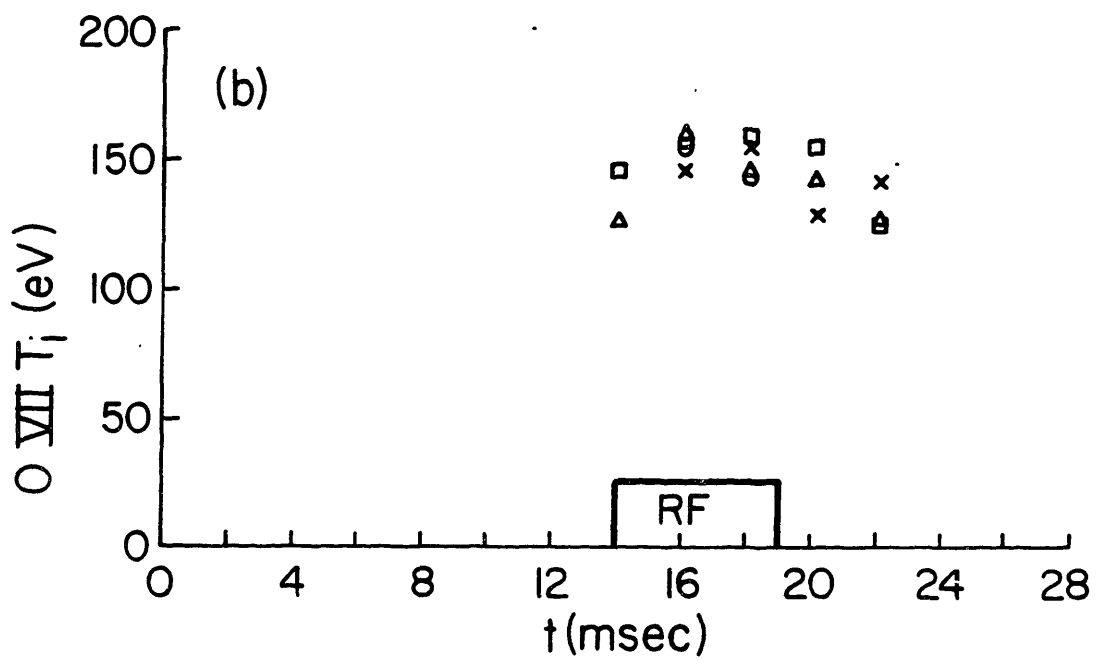
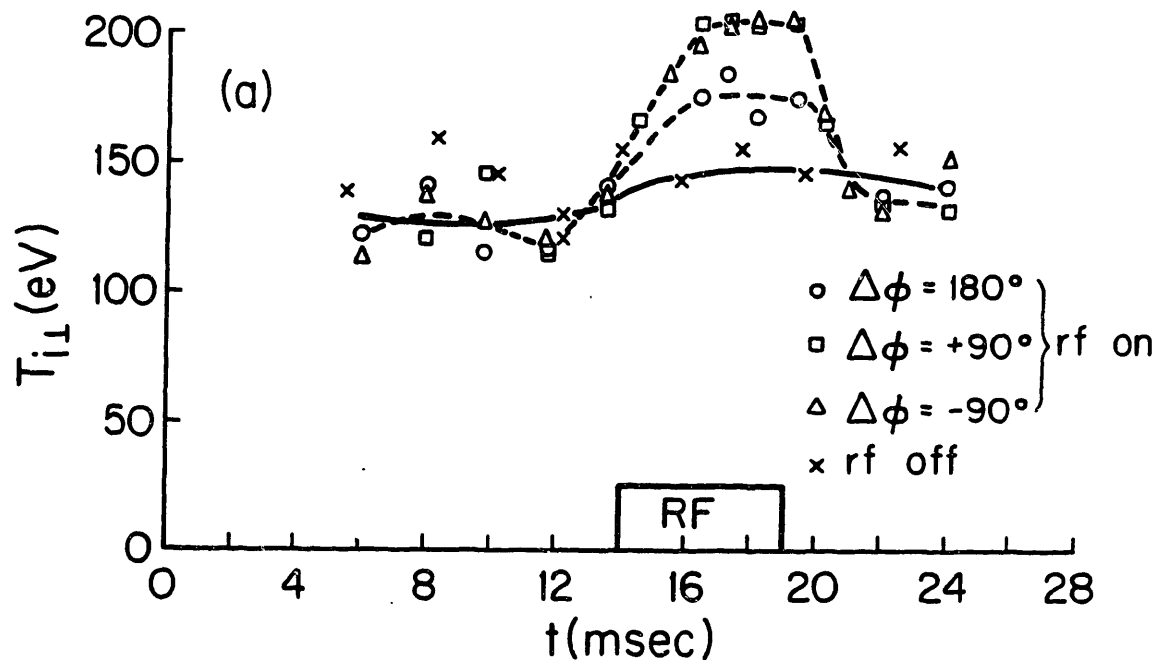


Figure 6.26. Temporal evolution of the central ion temperature during rf injection with the top-launcher as measured by: (a) Perpendicular charge-exchange; and (b) VUV Doppler broadening of the O VII 1623Å line for the cases of $\Delta\phi = +90^\circ$ (open squares), $\Delta\phi = -90^\circ$ (open triangles), and $\Delta\phi = 180^\circ$ (open circles) at $P_{rf} = 100$ kW, and no rf injection (x's). The plasma density is $\bar{n}_e = 2.6 \times 10^{13} \text{ cm}^{-3}$.

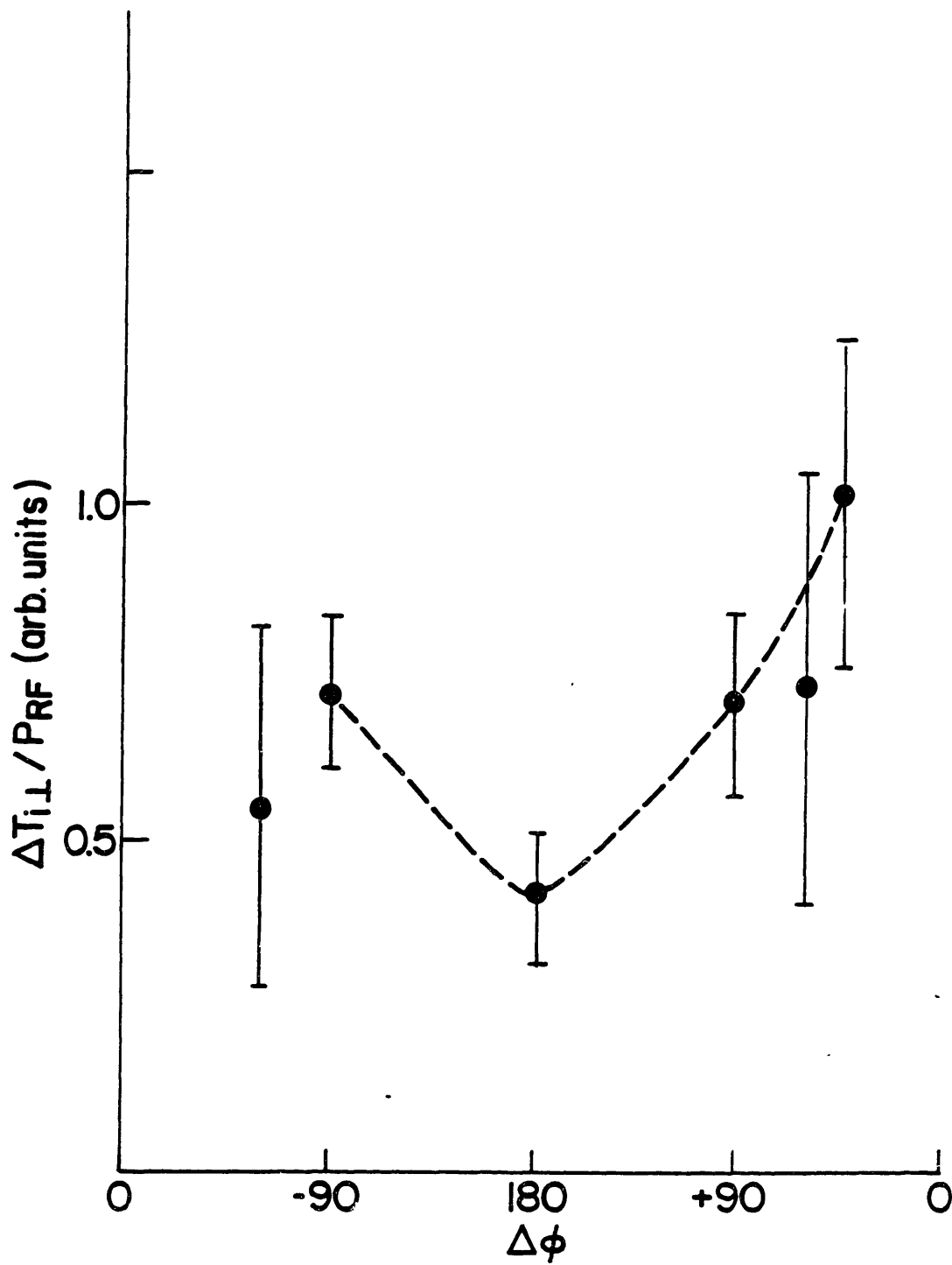


Figure 6.27. Apparent temperature increase during rf injection from perpendicular charge-exchange, normalized to the transmitted power, versus $\Delta\phi$ at $\bar{n}_e = 2.6 \times 10^{13} \text{ cm}^{-3}$

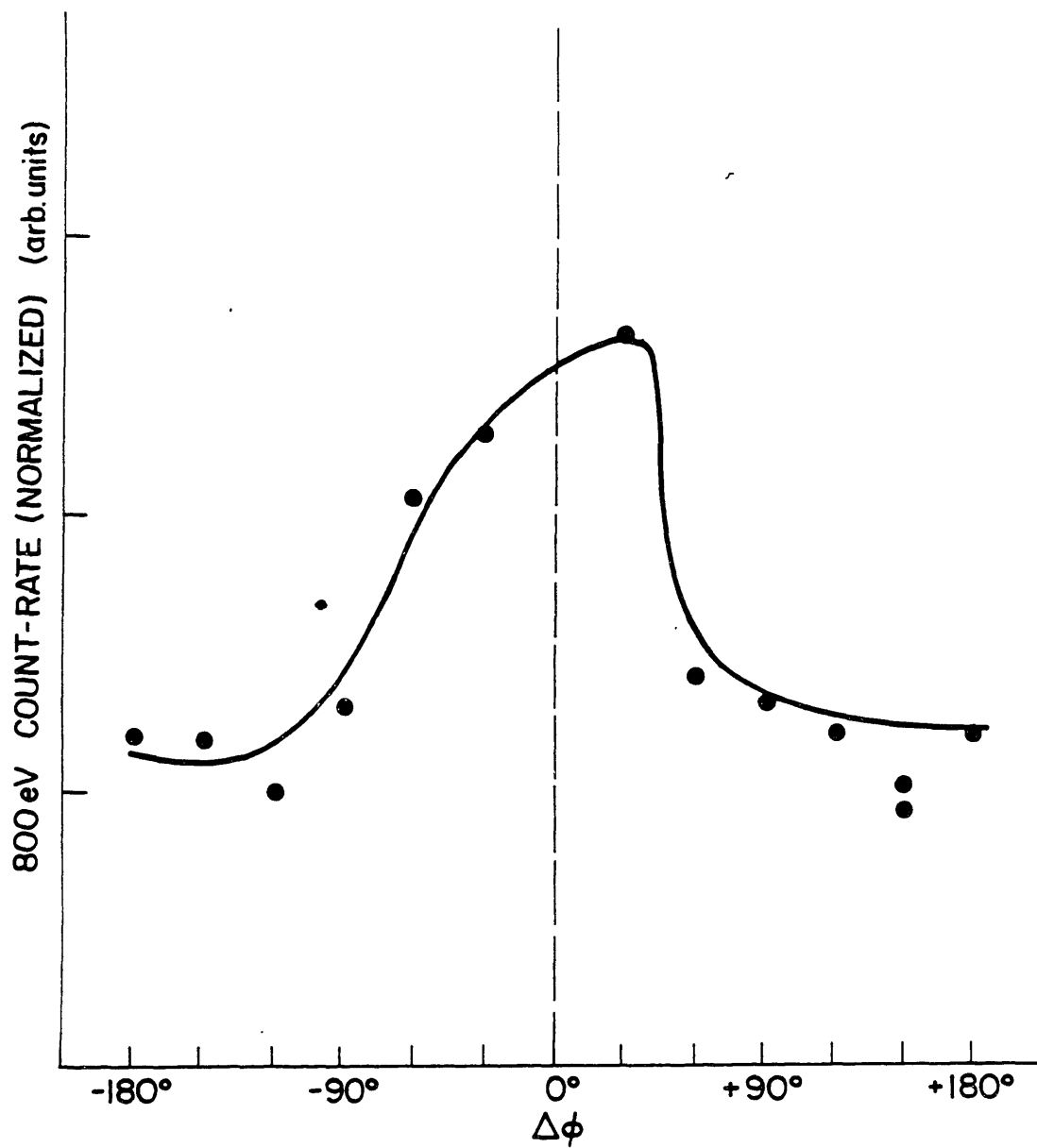


Figure 6.28. 800 eV charge-exchange neutral flux, normalized to the transmitted power, versus $\Delta\phi$ for $P_{rf} = 30$ kW and $\bar{n}_e = 2.5 \times 10^{13} \text{ cm}^{-3}$

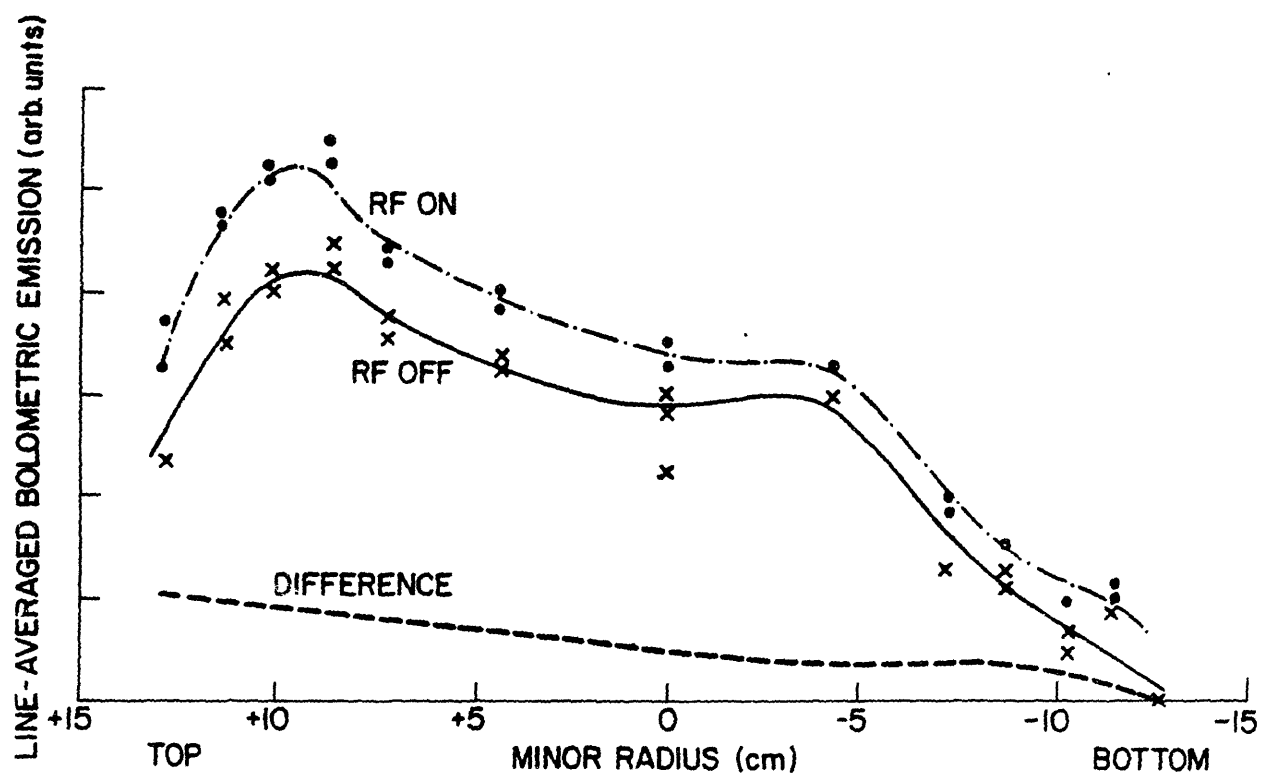


Figure 6.29. Line-averaged bolometric emission profile versus chord height both before and during the rf pulse. Also shown is the difference of the two. $P_{rf} = 85 \text{ kW}$, $\Delta\phi = 45^\circ$, $\bar{n}_e = 2.6 \times 10^{13} \text{ cm}^{-3}$

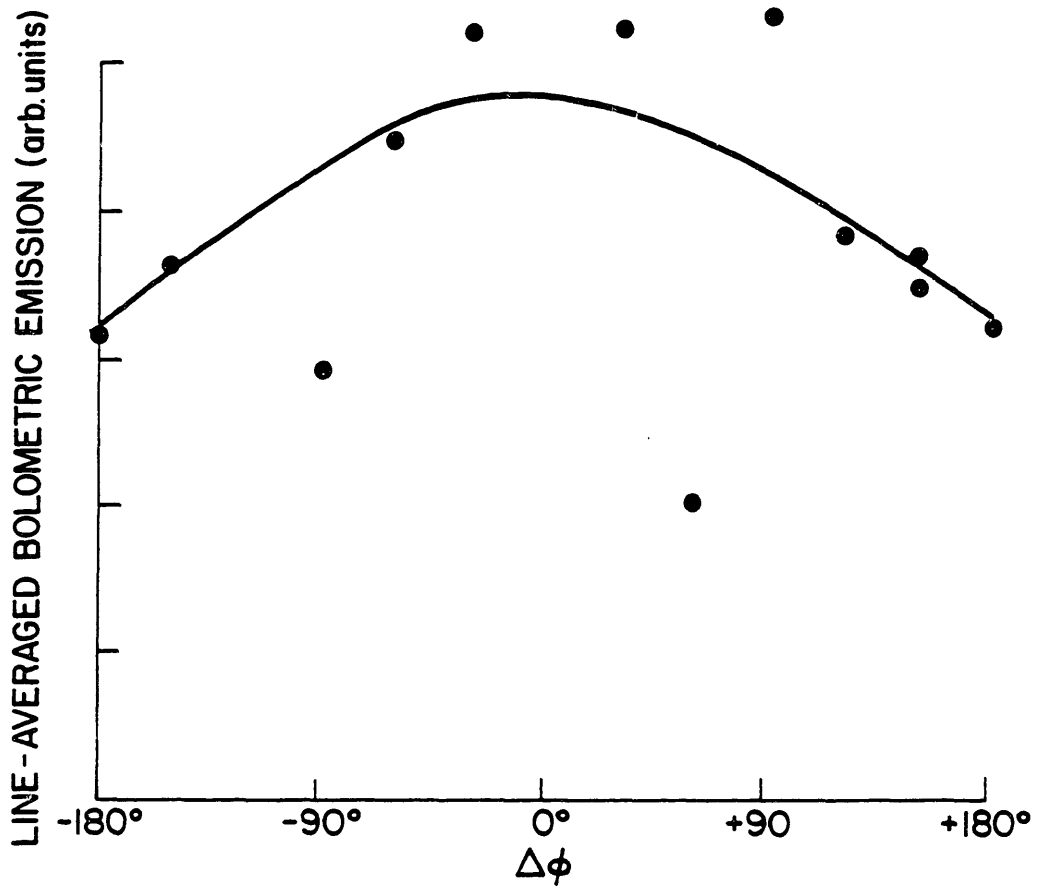


Figure 6.30. Line-averaged bolometric emission at a chord height of +9 cm. versus $\Delta\phi$ for the same conditions as Fig. 6.28.

with regard to the charge-exchange measurements. As in the previous case of the side-launching studies, the origin of the additional neutral flux cannot be determined from the measurement. However, it is unlikely to be coming from the plasma center. If we assume the central ion distribution to be correctly represented by the charge-exchange spectrum of Fig. 6.23 then the collisional heating power of the observed tail, calculated from Eq. (2.57), is between 200 and 700 mW/cm³ for bulk/tail intercept energies between 300 and 500 eV and a target plasma with $T_{i0} = 150$ eV and $n_{e0} = 4 \times 10^{13}$ cm.⁻³. These values are comparable to the central electron-ion collisional power density calculated in Section 6.1.1; hence the presence of a tail distribution of such high density, albeit low temperature, should result in measurable ion heating if it was generated at the plasma center. The lack of ion heating as determined by Doppler broadening measurements of the impurity lines is evidence that the fast ions are not localized in the core of the plasma. The qualitative information provided by the enhancement of the bolometric emission during rf injection indicates that the emission also does not originate in the core, although in light of the significant asymmetry in the profile, the interpretation of the bolometric signal is not at all clear.

We believe that the results of the top launching experiment are consistent with the injected lower-hybrid wave being absorbed in the outer layers of the plasma, both for the reasons given above and from comparisons with the qualitative theoretical models of quasi-linear damping presented in Chapter 2. We see from the charge-exchange spectra that the bulk/tail intercept energy of the low-energy ion tail must be 500 eV or less. By the criterion of Eq. (2.37), the ion temperature at the damping location must be less than 56 eV; hence the damping location itself must be outside a radius of approximately 10 cm. From Figs. 2.7 and 2.24, it is evident that damping well off-axis is plausible from consideration of both slab and toroidal propagation models. We note from Fig. 3.4 that the spectrum of the top launching grill extends over a range $1 < |n_{||}| < 30$ for $\Delta\phi = 90^\circ$ with an $n_{||}$ value of about seven at the peak power level of the spectrum. For this spectrum, the damping region extends from the center to the edge in the slab model and from $r/a \approx 0.2$ to the edge in the toroidal propagation scenario for the density range of the experiment. Observation of a high temperature ion tail created by the damping of relatively low $n_{||}$ waves in the center of the plasma may be masked by the increase in the neutral flux in the 500–1500 eV range, though a relatively high energy tail is indeed apparent in some of the charge-exchange spectra (see Fig. 6.25). In addition, the waves of lower $n_{||}$ may be significantly damped on the non-thermal tail generated by the higher $n_{||}$ components, as has been considered in the simple example in Section 2.5 and calculated in Ref. 65. We have not explicitly considered this effect in a self-consistent manner for the Versator plasma, and hence we cannot state to what extent it may be important. The limiting value of the bulk/tail intercept energy observed in the experiment is in rough agreement with the calculated value in Fig. 2.8 if we assume a significant portion of the spectrum is represented by values of $n_{||} \geq 14$, which is reasonable from a consideration of the calculated antenna spectrum. At the low phase angles,

the spectral components at high n_{\parallel} launched in the negative direction and the broadening of the fundamental spectral peak may provide enough power in the above range of n_{\parallel} to give roughly the same bulk/tail intercept energy for all phase settings of the grill, as is observed experimentally.

On the other hand, the noticeable variation in the tail temperature with $\Delta\phi$ (see Figs. 6.26 and 6.27) is explicable by the difference in the representative n_{\parallel} value of the maximum power for different phasings. We expect from consideration of Fig. 2.10 that the tail temperature for $\Delta\phi = 180^\circ$ (n_{\parallel} (typ.) ≈ 15) would be less than for $\Delta\phi = 90^\circ$ (n_{\parallel} (typ.) ≈ 7), which is indeed evident from the experimental results. Alternatively, waves of lower n_{\parallel} are calculated to be absorbed on higher energy ions, as indicated in Fig. 2.8. This could also give rise to the variation in the tail temperature illustrated in Fig. 6.27.

The question of whether or not the lower-hybrid wave propagation is influenced by the toroidal effects discussed in Section 2.7 cannot be answered conclusively by an examination of our results. A difficulty with the interpretation of this initial top-launching study is that we have performed the experiment both with a higher average n_{\parallel} antenna and at a different launch position than in the previous experiments. Consequently, we cannot unambiguously separate the changes in the plasma heating behavior effected by each alteration. In general, the absorption of rf power on lower energy ions in these experiments as opposed to the earlier side-launching studies suggests that the characteristic value of n_{\parallel} at the damping location is higher in this experiment than in the earlier one. This may be explained by the higher average n_{\parallel} content of the top launcher spectrum as compared to that of the side launcher, and not necessarily by the predicted upshift in n_{\parallel} due to toroidal effects. For example, in the Wega experiment¹⁹, the measured bulk/tail intercept energy decreased from 1600 eV to 1100 eV when a side-launching grill of n_{\parallel} (typ.) = 3 was switched for one with n_{\parallel} (typ.) = 6.

Furthermore, the results obtained in this experiment are at variance with the predictions of ray tracing theory discussed in Chapter 2. As shown in Fig. 2.24, lower-hybrid waves launched from the top of the plasma column should be predominantly lost to electron Landau damping rather than to the ions, except at high plasma densities. Moreover, the transport simulations of the top-launching experiments predict a definite asymmetry with respect to $\Delta\phi$ in the ion heating results, while in the experiment, no bulk heating and no such asymmetry in the fast ion tail was observed. The most likely explanation of this discrepancy is that the ion tail is not produced by linear damping of the lower-hybrid wave but by damping of parametric decay waves, as suggested in the explanation of the side-launching results. The relationship of the observed ion tail to the occurrence of parametric decay has not been investigated in detail in the top-launching experiments. When measured, however, the parametric decay spectrum was similar to that observed in the side-launching experiments. For the latter, it was conjectured that the lack of variation in the fast neutral flux with $\Delta\phi$ could indicate that the tail was produced by the damping of parametric decay waves, possibly because the linear mechanism was too weak for efficient damping of waves with

trajectories such as that illustrated in Figs. 2.15–2.17. It is not known if the significantly different, and phase-dependent, charge-exchange spectra obtained in the top-launching experiment can be explained by the same mechanism. We note that charge-exchange results similar to these were also observed in the Doublet-IIA lower-hybrid experiment²⁴ in which waves of $n_{\parallel} = 16$ –22 were launched from the top and bottom of the plasma column. The toroidal magnetic field and plasma density in that experiment were sufficiently low such that mode conversion in the plasma center was only possible for n_{\parallel} near 20, yet low energy ion tails with fast decay rates were detected. Parametric decay was also observed to occur during rf injection in that experiment as well, and was invoked as the probable mechanism of the ion tail production.

In conclusion, we can state that no evidence of bulk ion heating was obtained with the use of the top launching grill. The differences between the ion energy spectra obtained in the top-launching and side-launching experiments are believed to be related to the difference in the n_{\parallel} at the damping locations. There is a strong suggestion that the enhancement of the low energy charge-exchange spectrum is due to parametric processes; consequently, the influence of toroidal effects on the wave propagation has not been proven or disproven in this experiment. Some suggestions of further studies to clarify this problem are discussed in the next chapter.

6.4. Plasma Power Balance During Rf Injection

In this section, the power balance of the plasma is evaluated for the purpose of deducing the rf heating efficiency for the case discussed in Section 6.1.2 in which the apparent ion heating was reported. Knowledge of the density and temperature profiles for all species are required for accurate and self-consistent calculations of the heating efficiency and power flows. However, such quantities are not routinely measured in these experiments. Therefore, the following calculations only provide estimates of the actual quantities in question. Nonetheless, such estimates are useful in determining the possible heating scenarios which are consistent with the data obtained in this work.

The global power balance equations of the electrons, protons, and impurity ions are written as follows:

$$\frac{W_e}{\tau_e} = -P_{ep} - P_{eI} + P_e^{RF} + P_e^{OH} \quad (6.15a)$$

$$\frac{W_p}{\tau_p} = -P_{pe} - P_{pI} + P_p^{RF} \quad (6.15b)$$

$$\frac{W_I}{\tau_I} = -P_{Ie} - P_{Ip} + P_I^{RF} \quad (6.15c)$$

where W_{α} is the total energy of the population of species α , τ_{α} is the species global energy confinement time, P_{α}^{RF} is the total rf power deposited in the species, P_e^{OH} is the ohmic power deposited in the electrons, and $P_{\alpha\beta}$ is the collisional power from species α to species β . The

subscripts "e", "p", and "I" refer to the electrons, protons, and impurity species, respectively. The quantity W_α has the explicit form

$$\begin{aligned} W_\alpha &= \frac{3}{2} \int n_\alpha T_\alpha dV \\ &= 6\pi^2 R_o \int_0^a n_\alpha(r) T_\alpha(r) r dr \end{aligned} \quad (6.16)$$

under the assumption of poloidal and toroidal symmetry of the density and temperature profiles.

For simplicity, the proton and impurity ion equations are added together, and the effective ion energy confinement time is denoted τ_i . Equations (6.15) can then be written

$$\frac{W_e}{\tau_e} = -P_{ei} + P_e^{OH} + P_e^{RF} \quad (6.17a)$$

$$\frac{W_i}{\tau_i} = P_{ei} + P_i^{RF} \quad (6.17b)$$

where we have used the equality $P_{ei} = P_{ep} + P_{eI} = -P_{ie}$. The collisional power term is

$$P_{ei} = 4\pi^2 R_o \int_0^a n_e \nu_{ei} (T_e - T_i) r dr. \quad (6.18)$$

The power balance equations may be written in detail as

$$\begin{aligned} \frac{6\pi^2 R_o}{\tau_e} \int_0^a n_e(r) T_e(r) r dr &= -4\pi^2 R_o (9.9 \times 10^{-27}) \int_0^a \frac{n_e(r)^2}{T_e(r)^{3/2}} (T_e(r) - T_i(r)) \\ &\times \left[1 - \frac{n_I Z_I}{n_e} \left(1 - \frac{Z_I}{A_I} \right) \right] r dr + I_p V_l + P_e^{RF} \end{aligned} \quad (6.19a)$$

$$\begin{aligned} \frac{6\pi^2 R_o}{\tau_i} \int_0^a n_e(r) T_i(r) \left[1 - \frac{n_I}{n_e} (Z_I - 1) \right] r dr &= 4\pi^2 R_o (9.9 \times 10^{-27}) \int_0^a \frac{n_e(r)^2}{T_e(r)^{3/2}} (T_e(r) - T_i(r)) \\ &\times \left[1 - \frac{n_I Z_I}{n_e} \left(1 - \frac{Z_I}{A_I} \right) \right] r dr + P_i^{RF} \end{aligned} \quad (6.19b)$$

where Eq. (6.2) has been used, and all symbols, including the temperatures, are in CGS units. We have taken $\ln \Lambda = 15$. The ohmic power is written as the product of plasma current and loop voltage, which is reasonable for the portion of the discharge in which the plasma current is constant. To perform the above integrals, we choose analytic plasma profiles to match the profile data of Figs. 4.3–4.5. Specifically, we take

$$\begin{aligned} n_e(r) &= n_{eo} \left(1 - \frac{r^2}{a^2} \right) \\ T_e(r) &= T_{eo} \left(1 + \frac{r^2}{\lambda_{te}^2} \right)^{-3/2}; \quad \lambda_{te} = 7.5 \text{ cm.} \\ T_i(r) &= T_{io} \exp \left(-\frac{r^2}{\lambda_{ti}^2} \right); \quad \lambda_{ti} = 10.5 \text{ cm.} \end{aligned} \quad (6.20)$$

The radial dependence of the impurity density is unknown. For simplicity, the impurity terms in the square brackets are assumed to be independent of radius and are taken outside the integral signs. As in Chapter 2, the ratio of the effective impurity density to the electron density is chosen on the basis of the measured Z_{eff} and the average charge state Z_I :

$$\frac{n_I}{n_e} = \frac{Z_{eff} - 1}{Z_I(Z_I - 1)} \quad (6.21)$$

Unless otherwise specified, the value of Z_{eff} for these calculations is taken to be 2, based on the spread of values obtained in Chapter 4.

The power balance equations are first solved for the ohmic case $T_{eo} = 400$ eV, $T_{io} = 150$ eV, $n_{eo} = 4 \times 10^{13}$ cm⁻³, $I_p = 55$ kA, and $V_l = 2$ V. With the previously specified profiles, Eqs. (6.19) may be solved for the energy confinement times:

$$\begin{aligned} \tau_e &\simeq 1.2 \text{ msec} \\ \tau_i &\simeq 3.4 \text{ msec.} \end{aligned} \quad (6.22)$$

The so-called energy confinement time,

$$\tau_E = \frac{3/2 \int (n_i T_i + n_e T_e) dV}{I_p V_l}, \quad (6.23)$$

is 1.5 msec, which is intermediate between the "old" Alcator scaling law¹⁴⁴ prediction of 2.2 msec and the neo-Alcator confinement time¹⁴⁵ of 0.8 msec.

Now let us consider the case of rf ion heating in which the lower-hybrid wave is assumed to damp on ions only, i.e., $P_e^{RF} = 0$ in Eq. (6.19a). We take $T_{io} = 200$ eV and also assume Z_{eff} , T_e , and τ_e to be unchanged. For the scaling of τ_i with T_i , we distinguish two cases: (1) τ_i remains constant, and; (2) τ_i is given by neoclassical scaling. The first has no physical justification, but is simple and provides a lower bound for the absorption efficiency. To calculate the neoclassical scaling, we first solve for ν_{*i} , the neoclassical collision parameter representing the ratio of the ion de-trapping frequency to the banana orbit bounce frequency:

$$\nu_{*i} = \nu_{ii} \left(\frac{R_o}{r} \right)^{3/2} \frac{\sqrt{2q} R_o}{v_{thi}}, \quad (6.24)$$

which is about 3 for Versator parameters in the ion heating regime. Since $\nu_{*i} > 1 > \nu_{*i}(\tau/R_o)^{3/2}$, the ion transport corresponds to diffusion in the plateau regime.⁸⁴

The experimental thermal conductivity can be compared to the theoretical value in this regime as follows: the local power balance equation for the ions can be written as

$$\frac{\partial}{\partial t} \frac{3}{2} (n_i T_i) = n_e \nu_{ei} (T_e - T_i) + \frac{1}{r} \frac{\partial}{\partial r} r \chi_i^{NC} \frac{\partial T_i}{\partial r} + p_i^{RF} \quad (6.25)$$

where χ_i^{NC} is the ion thermal conductivity and we have assumed thermal conduction to be the dominant power loss for ions, which should be true in the plasma core. The quantity p_i^{RF} is the local heating power density to the ions due to rf absorption. We solve for χ_i^{NC} in the inner region of the plasma for the ohmic case ($p_i^{RF} = 0$) by assuming steady-state conditions and integrating over the volume inside $r = a/2$ to obtain

$$\int_0^{a/2} n_e \nu_{ei} (T_e - T_i) r dr = 2 \frac{r^2}{\lambda_{ti}^2} \chi_i^{NC} T_i |_{r=0}^{a/2} \quad (6.26)$$

As defined previously, λ_{ti} is the Gaussian width of the ion temperature profile. Using the same profiles as before, we obtain $\chi_i^{NC}(a/2) = 4.5 \times 10^{17} (\text{cm-sec})^{-1}$

We compare this value to the theoretical one for plateau diffusion:⁸⁴

$$\chi_i^{NC} = 2n_i \left(\frac{T_i}{m_i} \right)^{3/2} \frac{q}{R_o \omega_{ci}^2}, \quad (6.27)$$

which is about $1.7 \times 10^{17} (\text{cm-sec})^{-1}$ at $r = a/2$. Thus the measured ion thermal conductivity is only several times the neoclassical value. If plateau diffusion represents the major energy loss for ions, then from Eqs. (6.25) and (6.27) the ion energy confinement time should scale as $T_i^{-3/2}$

In calculating the heating efficiency, we first assume the temperature profiles to be unchanged during rf heating. For neoclassical confinement and $\Delta T_i = 50$ eV, we solve Eq. (6.19b) and find that τ_i is 2.2 msec and the absorbed auxiliary power on the ions must be 23 kW, or 47% of the transmitted rf power. For the case of constant τ_i , the required absorbed power is 15 kW, giving a heating efficiency of 30%. For comparison, the collisional power coupled to the ions is only 8.5 kW, or almost half of the collisional power to the ions in the ohmic case. If the ion temperature profile in the rf-heated case is narrower than for the ohmic case, the total power needed to cause the observed central temperature increase may be less than the above estimates. A simple calculation of the central auxiliary power density required to produce the 50 eV rise on axis can be made with the use of Eq. (6.25) in which we let the ion thermal conductivity have the functional form of the neoclassical value Eq. (6.27). With the derivative of the thermal diffusion term in Eq. (6.27) evaluated under the assumption of a flat q -profile near the axis, the equation for the central ion power balance becomes

$$n_{e0} \nu_{ei} (T_{e0} - T_{i0}) - \frac{4}{\lambda_{ti}^2} \chi_{i0}^{NC} T_{i0} + p_i^{RF} = 0. \quad (6.28)$$

We note from the above equation that the effective ion energy confinement time on axis is proportional to $\lambda_{ti}^2 T_{i0}^{-3/2}$. For the ohmic case ($T_{i0} = 150$ eV, $\lambda_{ti} = 10.5$ cm.), the collisional power to the ions is 350 mW/cm³ and the calculated ion thermal conductivity is $4.0 \times 10^{17} (\text{cm-sec})^{-1}$. For the case of the ion temperature increase ($T_{i0} = 200$ eV) the auxiliary power required is 180 mW/cm³ if the thermal conductivity remains at its previous value or 430 mW/cm³

if the central thermal conductivity scales neoclassically. For both of these possibilities, the ion temperature profile is considered to have the same width as the ohmic one; if the rf-heated profile is in fact narrower, the required central auxiliary power densities are greater. For any of these cases, the local power absorption rates are at least 20 times greater than the maximum experimentally-estimated rate obtained in Section 6.1.1.

Alternatively, it is conceivable that the ion temperature profile during rf heating is broader than the ohmic profile, i.e., the rf absorption on ions occurs mainly off-axis, as suggested by the results of Chapter 2. Based on an evaluation of Eq. (6.25) with $p_i^{RF}(\text{on axis}) = 0$, the 50 eV central ion temperature rise can be modelled by an increase of the central λ_{ti} to 13.6 cm from 10.5 cm for constant ion thermal conductivity, or by an increase of λ_{ti} to 16.8 cm for neoclassical scaling. The global power balance for ions can be recalculated with a wider ion temperature profile; we pick $\lambda_{ti} = 16$ cm, and $\tau_i = 2.2$ msec (neoclassical scaling). The total auxiliary power absorbed by the ions required to maintain such a profile is 42 kW, or 84% of the transmitted rf power. The reduction of the collisional coupling between electrons and ions allows the central electron temperature to rise by 50 eV for no loop voltage change if the electron temperature profile does not broaden.

Because of the ambiguity in interpreting the charge-exchange data for off-axis energy deposition, this model of the heating results cannot be directly substantiated without experimental evidence of the wave damping location. However, this scenario is perhaps more plausible than the previous one in that the charge-exchange data provides a limit on the central damping rate which is far less than that needed to explain the observed heating. The small increase in electron temperature predicted by the decoupling of the ions from the electrons is consistent with the observed behavior of the O VII intensity during the apparent ion heating. However, we have no evidence to suggest that a broad ion temperature profile was indeed present in the rf-heated plasma. In fact, the relative measurements of the O VII and C V temperature increases during rf heating shown in Fig. 6.5 would suggest that the ion temperature profile does not broaden in the cases in which ion temperature increases are observed. Unless the central auxiliary power deposition rate is much higher than that estimated from the charge-exchange data, the observed ion heating is difficult to explain if only rf absorption by ions is considered.

We also consider the possibility of electron heating being responsible for the observed increase in the ion temperature. Electron heating may arise from electron Landau damping of the lower-hybrid wave or by a rise in the plasma impurity content, or a combination of both. Unfortunately, the electron temperature was not directly measured during any of the runs in which the bulk ion heating was observed. The increase in the central impurity emission concurrent with the ion temperature rise suggests that the electron temperature may have indeed increased during rf injection. However, the lack of a loop voltage change may indicate that no temperature increase occurred, unless the impurity content of the plasma simultaneously rose to keep the

electrical resistivity constant. Regardless of whether or not electron heating actually occurred, no value of the electron temperature in Eq. (6.19b) can cause a 50 eV rise in the ion temperature, as the effectiveness of collisional heating is diminished with increasing electron temperature. Considering the global ion power balance under the assumption of electron heating, we find that by differentiating Eq. (6.19a) with respect to T_{eo} , the maximum collisional power flow to the ions occurs for $T_{eo} = 4.65 T_{io}$ assuming the profiles of Eqs. (6.20) to be valid. Solving Eq. (6.19b) for T_{io} under this condition gives

$$T_{io}^{3/2} = 1.6 \times 10^{-8} (n_{eo} \tau_i) \quad (6.29)$$

i.e., $T_{io} = 165$ eV and $T_{eo} = 770$ eV for the case of ion confinement remaining constant or $T_{io} = 160$ eV and $T_{eo} = 740$ eV for ion confinement being neoclassical. We have assumed that the density does not increase, which is valid for the experiment in which the ion heating was observed. Such a large increase in electron temperature is inconsistent with the experimental observations; furthermore, it cannot account for the 50 eV rise in the central ion temperature.

Again, we can consider the local power balance at the center, with the possible justification that the ion temperature profile may not be the same as in the ohmic discharge. From Eq. (6.25), the maximum collisional power flow to the ions is seen to take place for $T_{eo} = 3 T_{io}$. Solving Eq. (6.25) under this condition (and $p_i^{RF} = 0$) gives

$$T_{io}^{3/2} = 4.7 \times 10^{-9} \left(\frac{n_{eo}^2 \lambda_{ti}^2}{\chi_{io}^{NC}} \right) \quad (6.30)$$

or $T_{io} = 160$ eV for n_{eo}, λ_{ti} , and χ_{io}^{NC} remaining the same as in the ohmic case. As in the previous example, only if the ion temperature profile is substantially broadened can the central ion temperature rise to 200 eV, i.e., for $\lambda_{ti} = 12.3$ cm with χ_{io}^{NC} constant or for $\lambda_{ti} = 15.2$ cm with χ_{io}^{NC} given by neoclassical scaling. To account for the 50 eV central ion temperature rise in such a case, we find that the central electron temperature must increase to 600 eV. With the loop voltage and plasma current remaining constant during this heating, the value of Z_{eff} must approximately double; if the electron temperature profile broadens as well, the impurity content must be even higher. Using the global electron power balance equation (6.19a) with the ohmic profiles and assuming τ_e to be unchanged, we find that approximately 50 kW of rf power (100%) must be absorbed on the electron population to account for a 600 eV central electron temperature. However, the electron energy confinement time is generally believed to deteriorate with auxiliary heating,⁸⁷ and we reiterate that the profiles must be broader than the ohmic profiles if the observed ion heating is to be considered plausible; hence the required power flow to the electrons is greater than the available rf power. Moreover, the experimental data does not support a claim of such a large increase in electron temperature or impurity content. If the central density of a light impurity, e.g. carbon ($Z=6, A=12$), increases simultaneously with rf injection, then the observed ion heating may result from an increased collisional power flow from electrons to ions.

However, because the emission levels of the edge spectroscopic lines of carbon and oxygen do not increase significantly during rf injection, such an increase in light impurity concentration cannot be explained by an influx of impurities from the edge. In the future, efforts to obtain a direct measurement of the central impurity content should be made to assess the validity of this possible heating mechanism.

In summary, the observed ion heating results are consistent with absorption of the lower-hybrid wave on the ion population, rather than electron heating and collisional transfer of power to the ions. Furthermore, we suggest that if the maximum central heating rate obtained from the charge-exchange data is correct, the ion temperature profile in the rf-heated plasma must be broader than the profile in the ohmic plasma to explain the observed ion temperature increase. As mentioned earlier, however, the small amount of ion temperature profile data we have obtained does not support the suggestion that the profile broadens during rf injection or that a significant amount of rf power is indeed deposited off-axis. If the ion heating takes place because of rf power deposition near the center, then the power required to cause a 50 eV rise in the central ion temperature is only 30–50% of the transmitted power. However, it does not appear that the local absorption rate at the center can be explained by collisional damping of the observed ion tail.

7. Summary and Conclusion

In this chapter, the major experimental results of this work are summarized, and some suggestions are offered regarding the direction of future research in lower-hybrid ion heating. Most of the suggestions are specifically related to the continuation of the study of rf heating on Versator, but some have general applicability.

7.1. Rf Coupling

The maximum coupling efficiency of the lower-hybrid antenna to the plasma was measured to be approximately 85%. The experimental coupling behavior has been found to be in reasonable agreement with predictions of the Brambilla coupling model in which corrections have been made for finite waveguide height and finite plasma density at the grill mouth. The major source of uncertainty in the comparison of the experimental data to the theory is the interpretation of the Langmuir probe measurement of the absolute density. If a more accurate comparison is desired, the density obtained by Langmuir probe measurements could be carefully checked against those from microwave interferometry at the edge. Regarding improvements to the theory, the replacement of the linear density gradient with an exponential one should be made for the sake of consistency, as the experimental edge density profiles in tokamaks are exponential. The difference in the calculated coupling behavior for the two cases may well be significant for antenna spectra not characterized by $n_{\parallel}^2 \gg 1$ (compare Eqs. 3.27 and 3.41). Such antennas are likely to be used in future lower-hybrid heating experiments on hotter plasmas.

7.2. Grill Behavior at High Power

With vacuum bake-out and rf conditioning of the side-launching grill, the full available incident power of 110 kW can be coupled into vacuum with no evidence of plasma formation. Under these conditions, the coupling coefficient is relatively constant over the entire range of incident power. Breakdown in the conditioned grill during tokamak operation is suppressed by an auxiliary magnetic field which raises the residual field above the cyclotron resonant value everywhere in the waveguide. A maximum power density of 0.94 kW/cm² was achieved, and higher power densities are believed to be attainable. With a carbon-coated grill launching from the top of the plasma column, a power density of 1.4 kW/cm² was reached, again with no evidence of this being a limit.

In light of our experience and from the knowledge we have gained from others, some general recommendations on lower-hybrid grill preparation can be made. These suggestions apply in particular to designs in which the vacuum seals cannot be made in the waveguides themselves but outside the cyclotron resonance layer, i.e. for antennas in which electron loading is severe. Degassing and mechanical preparation of the surface is important. To reduce electron-stimulated desorption, baking of the metal before assembly should prove useful. The baking of the material

should be performed before the assembly of the grill rather than after because higher temperatures can be employed in the former. Roughening the surface of the guides has been shown to reduce secondary electron emission;¹²⁰ simple sanding and electropolishing has beneficial effects and should be implemented.

A supplemental magnetic field to raise the total field above cyclotron resonance is a convenient external solution to the breakdown problem. Fields perpendicular to the waveguide width appear to be preferable to those parallel; however, we have not made conclusive experimental tests to verify this point.

Though carbon coating is shown to increase the power handling ability of the antenna, its apparent susceptibility to contamination in our usage warrants more study before being recommended for further application. Clearly, however, the promise of carbon-coating or similar surface treatments is great and should continue to be developed.

7.3. Heating Results

The major goal of this present work has been to demonstrate bulk ion heating with the injection of sufficient rf power and to determine under what conditions heating is most efficient. In the ion heating experiments, a maximum bulk central ion temperature increase of 50 eV at $\bar{n}_e = 2.6 \times 10^{13} \text{ cm}^{-3}$ and $B_o = 14 \text{ kG}$ was recorded for 50 kW transmitted power. The mode conversion layer for these parameters is calculated to be in the plasma center. By the efficiency criterion defined in Chapter 1, this temperature rise corresponds to a heating efficiency of $2.6 \text{ eV/kW} \cdot 10^{-13} \text{ cm}^3$. However, such heating was observed only rarely, and the reasons for the variability in the heating efficiency have not been uncovered in this study. A short-lived perpendicular ion tail was routinely observed in these experiments, but the radial location of the tail could not be explicitly measured. As a result, the wave damping location is unknown. The energy density of the ion tail is also uncertain, although a maximum estimate calculated in Chapter 6 suggests that a few percent of the transmitted rf power can account for the magnitude of the central ion tail. No electron heating was measured to occur. Heating experiments performed with a novel top-launching antenna evidenced no bulk ion heating, although the observed charge-exchange spectra were significantly different than those obtained during side-launching experiments. In general, the results of the Versator lower-hybrid studies are similar to those on other tokamaks with regard to the variability of the ion temperature increase and the observation of a fast ion tail which appears to be poorly confined.

Though the central ion temperature increase occasionally observed during rf injection is consistent with wave damping occurring primarily off-axis and the ion temperature profile becoming broader, no such broadening was actually observed. Ion temperature profile broadening has not been observed in other lower-hybrid experiments. In the JFT-2^{27,31} and recent Petula²³ experiments in which relatively efficient ion heating was reported, the ion temperature profile in the

rf-heated plasma was observed to be narrower than in the ohmic plasma, indicating that the wave damping was likely to be occurring at the center. In those experiments, however, the corresponding perpendicular charge-exchange spectra were not inconsistent with strong central damping: the apparent bulk/tail intercept energy was only about 5 times the central ion temperature, indicating that the fractional central tail density may be over 50 times that estimated for our experiment. Thus the achievement of efficient heating as a result of wave absorption in the plasma core in those experiments is not surprising.

The scenario of the ion heating behavior in Versator is in reasonable agreement with the models put forth in Chapter 2. Consideration of the cylindrical slab model, and especially the toroidal propagation model, suggests that wave damping outside the plasma core ($r/a \geq 0.4$) is likely in Versator. Transport code simulations of the ion heating experiment on Versator show the ion temperature profiles of the rf-heated plasma to be broader than the ohmic profiles. If off-axis absorption accurately describes the actual heating behavior, the observed variability of the heating efficiency is easier to understand, as small density or temperature profile changes can shift the wave damping location such that collisional and orbit losses may be greatly different from run to run.

The first recommendation regarding future lower-hybrid heating studies on Versator is purely technical. The Versator tokamak is not an ideal device for lower-hybrid ion heating experiments, and further studies would benefit from a few improvements in the operating characteristics. The relatively high plasma densities required for mode conversion are difficult to achieve for a period greater than 5–8 msec within the 25–30 msec discharge duration. Strong gas puffing in the initial evolutionary stage of the plasma current buildup is required to attain these densities within the available period. Variations in the puffing rate might lead to significant differences in the temperature profiles;¹³⁷ we have noted qualitatively that the evolution of the ion temperature in high density discharges is not always the same in different runs. If the discharge duration of the Versator plasma could be lengthened (and the temporal decay of the TF current reduced with the use of an upgraded power supply), the quality of the experiments is likely to be improved. In addition, the plasma current should be increased to improve the fast ion confinement. As illustrated in Fig. 2.14, the energetic ions created at the wave damping location should be adequately confined if the plasma current could be raised to 100 kA. These changes should be satisfied by the general machine upgrade presently being carried out for the purpose of rf current drive studies.

As the attainment of consistent ion heating was not a success, and the underlying causes of the variability are not understood, we suggest that in future experiments more attention be paid to such plasma parameters such as temperature and density profile widths and evolution, edge temperature, and impurity content. The empirical relationship of these quantities to the observed neutral flux, parametric decay spectrum, and bulk heating behavior is not well-known, and should be clarified. Of primary importance in this regard is the improvement of the relevant diagnostics.

A near-perpendicular charge-exchange analyzer capable of a radial scan would prove to be of great value in localizing the neutral particle emission. In other lower-hybrid experiments, the location of the tail is rarely known; in instances in which the neutral flux profile has been measured, the results have not been well understood in light of the measured tail lifetime.²⁷ Direct profile measurements of the various impurity species location would be useful as well.

Though we have monitored edge temperatures during heating experiments in an attempt to note any distinction between "good" and "bad" discharges, controlled experiments in the spirit of the JFT-2 profile modification studies by neutral beam injection³¹ are more desirable. The effect of a controlled impurity influx on the fast neutral flux, either by injection with a fast puff valve or laser blow-off, could be helpful in understanding the relationship of the impurity content to heating behavior, particularly if the impurity injection is noted to change the temperature profiles. Continued work in the comparison of top-launching and side-launching antennas is recommended because of the observed differences in the charge-exchange spectra in the two experiments. Specifically, the top-launching antenna should be installed in a side port to compare top and side-launching results with use of the same antenna. In this manner, the importance of toroidal effects on lower-hybrid wave propagation may be clarified. Profile information on the fast neutral flux would be particularly useful in this comparison.

Experimental knowledge of the wave trajectory would be of help in determining whether or not a significant fraction of the injected rf power indeed reaches the core of the plasma. It is hoped that the planned microwave scattering measurements on Versator and ongoing laser scattering studies on Alcator C will provide an answer to this question. Finally, we recall from the results of this experiment and the others that the observed fast ion tail appears to be related to the occurrence of parametric decay of the pump wave. Accordingly, the parametric decay phenomenon may be fundamental to the lower-hybrid heating process, and further studies should be aimed at determining its location in the plasma, its relation to fast ion production, and the extent to which it can be controlled.

Appendix A: Derivation of the Warm Plasma Dispersion Relation

In this appendix, the warm plasma dispersion relation for electrostatic lower-hybrid waves is derived from the hot plasma dispersion relation Eq. (2.12). We first consider the limits $k_{\perp} \rho_{ce}, k_{\perp} \rho_{ci} \ll 1$, and $|\xi_{ne}|, |\xi_{ni}| \gg 1$. The Bessel functions and exponentials of Eq. (2.13) are expanded for small b_{α} ($b_{\alpha} = k_{\perp}^2 v_{th\alpha}^2 / 2\omega_{c\alpha}^2$) and the asymptotic expression for the plasma dispersion function is used. Terms to order $v_{th\alpha}^4$ are kept. The terms of separate n are:

$$\begin{aligned}
 I_0(b_{\alpha})e^{-b_{\alpha}} \xi_{0\alpha} Z(\xi_{0\alpha}) &\simeq -1 + b_{\alpha} - \frac{1}{2\xi_{0\alpha}^2} + \frac{b_{\alpha}}{2\xi_{0\alpha}^2} \\
 &\quad - \frac{3}{4}b_{\alpha}^2 - \frac{3}{4}\frac{1}{\xi_{0\alpha}^4}; \\
 I_1(b_{\alpha})e^{-b_{\alpha}} \xi_{0\alpha} Z(\xi_{1\alpha}) + I_{-1}(b_{\alpha})e^{-b_{\alpha}} \xi_{0\alpha} Z(\xi_{-1\alpha}) &\simeq -\xi_{0\alpha} \left(\frac{b_{\alpha}}{2} - \frac{b_{\alpha}^2}{2} \right) \\
 &\quad \times \left[\left(\frac{1}{\xi_{1\alpha}} + \frac{1}{\xi_{-1\alpha}} \right) + \left(\frac{1}{2\xi_{1\alpha}^3} + \frac{1}{2\xi_{-1\alpha}^3} \right) \right]; \\
 I_2(b_{\alpha})e^{-b_{\alpha}} \xi_{0\alpha} Z(\xi_{2\alpha}) + I_{-2}(b_{\alpha})e^{-b_{\alpha}} \xi_{0\alpha} Z(\xi_{-2\alpha}) &\simeq -\xi_{0\alpha} \frac{b_{\alpha}^2}{8} \left(\frac{1}{\xi_{2\alpha}} + \frac{1}{\xi_{-2\alpha}} \right).
 \end{aligned} \tag{A.1}$$

For the case of the electrons ($\omega \ll \omega_{ce}$), we can write

$$\begin{aligned}
 \xi_{0e} \left(\frac{1}{\xi_{1e}} + \frac{1}{\xi_{-1e}} \right) &= 2 \frac{\omega^2}{\omega^2 - \omega_{ce}^2} \simeq -2 \frac{\omega^2}{\omega_{ce}^2} \\
 \xi_{0e} \left(\frac{1}{2\xi_{1e}^3} + \frac{1}{2\xi_{-1e}^3} \right) &= \frac{k_{\parallel}^2 v_{the}^2 \omega^4}{(\omega^2 - \omega_{ce}^2)^3} \simeq -\frac{k_{\parallel}^2 v_{the}^2 \omega^4}{\omega_{ce}^6} \\
 \xi_{0e} \left(\frac{1}{\xi_{2e}} + \frac{1}{\xi_{-2e}} \right) &= 2 \frac{\omega^2}{\omega^2 - 4\omega_{ce}^2} \simeq -\frac{1}{2} \frac{\omega^2}{\omega_{ce}^2}.
 \end{aligned} \tag{A.2}$$

For the case of the ions ($\omega \gg \omega_{ci}$), the denominator of each expression is expanded because the lowest order term is found to cancel in the summation:

$$\begin{aligned}
 \xi_{0i} \left(\frac{1}{\xi_{1i}} + \frac{1}{\xi_{-1i}} \right) &\simeq 2 \left(1 + \frac{\omega_{ci}^2}{\omega^2} + \frac{\omega_{ci}^4}{\omega^4} \right) \\
 \xi_{0i} \left(\frac{1}{2\xi_{1i}^3} + \frac{1}{2\xi_{-1i}^3} \right) &\simeq \frac{k_{\parallel}^2 v_{thi}^2}{\omega^2} \left(1 + 3 \frac{\omega_{ci}^2}{\omega^2} + 6 \frac{\omega_{ci}^4}{\omega^4} \right) \\
 \xi_{0i} \left(\frac{1}{\xi_{2i}} + \frac{1}{\xi_{-2i}} \right) &\simeq 2 \left(1 + 4 \frac{\omega_{ci}^2}{\omega^2} + 16 \frac{\omega_{ci}^4}{\omega^4} \right).
 \end{aligned} \tag{A.3}$$

Solving for the real parts of the electron and ion susceptibilities with the above approximations gives

$$\begin{aligned}
\text{Re } \chi_e \simeq & \frac{k_{\perp}^2 \omega_{pe}^2}{k^2 \omega_{ce}^2} \left(1 + \frac{\omega^2}{\omega_{ce}^2} - \frac{3 k_{\perp}^2 v_{the}^2}{8 \omega_{ce}^2} \right) \\
& - \frac{k_{\parallel}^2 \omega_{pe}^2}{k^2 \omega^2} \left(1 + \frac{3 k_{\parallel}^2 v_{the}^2}{2 \omega^2} - \frac{1 k_{\perp}^2 v_{the}^2}{2 \omega_{ce}^2} \right) \\
& - \frac{1 k_{\perp}^2 \omega_{pe}^2}{2 k^2 \omega_{ce}^2} \left(\frac{k_{\perp}^2 v_{the}^2 \omega^2}{\omega_{ce}^2 \omega_{ce}^2} - \frac{k_{\parallel}^2 v_{the}^2 \omega^6}{\omega^2 \omega_{ce}^6} \right)
\end{aligned} \tag{A.4}$$

and

$$\text{Re } \chi_i \simeq -\frac{\omega_{pi}^2}{\omega^2} \left(1 + \frac{3 k^2 v_{thi}^2}{2 \omega^2} \right) \tag{A.5}$$

Keeping the lowest order thermal corrections, we find that the electrostatic dispersion relation can be written

$$\begin{aligned}
\text{Re } D = 1 + & \frac{k_{\perp}^2 \omega_{pe}^2}{k^2 \omega_{ce}^2} \left(1 - \frac{3 k_{\perp}^2 v_{the}^2}{8 \omega_{ce}^2} \right) - \frac{\omega_{pi}^2}{\omega^2} \left(1 + \frac{3 k^2 v_{thi}^2}{2 \omega^2} \right) \\
& - \frac{k_{\parallel}^2 \omega_{pe}^2}{k^2 \omega^2} \left(1 + \frac{3 k_{\parallel}^2 v_{the}^2}{2 \omega^2} - \frac{1 k_{\perp}^2 v_{the}^2}{2 \omega_{ce}^2} \right) = 0
\end{aligned} \tag{A.6}$$

Using the terminology of the dielectric tensor Eq. (2.2) and equating k to k_{\perp} , we rewrite Eq. (A.6) as

$$\begin{aligned}
\text{Re } D = K_{xx} - & \frac{3}{2} n_{\perp}^2 \left(\frac{1 v_{the}^2 \omega_{pe}^2 \omega^2}{4 c^2 \omega_{ce}^4} + \frac{v_{thi}^2 \omega_{pi}^2}{c^2 \omega^2} \right) \\
& + \frac{n_{\parallel}^2}{n_{\perp}^2} K_{zz} \left(1 - b_e - \frac{3}{2} \frac{1}{\xi_{oe}^2} \right) = 0.
\end{aligned} \tag{A.7}$$

which reduces to Eq. (1.1) for $v_{th\alpha} = 0$.

For sufficiently high plasma densities, the inequality $k_{\perp} \rho_{ci} \ll 1$ is no longer valid, and as the resonant density is approached, the opposite inequality ($k_{\perp} \rho_{ci} \gg 1$) holds. In this limit, many terms in the sum of Bessel functions in Eq. (2.63) contribute significantly to χ_i . As shown by Brambilla, however, the ion susceptibility in this limit can be written in an alternative form which is an expansion in powers of $(k_{\perp} \rho_{ci})^{-1}$. The lowest order term in this expansion for the real part of the ion susceptibility is

$$\begin{aligned}
\text{Re } \chi_i = & \frac{1}{k^2 \lambda_{Di}^2} \left(1 + \zeta_i \text{Re } Z(\zeta_i) \right. \\
& \left. - \zeta_i \text{Im } Z(\zeta_i) \left[\cot \left(\pi \frac{\omega}{\omega_{ci}} \right) + \frac{1}{2\pi} \sum_{n=-\infty}^{\infty} \frac{\omega_{ci}}{\omega - n\omega_{ci}} \text{Re } \frac{dZ(\xi_{ni})}{d\xi_{ni}} \right] \right)
\end{aligned} \tag{A.8}$$

where $\zeta_i = \omega/k_{\perp} v_{thi}$. We expand this expression for the ion susceptibility in the asymptotic limit $\zeta_i \gg 1$. Since $\text{Im } Z(\zeta_i) = \sqrt{\pi} \exp(-\zeta_i^2)$, the contribution of the last term in brackets in Eq. (A.8) is negligible in this limit. The ion susceptibility is then

$$\text{Re } \chi_i \simeq -\frac{k_{\perp}^2 \omega_{pi}^2}{k^2 \omega^2} \left(1 + \frac{3}{2} \frac{k_{\perp}^2 v_{thi}^2}{\omega^2} \right), \quad (\text{A.9})$$

or the same as obtained for the opposite limit. Thus the dispersion of the lower-hybrid wave is adequately described by Eq. (A.7) for all values of $k_{\perp} \rho_{ci}$ in the limit $\zeta_i \gg 1$.

The second term on the right-hand side of Eq. (A.7) is significant if K_{xx} becomes small or if n_{\perp}^2 becomes large, both of which occur as the wave nears the lower-hybrid resonance. The other thermal corrections are less important, and are ignored in this thesis. Generalizing to the full electromagnetic dispersion relation Eq. (2.4), we see that the only significant thermal correction is to \mathcal{A} :

$$\mathcal{A} = K_{xx} - \frac{3}{2} n_{\perp}^2 \frac{\omega_{pi}^2 v_{thi}^2}{\omega^2 c^2} \left(1 + \frac{1}{4} \frac{\omega^4 T_e}{\omega_{ce}^2 \omega_{ci}^2 T_i} \right). \quad (\text{A.10})$$

The rest of the cold plasma dispersion relation remains the same.

Appendix B: Derivation of the Minimum Ion Loss Energy

The analytic calculation of the energy of a banana-trapped ion required for direct orbit loss to the limiter has been performed by Rome, McAlees, Callen, and Fowler.⁷⁷ The procedure is outlined in this appendix. The calculation is similar to numerical computations of banana orbits in that the orbit trajectories are determined with the use of conservation of the ion magnetic moment, conservation of energy, and conservation of canonical angular momentum in the toroidal direction. The simplifications which permit this problem to be treated analytically are the following. The plasma current density J is written as a polynomial expression

$$J = J_o \left[1 - \left(\frac{r}{a} \right)^n \right]^p \quad (B.1)$$

with n and p integers such that the toroidal vector potential $A_\phi(r)$ can be written in closed form, assuming the flux surfaces to be concentric. The analytic representation for $A_\phi(r)$ is given in Eq. (3.1) of Ref. 77, and is proportional to the plasma current. The Versator current profile is estimated from the electron temperature profile measured by Thomson scattering, which has a Gaussian half-width of approximately 7.5 cm. The choice of $n = 2$ and $p = 4$ in Eq. (B.1) is adequate in representing the experimental profile.

Also, the tips of the widest banana orbit for a given minimum minor radius r_b are assumed to lie in the midplane on a flux surface halfway between the minimum and maximum minor radii of the orbit.

From the conservation of the ion angular momentum in the toroidal direction, we have

$$eR_o A_\phi + m_i R v_\phi = \text{constant} \quad (B.2)$$

where R is the major radius of the ion location, and v_ϕ is the ion velocity in the toroidal direction. The velocity v_ϕ is calculated using the conservation of energy and conservation of magnetic moment. The velocity parallel to the magnetic field is

$$\begin{aligned} v_{\parallel} &= \pm v \left(1 - \frac{v_{\perp}^2}{v^2} \right)^{\frac{1}{2}} \\ &= \pm v \left(1 - \frac{R_b}{R} \sin^2 \psi \right)^{\frac{1}{2}} \end{aligned} \quad (B.3)$$

where ψ is the pitch angle of the ion orbit at major radius R_b corresponding to the minimum minor radius r_b . Since the poloidal magnetic field B_θ is much less than the toroidal field B_ϕ , we can approximate $v_\phi \approx v_{\parallel}$, and Eq. (B.1) may be written as

$$eR_o A_\phi \pm m_i v [R(R - R_b \sin^2 \psi)]^{\frac{1}{2}} = \text{constant}. \quad (B.4)$$

The above equation is solved under the condition that the ion orbit with minimum radius r_b intersects the limiter at $r = a$:

$$A_\phi(a) - A_\phi(r_b) = \frac{m_i v}{e R_o} (R_b |\cos \psi| + ((R_o + a)[(R_o + a) - R_b \sin^2 \psi])^{\frac{1}{2}}) \quad (B.5)$$

The value of ψ is obtained with the approximation of the orbit shape described earlier. The magnetic moment of the ion at $R = R_b$ is equated to that at the banana tip ($v_{\parallel} \approx 0$ at $R = R_o - a/2 + r_b/2$):

$$\sin^2 \psi_m \approx \frac{R_o + a/2 + r_b/2}{R_o + r_b} \quad (B.6)$$

This value of ψ_m is substituted into Eq. (B.5) and the velocity v is obtained, from which the minimum ion energy for loss to the limiter is calculated. This ion energy and the corresponding pitch angle ψ_m are plotted in Fig. 17 versus minimum minor radius r_b for several different values of the plasma current.

Appendix C: Rf Probe Tip Construction

The dimensions of the materials of the probe tips used to make rf fluctuation measurements at the plasma edge have been selected with some care so as to provide an electrical match between the coaxial probe tip and the rest of the transmission line. The insulating material used is commercially-available alumina ceramic tubing with a dielectric constant of about 9. The impedance of a coaxial line is

$$Z_c = \frac{60}{\sqrt{\epsilon}} \ln \frac{b}{a} \quad (\Omega) \quad (C.1)$$

where ϵ is the dielectric constant of the insulator, a is the radius of the inner conductor, and b is the inner radius of the outer conductor. The outer diameter of the outer conductor was selected such that it would fit snugly into a standard .085" 50 ohm SMA connector. Several pieces of transmission line were constructed with the above criterion and Eq. (C.1) in mind for which various sizes of inner conductors and ceramic tubes were tried. Each piece was tested by terminating it at 50 ohms at one end and measuring the reflectivity of power fed in from the other end. Measurements were performed over the frequency range 0.5–1.0 GHz. The most satisfactory line consisted of an inner conductor 0.014" in diameter surrounded by two concentric ceramic tubes of inner and outer diameters 0.016" and 0.032", and 0.043" and 0.067", respectively. The outer conductor was 14 gauge, 0.005" wall thickness stainless steel needle of outer diameter 0.081". The maximum measured reflectivity over the range 0.5–1.0 GHz was -17 dB, corresponding to a VSWR of 1.3.

Appendix D: Measurement of the Diffusion Coefficient in the Edge Plasma

In this appendix, the measured edge density profiles are used to calculate the particle diffusion coefficient in that region. Because $\lambda \gg a$, the plasma minor radius, the diffusion at the edge may be analyzed in slab geometry. The equation of continuity for ions is

$$\frac{\partial n_i}{\partial t} + \nabla \cdot (\Gamma_{\parallel} + \Gamma_{\perp}) = n_e n_n \langle \sigma v \rangle - n_e n_i \alpha_r \quad (D.1)$$

where n_e , n_i , and n_n are the local ion, electron, and neutral hydrogen densities, Γ_{\parallel} , Γ_{\perp} are the parallel and perpendicular ion fluxes relative to the magnetic field, and $\langle \sigma v \rangle$ and α_r are the ionization and recombination rates, respectively. Integrating over z and assuming all quantities except Γ_{\parallel} to be independent of z , we obtain

$$\frac{\partial n_i}{\partial t} + \frac{\partial}{\partial x} \Gamma_{\perp} - \frac{2}{w} \Gamma_{\parallel 0} = n_e n_n \langle \sigma v \rangle - n_e n_i \alpha_r \quad (D.2)$$

where w is the length between obstructions along the field, e.g. limiters or port walls, and $\Gamma_{\parallel 0}$ is the particle flux to such obstructions. This flux may be estimated to be $\Gamma_{\parallel 0} = n_i C_s / 4$, where C_s is the ion sound speed. This is the ideal flux to a floating plane probe. The diffusion equation may be written

$$\frac{\partial}{\partial x} (D_{\perp} \frac{\partial n_i}{\partial x}) - n_i (C_s / 2w - n_n \langle \sigma v \rangle - 1/\tau + n_i \alpha_r) = 0 \quad (D.3)$$

where τ is a phenomenological density decay time and we have replaced n_e with n_i . The last two terms in the parentheses are much smaller than the first two and are dropped. Though the edge neutral density is not known, it is probably on the order of 10^{12} cm^{-3} , which is close to the neutral gas fill density. For the measured electron temperatures, the ionization term is less than the parallel diffusion term inside the port, but the two are possibly comparable between the limiter and the wall, assuming the neutral density is not much lower than its assumed edge value. For the purposes of this discussion, however, the ionization term is dropped, and the assumption is made that D_{\perp} and C_s are independent of position in the edge region (which is not strictly valid since the electron temperature is not constant in the scrape-off layer, but is acceptable as the temperature gradient is smaller than the density gradient). The solution of Eq. (D.3) for the theoretical density profile then has an exponential form:

$$n_i(x) = n_i(0) e^{\sqrt{C_s/2wD_{\perp}} x} \quad (D.4)$$

Using the measured exponential density scale lengths and electron temperatures, we can calculate the perpendicular ion diffusion coefficient, though in light of the foregoing assumptions, the result is not expected to be more than an estimate. Table 2 shows the calculated diffusion coefficient, as well as the Bohm diffusion coefficient ($D_{\text{Bohm}} = \frac{1}{16}(cT_e/eB_0)$) for the five cases: with the limiters 2 cm. to either side of the grill port; 1.) probe toroidally outside limiters, 2.)

probe toroidally between limiters, radially between limiter edge and chamber wall, 3.) as in case (2) with probe radially inside grill port in front of grill; and with the limiters located 55 cm to either side of the grill port; 4.) same as (2), and 5.) same as (3).

Table 2

Comparison of Particle Diffusion Coefficients
Under Different Edge Conditions

Case	T_e (eV)	λ (cm)	D_{\perp} (cm ² /sec)	D_{Bohm} (cm ² /sec)
1	20	1.5	5×10^4	1.6×10^4
2	16	0.5	2.6×10^4	1.3×10^4
3	4	0.25	4.1×10^3	3.1×10^3
4	22	1.0	2.1×10^4	1.7×10^4
5	5	0.2	2.9×10^3	3.9×10^3

The experimental diffusion coefficient in Case 1 is uncertain because the width w between limiters is not well-defined for the probe situated 22° from the grill. In consideration of the roughness of the model, the measured edge diffusion coefficients are in reasonable agreement with Bohm diffusion values.

References

1. For a review of theoretical and experimental work on rf heating of plasmas, see M. Porkolab, *Radio-Frequency Heating of Magnetically Confined Plasmas* in Fusion Vol. I, E. Teller, ed., Academic Press (1981).
2. T.H. Stix, *Phys. Rev. Lett.* 15, 878 (1965).
3. J.J. Schuss, *Phys. Fluids* 18, 1178 (1974).
4. P. Bellan and M. Porkolab, *Phys. Fluids* 19, 995 (1976).
5. M. Brambilla, *Nuc. Fusion* 18, 493 (1978).
6. P. Lallia, *Proc. 2nd Topical Conf. on RF Plasma Heating* (Lubbock, Texas), Paper C3 (1974).
7. M. Brambilla, *Nuc. Fusion* 16, 47 (1976).
8. T.H. Stix, The Theory of Plasma Waves McGraw-Hill, N.Y. (1962).
9. M.D. Simonutti, *Phys. Fluids* 18, 1524 (1975).
10. M. Brambilla, *Plasma Phys.* 18, 669 (1976).
11. V.M. Glagolev, *Plasma Phys.* 14, 315 (1972).
12. V.E. Golant, *Sov. Phys.-Tech. Phys.* 16, 1980 (1972).
13. S. Bernabei *et al.*, *Proc. 3rd Symp. on Plasma Heating in Tor. Devices* (Varenna, Italy), E. Sindoni, ed., 68 (1976).
14. S. Suckewer and E. Hinnov, *Nuc. Fusion* 17, 945 (1977).
15. M. Porkolab, S. Bernabei, W. Hooke, R. Motley, and T. Nagashima, *Phys. Rev. Lett.* 38, 230 (1977).
16. P. Lallia, G.W. Pacher, and H.D. Pacher, *Proc. 3rd Symp. on Plasma Heating in Tor. Devices* (Varenna, Italy), E. Sindoni, ed., 79 (1976).
17. H.D. Pacher *et al.*, *Proc. 7th Int. Conf. on Plasma Phys. and Cont. Nuc. Fusion*, (Innsbruck, Austria) Vol. I, 97 (1978).
18. C. Gormezano *et al.*, *Nuc. Fusion* 21, 1047 (1981).
19. C. Gormezano *et al.*, *Proc. 3rd Joint Varenna-Grenoble Int. Symp. on Heating in Tor. Plasmas* (Grenoble, France) Vol. II, 439 (1982).
20. V.E. Golant *et al.*, *Proc. 7th Int. Conf. on Plasma Phys. and Cont. Nuc. Fusion* (Innsbruck, Austria) Vol. I, 113 (1978).
21. C.M. Singh, P. Briand, and L. Dupas, *Proc. 3rd Top. Conf. on Rf Plasma Heating* (Pasadena, Cal.) (1978).
22. P. Briand *et al.*, *Proc. 7th Int. Conf. on Plasma Phys. and Cont. Nuc. Fusion* (Innsbruck, Austria) Vol. I, 65 (1978).
23. C. Gormezano *et al.*, Presented at *11th European Conf. on Cont. Fusion and Plasma Phys.* (Aachen, W. Germany) (1983).
24. R.L. Freeman *et al.*, *Proc. 2nd Joint Varenna-Grenoble Int. Symp. on Heating in Tor. Plasmas* (Como, Italy) (1980).
25. J.J. Schuss *et al.*, *Phys. Rev. Lett.* 43, 274 (1979).
26. J.J. Schuss *et al.*, *Nuc. Fusion* 21, 427 (1981).
27. T. Nagashima and N. Fujisawa, *Proc. Joint Varenna-Grenoble Int. Symp. on Heating in Tor. Plasmas* (Grenoble, France) (1978).
28. T. Fujii *et al.*, *Proc. 7th Int. Conf. on Plasma Phys. and Cont. Nuc. Fusion* (Innsbruck, Austria) Vol. I, 85 (1978).

29. T. Imai *et al.*, *Phys. Rev. Lett.* 43, 586 (1979).
30. N. Suzuki *et al.*, *Proc. 8th Int. Conf. on Plasma Phys. and Cont. Nuc. Fusion Res.* (Brussels, Belgium) (1980).
31. K. Uehara and T. Nagashima, *Proc. 3rd Joint Varenna-Grenoble Int. Symp. on Heating in Tor. Plasmas* (Grenoble, France) Vol. II, 485 (1982).
32. K. Ohkubo, K. Matsuura, and the JIPP T-II Group, *IPPJ-366*, Nagoya University (1979).
33. K. Ohkubo, S. Takamura, and the JIPP T-II Group, *Proc. 3rd Joint Varenna-Grenoble Int. Symp. on Heating in Tor. Plasmas* (Grenoble, France) Vol. II, 543 (1982).
34. M. Porkolab *et al.*, *Proc. 3rd Joint Varenna-Grenoble Int. Symp. on Heating in Tor. Plasmas* (Grenoble, France) Vol. II, 543 (1982).
35. M. Porkolab *et al.*, *Proc. 9th Int. Conf. on Plasma Phys. and Cont. Nuc. Fusion Res.* (Baltimore, Md., 1982) IAEA, Vienna, Austria, Vol. I, 227 (1983).
36. M. Porkolab *et al.*, *Proc. 5th Top. Conf. on Rf Heating of Plasmas* (Madison, Wisc.) (1983).
37. M. Porkolab and the Alcator Group, Presented at *11th European Conf. on Cont. Fusion and Plasma Phys.* (Aachen, W. Germany) (1983).
38. J. Stevens *et al.*, *Proc. 3rd Joint Varenna-Grenoble Int. Symp. on Heating in Tor. Plasmas* (Grenoble, France) Vol. II, 455 (1982).
39. S.L. Davis, PDX and PLT Groups, *Plasma Phys.* 25, 189 (1983).
40. T. Yamamoto *et al.*, *J. Phys. Soc. Japan* 48, 1349 (1980).
41. K. Uehara *et al.*, *J. Phys. Soc. Japan* 51, 1958 (1982).
42. M. Porkolab, *Phys. Fluids* 17, 1432 (1974).
43. M. Porkolab, *Phys. Fluids* 20, 2058 (1977).
44. T. Yamamoto, T. Imai, M. Shimada, *Phys. Rev. Lett.* 45, 716 (1980).
45. S.C. Luckhardt, M. Porkolab, K.I. Chen, and S. Knowlton, *Proc. 4th Top. Conf. on Rf Heating in Plasmas* (Austin, Tex.) Paper B6 (1981).
46. S.C. Luckhardt *et al.*, *Phys. Rev. Lett.* 48, 152 (1982).
47. S.C. Luckhardt *et al.*, *Proc. 3rd Joint Varenna-Grenoble Int. Symp. on Heating in Tor. Plasmas* (Grenoble, France) Vol. II, 529 (1982).
48. K. Ohkubo *et al.*, *Proc. 4th Top. Conf. on Rf Heating in Plasmas* (Austin, Tex.) Paper B4 (1981).
49. Y. Terumichi, *Proc. 4th Top. Conf. on Rf Heating in Plasmas* (Austin, Tex.) Paper B11 (1981).
50. S. Tanaka *et al.*, *Proc. 3rd Joint Varenna-Grenoble Int. Symp. on Heating in Tor. Plasmas* (Grenoble, France) Vol. II, 615 (1982).
51. G. Tonon *et al.*, *Proc. 3rd Joint Varenna-Grenoble Int. Symp. on Heating in Tor. Plasmas* (Grenoble, France) Vol. II, 623 (1982).
52. N. Suzuki *et al.*, *J. Nuc. Materials* 93&94, 282 (1980).
53. B. Richards, D. Stone, A. Fisher, and G. Bekefi, *Comments Plasma Phys. and Cont. Fusion* 3, 117 (1978).
54. D. Stone, Ph.D thesis, Dept. of Physics, Massachusetts Institute of Technology (1979).
55. B. Richards, Ph.D thesis, Dept. of Physics, Massachusetts Institute of Technology (1981).
56. K. Hackett, Ph.D thesis, Dept. of Physics, Massachusetts Institute of Technology (1983).
57. A. Fisher, Ph.D thesis, Dept. of Physics, Massachusetts Institute of Technology (1983).

58. B. Fried and S. Conte, The Plasma Dispersion Function, Academic Press, N.Y. (1961).
59. J.P. Schmidt, *J. Plasma Phys.* 12, 51 (1974).
60. T. Tang, K.Y. Fu, and M.W. Farshori, *Plasma Phys.* 21, 127 (1979).
61. H. Kritz and O. Eldridge, *Nuc. Fusion* 15, 465 (1975)
62. D.W. Ignat, *Phys. Fluids* 24, 1110 (1981).
63. D.E. Baldwin and G. Rowlands, *Phys. Fluids* 9, 2444 (1966).
64. C.F.F. Karney, *Phys. Fluids* 22, 2188 (1979).
65. M. Brambilla and Y. Chen, *Nuc. Fusion* 23, 541 (1983).
66. S. Riyopoulos, E. Ott, and T. Antonsen, *Bull. Am. Phys. Soc.* 27, 1101 (1982).
67. N.J. Fisch, *Phys. Rev. Lett.* 41, 873 (1978).
68. C.F.F. Karney and N.J. Fisch, *Phys. Fluids* 22, 1817 (1979).
69. V. Decyk, G. Morales, and J. Dawson, *Proc. 3rd Joint Varenna-Grenoble Int. Symp. on Heating in Tor. Plasmas* (Grenoble, France) Vol. II, 517 (1982).
70. B.A. Trubnikov, in Reviews of Plasma Physics Vol. I, M.A. Leontovich, ed., Consultants Bureau, N.Y. (1965).
71. J.J. Schuss, T. Antonsen, and M. Porkolab, *Nuc. Fusion* 23, 201 (1983).
72. C.M. Surko, R.E. Slusher, J.J. Schuss, R.R. Parker, I.H. Hutchinson, D. Overskei, and L.S. Scaturro, *Phys. Rev. Lett.* 43, 1016 (1979).
73. P.T. Bonoli and E. Ott, *Phys. Rev. Lett.* 46, 424 (1981).
74. P.T. Bonoli and E. Ott, *Phys. Fluids* 25 359 (1982).
75. J.L. Kulp, Ph.D thesis, Dept. of Electrical Engineering and Computer Science, Massachusetts Institute of Technology (1978).
76. For a review of trapped particle effects, see B.B. Kadomtsev and O.P. Pogutse, *Nuc. Fusion* 11, 67 (1971).
77. J. Rome, D. McAlees, J. Callen, and R. Fowler, *Nuc. Fusion* 16, 55 (1976).
78. M. Greenwald, J.J. Schuss, and D. Cope, *Nuc. Fusion* 20, 783 (1980).
79. S. Tanaka, S. Takamura, and T. Okuda, *Proc. 3rd Joint Varenna-Grenoble Int. Symp. on Heating in Tor. Plasmas* (Grenoble, France) Vol. II, 607 (1982).
80. M. Brambilla and A. Cardinali, *Plasma Phys.* 24, 1187 (1982).
81. S. Bernabei and D.W. Ignat, *Nuc. Fusion* 22, 735 (1982).
82. S. Weinberg, *Phys. Rev.* 126, 1899 (1962).
83. R. Englade, P.T. Bonoli, and T. Antonsen, *Proc. 4th Top. Conf. on Rf Heating in Plasmas* (Austin, Tex.) Paper C14 (1981).
84. F.L. Hinton and R.D. Hazeltine, *Rev. Mod. Phys.* 18, 1160 (1975).
85. B. Coppi and E. Mazzucato, *Phys. Lett.* 71A, 337 (1979).
86. B. Coppi, *Comments Plasma Phys. and Cont. Fusion* 5, 261 (1980).
87. B. Coppi, *Comments Plasma Phys. and Cont. Fusion* 7, 1 (1982).
88. R.P.H. Chang and M. Porkolab, *Phys. Rev. Lett.* 32, 1227 (1974).
89. Yuichi Takase, Sc.D thesis, Dept. of Physics, Massachusetts Institute of Technology (1983).
90. A version of the original Brambilla code described in Ref. 7 was kindly supplied to us by S. Bernabei of PPPL.
91. M. Brambilla, *Nuc. Fusion* 19, 1343 (1979).

92. R.R. Parker, *MIT-Res. Lab. of Elec. Quart. Prog. Rep.* No. 102, 97 (1971).
93. A. Fukuyama, Ph.D thesis, Dept. of Electronics, Okayama University, Okayama, Japan (1980).
94. J. Stevens, M. Ono, R. Horton, and J.R. Wilson, *Nuc. Fusion* 21, 1259 (1981).
95. M. Abramowitz and I. Stegun, eds., Handbook of Mathematical Functions, Dover (1965).
96. P. Bellan and M. Porkolab, *Phys. Fluids* 17, 1592 (1974).
97. The Versator VUV spectrometer system was constructed by Kuo-In Chen.
98. The charge-exchange analyzer used on Versator was originally constructed for use on Alcator A by D. Cook [see D.L. Cook, Sc.D thesis, Dept. Of Nuclear Engineering, Massachusetts Institute of Technology (1976)] and adapted for operation on Versator by S. McDermott [see F.S. McDermott, B.S. thesis, Dept. of Physics, Massachusetts Institute of Technology (1979)].
99. D.L. Book, NRI Plasma Formulary, Supported by the Office of Naval Research (1978).
100. C.F. Barnett and J.A. Ray, *Nuc. Fusion* 12, 65 (1972).
101. F.S. McDermott, Private communication (1980); and K.I. Chen, Private communication (1982).
102. C. Wharton, "Review of Neutral Particle Plasma Diagnostics," Cornell University, Laboratory of Plasma Studies (1976).
103. The Thomson scattering diagnostic was built by A. Fisher (see Ref. 57).
104. The soft X-ray spectrometer was assembled by M. Mayberry and D. Hinshelwood.
105. The 75 GHz zebra stripe interferometer was constructed by T. Gentile.
106. C.E. Bush and J.F. Lyon, ORNL TM-6148 (1977).
107. K.I. Chen, Private communication (1982).
108. M. Mayberry, Private communication (1982).
109. S.P. Hirshman, R.J. Hawryluk, and B. Birge, *Nuc. Fusion* 17, 611 (1977).
110. The four-waveguide top-launching grill was designed by S.C. Luckhardt (1981).
111. The design of the Alcator C arc detector was provided by J.J. Schuss (1982).
112. J.G. LaFramboise, Institute for Aerospace Studies Report No. 100 (1966).
113. F.F. Chen, *Electric Probes*, in Plasma Diagnostic Techniques, R.H. Huddlestone and S.L. Leonard, eds., Academic Press, 113 (1965).
114. L.S. Scaturro and B. Kusse, *Nuc. Fusion* 18, 1717 (1978).
115. K. Uehara *et al.*, *Plasma Phys.* 21, 89 (1979).
116. R.K. Fisher and R.W. Gould, *Phys. Fluids* 14, 857 (1971).
117. F. Parlangue and the Petula Group, Proc. 2nd Joint Varenna-Grenoble Int. Symp. on Heating in Tor. Plasmas (Como, Italy) (1980).
118. G.W. Pacher *et al.*, Proc. 4th Top. Conf. on Rf Heating in Plasmas (Austin, Tex.), Paper E2 (1981).
119. W. Hooke, Private communication (1979).
120. D. Ruzic, R. Moore, D. Manos, and S. Cohen, *J. Vac. Sci. Technol.* 20, 1313 (1982).
121. A.J. Hatch, *Nuc. Instr. and Meth.* 41, 261 (1966); and references therein.
122. A.J. Hatch and H.B. Williams, *Phys. Rev.* 112, 681 (1958).
123. G.M. McCracken and P.E. Stott, *Nuc. Fusion* 19, 889 (1979).

124. J. Halbritter, *Proc. 10th Int. Symp. on Discharges and Electrical Insulation in Vacuum* (Columbia, S.C.) (1982).
125. J. Halbritter, *J. Appl. Phys.* 53, 6475 (1982).
126. M. Grundner and J. Halbritter, *J. Appl. Phys.* 51, 5396 (1980).
127. J. Lelegard and A. Schram, *J. Nuc. Mat.* 76&77, 637 (1978).
128. S.C. Luckhardt, Private communication (1983).
129. A. Massarotti and A. Turin, AERE-TRANS No. 890 (1962).
130. W.E. Luthiger, B.S. thesis, Dept. of Nuclear Engineering, Massachusetts Institute of Technology (1982).
131. J. Timberlake *et al.*, *J. Vac. Sci. Technol.* 20, 1309 (1982).
132. S. Cohen, Presented at *2nd Int. Conf. on Surf. Effects in Cont. Nuc. Fusion Devices* (San Francisco, Cal.) (1976).
133. F. Soeldner *et al.*, *Proc. 3rd Joint Varenna-Grenoble Int. Symp. on Heating in Tor. Plasmas* (Grenoble, France) Vol. II; 599 (1982).
134. J.L. Terry, E.S. Marmor, K.I. Chen, and H.W. Moos, *Phys. Rev. Lett.* 39, 1615 (1977).
135. S. Suckewer, E. Hinnov, and J. Schivell, *Bull. Am. Phys. Soc.* 23, 697 (1978).
136. K.I. Chen and M.E. Huber, *Bull. Am. Phys. Soc.* 27, 1060 (1982).
137. E. Hinnov, J. Hosea, F. Jobes, E. Meservey, G. Schmidt, and S. Suckewer, *Nuc. Fusion* 22, 325 (1982).
138. K.H. Burrell and S.K. Wong, *Nuc. Fusion* 19, 1571 (1979).
139. S. Suckewer *et al.*, *Nuc. Fusion* 21, 981 (1981).
140. E.R. Muller, K. Behringer, and H. Niedermeyer, *Nuc. Fusion* 22, 1651 (1982).
141. E.S. Marmor, J.E. Rice, J.L. Terry, and F.H. Seguin, *Nuc. Fusion* 22, 1567 (1982).
142. L.P. Mix and G. Bekefi, *Phys. Fluids* 15, 2020 (1972).
143. T. Sherlock, B.S. thesis, Dept. of Physics, Massachusetts Institute of Technology (1983).
144. R.R. Parker, Alcator Group Internal Report (1979).
145. R.R. Parker, *Bull. Am. Phys. Soc.* 27, 986 (1982).